Volume Electron Microscopy in Life Sciences: Scientific Achievements from Various Research Fields

Article Collection

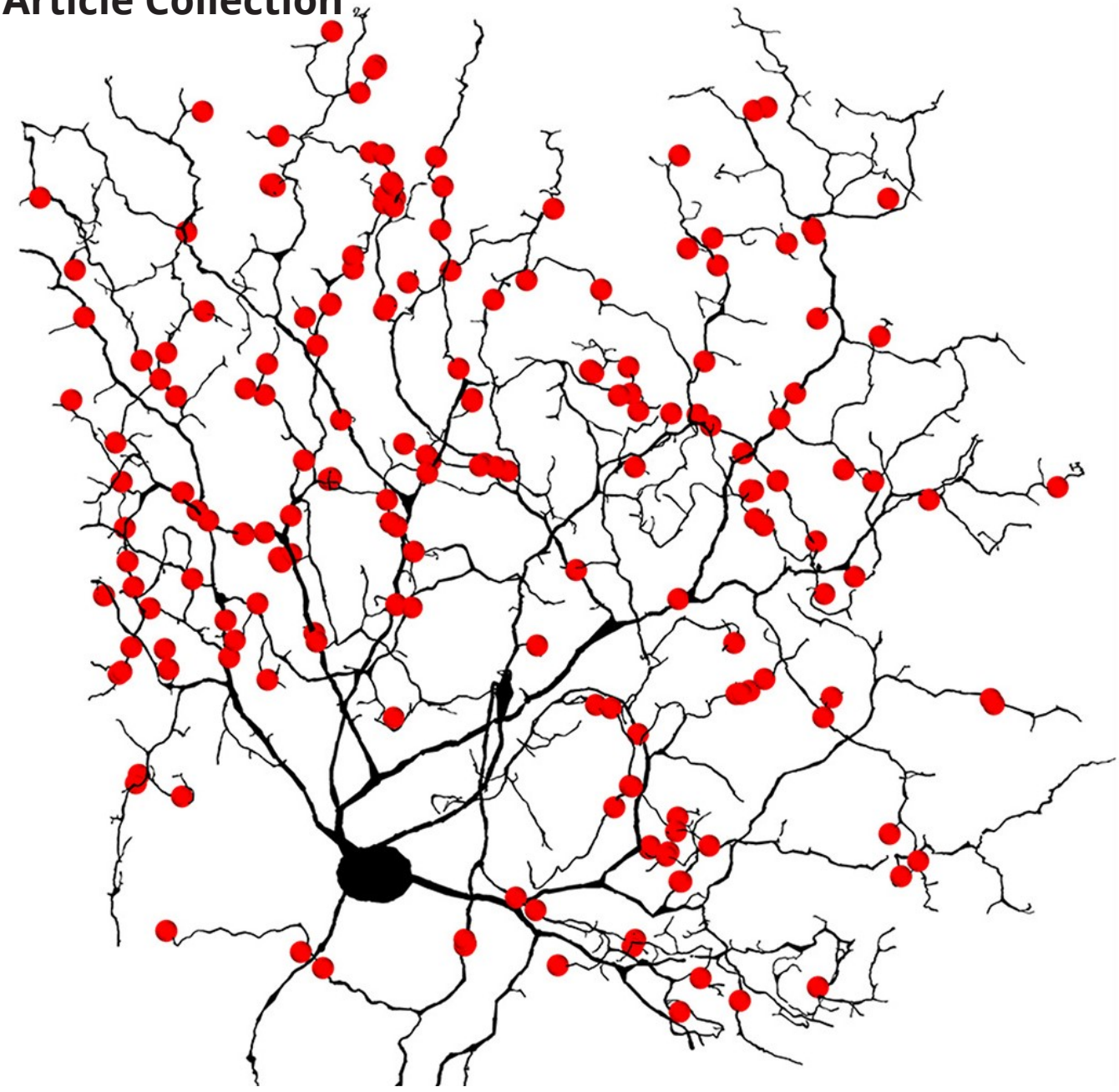

WILEY

CURRENT PROTOCOLS
A Wiley Brand

Sponsored by:

ZEISS
Seeing beyond

Cellular ultrastructure in 3D context

Seeing beyond

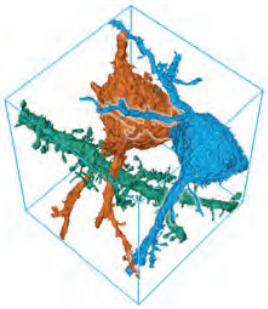

ZEISS Volutome

Transform your conventional FE-SEM to a serial block-face imaging system and acquire the ultrastructure of biological samples in 3D. Enjoy integrated processing and visualization of your data – and reveal the details that answer your scientific questions.

zeiss.com/volutome

Contents

Image was prepared with SBF-SEM tools and processing software and shows the distribution of synapses onto broad thorny ganglion cell 103.

Introduction

Even though life exists in 3D, until the beginning of this century, most electron microscopy methods provided only 2D image data. Thanks to recent advances, electron microscopy can now go deeper into the structure of cells and tissues. 3D EM technologies commonly known as volume electron microscopy (vEM) are declared to be the one of the seven technologies to be watched in 2023 (*Nature* 2023). The increasing number of publications in this area confirms the importance and interest of volume EM in the academic community.

Volume electron microscopy (vEM) is a group of techniques that encompasses high-resolution imaging methods used to reveal the 3D structure of cells, tissues, and small model organisms at nanometer resolution. vEM comprises imaging technologies based on scanning electron microscopy and transmission electron microscopy (TEM). In all cases, specimen images are generated and combined to form a digital representation of the specimen volume. Particularly, individual images are created by repeatedly slicing the specimen into thin sections and then imaging either the sections or the exposed face of the sample.

SEM-based vEM techniques such as array tomography (AT), serial block-face SEM (SBF-SEM), and focused ion beam SEM (FIB-SEM) all use the same strategy of capturing a series of images that are combined to form a 3D digital representation of the original sample volume. Lately, vEM has been widely employed to investigate cell structure and tissues in multiple fields, such as neuroscience, immunology, cancer research, developmental biology, plant biology, and biomaterials.

At the beginning of this article collection, you will find a study by Sampathkumar, V. *et al.* (2020), which uses genetic labeling combined with large-volume serial electron microscopy such as AT (i.e., "connectomics") to investigate the projection from clusters of neuronal cell bodies (thalamic posterior medial nucleus) to a specific cortex region (secondary somatosensory cortex) in mice. The research provides the first insights into the higher-order thalamocortical synaptic ultrastructure and highlights the need for more analyses as such connectivity likely represents most of the thalamocortical circuitry.

Following, Yang, R. *et al.* (2019) report the 3D reconstructions of mouse circumvallate taste buds. The study uses SBF-SEM to investigate the characteristics and interrelationships of taste cells in the circumvallate papillae of adult mice. Type I cells have an indented, elongated nucleus with invaginations, folded plasma membrane, and multiple apical microvilli in the taste pore, while Type II cells (i.e., receptor cells) and almost one-quarter of Type III cells (i.e., "synaptic cells") exhibit an atypical mitochondrion near nerve fibers. In murine circumvallate taste buds, Type I cells prevails with over 50% of the population.

Somorjai, I. M. & Holland, N. D. (2020) also employed SBF-SEM to describe the sensory peripheral nervous system (PNS) in the tail of a cephalochordate, *Asymmetron lucayanum*. The researchers discovered a relationship between specific neurons from cephalochordates and Rohon-Beard cells of vertebrates. Moreover, extramedullary neurons originating from the ventral epidermis in cephalochordates contrast with vertebrate sensory neurons arising from placodes and neural crest. These findings give essential information about the evolution of the PNS in the phylum Chordata.

The neural circuits accountable for primates' responses to moving stimuli are not entirely understood. Bordt, A. S. *et al.* (2021), aiming to gain insights into these neural circuits, produced a connectome from the central macaque retina using SBF-SEM, reconstructed a broad thorny cell, and analyzed its synaptic inputs. Considering the lack of bipolar cell inputs, the amacrine cells are likely to provide much of the excitatory input in addition to inhibitory input.

Furthermore, this collection also covers a study by Decelle, J. *et al.* (2021) on the photosymbiosis between colonial Collodaria and their microalga dinoflagellate (*Brandtodinium*) using multimodal subcellular imaging e.g. FIB-SEM for vEM imaging. The symbiosis is very dynamic, whereby symbionts interact with different host cells via extracellular vesicles within the colony. The findings enriched our understanding of oceanic photosymbiosis functioning, paving the way for more studies to further assess its biogeochemical significance.

Heinen-Weiler, J. *et al.* (2021) uses FIB-SEM to determine the mitochondrial features in cardiac tissue samples. The study evaluated whether classical 2D TEM analysis of the cardiomyocyte ultrastructure accurately describes the mitochondrial compartment, reflecting the mitochondrial number, size, dispersion, distribution, and morphology. By unmasking mitochondrial heterogeneity,

the researchers demonstrate the superiority of focused ion beam-scanning electron microscope tomography of cardiomyocytes over classical 2D TEM analyses.

Lastly, Guerin, C. J. & Lippens, S. (2021) review the relevance of correlative light and electron microscopy as a valuable tool to image samples across resolution scales and link data on structure and function. The recent advances in vEM technologies encouraged the development of 3D correlative light and volume electron microscopy (vCLEM), and vCLEM studies are getting more and more frequent. The community is very active and further development can be expected.

Overall, the field is evolving rapidly as more scientists recognize the potential of vEM to provide significant insights into the nanoscale spatial organization of organelles, cells, organs, and organisms. vEM has been attracting tool developers, including microscopists, physicists, chemists, engineers, and computational scientists, focused on improving the speed and throughput of vEM. These improvements are making vEM both easier to use and more accessible, even to those with little to no experience in electron microscopy.

Through the methods and applications presented in this article collection, we aim to educate researchers on new technologies and techniques about vEM. For more information, we encourage you to visit the Zeiss website to learn more and explore options to enhance your research.

Dr. Birgit Foltas
Editor at *Wiley Analytical Science*

References

Sampathkumar, V., Miller-Hansen, A., Sherman, S.M., Kasthuri, N. (2021) An ultrastructural connectomic analysis of a higher-order thalamocortical circuit in the mouse. *European Journal of Neuroscience,* 53(3). https://doi.org/10.1111/ejn.15092

Yang, R., Dzowo, Y. K., Wilson, C. E., Russell, R. L., Kidd, G. J., Salcedo, E., Lasher, R. S., Kinnamon, J. C., Finger, T.E. (2020) Three-dimensional reconstructions of mouse circumvallate taste buds using serial blockface scanning electron microscopy: I. Cell types and the apical region of the taste bud. *Journal of Comparative Neurology,* 528(5). https://doi.org/10.1002/cne.24779

Holland, N. D., and Somorjai I. M. L. (20202) The sensory peripheral nervous system in the tail of a cephalochordate studied by serial blockface scanning electron microscopy. *Journal of Comparative Neurology,* 528(15). https://doi.org/10.1002/cne.24913

Bordt, A. S., Patterson, S. S., Girresch, R. J., Perez, D., Tseng, L., Anderson, J. R., Mazzaferri, M. A., Kuchenbecker, J. A., Gonzales-Rojas, R., Roland, A., Tang, C., Puller, C., Chuang, A. Z., Mosinger Ogilvie, J., Neitz, J., Marshak D. W. (2021) Synaptic inputs to broad thorny ganglion cells in macaque retina. *Journal of Comparative Neurology,* 529(11). https://doi.org/10.1002/cne.25156

Decelle, J., Veronesi, G., LeKieffre, C., Gallet, B., Chevalier, F., Stryhanyuk, H., Marro, S., Ravanel, S., Tucoulou, R., Schieber, N., Finazzi, G., Schwab, Y., Musat N. (2021) Subcellular architecture and metabolic connection in the planktonic photosymbiosis between Collodaria (radiolarians) and their microalgae. *Environmental Microbiology,* 23(11). https://doi.org/10.1111/1462-2920.15766

Heinen-Weiler, J., Hasenberg, M., Heisler, M., Settelmeier, S., Beerlage, A.-L., Doepper, H., Walkenfort, B., Odersky, A., Luedike, P., Winterhager, E., Rassaf, T., Hendgen-Cotta U. B. (2021) Superiority of focused ion beam-scanning electron microscope tomography of cardiomyocytes over standard 2D analyses highlighted by unmasking mitochondrial heterogeneity. *Journal of Cachexia, Sarcopenia and Muscle,* 12(4). https://doi.org/10.1002/jcsm.12742

Guerin C. J., and Lippens S. (2021) Correlative light and volume electron microscopy (vCLEM): How community participation can advance developing technologies. *Journal of Microscopy,* 284(2). https://doi.org/10.1111/jmi.13056

Received: 13 June 2020 | Revised: 8 December 2020 | Accepted: 10 December 2020

DOI: 10.1111/ejn.15092

RESEARCH REPORT

EJN European Journal of Neuroscience FENS WILEY

An ultrastructural connectomic analysis of a higher-order thalamocortical circuit in the mouse

Vandana Sampathkumar | **Andrew Miller-Hansen** | **S. Murray Sherman** | **Narayanan Kasthuri**

Department of Neurobiology, University of Chicago, Chicago, IL, USA

Correspondence
S. Murray Sherman and Narayanan Kasthuri, Department of Neurobiology, University of Chicago, Chicago, IL 60637, USA.
Email: msherman@bsd.uchicago.edu; bobbykasthuri@uchicago.edu

Funding information
National Institutes of Health, Grant/Award Number: EY022388, NS094184 and NS113922; National Institute of Mental Health, Grant/Award Number: MH109100; National Eye Institute, Grant/Award Number: EY028812

Abstract

Many studies exist of thalamocortical synapses in primary sensory cortex, but much less in known about higher-order thalamocortical projections to higher-order cortical areas. We begin to address this gap using genetic labeling combined with large volume serial electron microscopy (i.e., "connectomics") to study the projection from the thalamic posterior medial nucleus to the secondary somatosensory cortex in a mouse. We injected into this thalamic nucleus a cocktail combining a *cre*-expressing virus and one expressing *cre*-dependent ascorbate peroxidase that provides an electron dense cytoplasmic label. This "intersectional" viral approach specifically labeled thalamocortical axons and synapses, free of retrograde labeling, in all layers of cortex. Labeled thalamocortical synapses represented 14% of all synapses in the cortical volume, consistent with previous estimates of first-order thalamocortical inputs. We found that labeled thalamocortical terminals, relative to unlabeled ones: were larger, were more likely to contain a mitochondrion, more frequently targeted spiny dendrites and avoided aspiny dendrites, and often innervated larger spines with spine apparatuses, among other differences. Furthermore, labeled terminals were more prevalent in layers 2/3 and synaptic differences between labeled and unlabeled terminals were greatest in layers 2/3. The laminar differences reported here contrast with reports of first-order thalamocortical connections in primary sensory cortices where, for example, labeled terminals were larger in layer 4 than layers 2/3 (Viaene et al., 2011a). These data offer the first glimpse of higher-order thalamocortical synaptic ultrastructure and point to the need for more analyses, as such connectivity likely represents a majority of thalamocortical circuitry.

Abbreviations: AAV, Adeno-associated virus; DV, Dorso-Ventral; ML, Medio-Lateral; AP, Antero-Posterior; APX-C, Cytoplasmic Targeted Ascorbate peroxidase; APEX2, Engineered Ascorbate peroxidase; ATUM, Automatic Tape-collecting Ultramicrotome; DAB, Di-Amino-Benzidine; FOV, Field of View; H_2O_2, Hydrogen Peroxide; L1, Layer 1; L2/3, Layer 2/3; L4, Layer 4; L5, Layer 5; L6, Layer 6; POm, Posterior medial nucleus of the thalamus; PSD, Postsynaptic density; S2, Second somatosensory cortical area; M1, Primary motor cortical area; VPm, Ventral Posteromedial nucleus of thalamus; S1, Primary somatosensory cortical area; SEM, Scanning Electron Microscope.

Edited by: Dr. László Acsády

1 | INTRODUCTION

Classification of thalamic nuclei into first- and higher-order relays was an important step in understanding principles of thalamocortical interactions (Sherman, 2016; Sherman & Guillery, 2013)). In this scheme, first-order thalamic nuclei transmit information from a subcortical source to primary cortical areas (e.g., retinal input to lateral geniculate nucleus to primary visual cortex), and higher-order nuclei transmit information from layer 5 neurons of one cortical area to another (e.g., as is the case for much of pulvinar and corticocortical communication between primary visual cortex and secondary visual areas). Because all cortical areas receive an input from thalamus and because higher-order thalamic nuclei underlie much of this trans-thalamic corticocortical processing (Sherman, 2016; Sherman & Guillery, 2013), it is of obvious importance to better understand the functional organization of higher-order thalamocortical circuitry. Such an understanding inevitably relies heavily on morphological analysis, and the "gold standard" for morphologically identifying neuronal connections remains electron microscopy. However, to date all or nearly all such studies have focused on first-order thalamocortical pathways, primarily from the lateral geniculate nucleus to primary visual cortex (Ahmed et al., 1994; Anderson et al., 2009; Hornung & Garey, 1981; Peters & Feldman, 1977; Peters et al., 1976) and the ventral posterior nucleus to primary somatosensory cortex (White & Rock, 1979; Hersch & White, 1981; White et al., 2004; Rah et al., 2013; Bopp et al., 2017; Rodriguez-Moreno et al., 2018; Motta et al., 2019; but see Zhou et al., 2018; Chomsung et al., 2010). What is sorely needed are ultrastructural data from further examples of higher-order thalamocortical circuitry.

To begin to address this, we have undertaken an ultrastructural analysis of the higher-order thalamocortical pathway from the posterior medial nucleus to the second somatosensory area in a mouse. To do so, we paired recent advances in engineering proteins for electron-dense genetic labeling with automated large volume serial electron microscopy (Kasthuri et al., 2015; Lam et al., 2015; Martell et al., 2017) to clearly identify the terminals and synapses of these higher-order thalamocortical neurons in all layers of secondary somatosensory cortex.

Our findings include evidence for significant differences between labeled thalamocortical terminals and synapses and unlabeled examples, evidence for laminar variation in the density and synaptic organization of thalamocortical connections, and evidence for differences in some parameters between our analysis of the higher-order relay and prior published data of the first-order relay from the ventral posterior nucleus to the primary somatosensory cortex.

Significance

Most thalamocortical projections are from higher-order thalamic nuclei to higher-order cortical areas, yet detailed ultrastructural studies have been mostly limited to first-order projections. To begin to bridge this gap, we used virally mediated labeling and serial electron microscopy to detail a higher-order thalamocortical projection from the posterior medial nucleus to the secondary somatosensory cortical area in the mouse. We document how labeled thalamocortical synapses differ from unlabeled ones, how these vary across cortical layers, and how this pathway differs from first-order projections. This extends our understanding of thalamocortical organization while piloting a useful approach for ultrastructural study of long-range projections. Further, such studies are needed to gain insights into this circuitry, which is so important to cognitive functioning.

Clearly, a better understanding of thalamocortical functioning requires additional characterization of these pathways, and we regard our effort as an early attempt at this effort.

2 | Methods

All procedures were performed in accordance with the University of Chicago Institutional Animal Use and Care Committee. Data were obtained from one male wild-type C57/bl6 mouse (JAX).

2.1 | Viral injections

We injected a cocktail (1:1 ratio, 60 nL total volume) of two types of AAV using stereotactic coordinates to target the posterior medial nucleus of the thalamus (from bregma in mm: DV, -3.3; ML, +1.3; AP, -1.3; Mo & Sherman, 2019). One virus expressed Cre in local neurons (pENN.AAV1.hSyn.Cre.WPRE.hGH Addgene viral prep # 105553-AAV1) and the second expressed APX-C in a cre-dependent fashion (rAAV9/AAV-CAG-DIO-APEX2NES made at the Gene therapy center vector core at UNC at Chapel Hill). AAV-CAG-DIO-APEX2NES was a gift from Joshua Sanes (Addgene plasmid # 79907; http://n2t.net/addgene:79907; RRID:Addgene_79907).

The mouse was injected with this cocktail at 10 weeks of age, returned to its cage for 4 weeks to allow for transgene expression and transport of the label, and then processed for

peroxidase staining and large volume electron microscopy as described below.

2.2 | Electron microscopy

The mouse was heavily anesthetized with pentobarbital (60 mg/kg intraperitoneal) to be non-responsive to toe pinch and transcardially perfused with 50 ml of 0.1M cacodylate buffer followed by 20 ml of buffered 2% paraformaldehyde and 2.5% glutaraldehyde at the rate of 3ml/min. The brain was removed, and vibratome sections (350 μm thick) were cut containing the cortical and thalamic regions of interest using the angle for cutting that maximizes connectivity in somatosensory thalamocortical connections (Agmon & Connors, 1991). The sections were then stained with Di-Amino-Benzidine (DAB) and H_2O_2 to visualize APX-C labeling (Joesch et al., 2016). The samples were evaluated at the macro scale for the intensity of the DAB reaction and its localization to the appropriate brain regions, namely, the posterior medial nucleus and second somatosensory cortical area. The posterior medial nucleus was distinguishable by eye, and the second somatosensory cortical area was localized based on its distinctive pattern of labeling via the observed projection from the posterior medial nucleus and its clear border with the primary somatosensory, or barrel cortex. Samples with appropriate staining were subsequently stained with multiple rounds of osmium and reduced osmium, *en bloc* uranium and lead, dehydrated, and then plastic embedded (Hua et al., 2015). Approximately three-thousand 50-nm-thick ultra-thin serial sections were cut with a cross-section of 1.7x1.1 mm, collected on Kapton tape, attached to wafers, and carbon coated (Kasthuri, 2015; Morgan et al., 2016). We subsampled this volume for higher-resolution tracing for each layer: about 200 sections for layers 1, 4, 5, and 6 and 100 sections for layers 2/3. Cortical layers were identified using cytological features like cell size and density and distance from pia and white matter tracts along with reference to the Allen Mouse Brain Atlas (© 2004 Allen Institute for Brain Science. Allen Mouse Brain Atlas, https://mouse.brain-map.org/static/atlas). Briefly, layer 1 was identified by the sparse population of cell bodies, in contrast with layer 2. Layers 2/3 were distinguished by cytoarchitecture and by being sufficiently distant from layers 1 and 4 using distance from pia and the Allen Institute Mouse Atlas. The border between layers 4 and 5 was seen due to a higher cell density in layer 4, and layer 5 can be identified by the presence of large pyramidal cells, in contrast with layers 4 and 6

Ultra-thin sections were then imaged with a backscatter detector on a Zeiss Gemini SEM 300 and ATLAS software. Low-resolution data were imaged at 40 nm x, y pixel resolution and large fields of view were collected by montaging individual tiles (three tiles each of 16k x12k pixels stitched together with 10% overlap to produce a 44.7k x 12k pixel image; because of the 10% overlap; the result is 44.7k x 12k pixels rather than 48k x 12k). Fine-resolution electron microscopic imaging was done at 6 nm resolution and was a single-tile FOV (12k x 12k pixels). Imaging rates were 0.8 μs per pixel for low-resolution images and 1.6 μs /pixel for fine-resolution images. Individual tiles for lower-resolution datasets were stitched in 2D and linearly aligned in 3D using a plugin, TrakEM2 (Cardona et al., 2012), in the open source image processing program *ImageJ*. Fine-resolution image stacks often required further alignment using non-linear deformations of the image, which was performed using the program *aligntk* (https://mmbios.pitt.edu/about-us/acknowledgements) on local desktops.

2.3 | Tracing neurons and their connections

For tracing APX-C labeled axons, classifying their postsynaptic targets morphologically, and identifying and characterizing their synaptic features (e.g., measuring spine, terminal, and glia diameters), we used Knossos annotation software (Boergens et al., 2017). For determining density of APX-C labeled terminals and synapses across all layers, we chose three subvolumes of cubes 5 μm on a side in each cortical layer, targeting a vertical zone of the highest APX-C labeling density as identified from the lower-resolution datasets. In these subvolumes, we annotated all unlabeled and APX-C-labeled synapses. In the same volumes, we randomly selected dendrites (>5 μm in diameter), annotated all potential spines from that dendrite in the volume, and classified it as aspiny or spiny, the latter defined as >0.5 spines/μm. Specifically in layers 2/3, where APX-C labeling was densest (see **Results**), we annotated every terminal as APX-C labeled or unlabeled on spines on those dendrites. We defined a 'potential synapse' in our datasets as any membrane to membrane apposition between a labeled axon with any sign of a synapse, either an axonal terminal (see below) or the presence of postsynaptic densities in targets immediately opposed to labeled terminals. We define axonal terminal as a swelling of the axon, often with clearly identified synaptic vesicles (Figure 2). We searched in the immediate vicinity of these axonal swellings to look for postsynaptic targets, which are identified by postsynaptic densities. In addition, for postsynaptic sites with a clear labeled terminal, we searched each postsynaptic site, particularly spines, for evidence of other synaptic contacts (i.e., we look for additional vesicle filled axonal boutons and other postsynaptic densities on the same spine). For measuring diameters of axonal terminals, spines, and glial appositions, we examined electron microscopic stacks and used the largest diameter for that object in the stack. We often relied on XZ or YZ projections as provided by the Knossos annotation software. Finally, we also cross checked our work

by having each synapse independently annotated by at least two of the authors, and only synapses agreed by each judge (which in our case was >99% agreement) were included for analyses.

Statistical analyses (Mann-Whitney, Chi-Square, and Kruskal-Wallis tests) were performed on the data using custom software in Matlab.

3 | Results

We injected a dual viral "cocktail" into the posterior medial thalamic nucleus using stereotactic coordinates (POm; Figure 1A). The first AAV construct expressed *cre* recombinase (pENN.AAV1.hSyn.Cre.WPRE.hGH) and the second AAV construct expressed cytoplasmic targeted, *cre*-dependent APEX2 (Lam et al., 2015; Martell et al., 2017);APX-C, Figure 1B). We found that this "intersectional" viral strategy works: vibratome sections viewed with the light microscope and containing the posterior medial nucleus and secondary somatosensory cortex showed dark staining with Di-Amino Benzene (DAB) (Joesch et al., 2016) in the posterior medial nucleus and putative axonal labeling in S2 cortex (Figure 1B, *bottom*). Serial electron microscopy of the posterior medial nucleus revealed thalamic neurons with APX-C labeling throughout their cytoplasm (Figure 1C, *top*) and synapses from axons of these neurons were clearly visualized along with their postsynaptic targets in S2 cortex (Figure 1C *bottom*).

We analyzed all layers from an individual animal with a single injection site to accurately describe synapses from a single population of labeled POm neurons. In our analyses, we did not assume that all posterior medial cells projecting to the second somatosensory cortex in our injection zone were labeled but rather that our sample is fairly representative of the projection.

We used the ATUM approach (Kasthuri, 2015) to section approximately 3000 50 nm sections from a vibratome slice of secondary somatosensory cortex containing all cortical layers (Figure 1C, 1.7 x 1mm x 0.05mm tissue volume). We

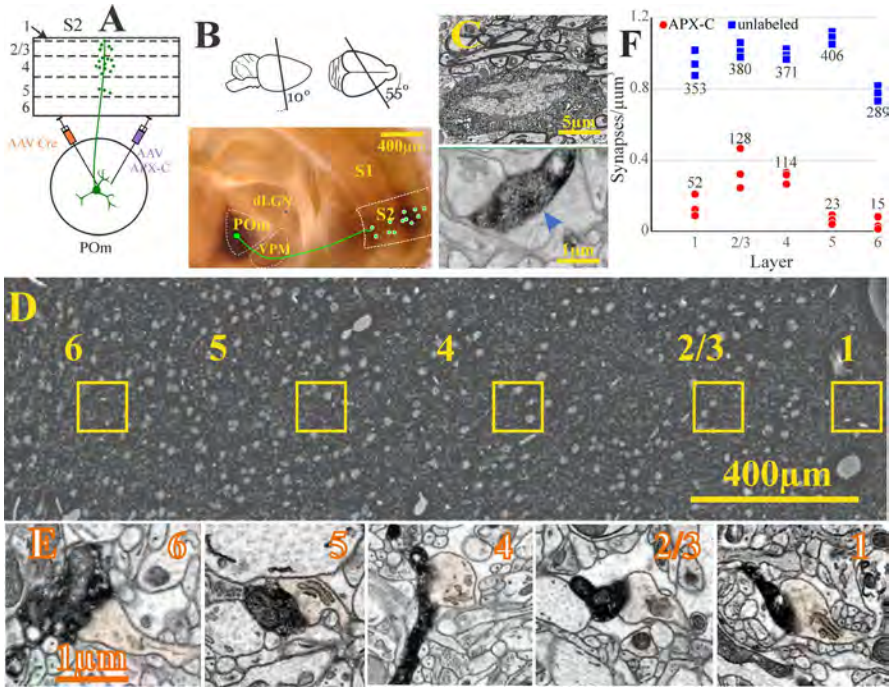

FIGURE 1 Overview of methodology. (A) We simultaneously injected two types of AAV in the POm of thalamus in wild-type mice: one AAV expressed *cre* recombinase in most or all neurons and a second that expressed APEX2 targeted to the cytoplasm (APX-C) in a cre-dependent fashion. (B) Diagram of slicing angles is shown in top. The bottom shows the APX-C staining. After injections, dark APX-C labeling is clearly visible at the light level in a vibratome slice stained with diaminobenzidine and hydrogen peroxide. The labeling in POm avoids the first-order somatosensory nucleus VPm and the characteristic laminar patterns of POm innervation are visible in S1 and S2 cortex. (C) Electron micrographs showing a POm neuron with the cytoplasm completely filled with APX-C label (*top*) and an APX-C labeled axonal terminal (*bottom*) in S2 (*blue arrow*) (D) We performed multiscale electron microscopy on the resulting sections which spanned the depth of cortex. At lower resolution, we established cortical areas and layers (*numbered)*, and at higher resolution within cortical layers (*yellow boxes*), we reconstructed APX-C labeled and unlabeled synapses. (E) Example synapses onto spines made by APX-C labeled axons from POm in all layers; the layers indicated by the numbers in the upper left corner of each panel. The orange shading denotes postsynaptic spines. (F) Synaptic density (synapses/μm^3) plots for three volumes separately selected from within each of the yellow boxes in (D). For each volume, every APX-C labeled and unlabeled synapse was identified and counted. The total numbers of synapses for each grouping are also shown

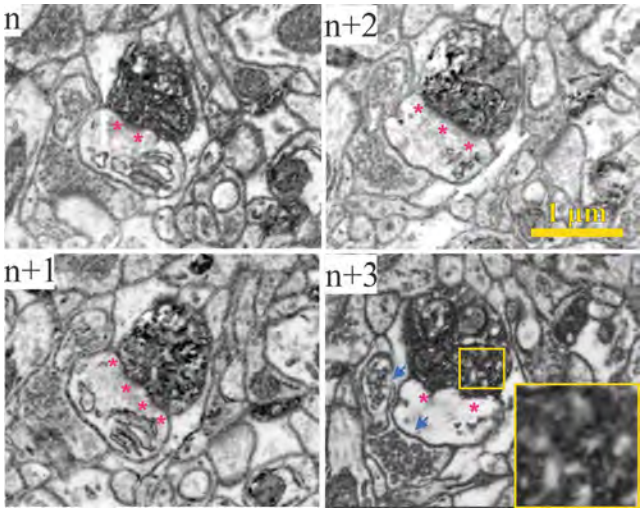

FIGURE 2 Example of a POm synapse. Shown are four serial electron micrographs (~40 nm thick) of an APX-C labeled synapse onto a spine in layer 4. Purple asterisks mark sites of the postsynaptic density, and synaptic vesicles can be seen in the APX-C labeled terminal (e.g., see slice n+3 and *inset*, which is magnified 2.5 times the rest of the micrographs). Synaptic vesicles in nearby synapses are highlighted by blue arrows for comparison

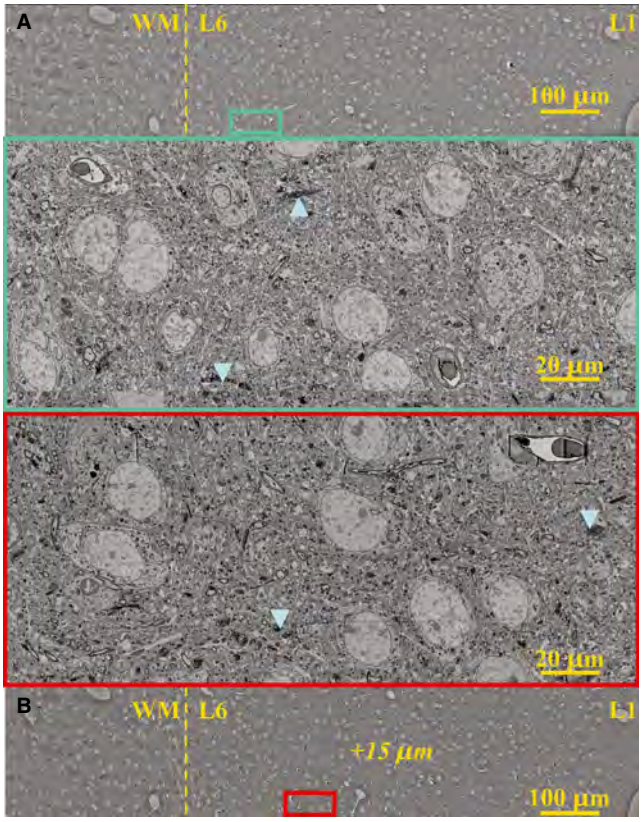

FIGURE 3 Lack of retrogradely APX-C labeling. Shown are two EM sections ~15 µm apart in a lower-resolution EM stack (40 nm x, y, and z resolution, *top* and *bottom* panels, A and B) of S2 cortex from this dataset. These lower-resolution images show all layers of cortex from layer 1 to white matter (*WM*). Higher-resolution insets within layer 6 are shown from the two labeled fields of view (red and green rectangles). No cell body or dendrite in any layer, and especially layers 5 and 6, showed APX-C labeling throughout the depth of the EM stack (~50 µm thick total). Clear APX-C labeling was seen in myelinated axons (blue arrows) and occasionally in unmyelinated axons (see text)

first performed low-resolution (i.e., 40 nm voxel resolution) serial electron microscopy on ultra-thin sections of cortex in order to identify cortical layers (see **METHODS**) and estimate APX-C labeling density (Figure 1D). We identified zones in each layer (yellow boxes in Figure 1D) for further analysis, and took care to avoid regions near laminar borders. We found axons from the posterior medial nucleus throughout cortex, and closer inspection of the same sections with finer resolution (i.e., 6 nm x & y resolution) showed uniform staining of APX-C even in the finest tips of axons, millimeters away from their cell bodies in thalamus, including clear labeling in layer 1 (Figure 1E). This indicated that the expression of APX-C labels all neuronal processes and overcomes a potential disadvantage of similar experiments with dye injection requiring diffusion of the dye inside the neuron. We then re-imaged five subvolumes of the full cortex dataset at roughly 6 nm x & y resolution for examining the connectivity of labeled thalamocortical axons in each of the cortical layers (Figure 2). As expression depends on a neuron being infected with both viruses, accidental retrograde labeling can be reduced or eliminated. Indeed, we found no labeled cells in cortex, and thus the thalamic injections did not label corticothalamic cells retrogradely (Figure 3).

We found APX-C labeled thalamocortical synapses in all cortical layers. We determined for each layer the relative innervation density of labeled posterior medial synapses relative to all unlabeled synapses. To do this, we reconstructed three small volumes (approximately 125 μm^3 each; see Methods) in each cortical layer, identified every labeled and unlabeled synapse therein, and calculated synapse density for labeled and unlabeled synapses across cortex (Figure 1F). Even in regions with dense thalamocortical labeling, the synapses from the posterior medial nucleus in every layer were a minority of the synaptic population: based on 2131 total synapses in all layers, 332 APX-C labeled and 1799 unlabeled, we found 0.15 labeled synapse/μm^3 versus 1 unlabeled synapse/μm^3 (p = 2.8E-12 on a χ^2-test). We found a laminar relationship for the density of APX-C labeled synapses, with a higher density in layers 2-4 (Figure 1F; p = 1.3461E-09 on a χ^2-test). In contrast, there was no statistically significant laminar relationship for unlabeled synapses (p = 0.35 on a χ^2-test). Thus, the relative increased ratio of labeled-to-unlabeled synapses in layers 2-4 was due mainly to the increased density of labeled APX-C synapses in these layers.

We next characterized the frequency at which APX-C labeled terminals in each layer synapsed with dendritic spines

or dendritic shafts and furthermore whether the dendrite was spiny or aspiny (see Methods). We analyzed 1137 APX-C labeled terminals, across all cortical layers (by layer L1: 218, L2/3: 371, L4: 387, L5: 109, L6: 52; Figure 4A,B) and found that only 17 of 1137 synapses from the posterior medial nucleus contacted dendritic shafts. Only 6 of these were on aspiny dendrites; the other 11 were found on dendritic shafts between spines. In order to determine whether this low fraction of innervation on aspiny dendrites (6/1137, 0.53%) reflected an underlying distribution of aspiny dendrites in our dataset, we randomly reconstructed 20 or 21 dendrites in each layer of cortex (Figure 4C). We found that 28% (29/104 dendrites) of the dendrites reconstructed in each layer were aspiny, similar to values reported in the literature (Figure 4D; Sahara et al., 2012). Thus, the low innervation fractions of synapses from the posterior medial nucleus on aspiny dendrites were unlikely to have occurred by chance ($p = 1.1E\text{-}4$ on a χ^2- test) and instead suggests that synapses from the posterior medial nucleus selectively target spiny dendrites.

In order to better appreciate the pattern of thalamocortical connectivity on excitatory neurons, we reconstructed 444 spine synapses onto 21 randomly selected dendritic segments in layers 2/3 of our dataset, thereby sampling the region of highest labeling density (Figure 4B). Of these 21 dendritic segments, 19 received at least one synapse from a posterior medial neuron and 16 received multiple labeled synapses (Figure 4E). As we likely failed to label all neurons of the posterior medial nucleus projecting to the secondary somatosensory cortex, and no other thalamic nuclei were labeled, this is a minimum estimate of the thalamic innervation of this cortical area. We next asked whether the pattern of connectivity onto spines of excitatory dendrites possibly reflected specific targeting by APX-C terminals or could have occurred by chance. APX-C labeled axons innervated 51/444 or 9% of the spines on dendrites in this volume (Figure 4E). We found that the innervation pattern on individual dendrites was consistent with this average. It did not appear that APX-C axons clustered or showed preference for selectively targeting some spiny dendrites and avoiding others. Thus, we could not exclude the possibility that the frequency of APX-C innervation on individual excitatory dendrites differed from chance ($p = 0.35$ on a χ^2-test).

As the majority of APX-C labeled thalamocortical synapses occurred on spines, we next asked whether these spine synapses were distinct from unlabeled synapses on spines throughout all layers. We annotated APX-C and unlabeled

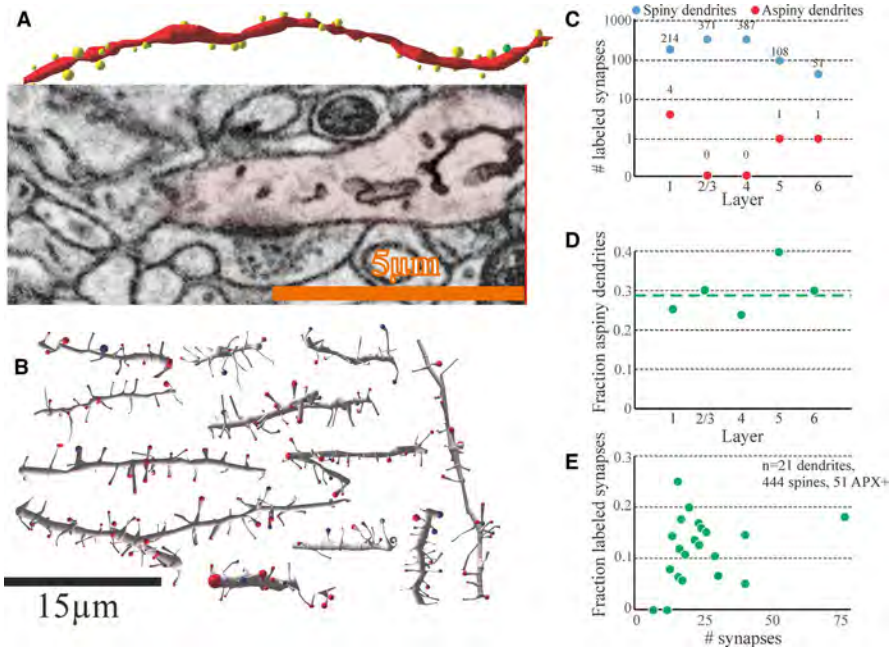

FIGURE 4 Axons from the posterior medial nucleus selectively target spiny dendrites. We reconstructed APX-C labeled and unlabeled synapses onto dendritic shafts (A) and spines (B) of randomly selected dendrites throughout the layers of S2 cortex. (A) Example reconstruction of an aspiny dendritic segment (red dendrite, *upper*) innervated only by unlabeled synapses where each shaft synapse and its size are annotated (yellow spheres). The single green sphere (*right*) is an unlabeled synapse shown in the electron micrograph below. Synapse density on this dendritic segment was 3 synapses/µm. (B) Example reconstructions of 12 spiny dendritic segments from layers 2/3 where every spine synapse was annotated as APX-C labeled (blue) or unlabeled (red); bouton sizes are also indicated. (C) Plot of the number of synapses made by APX-C labeled boutons on spiny (*blue dots*) and aspiny (*red dots*) dendrites by layer. The number of synapses sampled for each layer is indicated. For every layer, the proportion of APX-C labeled synapses on aspiny dendrites was significantly lower than chance (see text). (D) Plot of fraction of aspiny dendrites randomly selected in each layer. The dashed green line is the average percentage of aspiny dendrites across all layers. (E) The fraction of APX-C labeled synapses on dendritic segments in (B)

synapses randomly throughout each cortical layer (n= 1131 labeled and 891 unlabeled synapses) and focused on six measurements for comparison (Figure 5A): (a) the presence or absence of mitochondria in the terminal (Figure 5B); (b) the presence or absence of "coiled" smooth endoplasmic reticulum in the postsynaptic spine, also known as the spine apparatus ((Spacek, 1985); Figure 5C); (c) the diameter of the postsynaptic spine Figure 5D; (d) the diameter of the pre-synaptic axonal terminal (Figure 5E); (e) the diameter of associated glial processes, if any (Figure 5F); and (f) the number of postsynaptic spines per terminal (Figure 5G). We chose these specific parameters as they have all been implicated in synaptic function (see Discussion).

We found that APX-C labeled synapses are statistically different from unlabeled synapses for each of the above parameters. The labeled synapses derived from larger terminals (1.6 μm mean, 1.5 μm median, for labeled terminals vs. 1.25 μm mean, 1.2 μm median, for unlabeled (Figure 5E; p = 5.05e-15, on a Mann-Whitney U-test)) and contacted

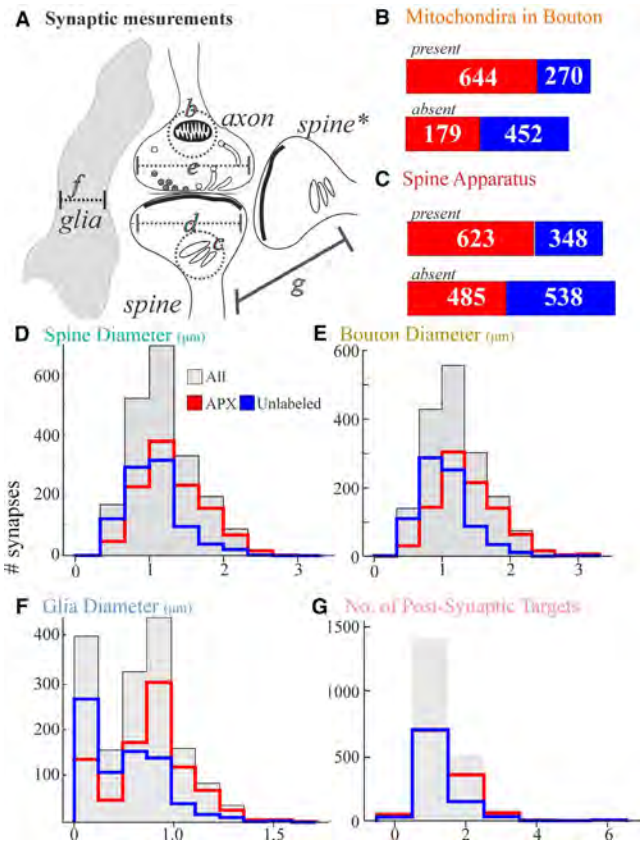

FIGURE 5 Quantitative differences between APX-C labeled and unlabeled synapses onto spines in cortex. (A) Cartoon parameters measured and illustrated in (B-G). (B) Presence or absence of mitochondria in the presynaptic bouton. (C) The presence of absence of spine apparatus in postsynaptic spines. (D) Maximum spine diameter. (E) Maximum bouton diameter. (F) Maximum diameter of glial process, if present, contacting the synapse. (G) Number of postsynaptic spines innervated by each bouton

larger spines (1.26 μm mean, 1.2 μm median, diameter unlabeled spines, 1.6 μm mean, 1.5 μm median, diameter APX-C spines, Figure 5D; p = 2.10E-44, on a Mann-Whitney U-test). The posterior medial synapses were more likely to have associated glial processes: of APX-C labeled synapses, 86% (828/964) had an associated glial process, whereas only 53% (296/563) of unlabeled synapses did (p = 8.16E-43 on a χ^2-test). Furthermore, the glial processes at their widest points on labeled synapses were larger, with labeled synapses having a glial diameter of 1.1 μm mean, 1.0 μm median, versus 0.7 μm mean, 0.75 μm median, for unlabeled synapses (p = 1.77E-19, on a Mann-Whitney U-test; Figure 5F). Labeled terminals were more likely to synapse with multiple targets (Figure 5G), averaging 1.4 targets versus 1.2 for unlabeled synapses (n=1085 labeled and 863 unlabeled; p = 3.71E-06, on a Mann-Whitney U-test). In addition, we randomly annotated 1,545 of all the axonal terminals annotated, 823 labeled and 722 unlabeled, for the presence of mitochondria in the terminal. Of labeled terminals, 78% (644/823) contained a mitochondrion, whereas only 37% (270/722) of unlabeled terminals did so (Figure 5B, p = 7.90E-07 on a χ^2-test). We then randomly analyzed 1994 spines, 1108 innervated by labeled terminals and 886, by unlabeled terminals, for the presence of a spine apparatus. We found that 49% (971/1994) had a prominent spine apparatus. Of spines innervated by labeled terminals, 56% (623/1108) had a spine apparatus, whereas 39% (348/886) of spines associated with unlabeled terminals had a spine apparatus (Figure 5C, p = 4.84E-04 on a χ^2- test).

Finally, we asked how labeled synapses from the posterior medial nucleus differed from unlabeled synapses for the 6 metrics from Figure 5 but now analyzed separately for each cortical layer (Figure 6, see also Table 1). We found that APX-C labeled terminals and synapses differed statistically from unlabeled synapses, with larger values for postsynaptic spine diameter, terminal diameter, associated diameter of glia, presence of mitochondria and postsynaptic spine apparatuses, and number of postsynaptic spines per terminal, in 24 of the 30 comparisons across layers (Mann-Whitney U-test and χ^2-test; Table 1). These differences had clear laminar correlations: APX-C labeled synapses showed the largest deviations from unlabeled synapses in layers 2/3, and to a lesser extent in layer 4, and the six comparisons for which we could not statistically distinguish between APX-C and unlabeled synapses occurred in layers 5 and 6. For example, in layers 2/3, APX-C labeled terminals synapsed onto larger spines than did unlabeled terminals: 1.92±.03 μm (mean ± sem; 1.96 μm median) in diameter versus 1.29±.04 μm, 1.33 median, p = 7.09E-27 on a Mann-Whitney U-test. Conversely, in layer 6, APX-C labeled terminals contacted spines that were not significantly different in diameter from those contacted by unlabeled terminals (1.47±.06 μm vs. 1.24±.06, 1.35 vs. 1.18 median, p = 0.17 on a Mann-Whitney U-test). Moreover, spine diameters contacted by APX-C

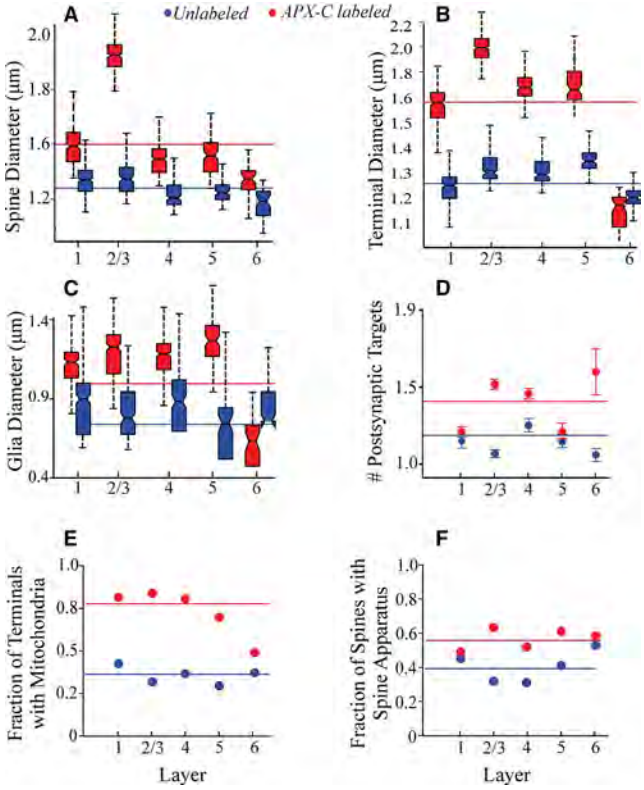

FIGURE 6 Layer-specific differences between APX-C labeled and unlabeled synapses in cortex. (A-C) Plots showing medians and interquartile ranges. (D) Plot showing means ± SEM. (E-F) Plots showing fraction of synapses. The solid blue and red lines show the mean across all layers for labeled (red lines) and unlabeled (blue lines) synapses

labeled terminals showed clear statistical laminar differences across layers (APX-C spine diameter across layers; $p = 1.2E-12$, Kruskal-Wallis), whereas those contacted by unlabeled terminals showed no laminar difference in size (p= 0.47 Kruskal-Wallis). We found similar results across the 5 remaining synaptic measures (see Table 1 for statistical values) as follows. The largest differences between APX-C labeled and unlabeled synapses occurred in layers 2/3 (Figure 6A-C). APX-C labeled synapses showed clear laminar differences in the synaptic measures shown in Figure 6A-E, whereas unlabeled synapses showed no such laminar differences. The lone exception to this pattern was the presence of spine apparatuses in postsynaptic profiles (Figure 6F). Although overall, APX-C labeled terminals more frequently contacted spines with spine apparatuses than did unlabeled terminals, this parameter showed a laminar difference for unlabeled terminals but not labeled ones.

4 | Discussion

We leveraged advances in automated serial electron microscopy paired with electron-dense genetic labeling using ascorbate peroxidase (APX-C) to analyze long distance connections in a mouse from the posterior medial nucleus of the thalamus to the second somatosensory area of cortex. We found that the labeling strategy works extremely well: clearly labeled synapses in cortex were identified millimeters away from their thalamic cell bodies of origin without signs of reduction in labeling from diffusion or pathological changes to the tissue at the ultrastructural level. We also found that the labeling was orthograde only. This avoids the potential problem of retrograde labeling, which in our case could have labeled corticothalamic cells from layer 5 or 6 and thereby marked local synaptic terminals from these cells, creating false-positive labeling.

However, we recognize at least two provisos in the interpretation of our quantitative analyses. One is that we cannot assume that all thalamocortical cells contributing to the pathway under study were successfully labeled, and of course, other thalamic nuclei innervating the second somatosensory area, such as the ventral posterior nucleus, would have contributed to the population of unlabeled thalamocortical terminals in our study. Related to this, we cannot exclude the possibility that we have labeled a particular population of thalamocortical neurons, and unlabeled ones from the posterior medial nucleus might exhibit properties different from those reported here. It's therefore likely that our analysis undersampled the totality of thalamocortical input. However, the significant differences still found between labeled and unlabeled synapses suggest that the distinctions we highlight here are robust. Additionally, as is common in ultrastructural studies of this type, the analyses are limited to a single animal. We cannot exclude minor individual differences, even among inbred mouse strains.

Figure 7 provides a highly schematized view of much of our work with more details below. Axons of the posterior medial nucleus of the thalamus (POm) innervate all layers of the second somatosensory cortical area (S2). There is laminar variation to this innervation pattern: layers 2/3 receive relatively denser innervation with larger terminals that tend to innervate larger spines, among other measures. In contrast, unlabeled terminals, whose origin is unknown, tend to be smaller and innervate smaller spines, and these terminals show relatively little laminar variation in these parameters.

4.1 | Ultrastructural properties of terminals labeled from the posterior medial nucleus

We found labeled synapses from the posterior medial nucleus in every layer of the second somatosensory area. In all layers, labeled terminals specifically targeted spines and spiny dendrites, suggesting a strong preference for innervating excitatory rather than inhibitory cortical neurons (McDonald & Pearson, 1989; Somogyi et al., 1983). While comparing

TABLE 1 Quantitative details of synaptic input from POm to S2

Spine Diameter								**Terminal Diameter**						
	Unlabeled			APX-C				Unlabeled			APX-C			
Layer	Mean, *n*	Median	SEM	Mean, n	Median	SEM	*p=	Mean, n	Median	SEM	Mean n	Median	SEM	*p=
L1	1.3, 353	1.32	0.02	1.56, 218	1.58	0.04	1.10E-06	1.3, 353	1.25	0.02	1.55, 218	1.6	0.04	2.68E-08
L2/3	1.29, 185	1.33	0.04	1.92, 371	1.96	0.03	7.09E-27	1.27, 185	1.33	0.04	2.01, 371	2	0.03	1.58E-32
L4	1.25, 189	1.2	0.03	1.48, 387	1.45	0.02	3.68E-10	1.26, 189	1.3	0.03	1.63, 387	1.7	0.02	8.80E-18
L5	1.22, 113	1.24	0.04	1.53, 108	1.5	0.05	3.45E-06	1.33, 113	1.35	0.04	1.73, 109	1.69	0.06	5.21E-06
L6	1.24, 52	1.18	1.47	1.47, 52	1.35	0.06	0.1696	1.17, 52	1.2		1.07, 52	1.15	0.09	0.05
	†p = 0.47			†p = 1.2E-12				†p = 0.21			†p = 8.8E-6			
Glia Width								**No. of mitochondria**						
	Unlabeled			APX-C					Unlabeled		APX-C			
Layer	Mean, n	Median	SEM	Mean, n	Median	SEM	*p=		PRESENT	ABSENT	PRESENT	ABSENT		§p=
L1	0.84, 353	0.9	0.03	1.1, 218	1.2	0.04	1.20E-04		126	170	153	35		1.72E-04
L2/3	0.69, 185	0.74	0.03	1.32, 371	1.36	0.05	1.45E-13		38	81	154	30		1.04E-05
L4	0.78, 189	0.87	0.03	1.17, 387	1.27	0.05	0.0025		58	100	250	61		2.54E-18
L5	0.74, 113	0.8	0.03	1.23, 109	1.3	0.05	0.0013		29	69	62	27		4.94E-06
L6	0.51, 52	0.6	0.02	0.6, 52	0.55	0.02	0.4347		19	32	25	26		0.23
	†p = 0.16			†p = 1.8E-5					§p = 0.32		§p = 0.011			
No. of Postsynaptic Targets								**Spine Apparatus**						
	Unlabeled			APX-C					Unlabeled		APX-C			
Layer	Mean, n	Median	SEM	Mean, n	Median	SEM	*p=		PRESENT	ABSENT	PRESENT	ABSENT		§p=
L1	1.15, 353	1.1	0.05	1.23, 218	1.28	0.03	1.93E-10		158	193	101	105		1.87E-07
L2/3	1.09, 185	1.2	0.02	1.55, 371	1.6	0.03	8.93E-18		59	126	232	135		7.7E-10
L4	1.26, 189	1.33	0.03	1.46, 387	1.52	0.03	3.14E-05		58	129	198	184		2.02E-04
L5	1.15, 113	1.25	0.04	1.23, 109	1.13	0.05	0.62		46	66	64	41		.0034
L6	1.08, 52	1.15	0.04	1.63, 52	1.58	0.14	4.50E-04		27	24	28	20		0.59
	†p= 0.19			†p = 2.1E-4					§p = $ 0.023		§p = 0.14			
Statistical Tests:			* Mann-Whitney *U*				§χ^2		†Kruskal-Wallis					

Statistical tests at the end of rows in the table are comparisons between labeled and unlabeled synapses in that layer for that measure. Statistical tests at the end of columns are comparisons of either labeled or unlabeled synapses across layers for that measure.

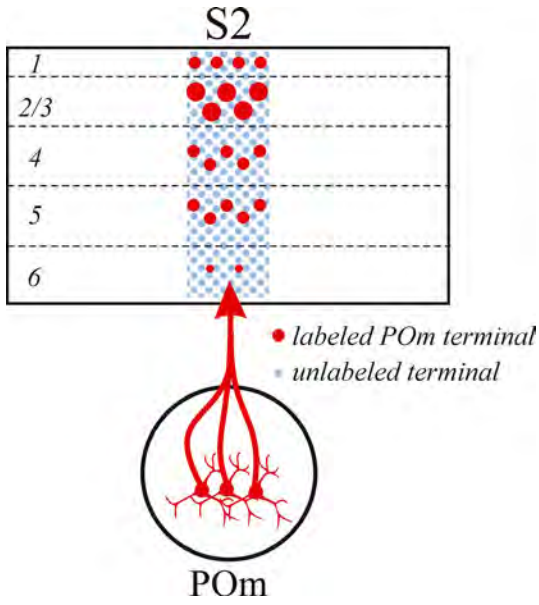

FIGURE 7 Cartoon summary of results. See text for details

ultrastructural data with physiology and light-level anatomy can be difficult, this result is surprising given that thalamic projections to primary cortical areas affect cortical activity through monosynaptic connections with both excitatory and inhibitory cells (Kloc & Maffei, 2014; Wall et al., 2016). There is, however, some precedent for this result. A previous ultrastructural study showed that thalamocortical projections avoid inhibitory neurons in layer 4 of M1 (Bopp et al., 2017), and a recent comparison of terminals from the posterior medial nucleus to primary motor and primary somatosensory cortices also determined that there were very few labeled terminals on inhibitory interneurons in motor cortex (Rodriguez-Moreno et al., 2020). Combined with the current findings, this observation may represent a difference for higher-order thalamic nuclei projecting to primary or higher-order cortical areas. That is, higher-order thalamocortical projections to motor cortex and higher-order sensory areas, projections that densely innervate layer 4 of cortex and display the properties of glutamatergic driver synapses (Mo & Sherman, 2019), largely avoid monosynaptic connections with inhibitory interneurons; whereas higher-order thalamic projections to primary sensory cortex, projections that densely innervate layers 5 and 1 and display the properties of glutamatergic modulator synapses (Viaene et al., 2011) target both excitatory and inhibitory postsynaptic targets.

Furthermore, the parameters of these labeled synapses varied with layer: layers 2/3 received the largest relative number of terminals from the posterior medial nucleus, and layer 6, the smallest. Labeled synapses in layers 2/3 also had larger terminals and targeted larger spines than did those in other layers (summarized in Figure 7). Finally, other common properties of the labeled thalamocortical terminals included the presence of mitochondria, the presence of spine apparatuses in their postsynaptic spine targets, and the presence of a relatively thick glial wrapping.

The synaptic metrics measured here have known functional implications. The size of postsynaptic spines is associated with spine stability over time and spine size has a strong, positive linear relationship with the magnitude of synaptic currents (Holler-Rickauer et al., 2019). Mitochondria in the bouton serve potentially important roles in vesicle recycling, enhancing short-term plasticity, and stabilizing synaptic connections over time and often suggest highly active terminals (Cserép et al., 2018; Feldman & Peters, 1978; Lees et al., 2020). The presence of a spine apparatus in spine is correlated with potentiated synapses (Deller et al., 2003; Jedlicka et al., 2009). Finally, increasing evidence suggests that glia interact with neurons directly at synapses to modify synaptic function (Eroglu & Barres, 2010). Overall, our anatomical findings strongly suggest that thalamocortical synapses from the posterior medial nucleus to the second somatosensory cortex tend to be functionally more robust and stable than other synapses, which is consistent with limited evidence that these synapses are glutamatergic drivers (Lee & Sherman, 2008; Viaene et al., 2011b).

4.2 | Differences between labeled and unlabeled terminals

The labeled terminals differed from unlabeled ones along a number of parameters. For one thing, unlike the labeled synapses, unlabeled ones showed very little evidence of laminar variations in the parameters we measured. Overall, compared to unlabeled terminals, labeled terminals were larger, targeted larger spines that more frequently had spine apparatuses, more often targeted multiple spines, more often had mitochondria, and tended to be associated with larger glial profiles. Because of the variation in layering with these parameters for labeled terminals, the differences between labeled and unlabeled terminals were greatest in layers 2/3.

4.3 | On difference between first- and higher-order somatosensory thalamocortical projections

One of our observations for the higher-order somatosensory projection is that labeled terminals are significantly larger in layers 2/3 than in layer 4. This is in stark contrast to the first-order projections from the ventral posterior nucleus to the primary somatosensory cortex and the ventral division of the medial geniculate nucleus to the primary auditory cortex in which the terminals in layer 4 were described as significantly larger than those in layers 2/3 (Viaene et al., 2011a). This is

in keeping with a presumed important functional difference between these first- and higher-order thalamocortical projections. In the first-order projection, thalamocortical inputs to layers 4-6 are all glutamatergic drivers, whereas those to layers 2/3 are mostly glutamatergic modulators, in keeping with the smaller size of thalamocortical terminals in layers 2/3 (Viaene et al., 2011a). This suggests that, whereas most first-order thalamocortical somatosensory and auditory inputs to layers 2/3 are modulators, in the higher-order somatosensory projection, most or all may be drivers.

5 | Conclusions

We draw two main conclusions from this work. First, our use of an intersectional viral tracing method for ultrastructural connectivity offers many advantages, including more complete electron-dense labeling compared to labeling often seen with intracellular diffusion of various dyes, and the orthograde labeling we achieved with this technology is free of artifacts often presented by unwanted and uncontrolled retrograde labeling seen with most dye labeling. Our approach is amenable to more general ultrastructural studies of long pathways in the central nervous system.

Second, we believe that this is the first detailed ultrastructural study of this higher-order thalamocortical pathway. Most studies to date have targeted projections to primary sensory cortices, such as from the lateral geniculate nucleus to primary visual cortex (Ahmed et al., 1994; Anderson et al., 2009; Hornung & Garey, 1981; Peters & Feldman, 1977; Peters et al., 1976) and from the ventral posterior nucleus to the primary somatosensory cortex (Bopp et al., 2017; Hersch & White, 1981; Rah et al., 2013; Rodriguez-Moreno et al., 2018; White & Rock, 1979; White et al., 2004). The few published studies of higher-order thalamocortical projections we could find (e.g. Chomsung et al., 2010; Zhou et al., 2018) concentrated on other more specific issues rather than the connectomics analysis of the present study. If we are to gain a better understanding of thalamocortical functioning writ large, we need more descriptions of higher-order thalamocortical examples. Indeed, we have above documented some clear differences between first- and higher-order somatosensory thalamocortical circuits that suggest important functional differences between them.

More generally, it is important to gain a broader understanding of higher-order thalamocortical functioning. First-order thalamic nuclei, such as the lateral geniculate nucleus and ventral posterior nucleus, and their projections to cortex have been relatively well studied. These nuclei relay information from the periphery to cortex (e.g., from the retina for the lateral geniculate nucleus and from the medial lemniscus for the ventral posterior nucleus). In contrast, higher-order thalamic nuclei such as the posterior medial nucleus relay information already in cortex from layer 5 of one area to another area, and thus play a key role in corticocortical communication (reviewed in Sherman, 2016; Sherman & Guillery, 2013)). It is thus especially important to gain a better understanding of these higher-order circuits.

Finally, we are confident in our annotation of synapses, as we independently verified each synapse with at least two scientists. However, if we have miscounted or annotated spines, it is likely that it is the smallest synapses that are potentially missed. These represent a small proportion of the >1000 synapses analyzed, ~10-15 %. The bulk of our results point to differences in POm innervation in the numbers of large synapses (Figure 4) across cortical layers, which we feel are less likely to suffer from potential misinterpretation of small synapses. Thus, even these potential errors in identifying synapses should have little effect on our results. Indeed, as much of our analyses are comparisons of POm synapses across layers, and such errors, if they occur, will occur in all layers. Our robust statistical results in these comparisons strongly suggest that that is not an issue in these analyses.

We view the current study as a bare beginning of an attempt to broaden our understanding of thalamocortical circuitry and the functioning of higher-order thalamocortical pathways. While a great deal more study of this issue is warranted, we hope that the strategy of combining virally mediated labeling with high-throughput electron microscopy contributes to our understanding of previously understudied projections in the brain.

6 | COMPETING INTERESTS

The authors have no competing financial interests to divulge.

ACKNOWLEDGEMENTS

N.K. and V.S. are supported from a technical award from the McKnight foundation, a Brain Initiative of the National Institutes of Health (U01 MH109100), and National Science Foundation Neuro Nex grant. A.M.-H. and S.M.S. are supported by a National Institutes of Health grant from the NINDS (NS094184) and NEI (EY022388). N.K. and S.M.S. are supported by a National Institutes of Health grant from the NINDS (NS113922). Finally, A.M.-H. is supported a National Institutes of Health grant from the NEI (EY028812).

AUTHOR CONTRIBUTIONS

N.K. and S.M.S. designed research; V.S., A.M.-H., and N.K. performed research; all authors analyzed data and wrote the study.

PEER REVIEW

The peer review history for this article is available at https://publons.com/publon/10.1111/ejn.15092.

Data Availability Statement

All authors will be responsible for overseeing the regular backup of the data from their laboratories. We will comply with the NIH Data Sharing requirement (http://grants.nih.gov/grants/policy/data_sharing). All tools (data, assays, libraries, research tools, reagents, etc.) will be made available, in accordance with the policy. Our practices are as follows:

- All datasets made available for sharing in accord with NIH timeliness guidelines. "no later than the date of acceptance for publication of the main findings from the final dataset."
- Data will be shared via electronic transfer or shipping of hard drives, etc., as required on request.
- Datasets shall consist of electronic copies of raw EM images, all annotations, protocols of injections, sequences for viruses, etc.
- All code (MATLAB) will be shared on request.

ORCID

Vandana Sampathkumar https://orcid.org/0000-0002-0577-7164
S. Murray Sherman https://orcid.org/0000-0002-1520-2778

REFERENCES

Agmon, A., & Connors, B. (1991). Thalamocortical responses of mouse somatosensory (barrel) cortex in vitro. *Journal of Neuroscience*, *41*, 365–379.

Ahmed, B., Anderson, J. C., Douglas, R. J., Martin, K. A., & Nelson, J. C. (1994). Polyneuronal innervation of spiny stellate neurons in cat visual cortex. *Journal of Comparative Neurology*, *341*, 39–49.

Anderson, J. C., da Costa, N. M., & Martin, K. A. (2009). The W cell pathway to cat primary visual cortex. *Journal of Comparative Neurology*, *516*, 20–35.

Boergens, K. M., Berning, M., Bocklisch, T., Bräunlein, D., Drawitsch, F., Frohnhofen, J., Herold, T., Otto, P., Rzepka, N., Werkmeister, T., Werner, D., Wiese, G., Wissler, H., & Helmstaedter, M. (2017). webKnossos: efficient online 3D data annotation for connectomics. *Journal of Nature Methods*, *14*, 691–694.

Bopp, R., Holler-Rickauer, S., Martin, K. A., & Schuhknecht, G. F. (2017). An ultrastructural study of the thalamic input to layer 4 of primary motor and primary somatosensory cortex in the mouse. *Journal of Neuroscience*, *37*, 2435–2448.

Cardona, A., Saalfeld, S., Schindelin, J., Arganda-Carreras, I., Preibisch, S., Longair, M., Tomancak, P., Hartenstein, V., & Douglas, R. J. (2012). TrakEM2 software for neural circuit reconstruction. *Journal of PloS One*, *7*.

Chomsung, R. D., Wei, H. Y., DayBrown, J. D., Petry, H. M., & Bickford, M. E. (2010). Synaptic organization of connections between the temporal cortex and pulvinar nucleus of the tree shrew. *Cerebral Cortex*, *20*, 997–1011.

Cserép, C., Pósfai, B., Schwarcz, A. D., & Dénes, Á. J. E. (2018) Mitochondrial ultrastructure is coupled to synaptic performance at axonal release sites. 5. https://doi.org/10.1523/ENEURO.0390-17.2018

Deller, T., Korte, M., Chabanis, S., Drakew, A., Schwegler, H., Stefani, G. G., Zuniga, A., Schwarz, K., Bonhoeffer, T., Zeller, R., Frotscher, M., & Mundel, P. (2003). Synaptopodin-deficient mice lack a spine apparatus and show deficits in synaptic plasticity. *Proceedings of the National Academy of Sciences*, *100*, 10494–10499.

Eroglu, C., & Barres, B. A. (2010). Regulation of synaptic connectivity by glia. *Nature*, *468*, 223–231.

Feldman, M. L., & Peters, A. (1978). The forms of non-pyramidal neurons in the visual cortex of the rat. *Journal of Comparative Neurology*, *179*, 761–793.

Hersch, S., & White, E. (1981). Quantification of synapses formed with apical dendrites of Golgi-impregnated pyramidal cells: variability in thalamocortical inputs, but consistency in the ratios of asymmetrical to symmetrical synapses. *Neuroscience*, *6*, 1043–1051.

Holler-Rickauer, S., Köstinger, G., Martin, K. A., Schuhknecht, G. F., & Stratford, K. J. (2019) Structure and function of a neocortical synapse. *bioRxiv*.

Hornung, J., & Garey, L. (1981). The thalamic projection to cat visual cortex: ultrastructure of neurons identified by Golgi impregnation or retrograde horseradish peroxidase transport. *Journal of Neuroscience*, *6*, 1053–1068.

Hua, Y., Laserstein, P., & Helmstaedter, M. (2015). Large-volume en-bloc staining for electron microscopy-based connectomics. *Nature Communications*, *6*, 7923.

Jedlicka, P., Schwarzacher, S. W., Winkels, R., Kienzler, F., Frotscher, M., Bramham, C. R., Schultz, C., Bas Orth, C., & Deller, T. (2009). Impairment of in vivo theta-burst long-term potentiation and network excitability in the dentate gyrus of synaptopodin-deficient mice lacking the spine apparatus and the cisternal organelle. *Hippocampus*, *19*, 130–140.

Joesch, M., Mankus, D., Yamagata, M., Shahbazi, A., Schalek, R., Suissa-Peleg, A., Meister, M., Lichtman, J. W., Scheirer, W. J., & Sanes, J. R. (2016). Reconstruction of genetically identified neurons imaged by serial-section electron microscopy. *Elife*, *5*, e15015.

Kasthuri, N., Hayworth, K. J., Berger, D. R., Schalek, R. L., Conchello, J. A., Knowles-Barley, S., Lee, D., Vázquez-Reina, A., Kaynig, V., Jones, T. R., Roberts, M., Morgan, J. L., Tapia, J. C., Seung, H. S., Roncal, W. G., Vogelstein, J. T., Burns, R., Sussman, D. L., Priebe, C. E., … Lichtman, J. W. (2015). Saturated Reconstruction of a Volume of Neocortex. *Cell*, *162*, 648–661.

Kloc, M., & Maffei, A. (2014). Target-specific properties of thalamocortical synapses onto layer 4 of mouse primary visual cortex. *Journal of Neuroscience*, *34*, 15455–15465.

Lam, S. S., Martell, J. D., Kamer, K. J., Deerinck, T. J., Ellisman, M. H., Mootha, V. K., & Ting, A. Y. (2015). Directed evolution of APEX2 for electron microscopy and proximity labeling. *Nature Methods*, *12*, 51–54.

Lee, C. C., & Sherman, S. M. (2008). Synaptic properties of thalamic and intracortical inputs to layer 4 of the first-and higher-order cortical areas in the auditory and somatosensory systems. *Journal of Neurophysiology*, *100*, 317–326.

Lees, R. M., Johnson, J. D., & Ashby, M. C. (2020). Presynaptic boutons that contain mitochondria are more stable. *Journal of Frontiers in Synaptic Neuroscience*, *11*, 37.

Martell, J. D., Deerinck, T. J., Lam, S. S., Ellisman, M. H., & Ting, A. Y. (2017). Electron microscopy using the genetically encoded APEX2 tag in cultured mammalian cells. *Nature Protocols*, *12*, 1792–1816.

McDonald, A. J., & Pearson, J. C. (1989). Coexistence of GABA and peptide immunoreactivity in non-pyramidal neurons of the basolateral amygdala. *Neuroscience Letters*, *100*, 53–58.

Mo, C., & Sherman, S. M. (2019). A sensorimotor pathway via higher-order thalamus. *Journal of Neuroscience*, *39*, 692–704.

Morgan, J. L., Berger, D. R., Wetzel, A. W., & Lichtman, J. W. (2016). The fuzzy logic of network connectivity in mouse visual thalamus. *Cell*, *165*, 192–206.

Motta, A., Berning, M., Boergens, K. M., Staffler, B., Beining, M., Loomba, S., Hennig, P., Wissler, H., & Helmstaedter, M. (2019). Dense connectomic reconstruction in layer 4 of the somatosensory cortex. *Science*, *366*.

Peters, A., & Feldman, M. L. (1977). The projection of the lateral geniculate nucleus to area 17 of the rat cerebral cortex, IV terminations upon spiny dendrites. *Journal of Neurocytology*, *6*, 669–689.

Peters, A., Feldman, M., & Saldanha, J. (1976). The projection of the lateral geniculate nucleus to area 17 of the rat cerebral cortex. II. Terminations upon neuronal perikarya and dendritic shafts. *Journal of Neurocytology*, *5*, 85–107.

Rah, J.-C., Bas, E., Colonell, J., Mishchenko, Y., Karsh, B., Fetter, R. D., Myers, E. W., Chklovskii, D. B., Svoboda, K., & Harris, T. D. (2013). Thalamocortical input onto layer 5 pyramidal neurons measured using quantitative large-scale array tomography. *Frontiers in Neural Circuits*, *7*, 177.

Rodriguez-Moreno, J., Porrero, C., Rollenhagen, A., Rubio-Teves, M., Casas-Torremocha, D., Alonso-Nanclares, L., Yakoubi, R., Santuy, A., Merchan-Perez, A., DeFelipe, J., Lubke, J. H., & Clasca, F. (2020). Area-specific synapse structure in branched posterior nucleus axons reveals a new level of complexity in thalamocortical networks. *Journal of Neuroscience*, *40*, 2663–2679.

Rodriguez-Moreno, J., Rollenhagen, A., Arlandis, J., Santuy, A., Merchan-Pérez, A., DeFelipe, J., Lübke, J. H., & Clasca, F. (2018). Quantitative 3D ultrastructure of thalamocortical synapses from the "lemniscal" ventral posteromedial nucleus in mouse barrel cortex. *Cerebral Cortex*, *28*, 3159–3175.

Sahara, S., Yanagawa, Y., O'Leary, D. D., & Stevens, C. F. (2012). The fraction of cortical GABAergic neurons is constant from near the start of cortical neurogenesis to adulthood. *Journal of Neuroscience*, *32*, 4755–4761.

Sherman, S. M. (2016). Thalamus plays a central role in ongoing cortical functioning. *Nature Neuroscience*, *19*, 533.

Sherman, S. M., & Guillery, R. W. (2013). *Functional connections of cortical areas: a new view from the thalamus*, Cambridge, MA: MIT Press.

Somogyi, P., Kisvarday, Z., Martin, K., & Whitteridge, D. (1983). Synaptic connections of morphologically identified and physiologically characterized large basket cells in the striate cortex of cat. *Journal of Neuroscience*, *10*, 261–294.

Spacek, J. (1985). Three-dimensional analysis of dendritic spines. II. Spine apparatus and other cytoplasmic components. *Journal of Anatomy and Embryology*, *171*, 235–243.

Viaene, A. N., Petrof, I., & Sherman, S. M. (2011a). Synaptic properties of thalamic input to layers 2/3 and 4 of primary somatosensory and auditory cortices. *Journal of Neurophysiology*, *105*, 279–292.

Viaene, A. N., Petrof, I., & Sherman, S. M. (2011b). Properties of the thalamic projection from the posterior medial nucleus to primary and secondary somatosensory cortices in the mouse. *Proceedings of the National Academy of Sciences*, *108*, 18156–18161.

Wall, N. R., De La Parra, M., Sorokin, J. M., Taniguchi, H., Huang, Z. J., & Callaway, E. M. (2016). Brain-wide maps of synaptic input to cortical interneurons. *Journal of Neuroscience*, *36*, 4000–4009.

White, E., & Rock, M. (1979). Distribution of thalamic input to different dendrites of a spiny stellate cell in mouse sensorimotor cortex. *Neuroscience Letters*, *15*, 115–119.

White, E. L., Weinfeld, E., & Lev, D. L. (2004). Quantitative analysis of synaptic distribution along thalamocortical axons in adult mouse barrels. *Journal of Comparative Neurology*, *479*, 56–69.

Zhou, N., Masterson, S. P., Damron, J. K., Guido, W., & Bickford, M. E. (2018). The mouse pulvinar nucleus links the lateral extrastriate cortex, striatum, and amygdala. *Journal of Neuroscience*, *38*(2), 347–362.

Received: 3 May 2019 | Revised: 21 August 2019 | Accepted: 7 September 2019

DOI: 10.1002/cne.24779

RESEARCH ARTICLE

JCN RESEARCH IN SYSTEMS NEUROSCIENCE THE JOURNAL OF COMPARATIVE NEUROLOGY WILEY

Three-dimensional reconstructions of mouse circumvallate taste buds using serial blockface scanning electron microscopy: I. Cell types and the apical region of the taste bud

Ruibiao Yang[1] | Yannick K. Dzowo[1,2] | Courtney E. Wilson[1] | Rae L. Russell[1,2] | Grahame J. Kidd[3,4] | Ernesto Salcedo[1,2] | Robert S. Lasher[1] | John C. Kinnamon[5] | Thomas E. Finger[1,2]

[1]Department of Cell and Developmental Biology, Rocky Mountain Taste and Smell Center, University of Colorado School of Medicine, Denver, Colorado

[2]Modern Human Anatomy Program, University of Colorado School of Medicine, Denver, Colorado

[3]Department of Neuroscience, Lerner Research Institute, Cleveland Clinic, Cleveland, Ohio

[4]3D-Electron Microscopy, Renovo Neural Inc., Cleveland, Ohio

[5]Department of Biological Sciences, University of Denver, Denver, Colorado

Correspondence
Thomas E. Finger, Department of Cell and Developmental Biology, University of Colorado School of Medicine, MS 8108. Room L18-11118, RC-1, 12801 E. 17th Ave., Aurora, CO 80045.
Email: Tom.Finger@CUanschutz.edu

Present address:
Rae L. Russell, Department of Neurosurgery, University of Louisville, Louisville, KY 40202.

Funding information
National Institutes of Health, Grant/Award Numbers: R01DC017679, R01DC014728

Abstract

Taste buds comprise four types of taste cells: three mature, elongate types, Types I–III; and basally situated, immature postmitotic type, Type IV cells. We employed serial blockface scanning electron microscopy to delineate the characteristics and interrelationships of the taste cells in the circumvallate papillae of adult mice. Type I cells have an indented, elongate nucleus with invaginations, folded plasma membrane, and multiple apical microvilli in the taste pore. Type I microvilli may be either restricted to the bottom of the pore or extend outward reaching midway up into the taste pore. Type II cells (aka receptor cells) possess a large round or oval nucleus, a single apical microvillus extending through the taste pore, and specialized "atypical" mitochondria at functional points of contact with nerve fibers. Type III cells (aka "synaptic cells") are elongate with an indented nucleus, possess a single, apical microvillus extending through the taste pore, and are characterized by a small accumulation of synaptic vesicles at points of contact with nerve fibers. About one-quarter of Type III cells also exhibit an atypical mitochondrion near the presynaptic vesicle clusters at the synapse. Type IV cells (nonproliferative "basal cells") have a nucleus in the lower quarter of the taste bud and a foot process extending to the basement membrane often contacting nerve processes along the way. In murine circumvallate taste buds, Type I cells represent just over 50% of the population, whereas Types II, III, and IV (basal cells) represent 19, 15, and 14%, respectively.

KEYWORDS
microvilli, mitochondria, nerve fibers, RRID: SCR_001622, RRID: SCR_002716, RRID: SCR_014199, RRID: SCR_008606, synaptic vesicles, taste, taste buds

1 | INTRODUCTION

In mammals, taste buds, the sensory end organs for the gustatory sense, comprise 50–100 spindle-shaped cells arranged like cloves in a garlic bulb. The apices of the taste cells extend into the taste pore, an opening in the epithelium, allowing interaction of tastants with the taste receptors situated on these apical extensions. The detailed ultrastructure of these and other cellular features of taste buds began with studies on rabbits (Engstrom & Rytzner, 1956a, 1956b) with the first ultrastructural studies on rodents being performed on the rat a decade

later (Farbman, 1965; Gray & Watkins, 1965) and subsequently on the mouse, starting in 1974 (Mattern & Paran, 1974). These studies converge on a common understanding of cell types and general features of mammalian taste buds (Kinnamon & Yang, 2008).

Farbman (1965) introduced the commonly adopted nomenclature for taste cells, including peripheral (or edge), dark (Type I), light (Type II), and basal (Type IV) types. These so-called basal (Type IV) cells of taste buds are postmitotic and despite the similarity in name should not be confused with the proliferative basal cells that underlie all epithelia. Ultrastructural defining features of the various taste bud cells have included nuclear size and shape, overall configuration of cellular processes (Pumplin, Yu, & Smith, 1997), apical microstructure (Kinnamon & Yang, 2008), and relationship to nerve fibers and other cells in the taste bud (Kinnamon, Taylor, Delay, & Roper, 1985). A distinct Type III cell, marked by readily identifiable synapses onto nerve fibers, was added to the original dark–light scheme (Takeda & Hoshino, 1975).

More recent studies show a correlation between functional–molecular features of taste cells and the older ultrastructural classifications. Type I cells exhibit many features of astrocytes including fine processes extending between the other cell types (Pumplin et al., 1997), neurotransmitter reuptake (Lawton, Furness, Lindemann, & Hackney, 2000) or breakdown (Bartel, Sullivan, Lavoie, Sevigny, & Finger, 2006), and K^+ homeostasis (Dvoryanchikov, Sinclair, Perea-Martinez, Wang, & Chaudhari, 2009). Type II cells express the receptors for bitter, sweet, or umami (Chaudhari & Roper, 2010) along with the downstream transduction components including PLCβ2, IP_3R_3, and TrpM5. Type II cells form unique synapses with nerve fibers involving large mitochondria with tubular cristae (the so-called "atypical" mitochondria) closely apposed to the CALHM1/3 ATP release channels in the cell membrane (Ma et al., 2018; Romanov et al., 2018; Taruno et al., 2013). Strong depolarization of the Type II cells gates opens the CALHM1/3 channels to release the neurotransmitter, ATP, into extracellular space. In contrast, Type III cells, which mediate sour, and possibly some portion of salty taste form typical chemical synapses with nerve fibers including a small accumulation of presynaptic vesicles in the presynaptic compartment (Kinnamon et al., 1985; Yee, Yang, Bottger, Finger, & Kinnamon, 2001). Both Types II and III cells are more regular, spindle-shaped cells than Type I cells, which have diaphanous processes wrapping around other cells and nerve processes within the bud (Pumplin et al., 1997). Type IV cells express sonic hedgehog (Shh) and are recently generated, postmitotic cells with nuclei lying in the bottom half of the taste bud and capable of differentiating into any of the three elongate taste cell types (Miura et al., 2004; Miura, Scott, Harada, & Barlow, 2014). Other details regarding the morphology and interrelationships of these basal cells are unknown.

In the present study, we have used serial blockface scanning electron microscopy (sbfSEM) to generate three-dimensional (3D) reconstructions of longitudinal serial sections taken through circumvallate taste buds of mice. The sbfSEM technique, which entails large field, high-resolution imaging of tissues prepared for electron microscopy became practical for routine use only in the last decade (Denk & Horstmann, 2004). Previously, laborious reconstructions from serial sections of rodent and rabbit taste buds imaged with transmission electron microscopy were carried out by Kinnamon, Sherman, and Roper (1988). In contrast, sbfSEM, where the imaging and serial sectioning are done automatically, permits acquisition of very large image stacks with better than 10 nm resolution encompassing nearly complete taste buds. This permits a more quantitative and complete analysis of ultrastructural features and classifications of cell types than with the previous technology. This article focuses on the overall structure of taste buds of the circumvallate papilla of mice and the constituent cell populations. Later studies will concern the interactions between cells and their relationships with nerve fibers.

2 | MATERIALS AND METHODS

2.1 | Serial blockface scanning electron microscopy

Mice (C57BL/6) were anesthetized with Fatal-Plus Solution® and perfused through the heart with 0.1% $NaNO_2$, 0.9% NaCl, and 200 units sodium heparin in 100 ml 0.1 M phosphate buffer (pH 7.3), at 35 °C to clear the circulatory system. The mice were then perfusion fixed with 2.5% glutaraldehyde and 2% formaldehyde containing 2 mM $CaCl_2$ in 0.025 M sodium cacodylate buffer (pH 7.3) at 35 °C for 10 min. Tongues were then removed and placed in the same fixative for 2–3 hr at 4 °C. The circumvallate papillae were then sliced into 200-μm thick vibratome sections.

For conventional transmission electron microscopy, a subset of sections were rinsed in buffer, then reacted with 2% osmium tetroxide in 0.05 M sodium cacodylate buffer for 30 min. After three ddH_2O rinses, the sections were placed overnight in 1% uranyl acetate in ddH_2O and then stained en bloc in Walton's lead aspartate at 60 °C for 40 min prior to embedding in Luft's Epon.

Sections (200 μm thick) for sbfSEM were washed with 0.025 M cacodylate buffer (pH 7.3) with 2 mM $CaCl_2$, then incubated for 1 hr at 0 °C in a solution containing 3% $K_4(Fe[CN]_6)$ in 0.025 M cacodylate buffer of pH 7.3 with 2 mM $CaCl_2$ combined with an equal volume of 4% aqueous OsO_4. After the first heavy metal incubation, the sections were washed with H_2O at room temperature 5 × 3 min and then placed in 1% thiocarbohydrazide solution for 20 min at room temperature. After washing, the sections were placed in 2% OsO_4 for 30 min at room temperature. Following this second exposure to osmium, the tissues were washed in H_2O 5 × 3 min at room temperature, then placed in 1% $UO_2(OCOCH_3)\cdot 2H_2O$ at 4 °C overnight. The next day, the tissues were stained en bloc with Walton's lead aspartate for 30 min at 60 °C in 0.066 g of $Pb(NO_3)_2$ in 10 ml of aspartic acid stock and pH adjusted to 5.5 with 1 N KOH. Sections were then dehydrated using an increasing series of ice-cold alcohol solutions before transferring to propylene oxide 3 × 5 min and final embedment in Luft's Epon 3:7 at 60 °C overnight.

Semithin sections of the tissue blocks were examined to identify regions containing taste buds. The blocks then were trimmed and mounted on an aluminum pin, coated with colloidal silver paste around the block edges, and then examined with a Zeiss Sigma VP system equipped with a Gatan 3View in-chamber ultramicrotome stage with low-kV backscattered electron detectors optimized for 3View systems. Areas of the blockface containing

taste buds were identified and then these regions were imaged routinely at 2.25 kV, at 7–10 nm/pixel resolution (30 μm aperture, high current mode, high vacuum), with field sizes between 80 and 250 μm in *x*,*y* and approximately 500 slices with 70–85 nm thickness were generated. The resulting image stacks are aligned in Image J and montaged in Photoshop (Adobe Systems; RRID: SCR_014199). Segmentation and reconstruction were carried out using *Reconstruct* software (Synapse Web Reconstruct, RRID: SCR_002716) (Fiala, 2005). Each composite image was viewed separately, and cell membranes, nuclei, and so forth were segmented using the pencil feature. Segmentations from each image for each structure were combined to create 3D-rendered images in *Reconstruct*.

For 3D models and representations of the EM data, segmentations from each image for each structure were combined to render 3D surface models in *Reconstruct* and *Blender* (Blender Foundation, Amsterdam, the Netherlands; RRID:SCR_008606). MATLAB (The Mathworks, Natick, MA; RRID:SCR_001622) was used to approximate 3D renders of synaptic vesicles as spheroids based on the maximal cross-sectional area of vesicular segmentations because the *Reconstruct* software tended to conglomerate the small adjacent profiles of the synaptic vesicles.

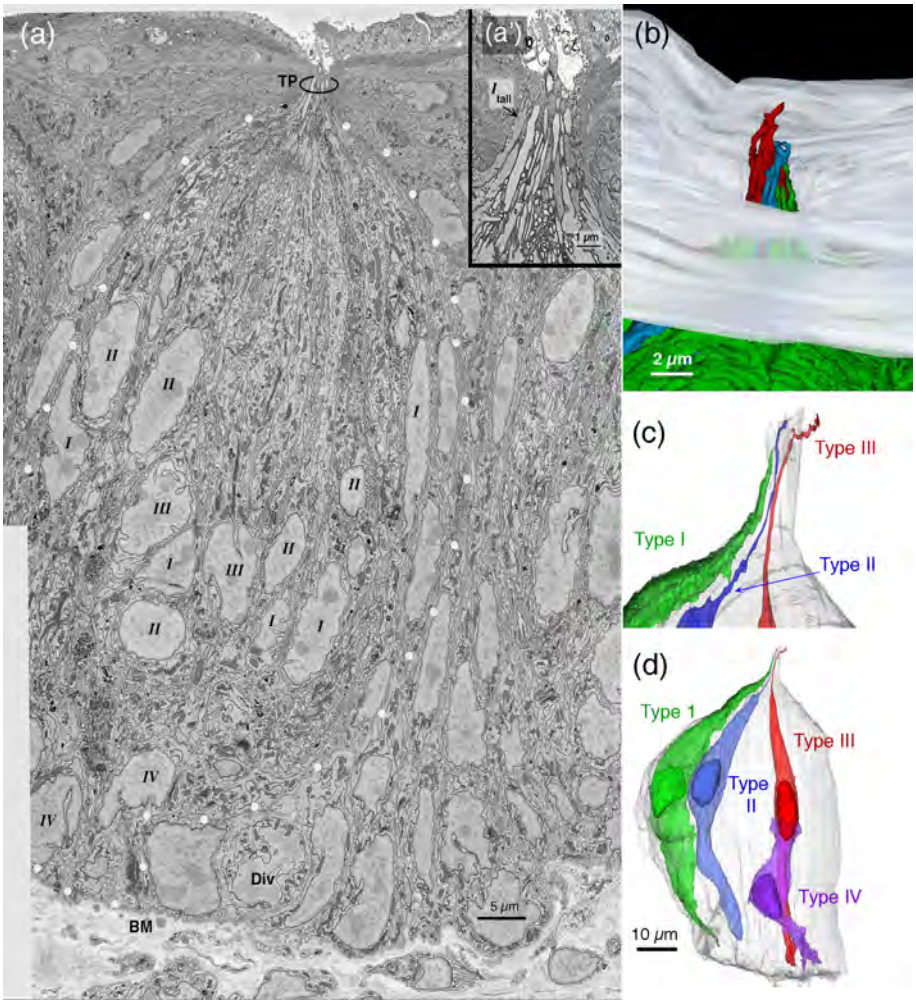

FIGURE 1 (a) A single-plane, low-magnification micrograph from the sbfSEM data set (DS2-TB3) showing a mouse circumvallate taste bud delimited by white dots, from basement membrane (BM) to a TP. Although this taste bud was not fully contained within the imaging volume, we identified 54 taste cells, some with a large, circular nucleus (Type II cells), others with irregular, elongate nuclei with nuclear invaginations (Type I or Type III cells) as well as postmitotic basal cells (Type IV cells). Div = dividing epithelial basal cell situated outside of the taste bud. The proportion of different taste cell types in the segmented volume was 32 Type I cells, 12 Type II cells, 5 Type III cells and 5 Type IV cells. These proportions are similar to other taste buds examined from the data sets (see Figure 5b). (a′) enlargement of the apical pore region showing the morphology of an arboriform (tall) type I cell. (b). 3D reconstruction of the surface epithelium and taste pore of a different taste bud showing the three different types of elongate cells in relation to the surface of the epithelium (gray). Type I cell in green; Type II cell in blue, and Type III cell in red. Note that the Types II and III cells each extend a single microvillus farther into the taste pore than do the type I cells. (c) 3D reconstruction of a taste pore region from another taste bud (TB1 of TF21, shown more completely in (d) showing four taste cells, one of each type and the surrounding limits of the taste bud (gray). Note that the Type I cell (green) does not reach as far up into the taste pore as do the other cells. (d) Same taste bud as (c) but showing examples of the four different cell types. BM, basement membrane; sbfSEM, serial blockface scanning electron microscopy; TP, taste pore [Color figure can be viewed at wileyonlinelibrary.com]

3 | RESULTS

3.1 | General features

A longitudinal section through a circumvallate taste bud shows a prominent taste pore (TP in Figure 1) with examples of diverse apical processes from Types I–III cells along with Type IV basal cells which do not reach the pore (Figure 1; Video S1). We use the term taste pore in this article to denote both the opening of the taste bud at the surface or the epithelium as well as the acellular depression into which cell apices extend. This latter volume is sometimes referred to as the "taste pit" in older literature. The taste bud shown in Figure 1 contains 54 taste cells that we were able to identify. The boundaries of the taste bud—both lateral and basally—are somewhat arbitrary in terms of whether to include edge cells and cells situated basally along the basal lamina. We have taken a fairly conservative approach, including in our analysis only cells that are clearly within the confines of the taste bud and interacting with other cells and nerve fibers in the bud. In Figure 1, the rounded cells lying outside the taste bud along the basement membrane in the right half of the figure, including a dividing cell (Div) are not included in our analysis. These cells are not closely associated with other cells of the taste bud and have no apically directed processes extending within the taste bud. Adjacent Type IV cells touching the basal lamina are elongated in the direction of the taste pore and have intimate association with the taste nerves and so are included in the taste bud volume.

Even at this low magnification, diverse cell types are evident according to nuclear and cytoplasmic features, for example, cytoplasmic organelles vary and some nuclei are fairly smooth and round while others are crenulated. With conventional transmission electron microscopy, Type I cells have an electron-dense cytoplasm while Type II cells have an electron-lucent cytoplasm. The tissue preparation procedures for sbfSEM, however, leave the electron density of the different cell types less distinctive. This makes classification of the different cell types based on electron density problematic. Hence, we distinguish the different cell types primarily based on cell shape, organelles, nuclear morphology, and apical processes. We further note the presence of conventional synapses or atypical mitochondria at points of contact between the taste cells and nerve fibers. All three elongate cell types have apical processes that may extend into the taste pore, but Type I apical processes do not extend as far into the taste pore (Figures 1b,c and 2a,b; also see below) as the other two elongate cell types.

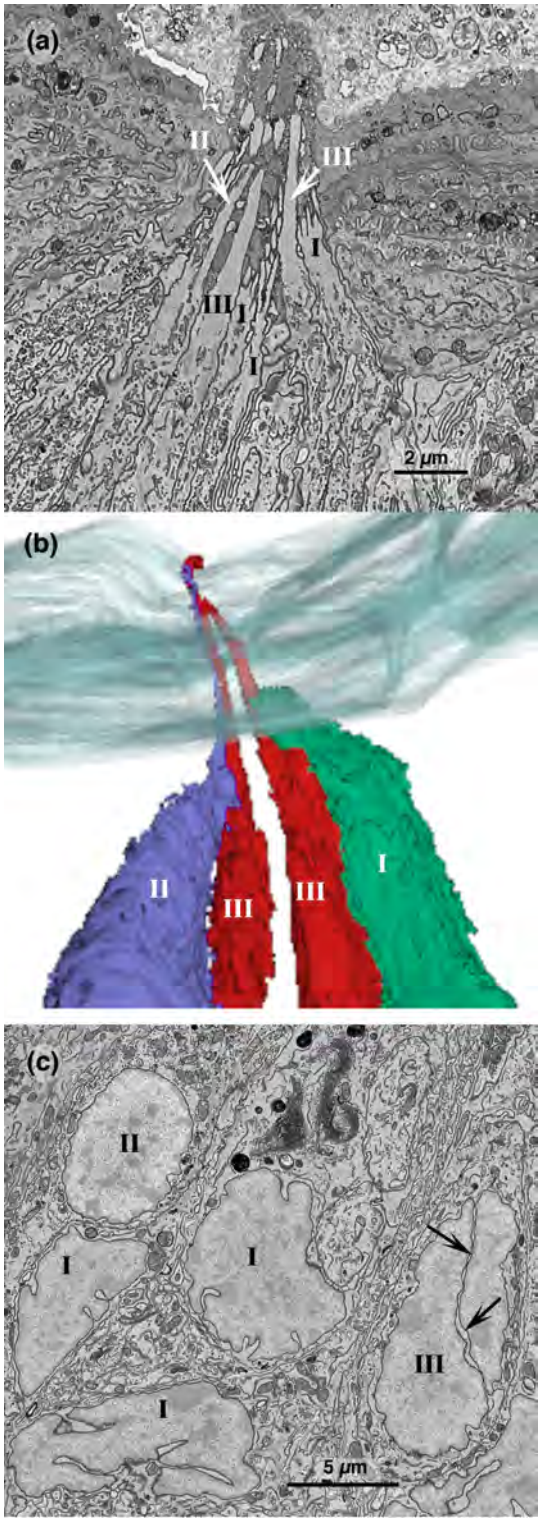

FIGURE 2 Legend on next column.

FIGURE 2 The different cell types are distinguishable by relationship to the taste pore and nuclear structure. (a) High magnification of the taste pore region showing some taste cells with single thick microvilli (Types II and III) extending high into the pore while others (Type I cells) extend branched microvilli ending in a bushy form near the base of the pore region. (b) Four taste cells from this taste pore rendered as individual objects showing the difference in height of apical extensions of the different cell types. (c) Single-plane image through a taste bud showing the different morphologies of cell nuclei of the different cell types. Type I cell nuclei (I) are irregular and often exhibit numerous invaginations of the nuclear envelope. Type II cell nuclei (II) are relatively round or oblate with a smooth nuclear envelope. Type III cell nuclei (III) are elongate and show one or more deep invaginations (arrows) of the nuclear membrane [Color figure can be viewed at wileyonlinelibrary.com]

3.2 | Distinguishing features of cell types

3.2.1 | Type I cells

The characteristic morphology of Type I cells shown in Figures 2–4 includes an irregular, indented nucleus, prominent Golgi apparatus, and refolded lamellate processes enwrapping nerve fibers and other cells. The Type I cell nuclei are generally elongate and may possess prominent invaginations, which can make distinguishing Type I cells from Type III cells challenging (Figure 2c). A hallmark of Type I cells is the presence of thin, lamellate processes, as thin as 0.2 μm, which envelop other taste cells or nerve processes (Figure 4). In single sections, these lamellate processes can appear similar to subsurface cisternae (SSC) as described previously in Type II taste cells (Clapp, Yang, Stoick, Kinnamon, & Kinnamon, 2004; Nishijima & Atoji, 2004; Royer & Kinnamon, 1988) and which we can identify in both Types II and III cells in our specimens as well (see below for description of SSC in Type III cells). Despite the appearance of the lamellate Type I cell processes in single-plane sections, they can be distinguished from SSCs and followed in adjacent sections to be continuous with adjacent Type I cells (Figure 4f–h). The lamellate processes of Type I cells can interdigitate with similar thin processes of adjacent cells of any morphological types; Figure 4i,j shows this interdigitation with processes of a Type III cell.

Although Type I taste cells come into extensive, intimate contact with nerve processes, we have not observed any distinctive organelles—

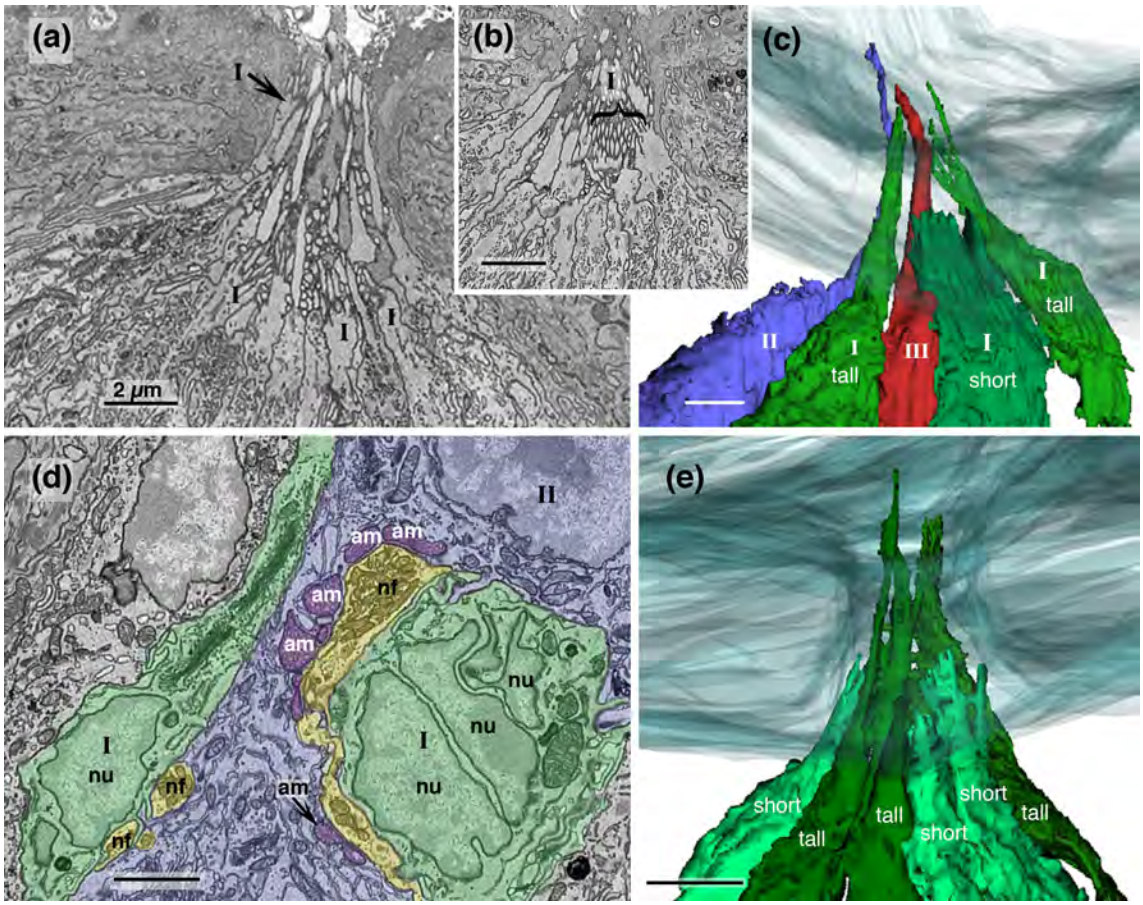

FIGURE 3 Type I cell morphological features. (a–d) Some Type I cells end in an apical tuft in or just below the base of the taste pore while other Type I cells extend a branched process outward into the taste pore but rarely reaching outward as far as Type II or Type III cell processes. (a) Single-plane image of the taste pore region. Two types of apical specializations are evident for Type I cells: bushy and elongate or arboriform (tree like). The apical processes of arboriform Type I cells (arrow) are stout and extend upward into the taste pore emitting several thick branches along the way. In contrast, bushy Type I cells (I) end below, or extend only a short distance into, the taste pore where they end as a terminal bush of short, thin microvilli. (b) Apical pore region showing the bushy type, fine microvillous processes of several Type I cells (bracket). (c) 3D reconstruction of three Type I cells (green) along with a Type III cell (red) and a Type II cell (blue) for comparison. The arboriform Type I cells are shorter than any of the Types II and III cells although they are taller than the bushy, short Type I cells. (d) The Type I cells (green) exhibit an irregular nucleus (nu) with nuclear invaginations. A common characteristic of Type I cells is that the membrane extends lamellate processes separate other taste cells (Type II cell, gray blue with atypical mitochondria [purple] at point of contact with the nerve fiber [yellow]). Despite close contact with nerve fibers (nf, yellow), Type I cells lack evidence for synaptic specializations, for example, vesicles or mitochondria, at points of contact. (e) 3D reconstruction of six Type I cells in a single taste bud showing the two different apical morphologies. Bushy cells (light green) end in a tuft of apical microvilli whereas arboriform Type I cells (dark green) have a longer branched apical process. [Color figure can be viewed at wileyonlinelibrary.com]

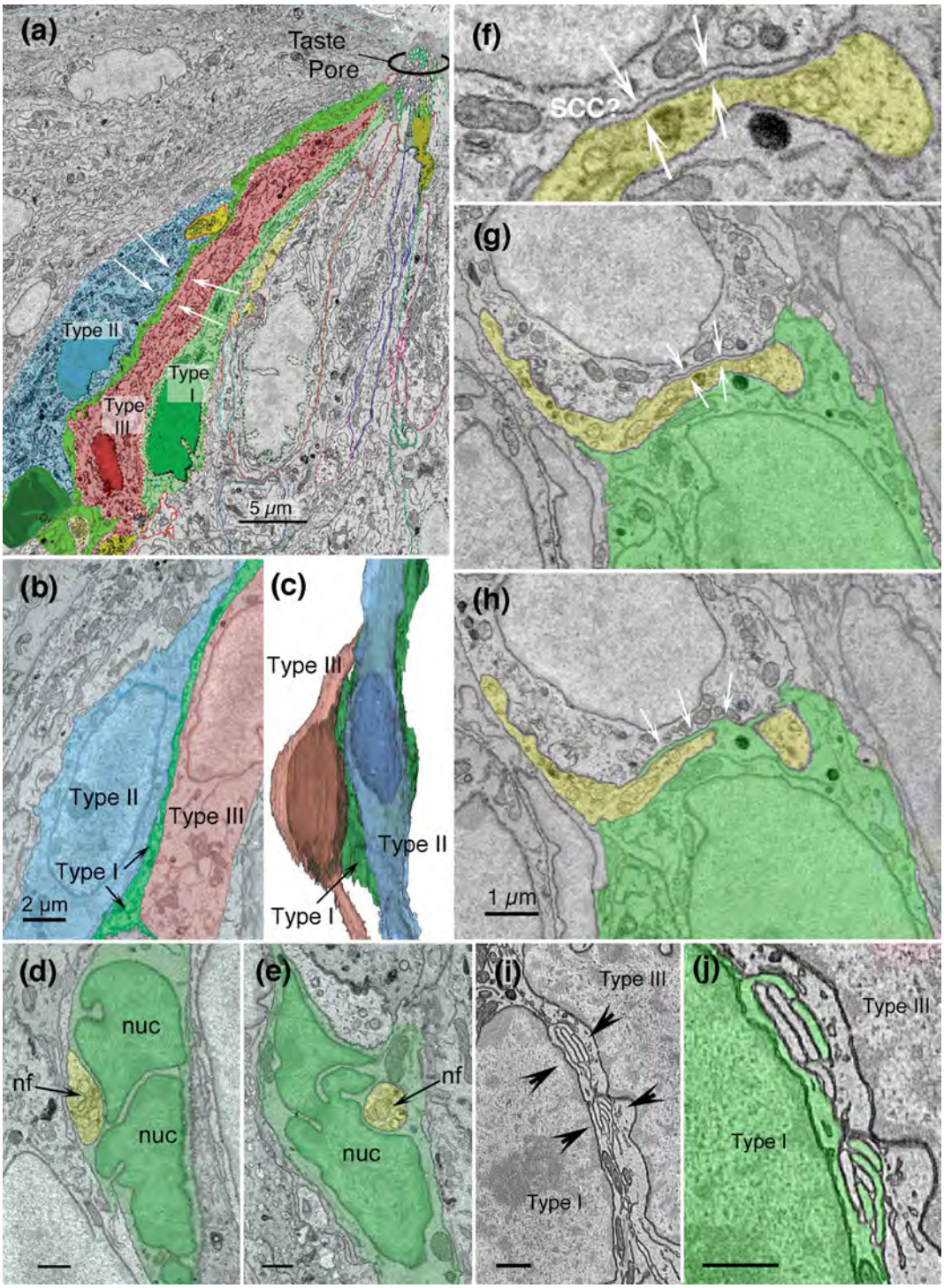

FIGURE 4 Features of Type I cells. (a,b) Type I cells (green and white arrows) separate Type II cells (blue) from Type III cells (red). Nerve fibers highlighted in yellow. (b) Higher magnification of another set of cells showing a narrow extension of a Type I cell lying between the Types II and III cells. These processes can be as thin as 0.2 μm, below the level of resolution of a light microscope. (c) 3D reconstruction of cell triplicate showing a Type I cell interposed between Types II and III cells. (d,e) The nucleus (nuc) of Type I cells (green) often lies in close association with nerve fibers (nf; yellow). In many cases, the Type I cells fully embrace (e) nerve fibers. Despite the intimate association of the nerve fibers and Type I cell nuclei, no membrane thickenings or synaptic specializations are evident at the point of contact. (f–h) When examined in serial sections, apparent SSC (f; SSC?) are infoldings of Type I cell processes. Nerve fiber highlighted in yellow. (g) Lower magnification view of the image in (f). Arrows show the identical regions in the two panels. The Type I cell is highlighted in green. (h) The same area as (g) but 170 nm (two sections) farther into the block. The apparent SSC (arrows) can be seen to be an infolded lamella of the Type I cell. (i,j) Interlocked lamellar processes (arrows) of adjacent Types I and III cells. (j) Higher magnification of interlocked membranes shown in (i) with the Type I cell color-coded green. SSC, subsurface cisternae [Color figure can be viewed at wileyonlinelibrary.com]

either vesicles or mitochondria—at points of contact between Type I cells and nerve processes or other taste cells. In many cases, the nerve process indents the cell in the region of the nucleus leaving scant cytoplasm in the space between the nerve fiber and the nucleus (Figure 4d,e). In some of these cases, either particles or strands of electron-dense material may lie in the narrow cytoplasmic space between the cell plasma membrane covering the nerve process and the nuclear membrane, but no obvious indications of synaptic specializations, for example, atypical mitochondria or synaptic vesicles, occur.

The apical processes of Type I cells appear to be of two different morphologies (Figure 3c,e) possessing either a single, stout, branched microvillus (arboriform [=tree-like]) or a fringe of numerous short microvilli (bushy subtype). The arboriform Type I cell has a stout microvillus which extends at least midway up into the taste pore. This apical microvillus often exhibits short lateral extensions, either at its root near the bottom of the taste pore or as short branches along the trunk of the process, giving it a somewhat shaggy appearance. These arboriform Type I cells also exhibit two slightly different morphologies. In one subtype, the long microvillus arises simply from the apex of the cell while in the other subtype, which we term a "mixed arboriform subtype", the apical microvillus arises from a small collection of short protuberances near the base of the taste pore, similar in appearance to the short microvilli of the bushy Type I cells. The bushy Type I cell has numerous apical microvilli which appear as a apical fringe, reaching upward a short distance and forming the floor of the taste pit, rarely reaching even midway up to the taste pore. The microvilli of the bushy Type I cells do not have thick branches like those of the arboriform Type I cells. Instead, the bushy Type I cell microvilli terminate in an expanded bush-like cluster. A 3D rendering of the two Type I cell apical specializations is shown in Figure 3c,e.

Some Type I cells do not extend outward as far as the floor of the taste pore although they lie entirely within the imaged volume. Despite the absence of an apical microvillus, these Type I cells exhibit the other characteristics of mature Type I cells including indented nucleus, prominent Golgi apparatus, and lamellate processes wrapping nerve processes and other cell types. Quantitative comparison of these two morphological subtypes of Type I cells shows that the arboriform subtype extends farther outward toward the epithelial surface than does the bushy subtype (Figure 5a). In four taste buds

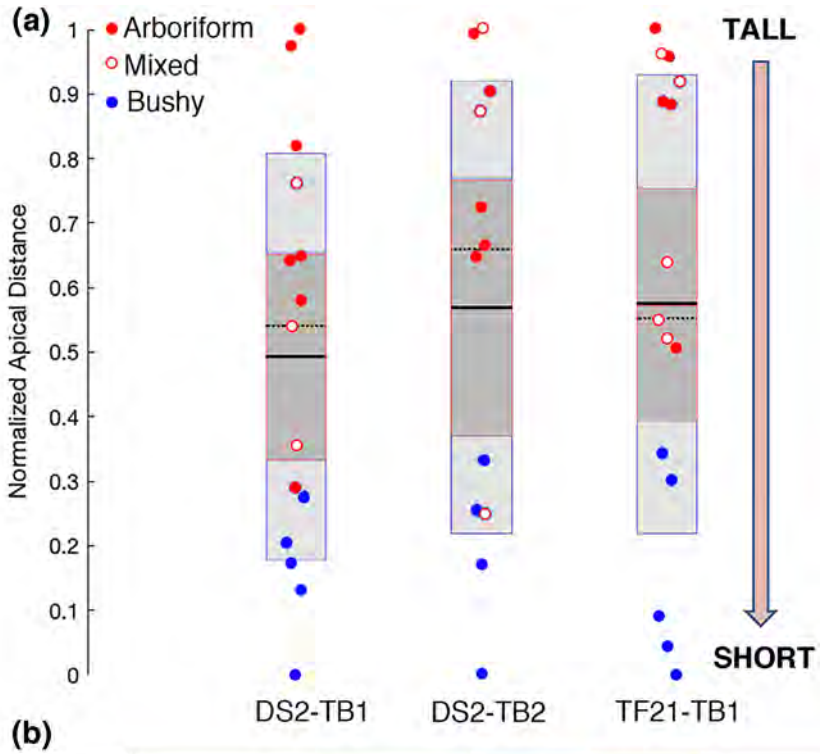

(b)

Taste Bud	Type I			Type II	Type III	Type IV
	Tall Microvilli	Short Microvilli	Did not reach pore			
TB0 (TF-21)	23.1 (3)	23.1 (3)	0.0 (0)	15.4 (2)	15.4 (2)	23.1 (3)
TB1 (TF-21)	14.0 (12)	25.6 (22)	11.6 (10)	19.8 (17)	12.8 (11)	16.3 (14)
TB1 (DS2)	27.0 (10)	16.2 (6)	10.8 (4)	18.9 (7)	21.6 (8)	5.4 (2)
TB2 (DS2)	29.2 (7)	25.0 (6)	4.2 (1)	16.7 (4)	12.5 (3)	12.5 (3)
Popul % (N)	**52.5%.** (84)			**18.8%** (30)	**15.0%** (24)	**13.8%** (22)
	20.0% (32)	**23.1%** (37)	**9.4%** (15)			

FIGURE 5 (a) Bar graphs showing the distribution of relative heights of Type I cells in three taste buds (TB0 not shown because it contains too few Type I cells to be worthwhile). Red dots indicate arboriform cells and blue dots the bushy subtype; open red circles mixed arboriform morphology. The horizontal solid line is the population mean; the dotted line is the median value for each bud. The arboriform Type I cells are all taller than the bushy cells. Mixed morphology cells tended to scale with arboriform cells and therefore were considered "tall" in subsequent analysis. For each taste bud, the shortest Type I cell of each bud was given the value of 0 while the tallest a value of 1 with other Type I cells scaled accordingly. Dark gray bars show 95% confidence interval; light gray indicates 1 *SD* for the population for each taste bud. (b) Percent population (and counts) of different types of taste cells in four taste buds of circumvallate papillae. TB0 is a complete taste bud; others are major portions (>50%) of different taste buds [Color figure can be viewed at wileyonlinelibrary.com]

measured quantitatively in this study, 38.1% of Type I cells were arboriform while 44.0% were bushy with the remainder failing to reach the TP (Figure 5b).

3.2.2 | Type II cells

The characteristic features of Type II cells are round, smooth nuclei and a single, thick apical microvillus that extends well into the taste pore, often reaching the level of the surface of the surrounding epithelium (Figures 1b and 6a). This contrasts with Type I microvilli, which extend only part way into the taste pore (Figure 1c). A common feature of Type II cells is a large, round nucleus with a predominately homogeneous nuclear matrix, although patches of heterochromatin may be present, especially adherent to the nuclear membrane (Figures 1a, 2c, and 6b,c). Most, but not all (40 of 42 identified Type II cells) Type II cells contain atypical mitochondria that occur exclusively at the close appositions between the Type II cell and a nerve process (Romanov et al., 2018). Although typical mitochondria usually contain lamellar cristae

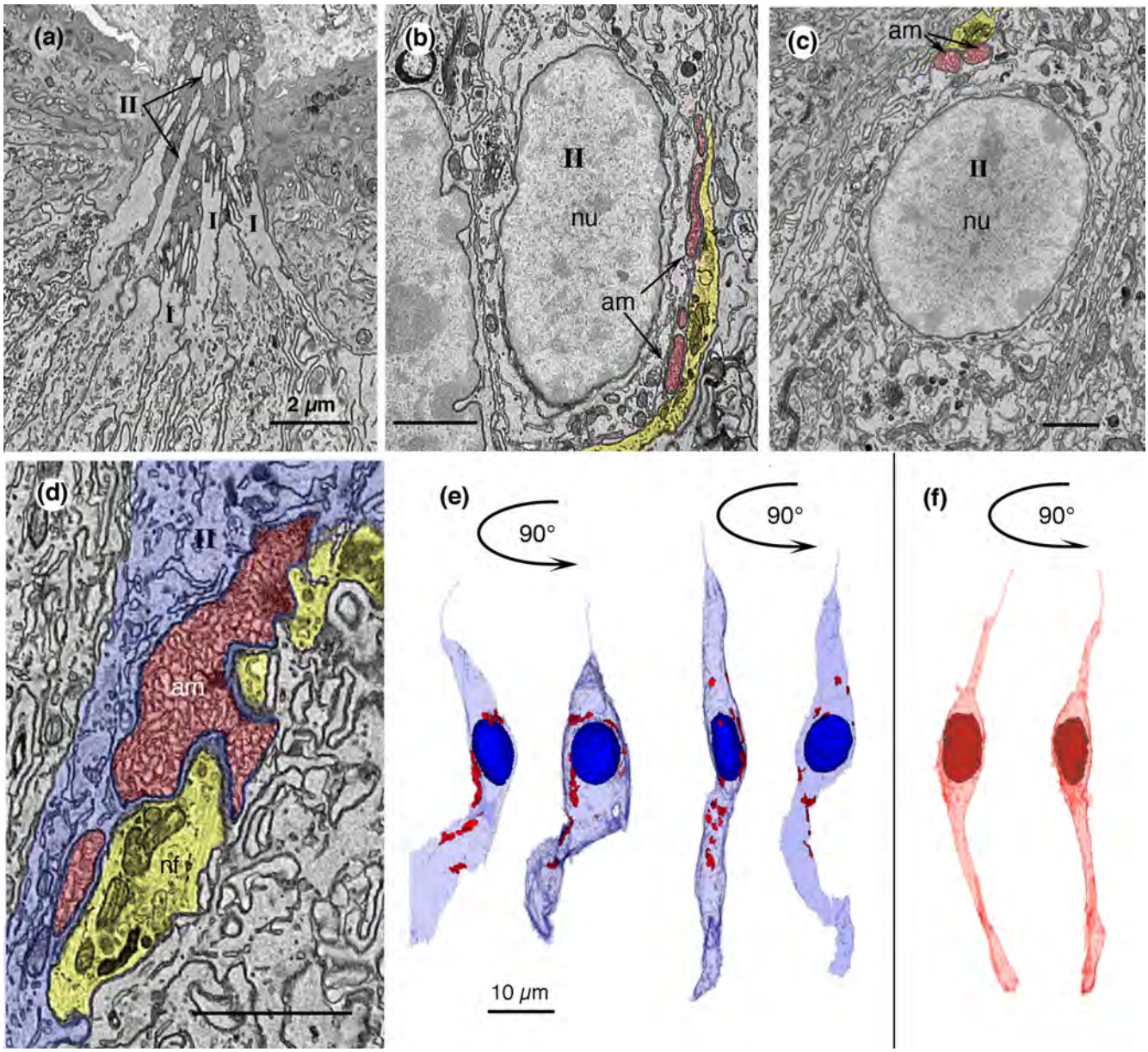

FIGURE 6 Morphological features of Type II cells. (a) Type II taste cells extend a single thick apical microvillus (II) high into the TP. (b,c) Type II cells have a large round nucleus (nu) with relatively sparse heterochromatin, and electron lucent cytoplasm. The nucleus may appear either circular or ovoid. At some points of contact with nerve fibers (yellow), atypical mitochondria (am; red) are evidence of synaptic specialization (see Romanov et al., 2018). (d) Higher magnification showing a large atypical mitochondrion (red) abutting the membrane facing the nerve fiber (yellow). (e) Reconstructions of two Type II cells with each cell showing its different appearance when rotated 90°. When viewed from different perspectives, the nucleus (dark blue) of a Type II cell can appear elongate (left side of each pair) or circular (right half of each pair). Red spots indicate the position of atypical mitochondria in each cell; TP up. (f) Similarly rotated reconstruction of a Type III cell does not show the marked nuclear asymmetry seen in Type II cells; Scale bar in (e) applies also to (f). TP, taste pore [Color figure can be viewed at wileyonlinelibrary.com]

arranged in a shelf-like configuration, atypical mitochondria contain tubular cristae with no apparent organization (Figure 6d). Of the 30 Type II cells examined, none had direct contact with a Type III cell; Type I cell processes always intervene. (Figure 4).

3.2.3 | Type III cells

Type III cells have a single, long, blunt microvillus that extends, like a Type II cell microvillus, well into the taste pore (Figures 1b, 2b, and 7a) often reaching to or even above the surface level of the surrounding epithelium. In general, the microvillus of a Type III cell extends farther outward than the microvilli of Type II cells in the same taste bud. Type III cells display an elongate nucleus with prominent, deep invaginations in the nuclear membrane (Figures 1a, 2c, 6f, and 7b). The most distinguishing feature of Type III cells is the presence of conventional synapses with a small accumulation of presynaptic vesicles. These synapses are characterized by the presence of 40–60 nm clear vesicles, some of which appose the presynaptic membrane (Figures 7b, 7s1, and 7s2) abutting a nerve process. In conventional transmission electron micrographs, the presynaptic membranes are thickened and electron dense; this is not as apparent with the sbfSEM technique.

In our examination of 23 Type III taste cells, we have identified 5 (21.7%) that also exhibited one or more atypical mitochondria with tubular cristae at a point of contact with a nerve fiber. This contact also shows an accumulation of presynaptic vesicles (Figure 8) although not all synaptic contacts of these cells exhibit an atypical mitochondrion. These cells have the characteristic features of a Type III cell, that is, indented nucleus and single long apical microvillus as well as an accumulation of vesicles where the cell membrane contacts a neural process. The mitochondria at the points of vesicle accumulation appear identical to the "atypical mitochondria" associated with neural contacts of Type II cells. The atypical mitochondria in both cell types are larger than the other mitochondria in the cell and have irregular, tubular cristae not common in other mitochondria of the same cell.

We also find SSC in Type III cells as has been described by others for Type II cells. The SSC appears at points of apposition to nerve fibers but is not necessarily associated with either presynaptic vesicles or atypical mitochondria. While the SSC appears similar in some respects to infoldings of Type I cells (see Figures 4 and 9), the SSC can be distinguished from these other features by continuity with smooth endoplasmic reticulum or by blindly ending within the cytoplasm of the taste cell (Figure 9a,b,e).

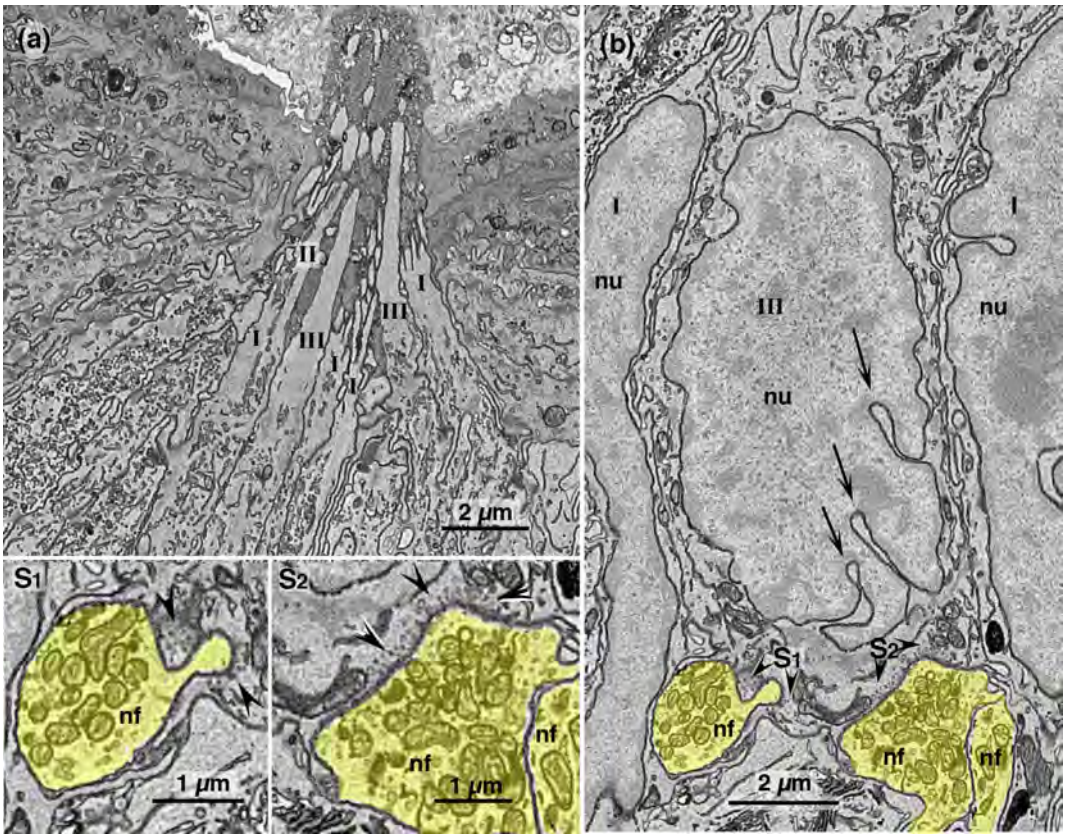

FIGURE 7 Morphological features of Type III cells. (a) Type III cells are slender extending a single, large, and blunt microvillus (III) into the TP. Note that the Type III cell microvillus is thicker than Type II cell (II) microvilli. (b) Type III cell nuclei are irregular and elongated, often with deep invaginations (arrows). Also visible are two adjacent Type I cell nuclei (nu) with small invaginations. Classical chemical synapses (S_1, S_2 enlarged at lower left) with synaptic vesicles (arrow heads) appear at some points of contact between the Type III cell and nerve fibers (nf, yellow). S_1, S_2: Enlargements from (b) showing several clear, synaptic vesicles (arrow heads) at points of contact with the nerve fibers. TP, taste pore [Color figure can be viewed at wileyonlinelibrary.com]

3.2.4 | 3D reconstructions of the taste pore region

Figures 1b and 2b show 3D reconstructions of the microvilli from a taste bud extending through the extragemmal epithelial surface. Figures 2a, 3a, and 5a show low-magnification images of the microvilli of two taste buds. A higher magnification 3D reconstruction of one of the taste buds demonstrates how the microvilli of the Type II cells (blue) and the Type III cells (red) extend farther into the oral cavity than the apical microvilli of either of the subtypes of Type I cells. A movie (Video S1) of the same taste bud graphically shows the apical processes of the different cell types and the extent to which they project into the oral cavity.

3.2.5 | Type IV cells ("basal" cells)

Type IV cells are characterized by a nucleus situated in the lower quarter of the taste bud (Figure 10a) and lacking an extensive apical process. Furthermore, these cells do not display any of the characteristic features by which we could assign them into other cell classes. Type IV cells have a spheroidal irregular nucleus with scattered patches of heterochromatin and a relatively thin rim of cytoplasm surrounding the nucleus. These cells assume two different morphologies related to their position in the taste bud. Type IV cells lying along the basolateral margin of the bud are flattened, disc-like cells (Figure 10c) while those situated more centrally are elongate in the longitudinal axis of the taste bud and have a basal extension contacting the basal lamina (Figure 10b,c) as well as the plexus of nerve fibers (Figure 10d) underlying the taste bud. Although basal cells contact nerve fibers, no apparent membrane thickenings or specialized contacts occur, including classical synapses with vesicles or contacts with atypical mitochondria. Although basal cells often abut one another or even other cell types in the bud, no apparent membrane specializations occur at these points of contact. Some Type IV cells have a short apical extension which may partially envelop surrounding elongate taste cells (Figure 10b).

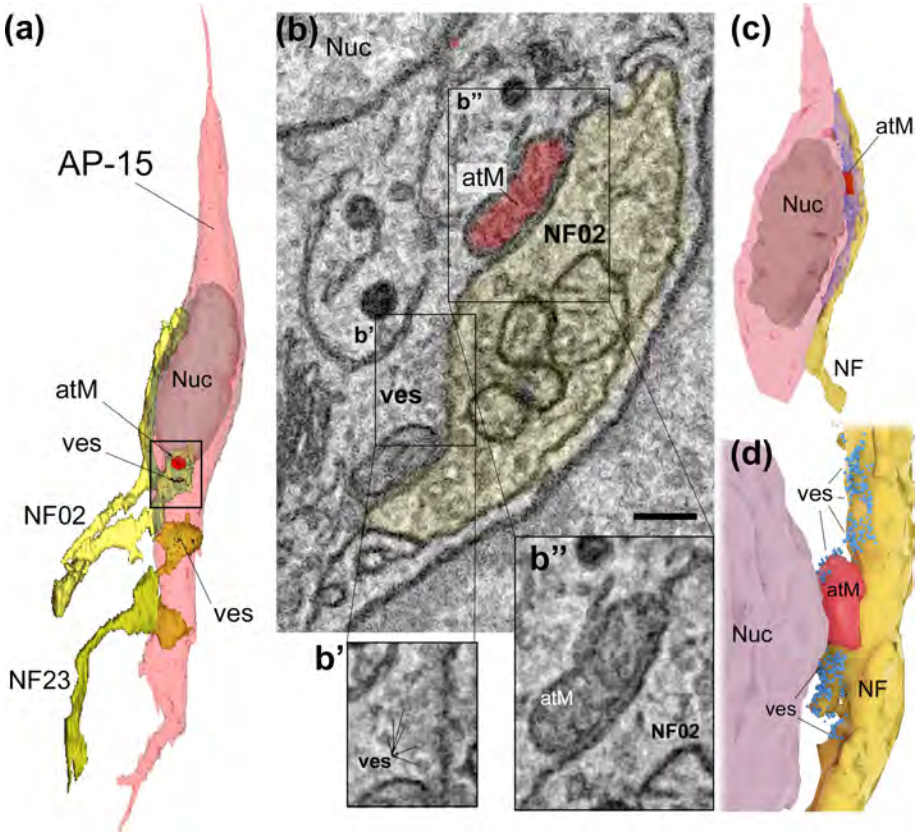

FIGURE 8 Some Type III cells exhibit mitochondria with irregular cristae associated with vesicle clusters at points of contact between the Type III cell and nerve fibers. (a) Reconstruction of a Type III taste cell (AP-15) and two associated nerve fibers (NF02 and NF23). Accumulations of vesicles (ves) near the point of cell-nerve contact are indicative of Type III cell synapses. At one of these contacts, we also find one or more mitochondria (red) with irregular cristae closely apposed to the cell membrane. (b) Single-plane sbfSEM image of the region containing the mitochondrion of interest showing the location of vesicles (ves) and mitochondrion (atM) in relation to the nerve process (NF02). (b′) Enlargement of the vesicular accumulation framed by the box in (b). This image was enlarged by 125% and filtered with a Photoshop Dust & Scratches Filter (3-pixel radius) to reduce graininess. (b″) Enlargement of the boxed area in (b) around the mitochondrion processed similarly to (b′) to show irregular cristae. (c) Reconstruction of another Type III cell (pink) with an irregular mitochondrion (red) at the point of contact with a nerve process (yellow). (d) Higher magnification 3D rendering showing the relative position of vesicles (blue), mitochondrion (red), and underlying nerve process (yellow). For purposes of visualization the cell membrane of the Type III cell was rendered transparent. sbfSEM, serial blockface scanning electron microscopy [Color figure can be viewed at wileyonlinelibrary.com]

3.2.6 | Atypical cells

Of the over 200 cells identified in our data sets, we encountered 2 cells of atypical morphology that did not fit into any of the morphological classes described above. Both cells ended apically as short, bushy microvilli, but cytologically appeared to be Type II cells. One cell had an atypical mitochondrion, but the other did not. We did not include either of these cells in our population counts.

3.3 | Cell type counts

We identified all taste cells by cell type in five taste buds, four of which were incomplete taste buds, from circumvallate papillae of two adult mice. These data allowed us to make population estimates of each cell type in each taste bud although we did not include any taste cells that extended outside of the boundaries of the data set (Figure 5b). We fully segmented all Types II and III cells that extended into or nearly into the TP along with several Type I cells some of which did not reach the TP but nonetheless lay entirely within the segmented volume. The diversity of appearance of the different fully segmented cells from one taste bud is shown in Figure 11. In addition, we characterized by cell type, without fully segmenting each one, all taste cells whose nuclei were fully contained within the sampling volume giving a total of 160 cells within four taste buds whose apical region made possible identification of Type I cell subtypes. The smallest sample included 13 cells from a small taste bud and 86 cells from the largest taste bud. Data for each of the four taste buds are given in the table shown in Figure 5b. Taken together, the cell type counts show that Type I cells comprise 52.5% of the population; Type II cells 18.8%; Type III cells 15%, and Type IV, 13.8%.

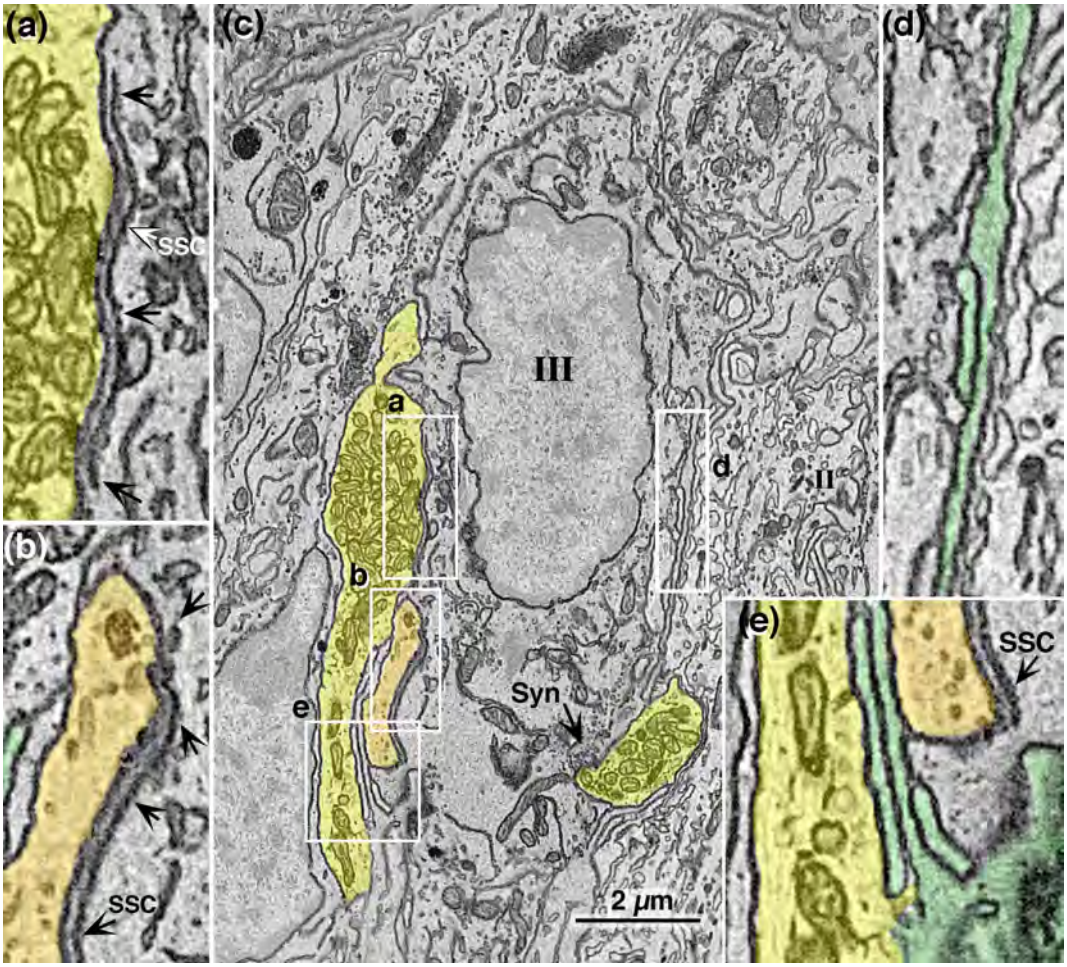

FIGURE 9 SSC in type III cells. (a) High-magnification view of area (a) from (c) showing a SSC (arrows) at a point of apposition to a nerve process (yellow). Note that the ends of the SSC end blindly within the cytoplasm. (b) Similar high-magnification view of another SSC from the same cell in apposition to a different nerve process. (c) Overview of SSC in a Type III cell compared to appearance of infolded Type I cell membranes (green). A synaptic contact from the Type III cells (Syn) onto another nerve process is indicated. (d) Type I cell lamellae (green) apposed to a Type III cell. Note that the Type I cell membranes form a complete loop closed off from the Type III cell cytoplasm. (e) Higher magnification view of region (e) from (c). Although SSCs have similar dimensions to the infolded lamellae of Type I cells (green), they can be distinguished from the latter by blinding ending within the cytoplasm rather than forming closed-off loops. SSC, subsurface cisternae [Color figure can be viewed at wileyonlinelibrary.com]

4 | DISCUSSION

The most commonly accepted contemporary delineation of mature taste cells divides them into three types of elongate, differentiated cells: Type I cells are considered glial like, Type II cells underlie transduction of sweet, bitter, and umami, forming unusual channel-based neurotransmitter release synapses with the afferent nerves (Romanov et al 2018), while Type III cells mediate sour taste and form classical synapses with synaptic vesicles at points of contact with nerve fibers. Our detailed analysis of the sbfSEM data confirms in broad terms this tripartite distinction between mature cell types.

These three morphological types of mature taste cells correlate well, but not exactly, with expression of immunochemical markers, whose expression has been used to estimate populations of different cell types in taste buds (Ma, Yang, Thomas, & Kinnamon, 2007; Ohtubo & Yoshii, 2011). In taste buds of fungiform papillae of mice (Ma et al., 2007), Type I cells are the most common cell type, representing over 50% of the total population, with Type II cells next most abundant (30–38%) and Type III cells described as relatively rare, about 5–6% (Chaudhari & Roper, 2010; Ohtubo & Yoshii, 2011). The proportions are somewhat different in taste buds of murine circumvallate papillae which show substantially greater proportions of Type III cells (roughly 15%) with slightly smaller proportions of Type II cells (20%) (Ma et al., 2007; Ueda, Fujii, El-Sharaby, Honma, & Wakisaka, 2003). Our analysis is consistent with the result from circumvallate papillae reported by Ma et al. (2007)), that is, Type III cells are somewhat less abundant than Type II cells but still represent about 15% of the population. In contrast, taste buds of fungiform papillae have a much lower proportion of Type III cells.

The most striking results of this study are as follows: (a) the presence of multiple subtypes of Type I cells distinguished by differences in apical microstructure and degree of extension toward the TP; (b) differences in structure of Type II taste cell apices between mouse and rats; (c) the presence of an atypical mitochondrion associated with presynaptic vesicle clusters in a significant proportion (21.7%) of Type III cells; and (d) the presence in Type IV cells, of a foot process that intertwines with gustatory nerve fibers and retains contact with the basal lamina.

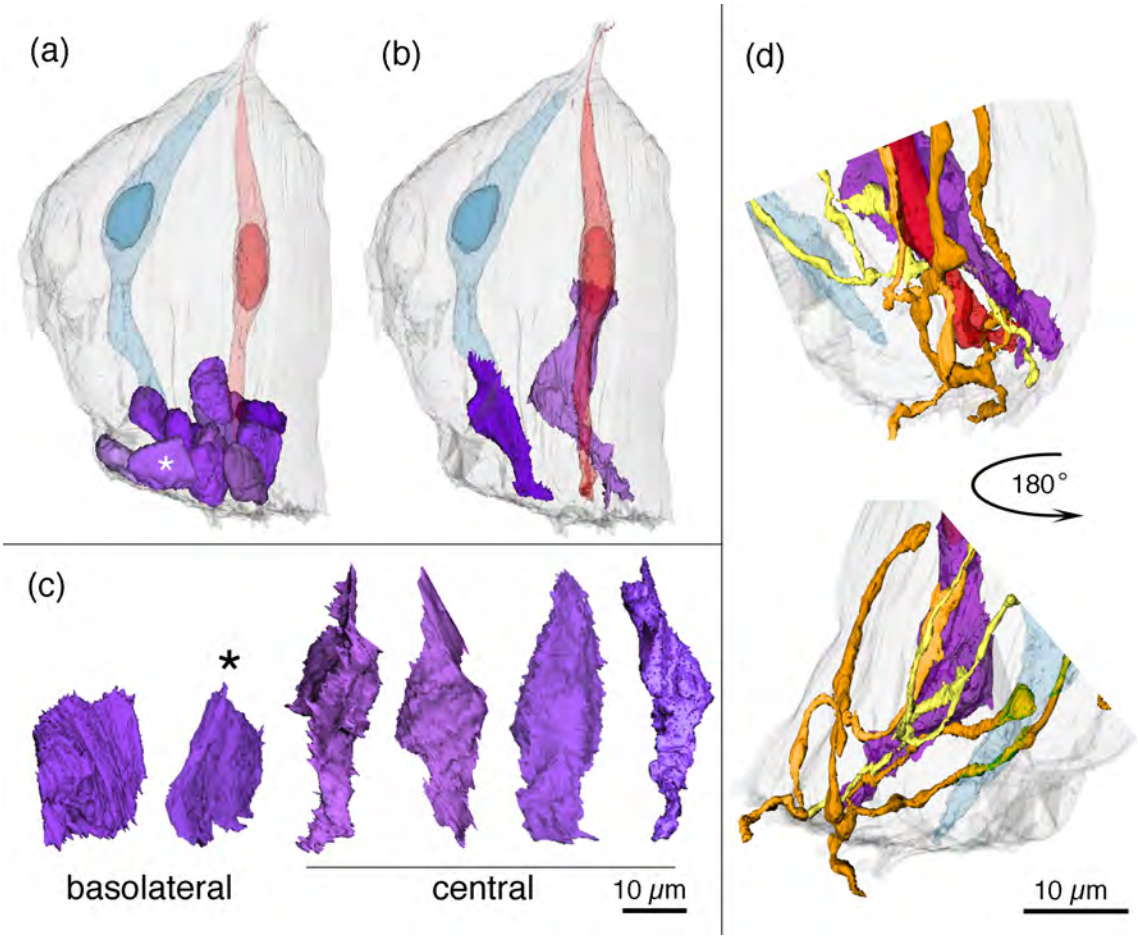

FIGURE 10 Type IV cell characteristics. (a) Only the nuclei of Type IV (basal) cells (magenta) are shown in this image to illustrate their situation in the lower quarter of the taste bud while the nuclei of typical Type II (blue) and Type III (red) cells lie higher in the bud. Asterisk symbol in (a) and (c) denotes the same cell to facilitate comparison. (b) Two fully segmented Type IV cells in relation to typical Type II (blue) and Type III (red) cells. The Type IV on the right embraces the Type III cell. (c) Type IV cells situated basolaterally are flattened and disc like. Those more centrally located are elongate and have a basal process extending to the basal lamina beneath the taste bud. (d) This basal process frequently contacts the plexus of nerve fibers (orange and yellow) penetrating the base of the bud. All 3D models reconstructed from TB1 of TF21 data set [Color figure can be viewed at wileyonlinelibrary.com]

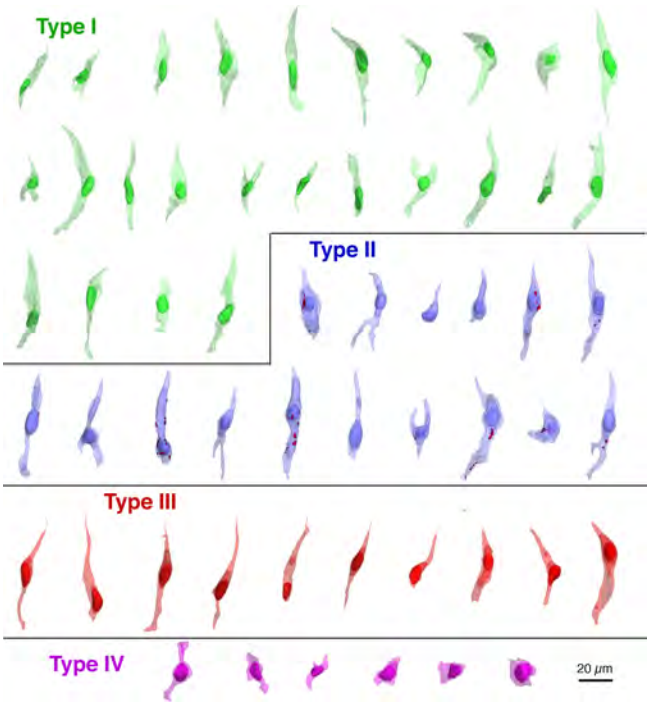

FIGURE 11 Composite image of 3D reconstruction of fully segmented cells from a single taste bud (TF21 TB1) showing the diversity of cellular morphologies of the different cell types. Although the cells vary substantially in overall extent, these images are the full extent of each cell; none have been truncated by sectioning or imaging [Color figure can be viewed at wileyonlinelibrary.com]

4.1 | Type I cell subtypes

The 3D reconstructions reveal that some Type I cells end within the taste bud well below the TP region. The large majority of Type I cells extend to the TP but end apically in two different fashions: (a) short, bushy microvilli ending near the floor of the TP (bushy subtype), and (b) longer, thick slightly branched microvilli that extend outward more than half way up in the TP (arboriform subtype). The differences in apical microstructure of the different Type I cells may be related to the relatively rapid turnover of these cells in taste buds. The average lifespan of a Type I cell may be as short as 8 days (Perea-Martinez, Nagai, & Chaudhari, 2013), so at any time, 10–30% of Type I cells should be immature or senescent and apical microstructure may relate to the relative age of a Type I cell. For example, Type I cells not reaching the TP may be the youngest, while those with prominent long apical microvilli may be the most mature. Of course, other age-related schemes are possible. Furthermore, some Type I cells may live 24 days or longer (Perea-Martinez et al., 2013) and it may be that shorter- and longer-lived Type I cells display different apical microstructure.

Alternatively, the existence of multiple morphological subtypes of Type I cells leads to speculation that there may be corresponding functional subtypes. The very short Type I cells that lack apical microvilli and do not approach the TP likely serve the glial-like functions usually attributed to Type I cells: degradation and reuptake of neurotransmitters, or physical separation and isolation of other cell types, and ionic buffering (Bartel et al., 2006; Chaudhari & Roper, 2010; Dvoryanchikov et al., 2009; Pumplin et al., 1997). In contrast, the Type I cells with apical microvilli reaching the TP might participate in ionic clearance (Dvoryanchikov et al., 2009).

Another possibility is that Type I cells directly respond to particular tastants and are involved in transduction or modulation of taste bud function. Relatively large molecules such as sugars and many organic bitter compounds may reach only the tall, arboriform Type I cells since the TP is filled with a mucus substance permeable to small molecules such as lanthanum (Holland, Zampighi, & Simon, 1991) but would likely be a barrier to larger molecular species. Small ionic taste substances such as salts and protons (sour), likely permeate well into the TP and therefore could directly interact with even the short, bushy Type I cell apices. Furthermore, both tall and short subtypes of Type I cells would be adequately acidified by any acids applied to the apical surface (Richter, Caicedo, & Roper, 2003) and thus could participate in transduction of acids as well.

Although Types II and III cells are generally considered to be responsible for transduction of, respectively, bitter, sweet, and umami (Type II) and sour (Type III) (Chaudhari & Roper, 2010), the possibility of Type I cells participating in transduction is not without precedent. Vandenbeuch, Clapp, and Kinnamon (2008)) identified a population of taste cells expressing the amiloride-sensitive Na^+ channel potentially underlying some components of salt transduction, but that lacked the physiological hallmarks of both Types II and III cells, suggesting that Type I cells may respond to Na^+ ions. If a subset of Type I cells do participate in salt transduction, the question arises as to how the Type I cells might communicate with the nerve fibers. Although Type I cells have extensive areas of apposition to nerve fibers, the Type I cells exhibit no obvious synaptic specializations—either vesicular or mitochondrial—at these points of contact. Since all taste transmission requires activation of purinergic P2X receptors on the nerve fibers (Finger et al., 2005; Vandenbeuch et al., 2015), the lack of presynaptic specializations in Type I cells suggests an unconventional means of transmitter release, for example, by transporters or ion channels—similar to the means by which astrocytes release gliotransmitters in the brain (Bang, Kim, & Lee, 2016; Yoon & Lee, 2014). Alternatively, Type I cells may modulate responses of adjacent Types II and III cells to regulate transmission between those cells and the taste nerves.

4.2 | Apical microstructure of taste cells

Our reconstructions of apical microvilli in mouse circumvallate taste buds reveal differences in microstructure compared to previous reports on cell apices in both rat and bovine taste buds (Tabata et al., 2003; Yang, Tabata, Crowley, Margolskee, & Kinnamon, 2000). In circumvallate taste buds of both rats and cows, Type II cell microvilli are described as being short and brush-like with the microvilli being of the same length. They do not extend far into the TP. While one might question the reliability of cell identifications in these studies, both studies relied on immunocytochemistry for gustducin which is a widely used marker of Type II taste cells. In our preparations of mouse circumvallate taste buds, virtually all cells with short, branched microvilli are Type I cells.

In rat taste buds, the microvilli of Type I cells are the longest and extend well into and often above the TP. In the mouse, the Type I microvilli are the shortest and fall into two subtypes: short and tall—with even the tall microvilli of Type I cells not extending as far outward through the TP as either the Type II or Type III cell microvilli. The short bushy Type I cell microvilli that we describe are grossly similar to the microvilli described for the Type II cell of the rat circumvallate taste buds, that is, short and brush-like with the microvilli being of the same length. They do not extend far into the TP. This contrasts with the apical microvilli of mouse circumvallate Type II cells, which consist of a single, stout microvillus that extends through the TP into the oral cavity. Rat circumvallate Type III cells possess a single, short, thick, blunt microvillus that does not extend far into the TP (Yang et al., 2000), while mouse circumvallate Type III cells have a single, long microvillus that projects through the TP into the oral cavity. These apparent differences in apical structure may be species differences or might be attributable to different technical approaches or criteria for cell identification.

4.3 | Type III cell mixed synapses

The observation that a significant proportion of Type III cells also possess a mitochondrion with irregular cristae in association with vesicle clusters facing a nerve fiber might be explained in several ways. These Type III cells with nerve-associated mitochondria may represent a functional subset of Type III cells with particular roles in transduction of sour or highly salty tastes. Subsets of Type III cells have been described at the light microscopic level based on molecular properties (Lossow, Hermans-Borgmeyer, Behrens, & Meyerhof, 2017; Wilson, Finger, & Kinnamon, 2017). Whether these molecularly different subsets of Type III cells correspond to the differences we observe in ultrastructure requires further study. Alternatively, these different morphologies may represent a developmental stage in the natural progression of Type III cells from immature to mature. In either event, the presence of such distinctive mitochondria near the synaptic site may offer a source of ATP for ultimate synaptic release along with other neurotransmitters such as serotonin. Our previous work has shown that purinergic signaling is essential for transmission of Type III cell information (Finger et al., 2005; Larson et al., 2015; Vandenbeuch et al., 2013) although these cells show no evidence of channel-mediated ATP release as do Type II cells (Ma et al., 2018; Romanov et al., 2018; Taruno et al., 2013). It is possible that Type III cells release ATP from synaptic vesicles, but vesicular loading of ATP requires the vesicular nucleotide transporter which to date, has been localized only to Type II cells (Iwatsuki et al., 2009).

4.4 | Type IV cells

Type IV cells (aka "basal cells") in taste buds are a population of postmitotic, relatively immature cells that express Shh prior to their ultimate differentiation into the different types of elongate, fully mature taste cells (Miura et al., 2004; Miura et al., 2014). These cells are generally described as being spherical, based on the nuclear structure, but our analysis of sbfSEM images reveals that the nearly all of the basal cells have a basal process still in contact with the basal lamina perhaps reflecting their relatively recent migration from the more basal position where the proliferative taste bud progenitor cells reside (Miura et al., 2014). The residual contact with the basal lamina may be important in the final determination of cell fate for this population (Yang et al., 2011). Similarly, the basal process of Type IV cells intertwines with the basal nerve plexus which likely provides molecular signals crucial for differentiation (Castillo-Azofeifa et al., 2017).

The use of sbfSEM 3D reconstructions greatly enhanced our ability to extract and interpret information from a large data set embracing the full height of a taste bud from basal lamina to TP. We believe that this technical approach shows great promise for our future studies in which we plan to elucidate the patterns of synaptic connectivity in taste buds.

ACKNOWLEDGMENTS

The authors would like to thank Logan E. Savidge, Felicia Rodriquez, and Daniel Evans who assisted with segmentation of the taste buds, and Sue Kinnamon who provided thoughtful discussion and comment on drafts of this manuscript. We also thank the NIDCD of National Institutes of Health for support of this work R01DC014728; R01DC017679.

DATA AVAILABILITY STATEMENT

The data that support the findings of this study are available from the corresponding author upon reasonable request. The full image set from DS2 and TF21 will be available from the Electron Microscopy Public Image Archive (EMPIAR).

REFERENCES

Bang, J., Kim, H. Y., & Lee, H. (2016). Optogenetic and chemogenetic approaches for studying astrocytes and gliotransmitters. *Experimental Neurobiology*, *25*(5), 205–221. https://doi.org/10.5607/en.2016.25.5.205

Bartel, D. L., Sullivan, S. L., Lavoie, E. G., Sevigny, J., & Finger, T. E. (2006). Nucleoside triphosphate diphosphohydrolase-2 is the ecto-ATPase of type I cells in taste buds. *The Journal of Comparative Neurology*, *497*(1), 1–12. https://doi.org/10.1002/cne.20954

Castillo-Azofeifa, D., Losacco, J. T., Salcedo, E., Golden, E. J., Finger, T. E., & Barlow, L. A. (2017). Sonic hedgehog from both nerves and epithelium is a key trophic factor for taste bud maintenance. *Development*, *144*(17), 3054–3065. https://doi.org/10.1242/dev.150342

Chaudhari, N., & Roper, S. D. (2010). The cell biology of taste. *The Journal of Cell Biology*, *190*(3), 285–296. https://doi.org/10.1083/jcb.201003144

Clapp, T. R., Yang, R., Stoick, C. L., Kinnamon, S. C., & Kinnamon, J. C. (2004). Morphologic characterization of rat taste receptor cells that express components of the phospholipase C signaling pathway. *The Journal of Comparative Neurology*, *468*(3), 311–321. https://doi.org/10.1002/cne.10963

Denk, W., & Horstmann, H. (2004). Serial block-face scanning electron microscopy to reconstruct three-dimensional tissue nanostructure. *PLoS Biology*, *2*(11), e329. https://doi.org/10.1371/journal.pbio.0020329

Dvoryanchikov, G., Sinclair, M. S., Perea-Martinez, I., Wang, T., & Chaudhari, N. (2009). Inward rectifier channel, ROMK, is localized to the apical tips of glial-like cells in mouse taste buds. *The Journal of Comparative Neurology*, *517*(1), 1–14. https://doi.org/10.1002/cne.22152

Engstrom, H., & Rytzner, C. (1956a). The fine structure of taste buds and taste fibres. *The Annals of Otology, Rhinology, and Laryngology*, *65*(2), 361–375.

Engstrom, H., & Rytzner, C. (1956b). The structure of taste buds. *Acta Oto-Laryngologica*, *46*, 361–367.

Farbman, A. I. (1965). Fine structure of the taste bud. *Journal of Ultrastructure Research*, *12*(328–350), 328–350.

Fiala, J. C. (2005). Reconstruct: A free editor for serial section microscopy. *Journal of Microscopy*, *218*(Pt 1), 52–61. doi:https://doi.org/10.1111/j.1365-2818.2005.01466.x

Finger, T. E., Danilova, V., Barrows, J., Bartel, D. L., Vigers, A. J., Stone, L., … Kinnamon, S. C. (2005). ATP signaling is crucial for communication from taste buds to gustatory nerves. *Science*, *310*(5753), 1495–1499. https://doi.org/10.1126/science.1118435

Gray, E., & Watkins, K. (1965). Electron microscopy of taste buds of the rat. *Zeitschrift für Zellforschung Und Mikroskopische Anatomie*, *66*, 583–595.

Holland, V. F., Zampighi, G. A., & Simon, S. A. (1991). Tight junctions in taste buds: possible role in perception of intravascular gustatory stimuli. *Chemical Senses*, *16*(1), 69–79. https://doi.org/10.1093/chemse/16.1.69

Iwatsuki, K., Ichikawa, R., Hiasa, M., Moriyama, Y., Torii, K., & Uneyama, H. (2009). Identification of the vesicular nucleotide transporter (VNUT) in taste cells. *Biochemical and Biophysical Research Communications*, *388*(1), 1–5. Placeholder Texthttps://doi.org/10.1016/j.bbrc.2009.07.069

Kinnamon, J. C., Sherman, T. A., & Roper, S. R. (1988). Ultrastructure of mouse vallate taste buds: III. Patterns of synaptic connectivity. *The Journal of Comparative Neurology*, *270*, 1–10.

Kinnamon, J. C., Taylor, B. J., Delay, R. J., & Roper, S. D. (1985). Ultrastructure of mouse vallate taste buds. I. Taste cells and their associated synapses. *The Journal of Comparative Neurology*, *235*(1), 48–60.

Kinnamon, J. C., & Yang, R. (2008). Ultrastructure of taste buds. In S. Firestein & G. K. Beauchamp (Eds.), *The senses: A comprehensive reference* (pp. 135–155). Oxford, UK: Academic Press.

Larson, E. D., Vandenbeuch, A., Voigt, A., Meyerhof, W., Kinnamon, S. C., & Finger, T. E. (2015). The role of 5-HT3 receptors in signaling from taste buds to nerves. *The Journal of Neuroscience*, *35*(48), 15984–15995. https://doi.org/10.1523/JNEUROSCI.1868-15.2015

Lawton, D. M., Furness, D. N., Lindemann, B., & Hackney, C. M. (2000). Localization of the glutamate-aspartate transporter, GLAST, in rat taste buds. *The European Journal of Neuroscience*, *12*(9), 3163–3171.

Lossow, K., Hermans-Borgmeyer, I., Behrens, M., & Meyerhof, W. (2017). Genetic labeling of Car4-expressing cells reveals subpopulations of Type III taste cells. *Chemical Senses*, *42*(9), 747–758. https://doi.org/10.1093/chemse/bjx048

Ma, H., Yang, R., Thomas, S. M., & Kinnamon, J. C. (2007). Qualitative and quantitative differences between taste buds of the rat and mouse. *BMC Neuroscience*, *8*, 5–13. https://doi.org/10.1186/1471-2202-8-5

Ma, Z., Taruno, A., Ohmoto, M., Jyotaki, M., Lim, J. C., Miyazaki, H., … Foskett, J. K. (2018). CALHM3 is essential for rapid ion channel-mediated purinergic neurotransmission of GPCR-mediated tastes. *Neuron*, *98*(3), 547–561 e510. https://doi.org/10.1016/j.neuron.2018.03.043

Mattern, C. F., & Paran, N. (1974). Evidence of a contractile mechanism in the taste bud of the mouse fungiform papilla. *Experimental Neurology*, *44*, 461–469.

Miura, H., Kato, H., Kusakabe, Y., Tagami, M., Miura-Ohnuma, J., Ninomiya, Y., & Hino, A. (2004). A strong nerve dependence of sonic hedgehog expression in basal cells in mouse taste bud and an autonomous transcriptional control of genes in differentiated taste cells. *Chemical Senses*, *29*(9), 823–831. https://doi.org/10.1093/chemse/bjh248

Miura, H., Scott, J. K., Harada, S., & Barlow, L. A. (2014). Sonic hedgehog-expressing basal cells are general post-mitotic precursors of functional taste receptor cells. *Developmental Dynamics*, *243*(10), 1286–1297. https://doi.org/10.1002/dvdy.24121

Nishijima, K., & Atoji, Y. (2004). Taste buds and nerve fibers in the rat larynx: An ultrastructural and immunohistochemical study. *Archives of Histology and Cytology*, *67*(3), 195–209.

Ohtubo, Y., & Yoshii, K. (2011). Quantitative analysis of taste bud cell numbers in fungiform and soft palate taste buds of mice. *Brain Research*, *1367*(0), 13–21. https://doi.org/10.1016/j.brainres.2010.10.060

Perea-Martinez, I., Nagai, T., & Chaudhari, N. (2013). Functional cell types in taste buds have distinct longevities. *PLoS One*, *8*(1), e53399. https://doi.org/10.1371/journal.pone.0053399

Pumplin, D. W., Yu, C., & Smith, D. V. (1997). Light and dark cells of rat vallate taste buds are morphologically distinct cell types. *The Journal of Comparative Neurology*, *378*, 389–410.

Richter, T. A., Caicedo, A., & Roper, S. D. (2003). Sour taste stimuli evoke Ca^{2+} and pH responses in mouse taste cells. *The Journal of Physiology*, *547*(Pt 2), 475–483.

Romanov, R. A., Lasher, R. S., High, B., Savidge, L. E., Lawson, A., Rogachevskaja, O. A., … Finger, T. E. (2018). Chemical synapses without synaptic vesicles: Purinergic neurotransmission through a CALHM1 channel-mitochondrial signaling complex. *Science Signaling*, *11*(529). https://doi.org/10.1126/scisignal.aao1815

Royer, S. M., & Kinnamon, J. C. (1988). Ultrastructure of mouse foliate taste buds: Synaptic and nonsynaptic interactions between taste cells and nerve fibers. *The Journal of Comparative Neurology*, *270*(1), 11–24 58–59.

Tabata, S., Wada, A., Kobayashi, T., Nishimura, S., Muguruma, M., & Iwamoto, H. (2003). Bovine circumvallate taste buds: Taste cell structure and immunoreactivity to alpha-gustducin. *The Anatomical Record. Part A, Discoveries in Molecular, Cellular, and Evolutionary Biology*, *271*(1), 217–224. https://doi.org/10.1002/ar.a.10028

Takeda, M., & Hoshino, T. (1975). Fine structure of taste buds in the rat. *Archivum histologicum Japonicum*, *37*, 395–413.

Taruno, A., Vingtdeux, V., Ohmoto, M., Ma, Z., Dvoryanchikov, G., Li, A., … Foskett, J. K. (2013). CALHM1 ion channel mediates purinergic neurotransmission of sweet, bitter and umami tastes. *Nature*, *495*(7440), 223–226. https://doi.org/10.1038/nature11906

Ueda, K., Fujii, M., El-Sharaby, A., Honma, S., & Wakisaka, S. (2003). Human blood group antigen H is not the specific marker for type I cells in the taste buds. *Archives of Histology and Cytology*, *66*(5), 469–473.

Vandenbeuch, A., Anderson, C. B., Ford, A. P., Smith, S., Finger, T. E., & Kinnamon, S. C. (2013). A selective P2X3, P2X2/3 receptor antagonist abolishes responses to all taste stimuli in mice. *Chemical Senses*, *38*(Supp), 86. https://doi.org/10.1093/chemse/bjt036

Vandenbeuch, A., Clapp, T. R., & Kinnamon, S. C. (2008). Amiloride-sensitive channels in type I fungiform taste cells in mouse. *BMC Neuroscience*, *9*(1). https://doi.org/10.1186/1471-2202-9-1

Vandenbeuch, A., Larson, E. D., Anderson, C. B., Smith, S. A., Ford, A. P., Finger, T. E., & Kinnamon, S. C. (2015). Postsynaptic P2X3-containing receptors in gustatory nerve fibres mediate responses to all taste qualities in mice. *The Journal of Physiology*, *593*(5), 1113–1125. https://doi.org/10.1113/jphysiol.2014.281014

Wilson, C. E., Finger, T. E., & Kinnamon, S. C. (2017). Type III cells in anterior taste fields are more immunohistochemically diverse than those of posterior taste fields in mice. *Chemical Senses*, *42*(9), 759–767. https://doi.org/10.1093/chemse/bjx055

Yang, D. H., McKee, K. K., Chen, Z. L., Mernaugh, G., Strickland, S., Zent, R., & Yurchenco, P. D. (2011). Renal collecting system growth and function depend upon embryonic gamma1 laminin expression. *Development*, *138*(20), 4535–4544. https://doi.org/10.1242/dev.071266

Yang, R., Tabata, S., Crowley, H. H., Margolskee, R. F., & Kinnamon, J. C. (2000). Ultrastructural localization of gustducin immunoreactivity in microvilli of type II taste cells in the rat. *The Journal of Comparative Neurology*, *425*(1), 139–151. https://doi.org/10.1002/1096-9861(20000911)425:1<139::AID-CNE12>3.0.CO;2-#

Yee, C. L., Yang, R., Bottger, B., Finger, T. E., & Kinnamon, J. C. (2001). "Type III" cells of rat taste buds: Immunohistochemical and ultrastructural studies of neuron-specific enolase, protein gene product

9.5, and serotonin. *The Journal of Comparative Neurology*, *440*(1), 97–108.

Yoon, B. E., & Lee, C. J. (2014). GABA as a rising gliotransmitter. *Front Neural Circuits*, *8*, 141. https://doi.org/10.3389/fncir.2014.00141

SUPPORTING INFORMATION

Additional supporting information may be found online in the Supporting Information section at the end of this article.

Received: 19 August 2020 | Revised: 22 March 2021 | Accepted: 5 April 2021

DOI: 10.1002/cne.25156

RESEARCH ARTICLE

JCN RESEARCH IN SYSTEMS NEUROSCIENCE THE JOURNAL OF COMPARATIVE NEUROLOGY WILEY

Synaptic inputs to broad thorny ganglion cells in macaque retina

Andrea S. Bordt[1,2] | Sara S. Patterson[3] | Rebecca J. Girresch[4] | Diego Perez[1] | Luke Tseng[1] | James R. Anderson[5] | Marcus A. Mazzaferri[2] | James A. Kuchenbecker[2] | Rodrigo Gonzales-Rojas[6] | Ashley Roland[6] | Charis Tang[6] | Christian Puller[2,7] | Alice Z. Chuang[8] | Judith Mosinger Ogilvie[4] | Jay Neitz[2] | David W. Marshak[1]

[1]Department of Neurobiology and Anatomy, McGovern Medical School, Houston, Texas, USA

[2]Department of Ophthalmology, University of Washington, Seattle, Washington, USA

[3]Center for Visual Science, University of Rochester, Rochester, New York, USA

[4]Department of Biology, Saint Louis University, Saint Louis, Missouri, USA

[5]John A. Moran Eye Center, University of Utah, Salt Lake City, Utah, USA

[6]Department of BioSciences, Rice University, Houston, Texas, USA

[7]Department of Neuroscience, Carl von Ossietzky University, Oldenburg, Germany

[8]Department of Ophthalmology and Visual Science, McGovern Medical School, Houston, Texas, USA

Correspondence
Andrea S. Bordt, Department of Neurobiology and Anatomy, McGovern Medical School, Houston, Texas USA.
Email: andrea.s.bordt@uth.tmc.edu

Funding information
Deutsche Forschungsgemeinschaft, Grant/Award Number: PU 469/2-1; National Institutes of Health, Grant/Award Numbers: EY002576, EY007031, EY007125, EY027859, EY028927, NS099578, P30-EY001730, P30-EY014800, P51-OD010425/ORID; Research to Prevent Blindness, Grant/Award Number: N/A

Abstract

In primates, broad thorny retinal ganglion cells are highly sensitive to small, moving stimuli. They have tortuous, fine dendrites with many short, spine-like branches that occupy three contiguous strata in the middle of the inner plexiform layer. The neural circuits that generate their responses to moving stimuli are not well-understood, and that was the goal of this study. A connectome from central macaque retina was generated by serial block-face scanning electron microscopy, a broad thorny cell was reconstructed, and its synaptic inputs were analyzed. It received fewer than 2% of its inputs from both ON and OFF types of bipolar cells; the vast majority of its inputs were from amacrine cells. The presynaptic amacrine cells were reconstructed, and seven types were identified based on their characteristic morphology. Two types of narrow-field cells, knotty bistratified Type 1 and wavy multistratified Type 2, were identified. Two types of medium-field amacrine cells, ON starburst and spiny, were also presynaptic to the broad thorny cell. Three types of wide-field amacrine cells, wiry Type 2, stellate wavy, and semilunar Type 2, also made synapses onto the broad thorny cell. Physiological experiments using a macaque retinal preparation in vitro confirmed that broad thorny cells received robust excitatory input from both the ON and the OFF pathways. Given the paucity of bipolar cell inputs, it is likely that amacrine cells provided much of the excitatory input, in addition to inhibitory input.

KEYWORDS
connectomics, electron microscopy, interneuron, motion sensitivity, primate, RRID: SCR_001622, RRID:SCR_003584, RRID:SCR_005986, RRID: SCR_017350, vision

1 | INTRODUCTION

Movements of the body, head, and eyes generate moving stimuli on the retina, as do moving objects. Encoding this signal in the retina is the first step in visually guided reflexes, perception, and behavior (Wei, 2018). The neural circuits that generate motion sensitivity in ganglion cells, the projection neurons of the retina, have been studied extensively in mice and rabbits, and it is clear that input from amacrine cells, local circuit neurons of the inner retina that are generally inhibitory, plays a major role (Chen & Wei, 2018). The contributions of

amacrine cells to neural circuits that generate motion sensitivity in primate retinal ganglion cells are not as well-characterized, however. The focus of this work was on one type of motion-sensitive ganglion cell in macaque retina, the broad thorny cell. Broad thorny cells project to koniocellular Layer 3, located between the magnocellular and parvocellular layers, of the lateral geniculate nucleus (LGN) in marmosets (Percival et al., 2013) and to the LGN in macaques (Dacey et al., 2003). They also project to the superior colliculus in macaques and marmosets (Kwan et al., 2019; Peterson & Dacey, 2000; Rodieck & Watanabe, 1993). Broad thorny cells respond to small, moving stimuli, firing vigorously when a small spot enters or leaves the receptive field center, but they are insensitive to movements in the background. These characteristics make them particularly well-suited to guide "catch-up" saccades during smooth pursuit eye movements (Puller et al., 2015).

There have been two previous studies of the synaptic inputs to broad thorny ganglion cells from bipolar cells, excitatory local circuit neurons that convey signals from the photoreceptors to the inner retina. Serial ultrathin sections of central macaque retina were analyzed by transmission electron microscopy (TEM), and neurons that may be broad thorny cells and their presynaptic bipolar cells were reconstructed from serial, vertical sections. The bipolar cells were diffuse, receiving input from several cones, and they were identified as types DB2 and DB3 (Calkins & Sterling, 2007). These both have OFF responses to light, depolarizing to decrements in light intensity (Puthussery et al., 2013, 2014), and together, they provided 30% of the synaptic input to the putative broad thorny cells. Retrogradely labeled broad thorny ganglion cells in marmoset retinas were studied using light microscopic immunolabeling with markers of synaptic transmission. Using this technique, broad thorny cells had essentially the same spatial density of synaptic inputs from bipolar cells as two other, more common retinal ganglion cell types, midget cells and parasol cells (Percival et al., 2011). One of the presynaptic cell types was identified as DB3a (Masri et al., 2016).

The amacrine cells presynaptic to broad thorny cells have not been identified, but this is essential because amacrine cells contribute to motion sensitivity, surround inhibition, and adaptation to contrast (Appleby & Manookin, 2019; Puller et al., 2015). Based on light microscopic immunolabeling in marmoset retina, two amacrine cells with medium-sized dendritic fields, spiny cells, and starburst cells have been proposed as candidates (Weltzien et al., 2014; Masri et al., 2019). Here, two presynaptic narrow-field amacrine cells, knotty bistratified Type 1 and wavy multistratified Type 2, were identified. In addition, inputs from wiry Type 2, semilunar Type 2, stellate wavy, and other wide-field amacrine cells were identified. However, the broad thorny cell received a much smaller proportion of input from bipolar cells than expected. Less than 2% of its input was from bipolar cells, mainly the ON type that respond to increments in light intensity.

Broad thorny ganglion cells receive robust excitatory and inhibitory synaptic inputs both at light increments and decrements (Puller et al., 2015), but the neural circuits that generate these responses are not well-understood. Electrophysiological experiments were designed to determine how the ON and OFF pathways contribute to the responses. When the ON pathway was blocked with pharmacological agents, both inhibitory and excitatory inputs at light onset were eliminated while robust responses were still elicited at light offset. The electrophysiological experiments rule out synaptic effects like disinhibition as the sole source of the responses to decrements in light intensity.

2 | METHODS

2.1 | Electron microscopy

Retinal tissue was obtained from a terminally anesthetized, adult male macaque (*Macaca nemestrina*) through the Tissue Distribution Program at the Washington National Primate Center. All procedures were approved by the Institutional Animal Care and Use Committee at the University of Washington. Central retinal tissue was processed for serial block-face scanning electron microscopy (SBFSEM) as previously described (Patterson et al., 2019). Briefly, a 1×1 mm square was fixed in glutaraldehyde, stained en bloc with osmium ferrocyanide, uranyl acetate and lead aspartate, and then embedded in epoxy resin. The selected area, $\sim$2 mm temporal to the center of the fovea, was particularly well-suited for connectomic analysis because the neurons were small, but even relatively rare cell types were represented. The images were acquired using a Zeiss Sigma VP field emission scanning electron microscope equipped with a 3View system (Gatan, Inc.).

2.2 | Connectomic analysis

A macaque retinal volume, sectioned in the horizontal plane and acquired at a resolution of 7.5 nm/pixel, was studied. It contained 937 70 nm sections, spanning from the ganglion cell layer (GCL) to the inner nuclear layer (INL). This connectome was also used in a recent study of ON parasol ganglion cells (Patterson, Bordt, et al., 2020). Image registration was performed using Nornir (http://nornir.github.io RRID:SCR_003584), and the image tiles were reassembled into cohesive digital volumes and hosted on a 24-core server at the University of Washington.

The serial EM volume was annotated using the web-based, multiuser Viking software described previously (Anderson et al., 2011; http://connectomes.utah.edu RRID:SCR_005986.) Briefly, profiles of processes were annotated by placing circular discs with the same diameter at their centers of mass and linking them to annotations on adjacent sections. Synaptic densities were annotated with lines and linked to the neurons in which they were located. Neurons and other structures, such as synaptic densities, were numbered consecutively. The boundary between the INL and the inner plexiform layer (IPL) was designated as 0% and the IPL-GCL boundary as 100% depth.

The major cell types were identified using ultrastructural criteria (Dowling & Boycott, 1966; Tsukamoto & Omi, 2015, 2016). Axon

terminals of bipolar cells contained numerous synaptic vesicles and synaptic ribbons. Because the contrast of the synaptic ribbons in this connectome is not as high as in images from TEM, we confirmed the identity of the presynaptic bipolar cells by reconstructing the axon terminal and, wherever possible, the soma and primary dendrite. Axons and dendrites of amacrine cells contained fewer synaptic vesicles, and they were typically clustered at synapses. One broad thorny ganglion cell and the local circuit neurons providing its input were annotated. Whenever possible, the presynaptic neurons were identified by their morphology.

2.3 | Anatomical data analysis

Data analysis and 3D rendering were performed using an open-source Matlab (Mathworks, RRID: SCR_001622) program https://github.com/neitzlab/sbfsem-tools RRID: SCR_017350. The image rendering was performed using the RenderApp function (Bordt et al., 2019). Using the synapseSphere function, synapses were rendered as unit spheres centered at each synapse annotation's X, Y, and Z coordinates then scaled to optimize visibility. Processes of amacrine cells, axons of broad thorny cells, and axon terminals of bipolar cells were analyzed using the DendriteDiameter and IPLDepth functions (Patterson, Bordt, et al., 2020). The diameters of individual amacrine cell dendrites were computed with the single Dendrite Diameter function in SBFSEM-tools, described here for the first time. The annotations associated with a neuron and the links between the annotations were represented as the nodes and edges of a graph. The annotations of an individual branch were obtained by calculating the shortest path along the graph between two user-specified annotations at either end of the branch. Statistics were then calculated from the diameters of all annotations associated with the branch. Four representative distal dendrites from identified wide-field amacrine cells were analyzed.

2.4 | Statistical analysis

The processes of a subset of wide field amacrine cells presynaptic the broad thorny cell were assigned to groups using the clustering algorithm k-means (Maechler et al., 2013). The cytoplasmic electron density, light or intermediate, was converted to a numeric value, 1 or 2, respectively. Four features, IPL depth, process diameter (mean and standard deviation), and cytoplasmic electron density, were standardized for comparability. First, the number of clusters was determined by a plot of the within groups sum of squares by number of clusters extracted, and the optimal number of clusters was identified by a plateau in the plot. An analysis of variance (ANOVA) based on a one-way ANOVA with Dunnett multiple comparison or a two-sample *t*-test was used to compare each feature among groups. A p-value <.05 was considered statistically significant. Statistical calculations were performed using the Cluster package in R version 3.6.0 (R Project for Statistical Computing, RRID:SCR_001905).

2.5 | Electrophysiology

Eyes were dissected from terminally anesthetized adult female macaques (*M. nemestrina*), obtained through the Tissue Distribution Program of the National Primate Research Center at the University of Washington. All procedures were approved by the University of - Washington Institutional Animal Care and Use Committee. Small pieces (2–4 mm on a side) of peripheral retina (>5 mm away from the fovea) were dissected away from the supporting layers under infrared light in warm (∼32°C) carboxygenated Ames' medium (Sigma-Aldrich). Retinal pieces were mounted photoreceptor-side down onto a polylysine-coated glass slip and transferred to the recording chamber, where the tissue was continuously superfused with warm Ames medium.

Broad thorny ganglion cells were identified based on their characteristic soma shape and ON–OFF light response pattern (Puller et al., 2015). Light-evoked spikes were recorded in cell-attached mode with glass pipettes filled with Ames medium. Light-evoked excitatory or inhibitory ganglion cell synaptic input was characterized at holding potentials of −60 or 10–30 mV, respectively, using whole-cell voltage-clamp recordings. The pipettes were filled with a solution containing (in mM) 105 $CsCH_3SO_3$, 10 TEA-Cl, 20 HEPES, 10 EGTA, 2 QX-314, 5 Mg-ATP, and .5 Tris-GTP (pH ∼ 7.3 with CsOH, ∼280 mOsm). Series resistance for voltage-clamp recordings was compensated by 50% at the time of recording and the remaining 50% offline. The membrane potential was corrected offline for the ∼10 mV liquid junction potential between the recording solution and the extracellular medium. The pipette solution also contained .1% Lucifer yellow CH (Sigma-Aldrich) to reveal cellular morphology, confirming the cell type.

Light responses were recorded in control conditions and while signal transmission from cones to ON bipolar cells was blocked via superfusion of the tissue with a mixture of the mGluR antagonist LY341495 (7.5 μM) and agonist L-AP4 (5 μM) in Ames (Ala-Laurila et al., 2011).

Stimuli from an oLED monitor (eMagin Corporation) were focused on the photoreceptors through a condenser lens. The monitor illuminated a circular area (∼1 mm in diameter) centered on the recorded cell's soma (vertical refresh, 60 Hz). All recordings were performed at a background in the photopic regime (quantal catch in R*/cone/sec: L/M-cone, $\sim 13 \times 10^3$). Signals were sampled at 10 kHz with an ITC-18 analog-digital board (HEKA Instruments), amplified with a Multiclamp 700B amplifier (Molecular Devices), and Bessel filtered at 3 kHz. Data analyses were performed in MATLAB (MathWorks, RRID: SCR_001622).

The stimulus was either a black spot centered on the soma (diameter, 288 μm) and presented for 1 s, or a 2 Hz square-wave modulated spot (diameter, 315 μm, 100% Michelson contrast), all presented at a photopic background (see Puller et al., 2015 for details). Measurements of the OFF-response kinetics before and after drug application were taken by analyzing synaptic currents averaged across five cycles of the square-wave stimulus.

2.6 | Figures

Figures were prepared using Adobe Photoshop CS6 and SBFSEM-tools. Whenever possible, the color palette was selected so that the figures could be interpreted by individuals with all of the common forms of color blindness http://mkweb.bcgsc.ca/colorblind/. The code and data used to generate the figures in this study will be made available upon request.

3 | RESULTS

The morphology and stratification pattern indicated that cell 103 in the temporal connectome was the broad thorny type (Dacey et al., 2003; Puller et al., 2015; Yamada et al., 2005). The dendritic arbor was asymmetric, and the dendrites were tortuous, branched frequently, and had numerous spine-like terminals. The dendrites terminated in a broad band extending from 30% to 80% of the IPL depth, with a peak at 60% (Figure 1). The axon was ~.2 μm in diameter (median = .209 μm) with varicosities .5 to .6 μm in diameter.

Broad thorny ganglion cell 103 received 1094 synapses, and bipolar cells provided only 1.4% (15/1094) of the inputs (Figure 2). The remaining 98.6% of the synapses (1079/1094) were from amacrine cells (Tables S1 and S2). Most of these synapses, 82% (887/1079), came from narrow-field or medium-field amacrine cells. A motif seen frequently was two or three of these amacrine cell processes converging onto a relatively thin ganglion cell dendrite (Figure 3). Axons and dendrites of wide-field amacrine cells, whose processes were unbranched, straight and 100 μm or longer, also provided a considerable amount of input to the broad thorny ganglion cell. They provided 18% (192/1079) of its amacrine cell input, and some of them were also presynaptic to the ON parasol cells studied previously (Patterson, Bordt, et al., 2020). The distribution of synapses onto broad thorny cell 103 is illustrated in Figure 4.

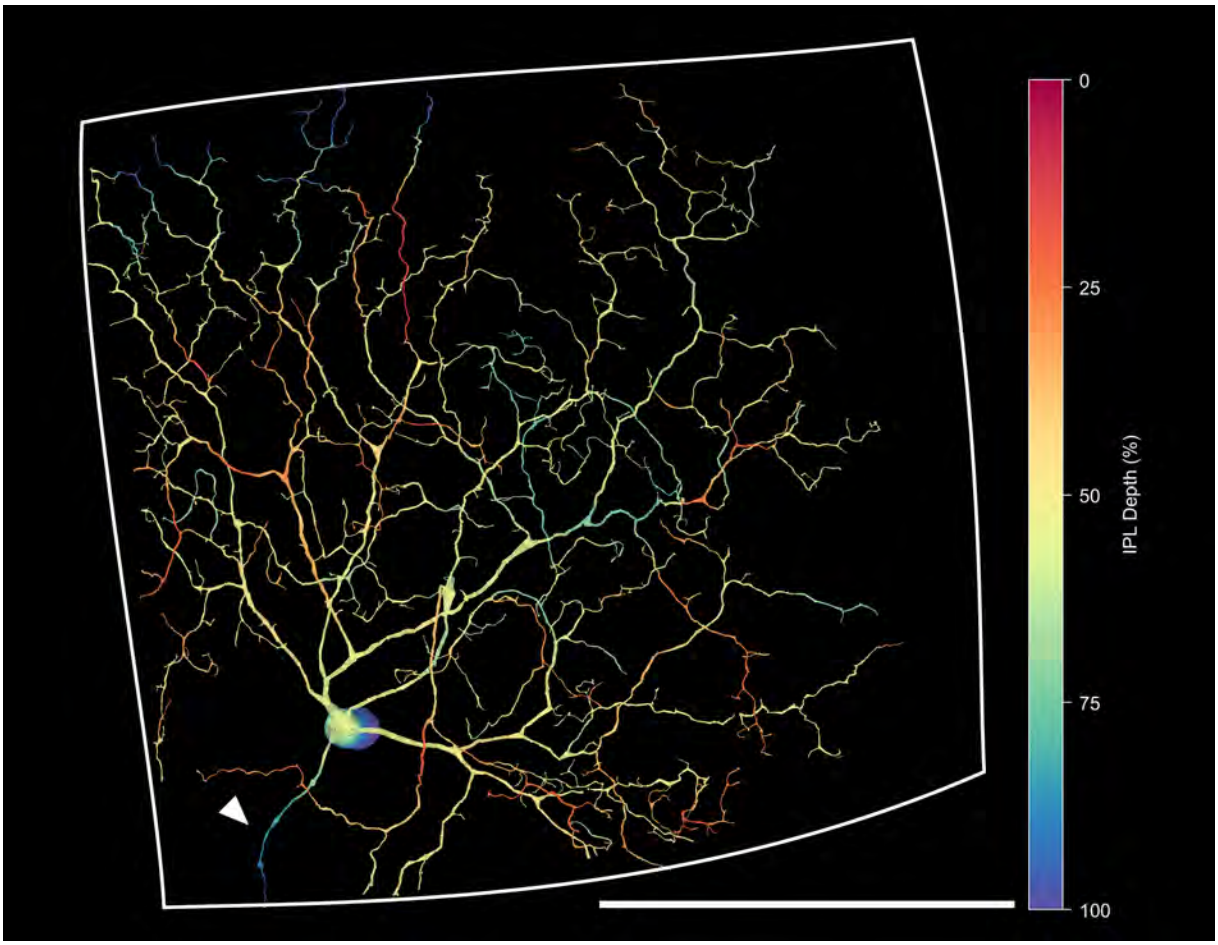

FIGURE 1 Broad thorny ganglion cell 103 and the approximate boundaries of the connectome (white) are shown as they would appear in a flat mount preparation viewed from the scleral side of the retina. The cell is colored according to depth in the inner plexiform layer (IPL), with red as the inner nuclear layer and violet as the ganglion cell layer; the dendrites stratify broadly in the three middle strata. Some dendrites on the left were truncated when they reached the edge of the connectome. Note the varicose axon at the lower left (arrowhead). Scale bar = 100 μm [Color figure can be viewed at wileyonlinelibrary.com]

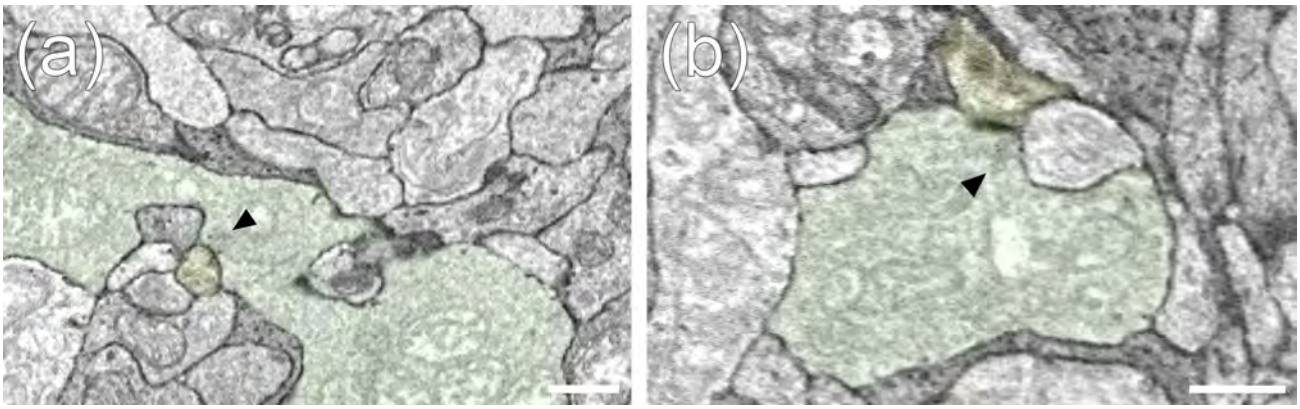

FIGURE 2 Two bipolar cell axon terminals (green) make ribbon synapses (arrowheads) onto dendrites of broad thorny ganglion cell 103 (yellow). The synapses are shown at low (a) and somewhat higher (b) magnification. In this and in all subsequent figures, the markers are located in the presynaptic cells. Synapses like these provided less than 2% of the input to this ganglion cell. Scale bars = 500 nm [Color figure can be viewed at wileyonlinelibrary.com]

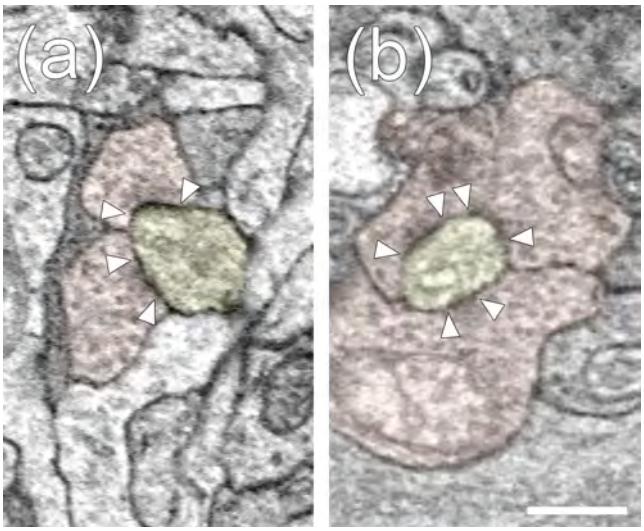

FIGURE 3 It was common to observe two (a) or three (b) amacrine cell dendrites (orange) converging onto spines of ganglion cell 103 (yellow) and making synapses (arrowheads). Scale bar = 500 nm [Color figure can be viewed at wileyonlinelibrary.com]

3.1 | Presynaptic bipolar cells

Fourteen bipolar cells made one synapse each, and one bipolar cell made two synapses onto broad thorny ganglion cell 103 (Figure 4). Based on the depth of their axon terminals in the IPL, 12 of these were expected to have ON responses to light and three were expected to have OFF responses (Figures 5 and 6). The ON cells terminated at 60% (30586, 39248, 41007, 41946, 41953, 43602, 43616), 70% (40761), 80% (42569), or 90% (40029, 42040) of the depth in the IPL. The presynaptic OFF bipolar cells terminated at IPL depths of 40% (41145, 42721), 30% (43119), and 20% (43128).

3.2 | Presynaptic amacrine cells

Two types of narrow-field amacrine cells presynaptic to broad thorny cell 103 were identified morphologically. Cells 43016, 38098, 42714 and 43233 had somas in the INL and small dendritic fields, ~35 μm in diameter (Figure 7). They had varicose dendrites ramifying broadly in the center of the IPL, with peaks in density at 20–30% and 40–60% of the IPL depth. These resembled the knotty bistratified Type 1 cells of macaque retina (Mariani, 1990) and the A4 cells of human retina (Kolb et al., 1992). They also resembled the cells that contain immunoreactive vesicular glutamate transporter 3 (vGluT3) in baboon retina (Marshak et al., 2015). Each of these three knotty bistratified Type 1 cells made one synapse onto broad thorny cell 103.

Three presynaptic amacrine cells were identified morphologically as wavy multistratified Type 2 (Mariani, 1990). Amacrine cell 42338 made three synapses onto broad thorny cell 103, including one onto a spine where two other amacrine cells also made synapses. Its soma was located in the INL, and its dendritic arbor was larger than those of the knotty bistratified cells. The exact dimensions were uncertain because the soma was located near the edge of the connectome, and several of its dendrites were truncated. Its dendrites were relatively tortuous and ramified broadly around the center of the IPL, with a peak at 50% depth. The morphology of cell 43446 was very similar, and its dendritic arbor was also truncated; it made three synapses onto broad thorny cell 103. Cell 40879 made five synapses onto broad thorny ganglion cell 103, including two onto spines alongside -other synapses. It was morphologically very similar to the other two wavy multistratified cells and had a more completely annotated dendritic arbor, whose diameter was ~60 μm (Figure 8).

Two types of medium-field amacrine cells presynaptic to the broad thorny ganglion cells were identified (Grünert & Martin, 2020). Cell 40654 was identified as the spiny amacrine cell type (Kolb et al., 1992; Mariani, 1990). It had a dendritic field ~150 μm in diameter, and its soma was located in the GCL. Its dendrites were tortuous,

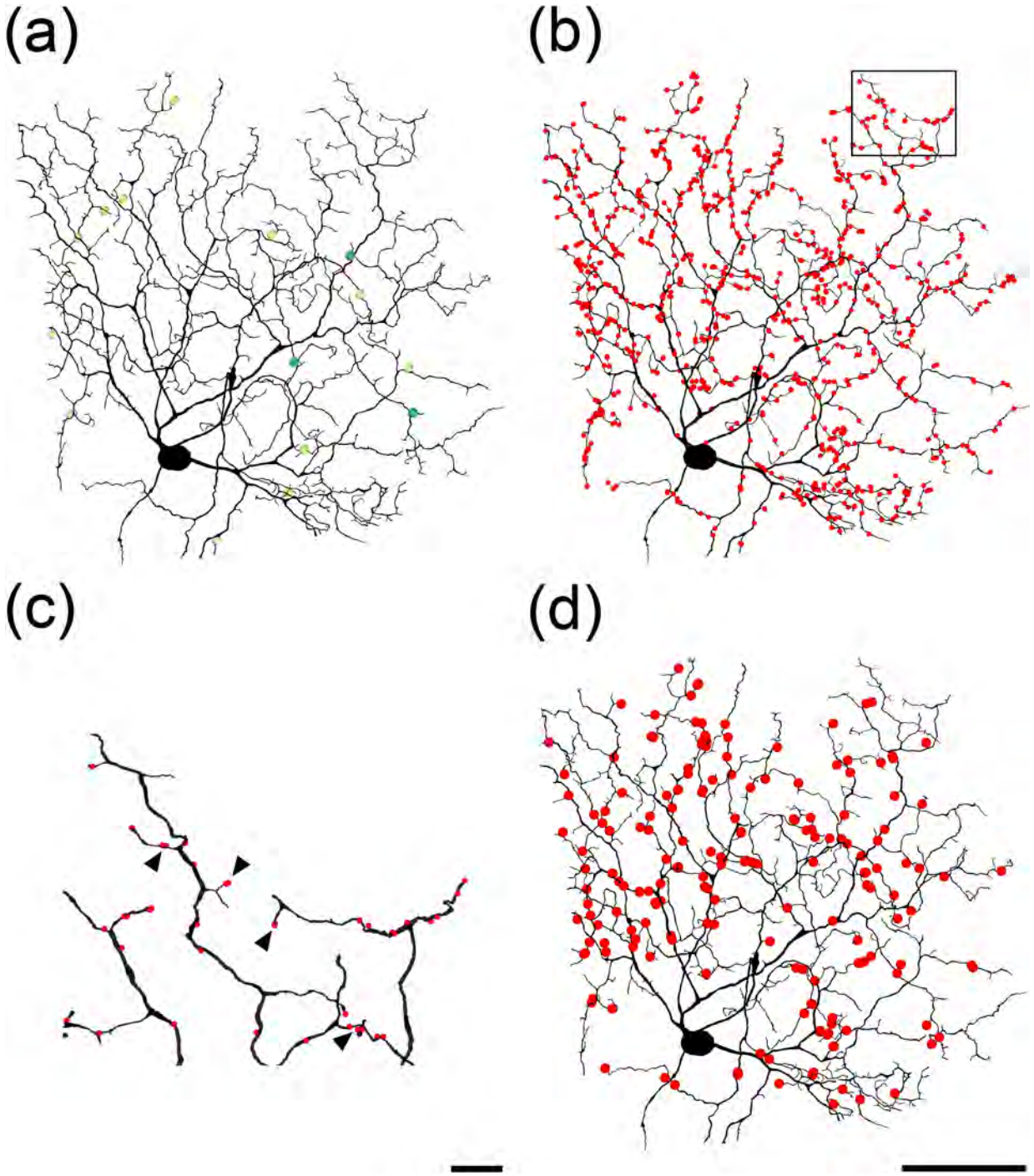

FIGURE 4 (a) Distribution of synapses from bipolar cell axons (green) onto broad thorny ganglion cell 103. Inputs from ON bipolar cells (light green) are more numerous than those from OFF bipolar cells (dark green). Note that only 15 of more than 1000 synapses originated from bipolar cells and that the distribution appeared to be random. (b) Inputs from amacrine cell axons and dendrites (red) were far more common. The box indicates the area shown at higher magnification in panel (c) Note that there are four clusters of synapses (arrowheads) onto cell 103. Inputs from wide-field amacrine cells are shown in panel (d). These also appear to be randomly distributed. Panels a, b, and d scale bars = 50 μm; panel c scale bar = 5 μm [Color figure can be viewed at wileyonlinelibrary.com]

branched frequently, and had small spines (Figure 9). The dendrites ramified broadly in the center of the IPL, with a peak density at 50% of the IPL depth. Cell 40654 made five synapses onto broad thorny cell 103.

Amacrine cell 3111 was classified as a medium-field amacrine cell based on previous descriptions of starburst cells in primate retinas (Kolb et al., 1992; Mariani, 1990; Rodieck, 1989). It had a small soma in the GCL, and its proximal dendrites were very thin, tortuous and

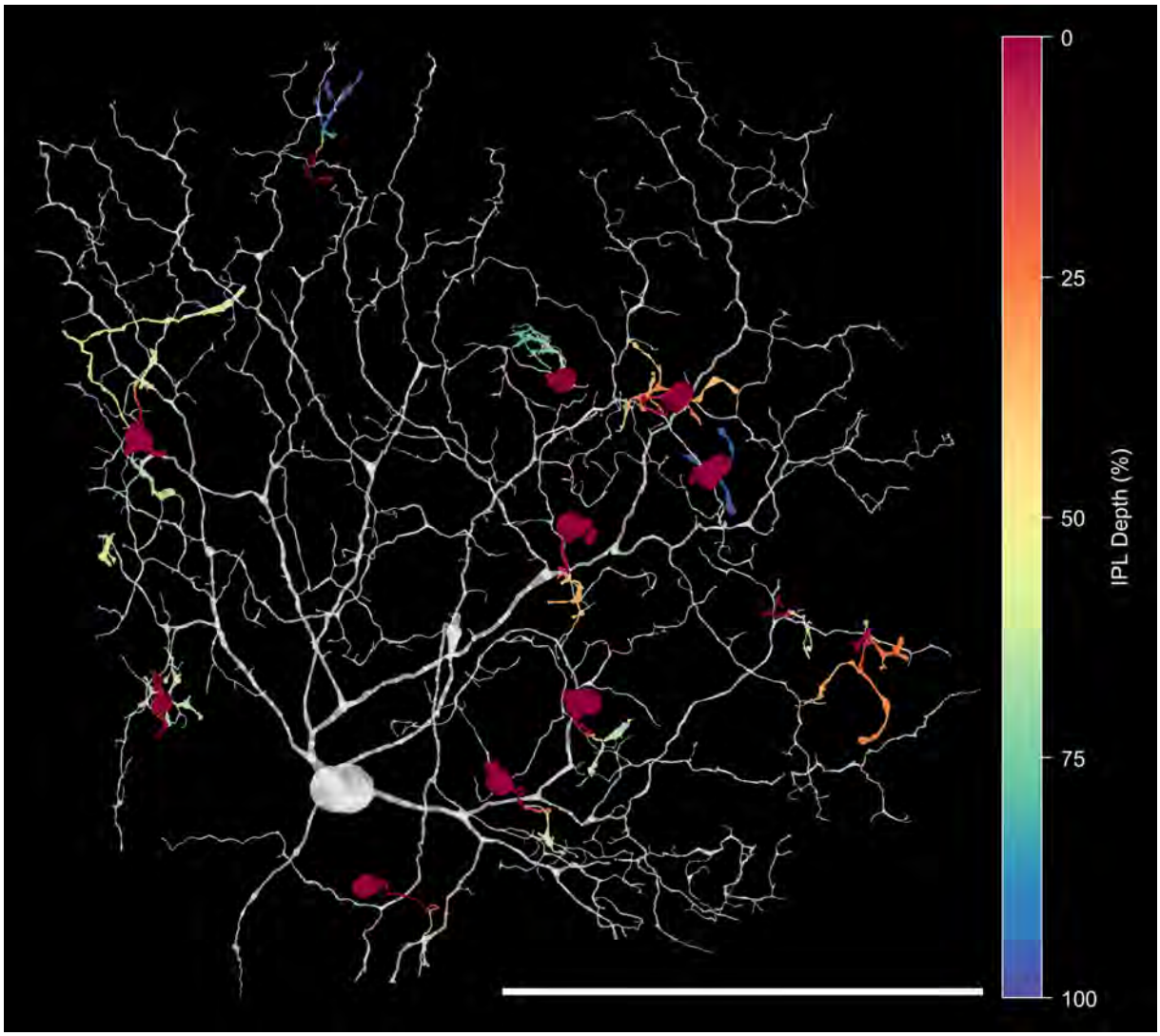

FIGURE 5 Bipolar cell inputs to broad thorny ganglion cell 103 as they would appear in a flat mount preparation. Thirteen bipolar cells made one synapse each, and one, a giant bipolar cell, made two synapses. The depth code in this and subsequent figures is the same as in Figure 1. Scale bar = 100 μm [Color figure can be viewed at wileyonlinelibrary.com]

relatively electron dense. The distal dendrites were enlarged, and the majority were found at a depth of 70% in the IPL. It made one synapse onto cell 103 (Figure 10).

Three types of wide-field amacrine cells presynaptic to broad thorny cell 103 were identified. The first type identified were wiry Type 2, a common type of wide-field amacrine cell in primate retina (Kolb et al., 1992; Mariani, 1990). Two of them (4651 and 182) also made synapses onto ON parasol cells (Patterson, Bordt, et al., 2020), and one (41444) is described here for the first time. Wiry Type 2 amacrine cells had ovoid somas that were located in the GCL. They had one or two short primary dendrites, relatively short secondary dendrites and tertiary dendrites each that bifurcated, giving rise to long, relatively straight distal dendrites that did not branch again. Their distal dendrites had a small diameter (mean = .352 μm, *SD* = .11 μm) and ramified in a narrow stratum of the IPL at 60% depth. Together, the three identified wiry amacrine Type 2 cells made 11 synapses onto broad thorny cell 103 (Figure 11).

Two other types of wide-field amacrine cells presynaptic to broad thorny cell 103 were identified. Cell 4781, which made two synapses onto cell 103, was a semilunar Type 2 cell that also made synapses onto ON parasol cells (Patterson, Bordt, et al., 2020). It had a relatively large soma and an extensive dendritic arbor centered at 59% IPL depth. Its dendrites had a larger diameter (mean = .66 μm, *SD* = .19 μm) and branched at larger angles than those of wiry cells. Thinner axons originated from some of the dendrites and the soma (Figure 12).

The third type of identified presynaptic wide-field amacrine cell, 4308, was similar in some respects to semilunar Type 2 cell 4781, but the dendrites had a smaller diameter (mean = .61 μm, *SD* = .12 μm), and the cytoplasm was more electron lucent. One slender, varicose process originating from a secondary dendrite appeared to be an

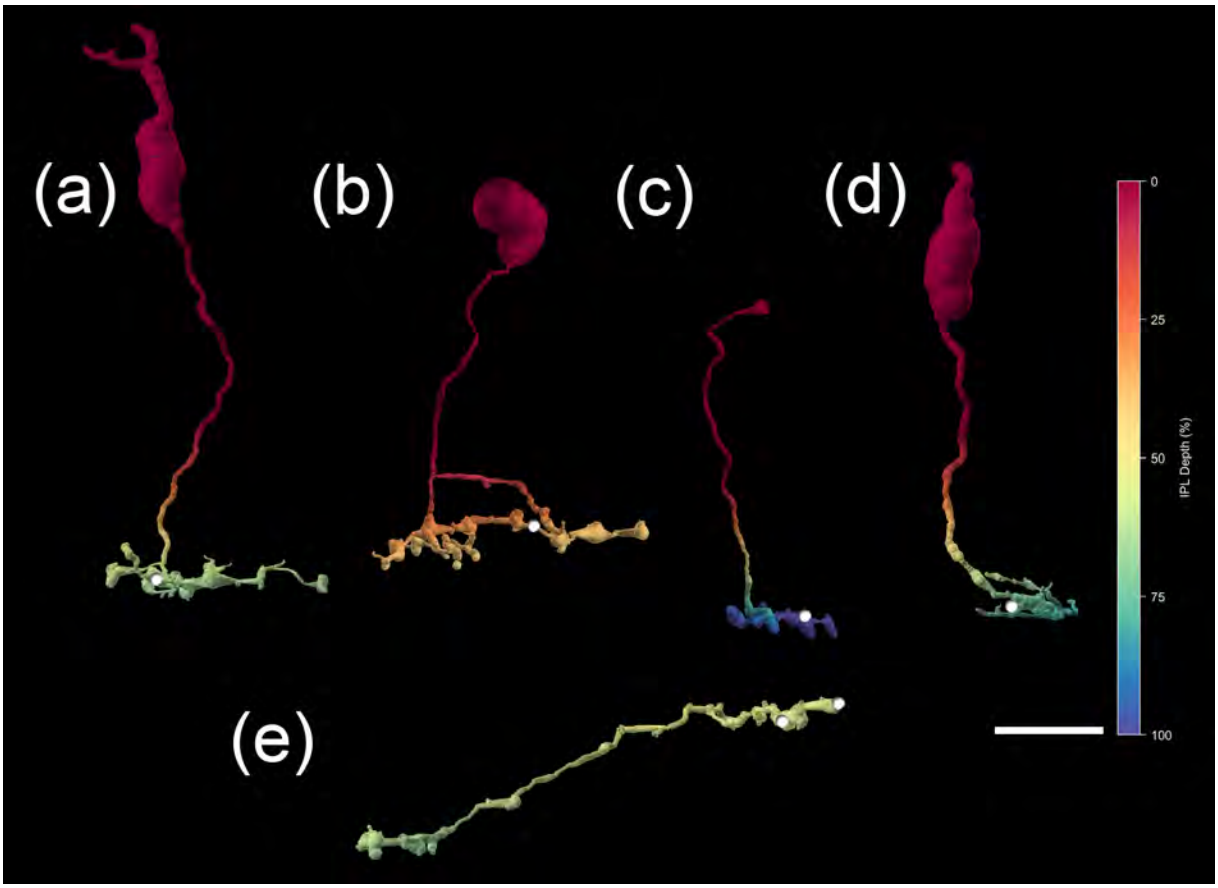

FIGURE 6 Representative presynaptic bipolar cells as they would appear in vertical sections. Synapses onto cell 103 are indicated with white circles. (a) Diffuse bipolar cell 40761 ramifying at 60–70% depth. (b) Diffuse bipolar cell 41145 ramifying at 35–45%. (c) Diffuse bipolar cell 42040 ramifying at 90–100% depth, (d). Diffuse bipolar cell 42569 ramifying at 70–80%, (e) giant bipolar cell 30586 axon terminal ramifying at 50–60% depth. Scale bar = 10 μm [Color figure can be viewed at wileyonlinelibrary.com]

axon, and similar processes emerged from the tips of two distal dendrites. The sparse dendritic arbor was centered at 26% depth in the IPL. Cell 4308 made three synapses onto broad thorny cell 103 (Figure 13). Of the morphological types described previously in macaque and human retina, this amacrine cell most closely resembled the stellate wavy cell (Kolb et al., 1992; Mariani, 1990).

Most types of wide-field cells presynaptic to broad thorny cell 103 could not be followed to their somas, however. The processes of a subset of wide-field amacrine cells without somas in the volume (n = 98) were analyzed using the IPLDepth and DendriteDiameter functions in SBFSEM-tools. They were also classified as light or intermediate in cytoplasmic electron density. Based on these parameters, dendrites were grouped using a cluster analysis. A plot of the within groups sum of squares by number of groups was used to determine the appropriate number of clusters (not illustrated), and six groups were identified.

Three groups of processes with light cytoplasmic electron density were identified. The first light group (1) had a mean diameter of .52 μm (n = 11, SD = .087 μm) and ramified at 50% depth in the IPL, on average. The second light group (2) had a smaller diameter (n = 15, mean = .425 μm, SD = .028 μm), and they ramified at 60.5% depth in the IPL. The differences between the two groups were significant at the .05% level for both stratification depth and diameter. The dendrites in the third light group (6) were the most common and had a slightly larger diameter than those in the second (n = 28, mean = .48 μm, SD = .068 μm) and ramified at 29% of the IPL depth.

There were also three groups of processes with darker cytoplasmic electron density. The first group (3) had a mean diameter of .46 μm (n = 14, SD = .061) and ramified at 28% IPL depth. Another group of processes with intermediate cytoplasmic electron density (4) was clearly different, having a larger average diameter (n = 8, mean = .56 μm, SD = .086 μm) and ramifying at 44% depth in the IPL, on average. The third group (5) was the most common and had the smallest diameter (n = 22, mean = .45 μm, SD = .073 μm), and they ramified at a depth of 62%, on average. The wide-field amacrine cell processes in Group 5 were morphologically similar to the dendrites of the identified wiry Type 2 cells. Because wiry Type 2 somas have a high spatial density and their long dendrites form a very dense plexus (Majumdar et al., 2008), they were likely to be the source.

Although the synaptic inputs and outputs of the amacrine cells presynaptic to broad thorny cell 103 were not analyzed completely, it was apparent that they also made synaptic contacts with one another

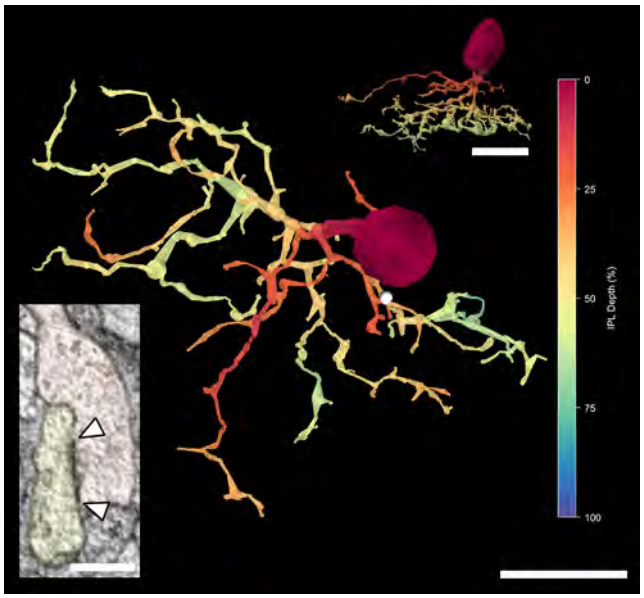

FIGURE 7 Knotty bistratified Type 1 amacrine cell 43016 was one type of narrow-field amacrine cell presynaptic to broad thorny ganglion cell 103 (white circle). It is shown as it would appear in flat mount and in a vertical section. Note that the soma is in the inner nuclear layer and that the dendrites ramify in two distinct strata near the center of the inner plexiform layer (IPL). The inset color scheme in this and subsequent figures is the same as in Figure 3. Arrowheads in the electron micrographs represent synaptic specializations in this and subsequent figures. Scale bars = 10 μm; inset scale bar = 500 nm [Color figure can be viewed at wileyonlinelibrary.com]

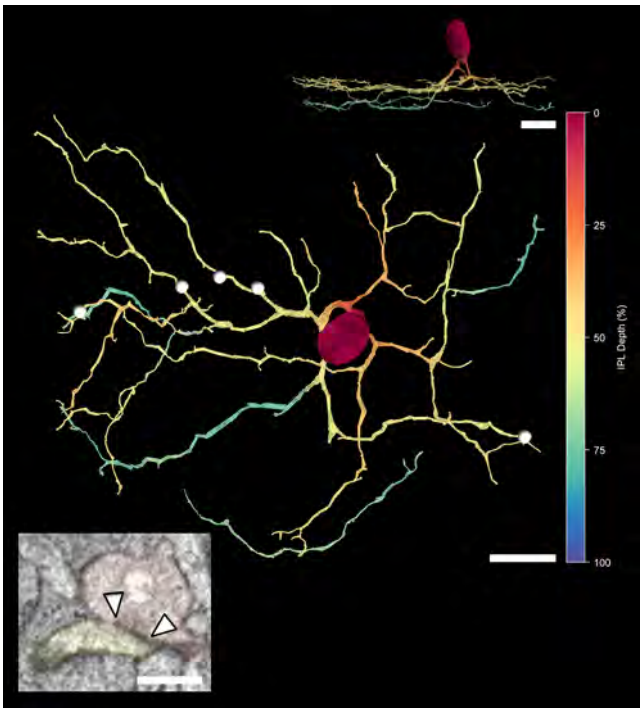

FIGURE 8 Wavy multistratified Type 2 amacrine cell 40879 was another type of narrow-field amacrine cell presynaptic to broad thorny ganglion cell 103. It is shown as it would appear in flat mount and in a vertical section. It made five synapses onto cell 103. The soma was in the inner nuclear layer, and the dendritic arbor was larger in diameter than that of the knotty bistratified cell illustrated in Figure 7. Scale bars = 10 μm; inset scale bar = 500 nm [Color figure can be viewed at wileyonlinelibrary.com]

and with parasol cells identified previously (Patterson, Bordt, et al., 2020). Wiry Type 2 cell 182 made nine synapses onto four ON parasol cells and one onto another wiry amacrine cell, 4315. Wiry Type 2 amacrine cell made four synapses onto two ON parasol cells. Wiry Type 2 amacrine cell 41444 made a synapse onto wiry Type 2 amacrine cell 182. If the processes of the wiry Type 2 amacrine cells that were tentatively identified were included in this analysis, there would be many more examples. Semilunar Type 2 cell 4781 made 13 synapses onto three ON parasol cells.

The same pattern was observed with smaller amacrine cells. One of the knotty bistratified Type 1 cells, 43016, made two synapses onto an ON parasol cell. A second knotty bistratified Type 1 cell, 38098, made five synapses onto the same ON parasol cell and also one onto wiry Type 2 cell 4651. A third knotty bistratified Type 1 cell, 42714, made a synapse onto OFF parasol cell 61. Taken together, these findings suggest that the same interconnected amacrine cells contribute to the neural circuits providing input to at least two types of motion-sensitive retinal ganglion cells.

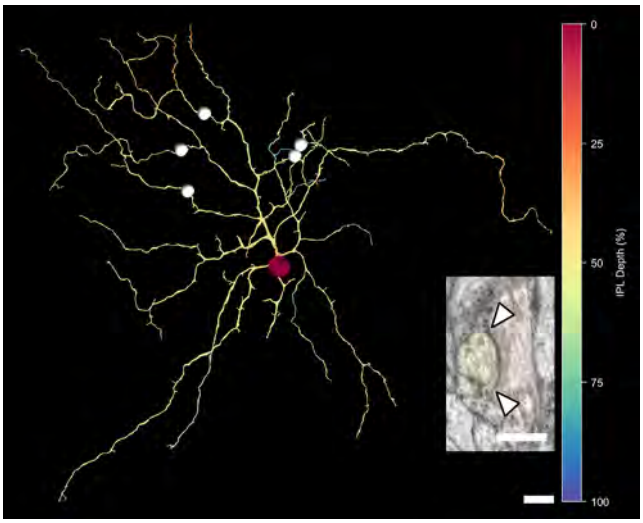

FIGURE 9 Spiny amacrine cell 40654 was a medium-field amacrine cell that made five synapses (white circles) onto broad thorny ganglion cell 103. Note that the soma is in the inner nuclear layer and the dendrites have small spines and mainly ramify in the center of the inner plexiform layer (IPL). Scale bar = 10 μm; inset scale bar = 500 nm [Color figure can be viewed at wileyonlinelibrary.com]

3.3 | Electrophysiology

Excitatory and inhibitory synaptic currents were recorded from three broad thorny ganglion cells under control conditions and during blockade of the ON pathway to gain insight into possible effects of ON pathway

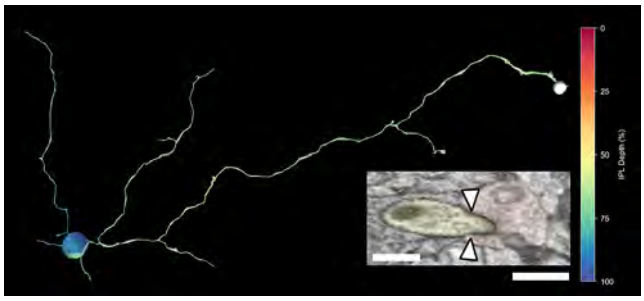

FIGURE 10 ON starburst amacrine cell 3111 was another medium-field amacrine cell presynaptic to ganglion cell 103. Although it was not completely reconstructed, it was classified based on its thin, tortuous dendrites ramifying at 65–70% depth in the inner plexiform layer (IPL) that were enlarged at their distal ends. Note that the soma is located in the ganglion cell layer. Scale bar = 10 μm; inset scale bar = 500 nm [Color figure can be viewed at wileyonlinelibrary.com]

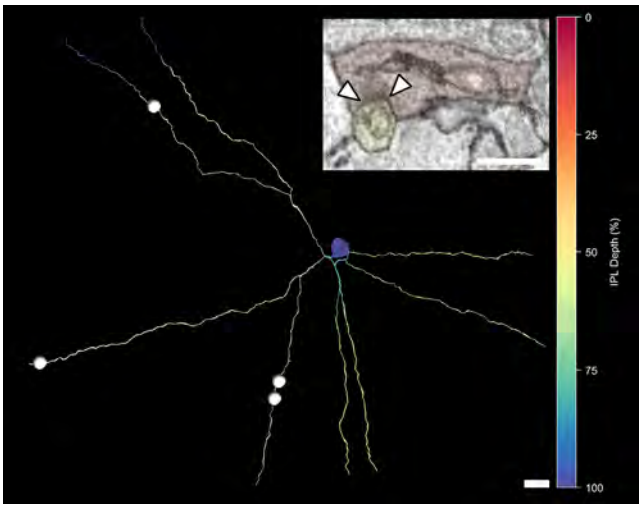

FIGURE 11 Wiry Type 2 amacrine cell 182 was a wide-field amacrine cell that made four synapses (white circles) onto broad thorny ganglion cell 103. Note that the soma was located in the ganglion cell layer and that the long, unbranched distal dendrites ramified at 60% depth in the inner plexiform layer (IPL). Scale bar = 10 μm; inset scale bar = 500 nm [Color figure can be viewed at wileyonlinelibrary.com]

signals on the OFF responses of the cells (Figure 14). Synaptic currents in control conditions were consistent with a previous report (Puller et al., 2015). During drug application, excitatory and inhibitory inputs persisted at light decrements but were abolished at light increments. We analyzed the OFF responses to a square-wave modulated spot to obtain further insight into the effects of ON pathway blockade on the response kinetics of the cells ($n = 3$, all measurements provided as mean ± *SEM*). The peak times relative to the stimulus transition time were only slightly shifted. Control excitation peaked at 117 ± 11 ms and inhibition at 55 ± 4 ms. When the drugs were applied, excitation peaked at 106 ± 7 ms, and inhibition at 59 ± 6 ms. The effect of the drugs on the

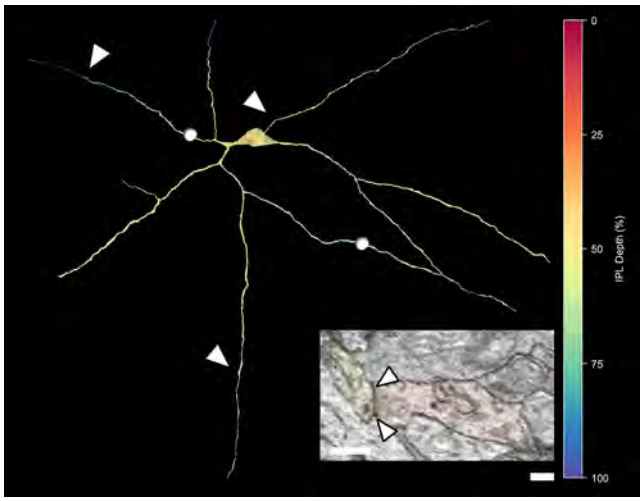

FIGURE 12 Semilunar Type 2 amacrine cell 4781 was another wide-field amacrine cell presynaptic to broad thorny ganglion cell 103. The soma was located in the inner plexiform layer (IPL) and the dendrites were larger in diameter than those of the wiry Type 2 cells illustrated in Figure 11. Thinner axons (arrowheads) arose from both the soma and the distal tips of the dendrites. Scale bar = 10 μm; inset scale bar = 500 nm [Color figure can be viewed at wileyonlinelibrary.com]

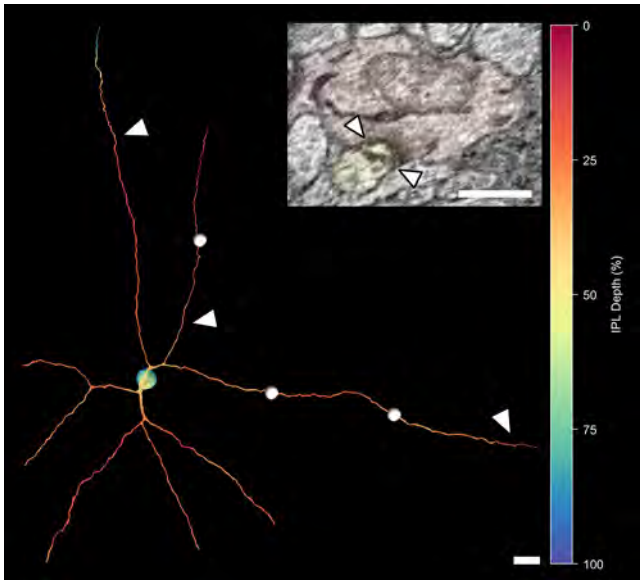

FIGURE 13 Stellate wavy amacrine cell 4308 was a third type of wide-field amacrine cell presynaptic to ganglion cell 103. It made three synapses (white circles). The soma was located in the ganglion cell layer, and the dendrites were intermediate in diameter between those of wiry and semilunar cells. Thinner axons (arrowheads) arose from secondary and distal dendrites, and both types of processes ramified between 20% and 30% depth in the inner plexiform layer (IPL), on average. Scale bar = 10 μm; inset scale bar = 500 nm [Color figure can be viewed at wileyonlinelibrary.com]

decay time constant τ (ms) appeared smaller for the excitation (control 187 ± 28 ms, drug 192 ± 19 ms) than for the inhibition (control 388 ± 109 ms, drug 198 ± 46 ms).

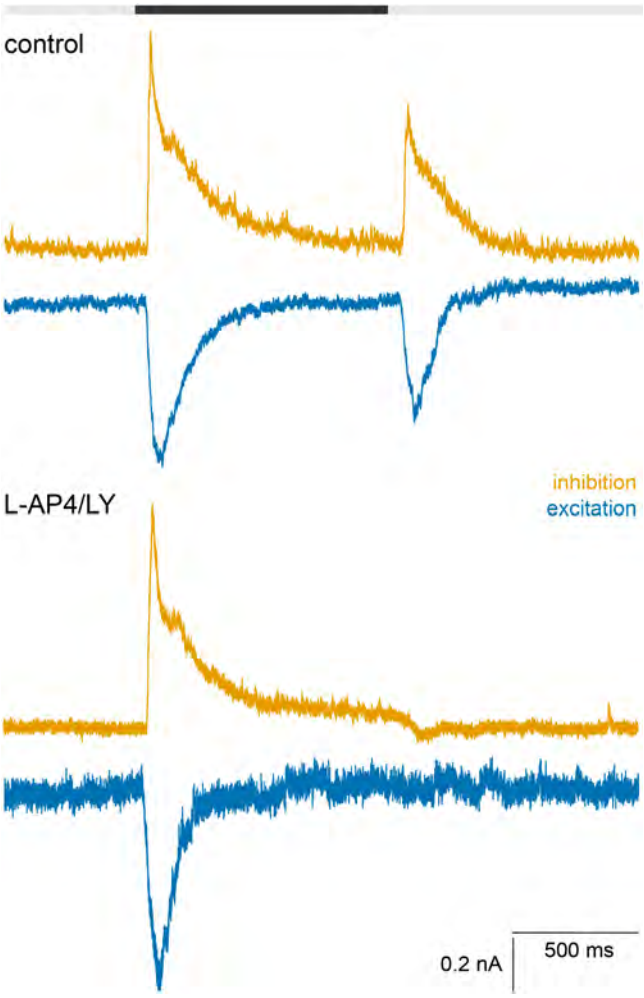

FIGURE 14 OFF responses of broad thorny ganglion cells do not depend on the ON pathway. (a) Whole-cell voltage-clamp responses of a broad thorny cell in control conditions at two different holding potentials to reveal excitatory and inhibitory synaptic currents. The stimulus is indicated above the recording traces. (b) Recording of the cell as above but during application of L-AP4 (5 μM) and LY341495 (7.5 μM) to block the ON pathway [Color figure can be viewed at wileyonlinelibrary.com]

4 | DISCUSSION

The major finding from this study was that broad thorny ganglion cells from central macaque retina received a very small percentage of their inputs from bipolar cells, smaller than any retinal ganglion cell described previously. This result is not attributable to under-sampling of bipolar cells. ON parasol cells in the same volume received a much larger proportion of their input from bipolar cells (Patterson, Bordt, et al., 2020). Typically, light responses of retinal ganglion cells are driven by bipolar cell input, and amacrine cells are usually thought to have more of a modulatory role. However, this is clearly not the case for broad thorny cells. They have highly specific responses compared with parasol ganglion cells, which respond to any moving textures (Puller et al., 2015). It may be that a preponderance of amacrine cell input is required to produce more nuanced response properties.

Broad thorny cells of macaque retina were different in this respect from broad thorny ganglion cells of marmoset retina, which received approximately the same proportion of inputs from bipolar cells as other, more common, types of retinal ganglion cells in a light microscopic study (Percival et al., 2011). It is uncertain whether this is attributable to methodological differences between their study and ours or to a difference between the two species. Old World and New World monkeys may be different in this respect, having diverged 40 million years ago. An alternative explanation is that the resolution of conventional light microscopy may be insufficient to distinguish synapses directly onto a labeled ganglion cell dendrite from those onto other processes nearby.

The percentage of bipolar cell input to the broad thorny cell was also different from the value reported for garland cells from macaque parafovea, which, in retrospect, were likely broad thorny cells. These received 30% of their input from bipolar cells, a value much lower than the percentages reported for midget cells or parasol cells at this eccentricity (Calkins & Sterling, 1996; Calkins & Sterling, 2007). Broad thorny cell 103 received less than 2% of its input from bipolar cells. Taken together, the two studies of broad thorny cells in macaques suggest that the proportion of bipolar cell input increases with proximity to the center of the fovea, but it remains lower than that of any other known type of primate retinal ganglion cell.

Robust excitatory inputs have been recorded from peripheral broad thorny ganglion cells using voltage clamp (Puller et al., 2015). The experiments reported here indicate that both the excitation and the inhibition recorded at the onset of light stimuli are conveyed via the ON pathway. Likewise, ON–OFF ganglion cells in marmoset retina receive excitatory input from both ON and OFF pathways (Protti et al., 2014). The changes in the OFF response kinetics after blockade of the ON pathway suggest the possibility that a cessation of crossover inhibition from the ON pathway contributes to the OFF excitatory responses in broad thorny cells, but the ON pathway is clearly not the sole source for generating responses at light decrements. Further experiments, including a greater number of cells and additional pharmacological agents, would be required to gain additional insight into the interactions of ON and OFF pathways in the neural circuit providing input to broad thorny ganglion cells.

Nevertheless, the results indicate that there are direct, light-stimulated excitatory synaptic inputs via both the ON and OFF pathways. Because there are so few inputs from bipolar cells to the thorny amacrine cell, amacrine cells are likely to provide most of the excitatory input. An additional synapse in the input pathway would account for the finding that light responses of broad thorny cells have longer latencies than other types of third-order neurons ramifying in the center of the IPL (Puller et al., 2015). This excitatory amacrine cell input is expected to be particularly important in the OFF pathway because the majority of the bipolar cell inputs to broad thorny ganglion cells came from ON bipolar cells.

The amacrine cells presynaptic to broad thorny cells described in this study are likely sources of the excitatory input. Acetylcholine from the ON starburst cells acting at nicotinic receptors and glutamate from the knotty bistratified Type 1 cells acting at ionotropic receptors are both excitatory (Marshak, 2016). Glycine acting at certain subtypes of NMDA receptors might also be excitatory (Otsu et al., 2019). If macaque retinas

have the amacrine cells described recently in human retina that contain neither glycine nor GABA, these would be another possible source of excitatory input (Yan et al., 2020).

One type of narrow-field amacrine cell presynaptic to broad thorny ganglion cell 103 was identified morphologically as knotty bistratified Type 1 (Mariani, 1990). It also closely resembled the A4 type from human retina (Kolb et al., 1992). In baboon retina, these cells contain immunoreactive vGluT3, and they frequently make synapses onto retinal ganglion cell dendrites (Marshak et al., 2015). In mice, they make both glycinergic inhibitory synapses and glutamatergic excitatory synapses (Marshak, 2016). A second type of narrow-field amacrine cell presynaptic to broad thorny ganglion cell 103 was identified morphologically as the wavy multistratified Type 2 (Mariani, 1990). Two of these cells contributed to the pairs of synapses found on the spines of broad thorny cell 103. These synapses from wavy multistratified cells might provide cross-over inhibition to broad thorny cells (Werblin, 2010).

Broad thorny cell 103 also received a single synapse from an ON starburst amacrine cell, which was identified by its dendritic morphology and stratification depth in the IPL (Kolb et al., 1992; Mariani, 1990; Rodieck, 1989; Rodieck & Marshak, 1992). It is possible that it also receives cholinergic input at unspecialized sites, as reported recently in the mouse retina (Sethuramanujam et al., 2021).

Another medium-field amacrine cell presynaptic to broad thorny cell 103 resembled the stratified amacrine cells first described using the Golgi method in macaque central retina (Boycott & Dowling, 1969). These were named spiny in a later study of macaque retina using the same technique, and roughly equal numbers of these cells had somas in the GCL, like the spiny amacrine cell presynaptic to broad thorny cell 103 (Mariani, 1990). The first descriptions of the amacrine cells containing immunoreactive vasoactive intestinal peptide (VIP) identified those cells as spiny (Lammerding-Köppel et al., 1991; Marshak, 1989). However, more recently, the VIP-positive cells have been classified as the stellate varicose type, instead (Grünert & Martin, 2020). The spiny amacrine cells have a very high spatial density in marmoset retina, where they can be labeled using an antibody to secretagogin, and they constitute a single population, regardless of the positions of their somas (Weltzien et al., 2014).

Wide-field amacrine cells provided a major input to the broad thorny cell 103. These were identified as wiry Type 2 cells, semilunar Type 2 cells, and stellate wavy cells. Their inputs may account for two findings reported in an earlier electrophysiological study of broad thorny cells in macaque retina. Postsynaptic inhibition of broad thorny cells increases with the stimulus size, reaching a maximum at sizes larger than the dendritic field diameter, and broad thorny cell light responses are suppressed by global stimulus motion (Puller et al., 2015).

Semilunar Type 2 cells are coupled to ON parasol cells by gap junctions (Greschner et al., 2016; Jacoby et al., 1996), and they were also presynaptic to broad thorny cell 103. This pathway might enable ON parasol cells to inhibit broad thorny cells. Another prediction is that the axons of broad thorny ganglion cells should have relatively slow conduction velocities because of their narrow diameter. In this respect, they would resemble the "rarely encountered" ganglion cells of macaque retina (Schiller & Malpeli, 1977).

The amacrine cells presynaptic to broad thorny ganglion cell 103 were not specialized to provide inputs to this type of ganglion cell; many also provided input to parasol cells and to each other. In this respect, they were different from the highly specialized A12 amacrine cells that convey input from short wavelength-sensitive cone bipolar cells to intrinsically-photosensitive ganglion cells in macaque retina (Patterson, Kuchenbecker, et al., 2020) and other types of well-characterized primate amacrine cells that direct most of their output to a single type of postsynaptic cell (Grünert & Martin, 2020). The dendrites of broad thorny cell 103 extended to the boundaries of the connectome, stratified broadly and received over 1000 synapses from amacrine cells. But the identified presynaptic cells provided, at most, six synapses to cell 103. The same trend was seen with the unidentified amacrine cells. Taken together, these findings suggest that this ensemble of neurons contributes to the responses of many motion-sensitive ganglion cells.

ACKNOWLEDGMENTS

This research was supported by NIH grants EY027859, EY028927, EY002576, NS099578, EY007031, EY007125, P51-OD010425/ORID, P30-EY014800, and P30-EY001730, the German Research Foundation (DFG grant PU 469/2-1) and by Research to Prevent Blindness.

AUTHOR CONTRIBUTIONS

David W. Marshak, Jay Neitz, Judith M. Ogilvie, and Andrea S. Bordt designed the anatomical experiments. Christian Puller designed and executed the physiological experiments. James R. Anderson and Sara S. Patterson wrote software. James R. Anderson and James A. Kuchenbecker assembled the images into a volume. David W. Marshak, Sara S. Patterson, Christian Puller, and Andrea S. Bordt wrote the manuscript. Andrea S. Bordt, Sara S. Patterson, Rebecca J. Girresch, Diego Perez, Luke Tseng, Marcus A. Mazzaferri, Rodrigo Gonzales-Rojas, Ashley Roland, Charis Tang, and David W. Marshak annotated the connectome. Alice Z. Chuang performed the statistical analysis.

PEER REVIEW

The peer review history for this article is available at https://publons.com/publon/10.1002/cne.25156.

DATA AVAILABILITY STATEMENT

The serial EM volume was annotated using the web-based, multi-user Viking software described previously (Anderson et al., 2011; http://connectomes.utah.edu RRID:SCR_005986). The annotated volume is available in a read-only format. Data analysis and 3D rendering were performed using an open-source Matlab (Mathworks, RRID: SCR_001622) program https://github.com/neitzlab/sbfsem-tools RRID: SCR_017350. The code and data used to generate the figures in this study will be made available upon request.

ORCID

Andrea S. Bordt https://orcid.org/0000-0003-4076-2205

REFERENCES

Abbott, C. J., Percival, K. A., Martin, P. R., & Grünert, U. (2012). Amacrine and bipolar inputs to midget and parasol ganglion cells in marmoset retina. *Visual Neuroscience*, *29*(3), 157–168. https://doi.org/10.1017/S095252381200017X

Ala-Laurila, P., Greschner, M., Chichilnisky, E. J., & Rieke, F. (2011). Cone photoreceptor contributions to noise and correlations in the retinal output. *Nature Neuroscience*, *14*(10), 1309–1316. https://doi.org/10.1038/nn.2927

Anderson, J. R., Mohammed, S., Grimm, B., Jones, B. W., Koshevoy, P., Tasdizen, T., Whitaker, R., & Marc, R. E. (2011). The Viking viewer for connectomics: Scalable multi-user annotation and summarization of large volume data sets. *Journal of Microscopy*, *241*(1), 13–28. https://doi.org/10.1111/j.1365-2818.2010.03402.x

Appleby, T. R., & Manookin, M. B. (2019). Neural sensitization improves encoding fidelity in the primate retina. *Nature Communications*, *10*(1), 4017. https://doi.org/10.1038/s41467-019-11734-4

Bordt, A. S., Perez, D., Tseng, L., Liu, W. S., Neitz, J., Patterson, S. S., Famiglietti, E. V., & Marshak, D. W. (2019). Synaptic inputs from identified bipolar and amacrine cells to a sparsely branched ganglion cell in rabbit retina. *Visual Neuroscience*, *36*, E004. https://doi.org/10.1017/S0952523819000014

Boycott, B. B., & Dowling, J. E. (1969). Organization of the primate retina: Light microscopy. *Philosophical Transactions of the Royal Society of London, Series B Biological Sciences*, *225*, 109–184.

Calkins, D. J., & Sterling, P. (1996). Absence of spectrally specific lateral inputs to midget ganglion cells in primate retina. *Nature*, *381*(6583), 613–615. https://doi.org/10.1038/381613a0s

Calkins, D. J., & Sterling, P. (2007). Microcircuitry for two types of achromatic ganglion cell in primate fovea. *The Journal of Neuroscience: The Official Journal of the Society for Neuroscience*, *27*(10), 2646–2653. https://doi.org/10.1523/JNEUROSCI.4739-06.2007

Chen, Q., & Wei, W. (2018). Stimulus-dependent engagement of neural mechanisms for reliable motion detection in the mouse retina. *Journal of Neurophysiology*, *120*(3), 1153–1161. https://doi.org/10.1152/jn.00716.2017

Dacey, D. M., Peterson, B. B., Robinson, F. R., & Gamlin, P. D. (2003). Fireworks in the primate retina: In vitro photodynamics reveals diverse LGN-projecting ganglion cell types. *Neuron*, *37*(1), 15–27. https://doi.org/10.1016/s0896-6273(02)01143-1

Dowling, J. E., & Boycott, B. B. (1966). Organization of the primate retina: Electron microscopy. *Proceedings of the Royal Society B*, *166*(1002), 80–111. https://doi.org/10.1098/rspb.1966.0086

Greschner, M., Heitman, A. K., Field, G. D., Li, P. H., Ahn, D., Sher, A., Litke, A. M., & Chichilnisky, E. J. (2016). Identification of a retinal circuit for recurrent suppression using indirect electrical imaging. *Current Biology*, *26*(15), 1935–1942. https://doi.org/10.1016/j.cub.2016.05.051

Grünert, U., & Martin, P. R. (2020). Cell types and cell circuits in human and non-human primate retina. *Progress in Retinal and Eye Research*, 100844. https://doi.org/10.1016/j.preteyeres.2020.100844

Jacoby, R., Stafford, D., Kouyama, N., & Marshak, D. (1996). Synaptic inputs to ON parasol ganglion cells in the primate retina. *The Journal of Neuroscience: The Official Journal of the Society for Neuroscience*, *16*(24), 8041–8056.

Kolb, H., Linberg, K. A., & Fisher, S. K. (1992). Neurons of the human retina: A Golgi study. *The Journal of Comparative Neurology*, *318*(2), 147–187. https://doi.org/10.1002/cne.903180204

Kwan, W. C., Mundinano, I. C., de Souza, M. J., Lee, S. C., Martin, P. R., Grünert, U., & Bourne, J. A. (2019). Unravelling the subcortical and retinal circuitry of the primate inferior pulvinar. *The Journal of Comparative Neurology*, *527*(3), 558–576.

Lammerding-Köppel, M., Thier, P., & Koehler, W. (1991). Morphology and mosaics of VIP-like immunoreactive neurons in the retina of the rhesus monkey. *Journal of Comparative Neurology*, *312*(2), 251–263. https://doi.org/10.1002/cne.903120208

Maechler, M., Rousseeuw, P., Struyf, A., Hubert, M., & Hornik, K. (2013). Cluster: Cluster analysis basics and extensions. R package (Version 1.14.4).

Majumdar, S., Wässle, H., Jusuf, P. R., & Haverkamp, S. (2008). Mirror-symmetrical populations of wide-field amacrine cells of the macaque monkey retina. *The Journal of Comparative Neurology*, *508*(1), 13–27. https://doi.org/10.1002/cne.21666

Mariani, A. P. (1990). Amacrine cells of the rhesus monkey retina. *The Journal of Comparative Neurology*, *301*(3), 382–400. https://doi.org/10.1002/cne.903010305

Marshak, D. W. (1989). Peptidergic neurons of the macaque monkey retina. *Neuroscience Research Supplements*, *10*, S117–S130. https://doi.org/10.1016/0921-8696(89)90014-5s

Marshak, D. W. (2016). A tale of two neurotransmitters. *Visual Neuroscience*, *33*, E017. https://doi.org/10.1017/S0952523816000146

Marshak, D. W., Chuang, A. Z., Dolino, D. M., Jacoby, R. A., Liu, W. S., Long, Y. E., Sherman, M. B., Suh, J. M., Vila, A., & Mills, S. L. (2015). Synaptic connections of amacrine cells containing vesicular glutamate transporter 3 in baboon retinas. *Visual Neuroscience*, *32*, E006. https://doi.org/10.1017/S0952523815000036

Masri, R. A., Percival, K. A., Koizumi, A., Martin, P. R., & Grünert, U. (2016). Connectivity between the OFF bipolar type DB3a and six types of ganglion cell in the marmoset retina. *The Journal of Comparative Neurology*, *524*(9), 1839–1858. https://doi.org/10.1002/cne.23925

Masri, R. A., Percival, K. A., Koizumi, A., Martin, P. R., & Grünert, U. (2019). Survey of retinal ganglion cell morphology in marmoset. *Journal of Comparative Neurology*, *527*(1), 236–258. https://doi.org/10.1002/cne.24157

Otsu, Y., Darcq, E., Pietrajtis, K., Mátyás, F., Schwartz, E., Bessaih, T., Gerges, A., Rousseau, C. V., Grand, T., Dieudonné, S., Paoletti, P., Acsády, L., Agulhon, C., Kieffer, B. L., & Diana, M. A. (2019). Control of aversion by glycine-gated GluN1/GluN3A NMDA receptors in the adult medial habenula. *Science (New York, N.Y.)*, *366*(6462), 250–254. https://doi.org/10.1126/science.aax1522

Patterson, S. S., Bordt, A. S., Girresch, R. J., Linehan, C. M., Bauss, J., Yeo, E., Perez, D., Tseng, L., Navuluri, S., Harris, N. B., Matthews, C., Anderson, J. R., Kuchenbecker, J. A., Manookin, M. B., Ogilvie, J. M., Neitz, J., & Marshak, D. W. (2020). Wide-field amacrine cell inputs to ON parasol ganglion cells in macaque retina. *The Journal of Comparative Neurology*, *528*(9), 1588–1598. https://doi.org/10.1002/cne.24840

Patterson, S. S., Kuchenbecker, J. A., Anderson, J. R., Bordt, A. S., Marshak, D. W., Neitz, M., & Neitz, J. (2019). An S-cone circuit for edge detection in the primate retina. *Scientific Reports*, *9*(1), 11913. https://doi.org/10.1038/s41598-019-48042-2

Patterson, S. S., Kuchenbecker, J. A., Anderson, J. R., Neitz, M., & Neitz, J. (2020). A color vision circuit for non-image-forming vision in the primate retina. *Current Biology*, *30*(7), 1269–1274.e2. https://doi.org/10.1016/j.cub.2020.01.040

Percival, K. A., Martin, P. R., & Grünert, U. (2011). Synaptic inputs to two types of koniocellular pathway ganglion cells in marmoset retina. *The Journal of Comparative Neurology*, *519*(11), 2135–2153. https://doi.org/10.1002/cne.22586

Percival, K. A., Martin, P. R., & Grünert, U. (2013). Organisation of koniocellular-projecting ganglion cells and diffuse bipolar cells in the primate fovea. *The European Journal of Neuroscience*, *37*(7), 1072–1089. https://doi.org/10.1111/ejn.12117

Peterson, B. B., & Dacey, D. M. (2000). Morphology of wide-field bistratified and diffuse human retinal ganglion cells. *Visual Neuroscience*, *17*(4), 567–578. https://doi.org/10.1017/s0952523800174073

Protti, D. A., Di Marco, S., Huang, J. Y., Vonhoff, C. R., Nguyen, V., & Solomon, S. G. (2014). Inner retinal inhibition shapes the receptive

field of retinal ganglion cells in primate. *The Journal of Physiology*, *592* (1), 49–65. https://doi.org/10.1113/jphysiol.2013.257352

Puller, C., Manookin, M. B., Neitz, J., Rieke, F., & Neitz, M. (2015). Broad thorny ganglion cells: A candidate for visual pursuit error signaling in the primate retina. *The Journal of Neuroscience: The Official Journal of the Society for Neuroscience*, *35*(13), 5397–5408. https://doi.org/10.1523/JNEUROSCI.4369-14.2015

Puthussery, T., Percival, K. A., Venkataramani, S., Gayet-Primo, J., Grünert, U., & Taylor, W. R. (2014). Kainate receptors mediate synaptic input to transient and sustained OFF visual pathways in primate retina. *The Journal of Neuroscience: The Official Journal of the Society for Neuroscience*, *34*(22), 7611–7621. https://doi.org/10.1523/JNEUROSCI.4855-13.2014

Puthussery, T., Venkataramani, S., Gayet-Primo, J., Smith, R. G., & Taylor, W. R. (2013). NaV1.1 channels in axon initial segments of bipolar cells augment input to magnocellular visual pathways in the primate retina. *The Journal of Neuroscience: The Official Journal of the Society for Neuroscience*, *33*(41), 16045–16059. https://doi.org/10.1523/JNEUROSCI.1249-13.2013

Rodieck, R. W. (1989). Starburst amacrine cells of the primate retina. *Journal of Comparative Neurology*, *285*(1), 18–37. https://doi.org/10.1002/cne.902850104s

Rodieck, R. W., & Marshak, D. W. (1992). Spatial density and distribution of choline acetyltransferase immunoreactive cells in human, macaque, and baboon retinas. *The Journal of Comparative Neurology*, *321*(1), 46–64. https://doi.org/10.1002/cne.903210106

Rodieck, R. W., & Watanabe, M. (1993). Survey of the morphology of macaque retinal ganglion cells that project to the pretectum, superior colliculus, and parvicellular laminae of the lateral geniculate nucleus. *The Journal of Comparative Neurology*, *338*(2), 289–303. https://doi.org/10.1002/cne.903380211

Schiller, P. H., & Malpeli, J. G. (1977). Properties and tectal projections of monkey retinal ganglion cells. *Journal of Neurophysiology*, *40*(2), 428–445. https://doi.org/10.1152/jn.1977.40.2.428

Sethuramanujam, S., Matsumoto, A., de Rosenroll, G., Murphy-Baum, B., McIntosh, J. M., Jing, M., Li, Y., Berson, D., Yonehara, K., & Awatramani, G. B. (2021). Rapid multidirected cholinergic transmission in the central nervous system. *Nature Communications*, *12*, 1374. https://doi.org/10.1038/s41467-021-21680-9

Tsukamoto, Y., & Omi, N. (2015). OFF bipolar cells in macaque retina: Type-specific connectivity in the outer and inner synaptic layers. *Frontiers in Neuroanatomy*, *9*, 122. https://doi.org/10.3389/fnana.2015.00122

Tsukamoto, Y., & Omi, N. (2016). ON bipolar cells in macaque retina: Type-specific synaptic connectivity with special reference to OFF counterparts. *Frontiers in Neuroanatomy*, *10*, 104. https://doi.org/10.3389/fnana.2016.00104

Wei, W. (2018). Neural mechanisms of motion processing in the mammalian retina. *Annual Review of Vision Science*, *4*, 165–192. https://doi.org/10.1146/annurev-vision-091517-034048

Weltzien, F., Dimarco, S., Protti, D. A., Daraio, T., Martin, P. R., & Grünert, U. (2014). Characterization of secretagogin-immunoreactive amacrine cells in marmoset retina. *The Journal of Comparative Neurology*, *522*(2), 435–455. https://doi.org/10.1002/cne.23420

Werblin, F. S. (2010). Six different roles for crossover inhibition in the retina: Correcting the nonlinearities of synaptic transmission. *Visual Neuroscience*, *27*(1–2), 1–8. https://doi.org/10.1017/S0952523810000076

Yamada, E. S., Bordt, A. S., & Marshak, D. W. (2005). Wide-field ganglion cells in macaque retinas. *Visual Neuroscience*, *22*(4), 383–393. https://doi.org/10.1017/S095252380522401X

Yan, W., Peng, Y.-R., van Zyl, T., Regev, A., Shekhar, K., Juric, D., & Sanes, J. R. (2020). Cell atlas of the human fovea and peripheral retina. *Scientific Reports*, *10*(1), 9802. https://doi.org/10.1038/s41598-020-66092-9

SUPPORTING INFORMATION

Additional supporting information may be found online in the Supporting Information section at the end of this article.

Received: 10 March 2020 | Accepted: 12 March 2020
DOI: 10.1002/cne.24913

RESEARCH ARTICLE

JCN RESEARCH IN SYSTEMS NEUROSCIENCE THE JOURNAL OF COMPARATIVE NEUROLOGY WILEY

The sensory peripheral nervous system in the tail of a cephalochordate studied by serial blockface scanning electron microscopy

Nicholas D. Holland[1] | Ildiko M. L. Somorjai[2]

[1]Marine Biology Research Division, Scripps Institution of Oceanography, University of California at San Diego, La Jolla, California

[2]School of Biology, University of Saint Andrews, St Andrews, UK

Correspondence
Nicholas D. Holland, Marine Biology Research Division, Scripps Institution of Oceanography, University of California at San Diego, La Jolla, CA 92093.
Email: nholland@ucsd.edu

Abstract

Serial blockface scanning electron microscopy (SBSEM) is used to describe the sensory peripheral nervous system (PNS) in the tail of a cephalochordate, *Asymmetron lucayanum*. The reconstructed region extends from the tail tip to the origin of the most posterior peripheral nerves from the dorsal nerve cord. As peripheral nerves ramify within the dermis, all the nuclei along their course belong to glial cells. Invaginations in the glial cell cytoplasm house the neurites, an association reminiscent of the nonmyelinated Schwann cells of vertebrates. Peripheral nerves pass from the dermis to the epidermis via small fenestrae in the sub-epidermal collagen fibril layer; most nerves exit abruptly, but a few run obliquely within the collagen fibril layer for many micrometers before exiting. Within the epidermis, each nerve begins ramifying repeatedly, but the branches are too small to be followed to their tips with SBSEM at low magnification (previous studies on other cephalochordates indicate that the branches end freely or in association with epidermal sensory cells). In *Asymmetron*, two morphological kinds of sensory cells are scattered in the epidermis, usually singly, but sometimes in pairs, evidently the recent progeny of a single precursor cell. The discussion considers the evolution of the sensory PNS in the phylum Chordata. In cephalochordates, Retzius bipolar neurons with intramedullary perikarya likely correspond to the Rohon-Beard cells of vertebrates. However, extramedullary neurons originating from ventral epidermis in cephalochordates (and presumably in ancestral chordates) contrast with vertebrate sensory neurons, which arise from placodes and neural crest.

KEYWORDS

amphioxus, Cephalochordata, glia, lancelet, peripheral nervous system, SBSEM

1 | INTRODUCTION

Cephalochordates, commonly called amphioxus or lancelets, are the earliest branching clade in the phylum Chordata. Thus, they can provide insights into the relatively simple foundations on which much more elaborate vertebrate characters were built—a good example is neural crest evolution (Holland, Panganiban, Henyey, & Holland, 1996). One such character is the simple peripheral nervous system (PNS) of cephalochordates. It has neither ganglia nor an autonomic component. Moreover, neither neural crest nor placodes play a part in its development, and the distinction between cranial and spinal nerves is inconspicuous (Balfour, 1885; Fritzsch & Northcutt, 1993; Holland, 2009).

There have been many previous publications on the cephalochordate PNS, all limited to species in the genus *Branchiostoma*. Some of these descriptions were focused on embryos and larvae (Kaltenbach, Yu & Holland, 2009; Lu, Luo, & Yu, 2012; Yasui, Tabata, Ueki, Uemura, &

Zhang, 1998; Zieger, Garbarino, Robert, Yu, Croce, Candiani, & Schubert, 2018), and others concerned postmetamorphic and adult stages. These latter studies have spanned the range from low-resolution descriptions of whole animals (Retzius, 1898) through more detailed observations on smaller tissue samples (Demski, Beaver, & Morrill, 1996; Dogiel, 1903; Fusari, 1889; Heymans & van der Stricht, 1898; Johnston, 1905; Kutchin, 1913; Langerhans, 1876; Lele, Palmer, & Weddell, 1958; Reichert, 1870; Rohon, 1882) to fine-scale descriptions with transmission electron microscopy (TEM; Lacalli & Hou, 1999; Peters, 1963; Ruppert, 1997; Schulte & Riehl, 1977; Welsch, 1968). Because the TEM was based, at best, on limited serial sectioning, some of the results were difficult to place within the context of the anatomy as a whole. To help bridge gaps left by these earlier studies, the present investigation uses serial blockface scanning electron microscopy (SBSEM) to demonstrate the fine details of the PNS within a body region comprehensively reconstructed in three dimensions (3D). To date, SBSEM has most often been used for describing TEM-level details of cells within relatively small tissue volumes. In contrast, the technique has only infrequently been employed to describe larger body regions (Holland, 2018), first because such studies require relatively low magnification with concomitant loss of resolution, and second because extensive 3D reconstructions are time consuming. In spite of these drawbacks, high volume SBSEM, as exemplified by the present study, can provide new insights and serve to put less synoptic earlier work into a broad context.

The cephalochordate described here, *Asymmetron lucayanum*, the Bahamas lancelet, has a relatively small adult size (on the order of 2 cm), which is advantageous for reconstructing body regions in 3D. We focus here on the tail tip, which extends as a slender caudal process (Andrews, 1893), a well-defined body part that includes the region where the dorsal nerve cord gives rise to the most posterior peripheral nerves and then continues as a filum terminale. The peripheral nerves accompanying the filum terminale posteriorly are comparable to the cauda equine of some vertebrates. In the tail region investigated, the PNS is entirely sensory and is divisible into interconnected dermal and epidermal compartments. It helps to keep in mind that what are called *nerves* in the dermal compartment are actually complexes of glial cells and neurites. The nuclei associated with these nerves all belong to glial cells and not to the neuronal component—the perikarya of the latter either lie within the dorsal nerve cord (Bone, 1959) or comprise sensory cell bodies in the epidermis (Lacalli & Hou, 1999).

Here we provide a synoptic view of the PNS and its associated glia within the dermis, determine the size and distribution of nerves traversing fenestrae in the collagen fibril layer just beneath the dermal–epidermal junction, and describe the ciliated sensory cells within the epidermis. The discussion speculates that ancestral chordates resembled extant cephalochordates in having a sensory PNS comprising two classes of neurons: namely, those with intramedullary perikarya and those with extramedullary perikarya located in the epidermis. During chordate evolution, the component with intramedullary perikarya evidently carried over into vertebrates as Rohon-Beard cells, while the component with extramedullary perikarya originating from ventral epidermis was completely replaced in all vertebrates by sensory neurons differentiating from placodes and neural crest.

2 | MATERIALS AND METHODS

2.1 | Animals

Adults of *Asymmetron lucayanum* were sieved from the sandy substratum at ankle depth at low tide in the Bimini lagoon, Bahamas. A map of the collecting site (GPS coordinates: 25.72297°N, 79.29288°W) is in Holland (2011). The animals in the present study were 1.8 cm long, the commonest size class in the collection. These were fixed for light and electron microscopy a few days after collection.

2.2 | Light microscopy and conventional SEM

Inter-animal variability in the distribution of peripheral nerves was estimated by light microscopy of serial semi-thin sections of six specimens. Fixation was for several days at 4°C in 4% paraformaldehyde in 0.1 M MOPS buffer at pH 7.4 containing 0.5 M NaCl, 1 mM EGTA, and 2 mM $MgSO_4$. After fixation, the anterior 1.5 cm of each animal was cut away, leaving the posterior region to be processed for light microscopy. Fixed specimens were washed for 1 min in distilled water, stained in toto in 0.2% Ponceau S in 0.1% aqueous acetic acid for 90 min at room temperature, washed for 10 min in distilled water, dehydrated through an ethanol series, and embedded in Spurr's resin (Polysciences, Warrington, PA). After the resin was polymerized overnight at 70°C, a complete series of semi-thin (2.5-μm) sections was cut from each block with glass knives. Each section was transferred to a drop of water on a glass slide, flattened by evaporating the water on a hot plate, stained through the resin with 0.1% aqueous azure A, washed briefly in distilled water, dried, and mounted in immersion oil. For conventional SEM, the tails of six adults were fixed overnight at 4°C in 2% glutaraldehyde–sea water, rinsed for 30 s in distilled water, dehydrated in an ethanol series, transferred to hexamethyldisilazane (Braet, De Zanger, & Wisse, 1997), and air-dried. The dried specimens were mounted on double-sided adhesive tape affixed to SEM stubs, coated with iridium, and viewed in a Hitachi S4800 SEM.

2.3 | SBSEM and 3-D reconstructions

For SBSEM, four tails were processed for cross-sectioning. The best oriented one is illustrated here, although ancillary observations were made on the others before sectioning was terminated early when unfavorable orientation in the block became evident. The primary fixation was for 2 weeks at 4°C in 0.15 M cacodylate buffer (pH 7.4) containing 2.5% glutaraldehyde, 2% formaldehyde, and 2 mM $CaCl_2$ (Deerinck, Bushong, Lev-Ramm, Tsien, & Ellisman, 2010). After primary fixation, the samples were exposed successively to reduced osmium tetroxide, thiocarbohydrazide, osmium tetroxide, uranyl acetate, and lead aspartate under conditions in table 1 in Wanner, Genoud, & Friedrich (2016). Following ethanol dehydration at 4°C, the specimens were transferred through acetone and embedded in Durcupan resin.

The SBSEM was carried out with a 3View system (Gatan, Pleasanton, CA) installed in a Zeiss Merlin SEM. Each resin-embedded sample is placed

in a scanning electron microscope specimen chamber containing an ultramicrotome (Denk & Horstman, 2004; Peddie & Collinson, 2014; Titze & Genoud, 2016). After the microscope records an image of the blockface by backscattered electrons, the microtome shaves away a thin section from the specimen to expose a new blockface. This alternation of scanning and shaving generates uninterrupted serial images, each superficially resembling a conventional transmission electron micrograph. In the present study, blockfaces were scanned every 0.25 μm. From the most favorably oriented tail tip, we scanned a total of 2,240 block faces. The SBSEM image series was converted to 3D with *Reconstruct* software, available gratis from http://www.bu.edu/neural/Reconstruct.html (Borrett & Hughes, 2016; Fiala, 2005). In the reconstructions, the tissues were depicted as continuous Boissonnat surfaces (in some instances, rendered semitransparent to reveal the position of nuclei within the cells). Because the sections were at relatively low magnification (and thus at relatively low resolution), it was not possible to visualize intercellular boundaries in some of the tissues. Even so, the distribution of such cells can be shown by reconstructing their constituent nuclei. Finally, all cross-sections here are oriented as if viewed from the posterior end of the animal; thus left- and right-side structures are, respectively, toward the left and right in all the figures.

2.4 | Quantification and statistics

From the SBSEM data, we measured the diameters of all 117 nerves passing through fenestrae in the collagen fibril layer on the left and right side of the region studied. We also evaluated the spatial pattern of fenestrae in the collagen fibril layer and the distribution of epidermal sensory cells by measuring nearest neighbor relationships. A first index of dispersion was calculated from the SBSEM reconstruction of fenestrae on the left side of the tail, and a second index of dispersion was calculated for the sensory cells (Type I and Type II together) in conventional SEM of a comparable area on the left side of the tail of another animal; this was preferable to measuring sensory cells in the SBSEM reconstruction, some of which could not be identified with certainty. After the indices of dispersion were corrected for boundary strip errors (Donnelly, 1978), the two data sets were compared.

SBSEM data were also used to examine the distances separating the two kinds of epidermal sensory cells from the fenestrae on either side of the tail area studied. For this comparison, we included only sensory cells that were clearly identifiable with SBSEM on the left and right sides (in all, 39 Type I cells and 49 Type II cells). Images of these sensory cells were superimposed on the map of the fenestrae on the appropriate side of the tail, and the distance from the basal pole of each cell to the nearest fenestra was measured and plotted in 4-μm increments.

3 | RESULTS

3.1 | The PNS in the tail as seen by light microscopy

An adult specimen of *Asymmetron lucayanum* (Figure 1a), as already mentioned, has a post-anal tail terminating posteriorly in a caudal process (Figure 1b). The core tissues running the entire length of the tail are the dorsal nerve cord and notochord (Figure 1c,d). In the caudal process, the coelomic mesoderm is much reduced, lacking musculature and any segmental organization. As a consequence, none of the peripheral nerves studied here run within collagenous intersegmental myocommata (a conspicuous feature of the PNS in more anterior body regions).

Bordering the tail are dorsal and ventral fins, each consisting of a broad flange of dermal matrix overlain by a single-layered epidermis. As shown by the dashed lines in Figure 1e,f, the entire height of the fins could not be included in the field of view of our SBSEM except at the extreme posterior (Figure 1g). By light microscopy of 2.5-μm thick plastic sections, the peripheral nerves are not detectable in frontal view (Figure 1c,d), and, in cross-sections, only the nerves of large to medium diameter (Figure 1e,f, arrows) can be unequivocally identified. When these detectable nerves are compared among six different animals sectioned at equivalent levels of the tail, their branching patterns in the dermis differ considerably. This finding agrees with the extensive inter-animal variability in the distribution of peripheral nerve branches long known for *Branchiostoma* (Kutchin, 1913).

3.2 | Extracellular components of the dermis

For most of their length, the peripheral nerves run through a dermis (DE in Figure 2a,c), where even those with the smallest diameters (for example, the arrowed nerves in Figure 2c,d) can be unequivocally demonstrated. The dermis comprises a voluminous extracellular matrix that is finely granular (Figure 2b,d) and a bordering collagen fibril layer about 1 μm thick (FL in Figure 2b). Confusingly, the fibril layer has several synonyms in the literature: Grenzlamelle (Langerhans, 1876), cuticle (Fusari, 1889), homogene subepithelial Schicht (Dogiel, 1903), corium (Studnicka, 1909), and dermal collagenous mesh (Ruppert, 1997). Although our SBSEM does not resolve the detailed structure of the fibril layer, our unpublished TEM shows that, as in *Branchiostoma* (Welsch, 1968), the fibrils in *Asymmetron* each have a diameter about 50 nm and are aligned in thin abutting layers that are arranged orthogonally (i.e., fibrils in adjacent layers are oriented roughly at right angles to one another).

3.3 | Peripheral nerves in the dermis

All the peripheral nerves running in the dermis are complexes of neurites and glial cells (the latter are described in detail in section 3.5). Figure 3a,b is SBSEM reconstructions of the peripheral nerves, respectively, on the left and right sides of the tail region studied. These peripheral nerves are the most posterior ones in the body. After originating from the dorsal nerve cord, they extend posteriorly, branching through several orders of dichotomy (this pattern is interrupted in a few places by anastomoses). As a rule, the peripheral nerves within the dermis (Figure 4a, arrowhead) run in close proximity to the inner side of the collagen fibril layer although they can, in

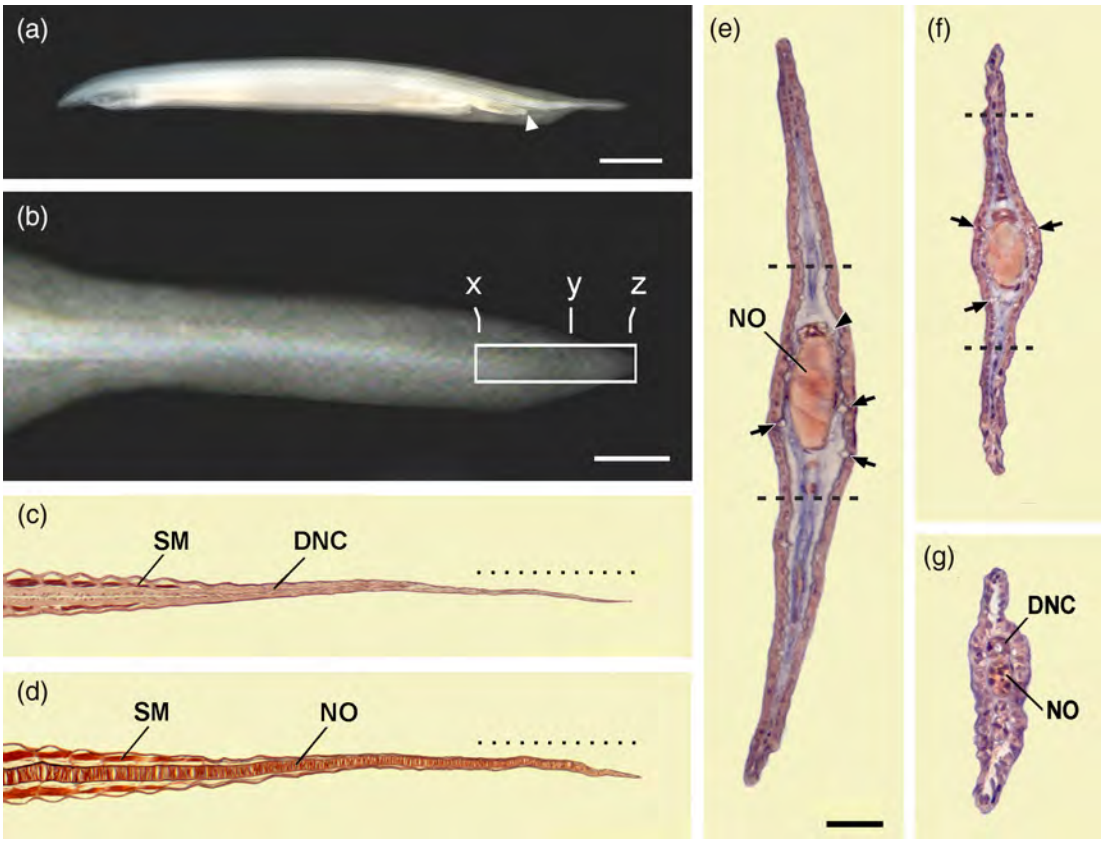

FIGURE 1 Bahamas lancelet (*Asymmetron lucayanum*). (a) Living adult; anus indicated by arrowhead. Scale line = 2 mm. (b) Tail of foregoing with studied region in rectangle; lower case letters show levels of cross-sections in 1e, g; scale line (also applicable to 1c, d) = 250 μm. (c) Frontal section through tail at level of dorsal nerve cord (DNC); segmented muscles (SM) toward left; length of SBSEM reconstruction indicated by dotted line. (d) Frontal section through tail at level of notochord (NO); segmented muscles (SM) toward left; length of SBSEM reconstruction indicated by dotted line. (e) Cross-section at Level *x* in 1b; fin regions dorsal and ventral to dashed lines outside SBSEM field of view; dorsal to notochord (NO), the dorsal nerve cord has a neuropil component (arrowhead); arrows point to some large peripheral nerves; scale line (also applicable to 1f, g) = 25 μm. (f) Cross-section at Level *y* in 1b; neural tube no longer includes neuropil; fin regions dorsal and ventral to dashed lines outside SBSEM field of view. (g) Cross-section at Level *z* in 1b, near blind posterior terminations of dorsal nerve cord (DNC) and notochord (NO) [Color figure can be viewed at wileyonlinelibrary.com]

places, run somewhat deeper in the dermal matrix (Figure 4b, arrowhead). Some older references (like Dogiel, 1903) described a fine plexus of peripheral nerves associated with the inner surface of the fibril layer in *Branchiostoma*; in contrast, our SBSEM reveals no such plexus in *Asymmetron*. The white arrows in Figure 3a,b indicate locations where the peripheral nerves of the dermis connect with the epidermal component of the PNS (described in detail in sections 3.6 and 3.7).

3.4 | Filum terminale

The peripheral nerves described in the present study diverge from the dorsal nerve cord at a level where the latter includes a neuropil component (Figure 4a,b, arrows). As the most posterior peripheral nerves originate, all of the neuropil accompanies them (Figure 4b,c), and the remainder of the dorsal nerve cord—evidently consisting entirely of ependymal glial cells—continues toward the tail tip as a filum terminale (FT in Figure 4c). According to Olsson (1955), the filum terminale of *Branchiostoma* consists entirely of glia without any neural elements and dilates into a conspicuous ampulla at the tip. In contrast, subsequent work by Soledad-Ruiz & Anadon (1991) showed that the *Branchiostoma* filum terminale has neurosecretory neurites running at the base of the glial cells. In the present study, we found neither a marked ampulla nor any neurosecretory neurites in the filum terminale of *Asymmetron*. Olsson (1955) also found a Reissner's fiber running within the neurocoel of *Branchiostoma*; however, if *Asymmetron* has a Reissner's fiber, it was not detectable in our low-resolution SBSEM.

3.5 | Glial cells of the PNS

The glial cells accompanying the PNS neurites in the dermis are derived from the neuropil of the dorsal nerve cord (section 3.4). Recent work on vertebrates also indicates that some of the PNS glial

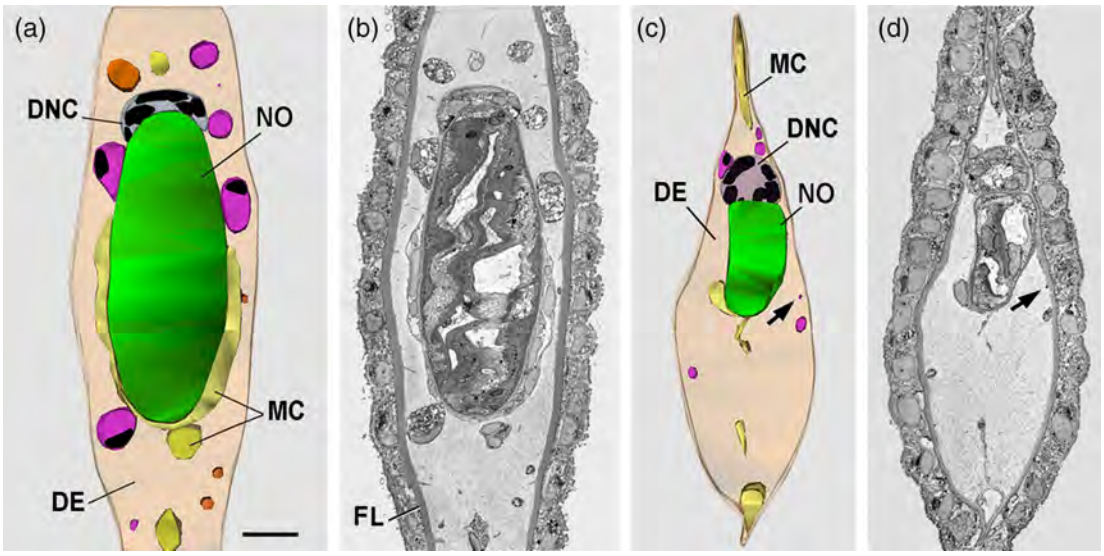

FIGURE 2 (a) Reconstruction of a 5-μm thick stack of SBSEM sections toward the anterior end of the sampled region, showing voluminous extracellular matrix of dermis (DE), dorsal nerve cord (DNC; semitransparent to show black nuclei), mesoderm cells (MC), and notochord (NO); epidermis is omitted. Peripheral nerves are semitransparent to show black nuclei; the orange nerves and pink nerves arise from the DNC, respectively, anterior and within the sampled region; scale line (also applicable to 2b–d) = 10 μm. (b) Single section midway in reconstruction a; the peripheral component of the dermis is the collagen fibril layer (FL). (c) Reconstruction of a 5-μm thick stack of SBSEM sections toward the posterior end of the sampled region; abbreviations are as in 2a; the arrow indicates a very small nerve. (d) Single section midway in reconstruction c; the arrow indicates a very small nerve [Color figure can be viewed at wileyonlinelibrary.com]

cells originate within the central nervous system (Suter & Jaworski, 2019) and not exclusively from neural crest as previously thought (Butler & Bronner, 2015). In the light of this more recent point of view, it seems likely that an intramedullary origin for PNS glia, as seen in cephalochordates, represents the ancestral condition in the phylum Chordata.

As already mentioned, the peripheral nerves running through the dermis (Figure 3a,b) are characterized by nuclei belonging to their glial and not their neural component. Each of the 68 glial cell nuclei enumerated here averages about 15 μm long and 3 μm wide. Low magnification SBSEM lacks the resolution to demonstrate the cytoplasmic boundaries between neighboring glial cells. However, the spacing of their nuclei—crowded in some places, but well spread out in others—suggests that the extent of their cytoplasm varies from one cell to the next. As a rough estimate, one can divide the total length of all the peripheral nerves sampled (5,745 μm) by the 68 nuclei to calculate an average cell length to be about 70 μm. That calculation assumes no overlap between neighboring glial cells; actually, such overlapping can occur, as demonstrated by Peters (1963).

Figure 5 shows the relation between glia and PNS neurites in SBSEM sections through the nuclear region of glial cells. Neurites (indicated by single arrows) are located in deep invaginations in the glial cytoplasm. The appearance of individual neurites varies from relatively lucent to very dense, and their diameters range mostly between 0.1 and 0.3 μm, although a few of the lucent variety can range up to about 1 μm. The number of neurites running in each invagination varies from one (Figure 5a) to half a dozen or more (Figure 5b). The surface of the glia-neurite complex is surrounded by a thin external lamina. In sum, at the fine-structural level, the glia/neurite complexes in the PNS of the *Asymmetron* tail closely resemble the association of neurites with nonmyelinated Schwann cells (Remak cells) of vertebrates (Harty & Monk, 2017), as was first demonstrated in cephalochordates for *Branchiostoma* by Peters (1963).

In *Asymmetron*, the peripheral nerves in the dermis ultimately connect with the epidermal component of the PNS (described in section 3.7). Our SBSEM lacks the resolution for determining whether extensions of glial cells accompany the neurites as they enter the epidermis. In vertebrates, glial extensions may accompany peripheral neurites into the epidermis, but only for a short distance (Whitear, 1983). In *Asymmetron*, the glial component evidently does not accompany PNS neurites very far after they enter the epidermis because TEM of *Branchiostoma* shows neurites without a glial sheath running between epidermal cells of embryos (Yasui, Tabata, Ueki, Uemura, & Zhang, 1998) and adults (Bereiter-Hahn, 1984).

3.6 | Peripheral nerves reaching the epidermis via fenestrae in the collagen fibril layer

The peripheral nerves exit from the dermis to the epidermis—either as *en passant* branches or at their posterior terminations (only a few end blindly within the dermis). The nerves traverse the collagen fibril layer at exit sites we will call fenestrae. In Figure 3a,b, the position of each fenestra is shown by an up- or down-pointing white arrow (in actual fact, each of them exits directly toward the viewer). We measured the diameters of the nerves passing through the 117 fenestrae on both

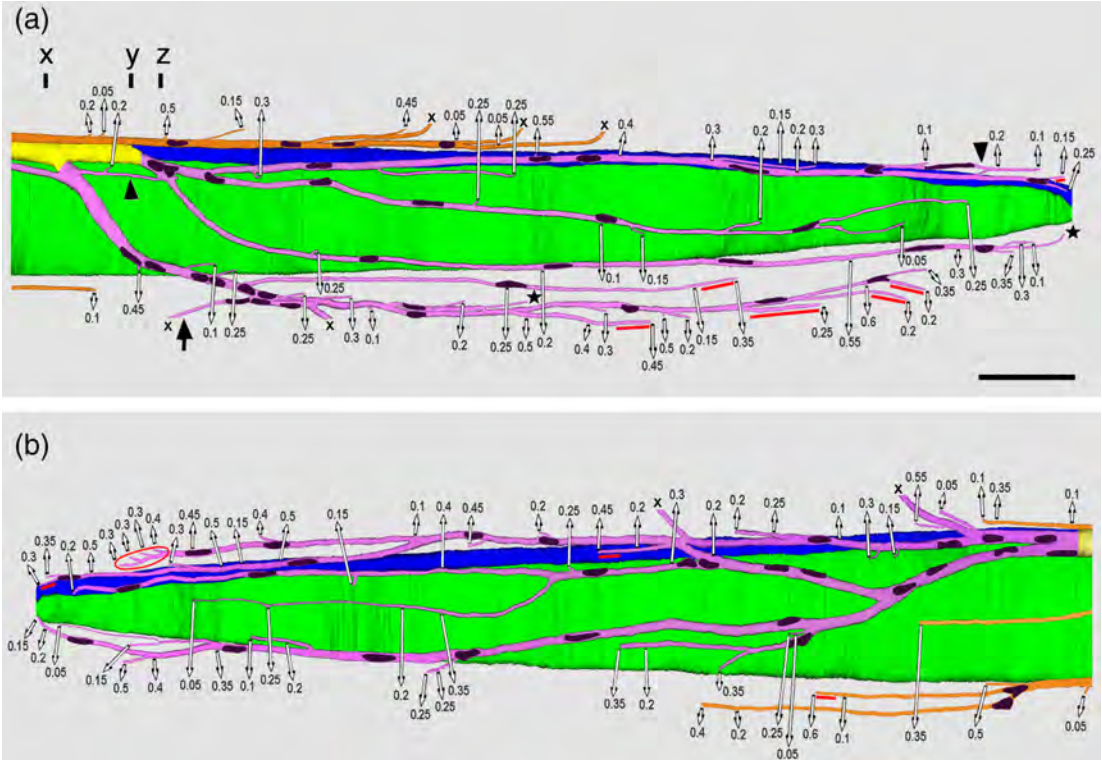

FIGURE 3 (a) Peripheral nerves on the left side of the region sampled (the rectangle in 1b). The truncation at the far right is due to the cutting away of the posterior 10 μm of the tail during orientation of the specimen for sectioning. The notochord is green, and the dorsal nerve cord with and without neuropil, respectively, is shown in yellow and blue. The peripheral nerves are semitransparent to show black nuclei of the glial cells. Peripheral nerves arising from the dorsal nerve cord anterior and within the region sampled by SBSEM are, respectively, orange and pink. Each white arrow marks where a branch or terminus of a peripheral nerve crosses the dermal–epidermal boundary by passing through fenestrae in the collagen fibril layer (for clarity, the arrows are shown pointing up or down, although each nerve actually exits toward the viewer). The number associated with each arrow is the diameter in micrometers of each fenestra. Segments of nerves underlined in red angle gradually within the fibril layer before exiting to the epidermis. Nerve branches extending too far dorsally or ventrally to remain in the field of view are indicated by an *x*. likely and definite anastomoses are indicated, respectively, by black arrow and arrowheads. Stars indicate nerve branches terminating blindly without passing into fenestrae. Scale line (also applicable to 3b) = 50 μm. (b) Peripheral nerves on the right side of the foregoing reconstruction. The colors and annotations are as explained for 3a (except the red oval, which indicates a whole cluster of nerves running as a group within the collagen fibril layer) [Color figure can be viewed at wileyonlinelibrary.com]

sides of the sampled tail region. The size distribution is shown graphically in Figure 6. The nerve diameters ranged from 0.05 to 0.60 μm with a mean of 0.27 μm (*SD* = 0.14). Previous information on nerves passing through fenestrae in adult cephalochordates is limited to a few fortuitously-cut TEM sections of *Branchiostoma* (Baatrup, 1981; Ruppert, 1997; Schulte & Riehl, 1977); the exiting nerves were larger than in *Asymmetron* (~1 μm in diameter), possibly due to species differences and/or to sampling different body regions.

In *Asymmetron*, the individual nerve passing through a given fenestra probably consists of several neurites and perhaps an extension of glial cell cytoplasm. If one considers the left side of the sampled region, each of the 66 fenestrae accommodates an average of 4 or 5 neurites (calculated from epidermal sensory cell densities given in section 3.7 below). The nerves entering the fenestrae in the collagen fibril layer follow one of two different trajectories. About 10% of the nerves enter the layer and then run within it for about 5–20 μm, gradually approaching its outer surface before exiting to the epidermis. Regions where nerves exit gradually through the fibril layer are indicated by red underlining in Figure 3a,b. A side view of such a nerve passing within the fibril layer is shown in 3D in Figure 7a, and a sequence of individual SBSEM cross-sections showing the passage is illustrated in Figure 7b–h. In contrast, most of the exiting nerves (~90%), pass abruptly and almost perpendicularly through the collagen fibril layer (Figure 8a–d). The data presented here are static, and only dynamic studies could determine whether the nerves in the fenestrae become passively immured thereby tissue growth and/or actively dissolve a channel through the extracellular material to reach the epidermis, as discussed for nerves in general by Seeds, Siconolfi, & Haffke (1997).

3.7 | Epidermal components of the PNS

Neurites with denser cytoplasm can be detected after entering the epidermis (Figure 8e, arrow). Figure 8f,g shows SBSEM-based 3D models of an exited peripheral nerve as it begins branching among adjacent epidermal cells. Because of the low resolution of our SBSEM,

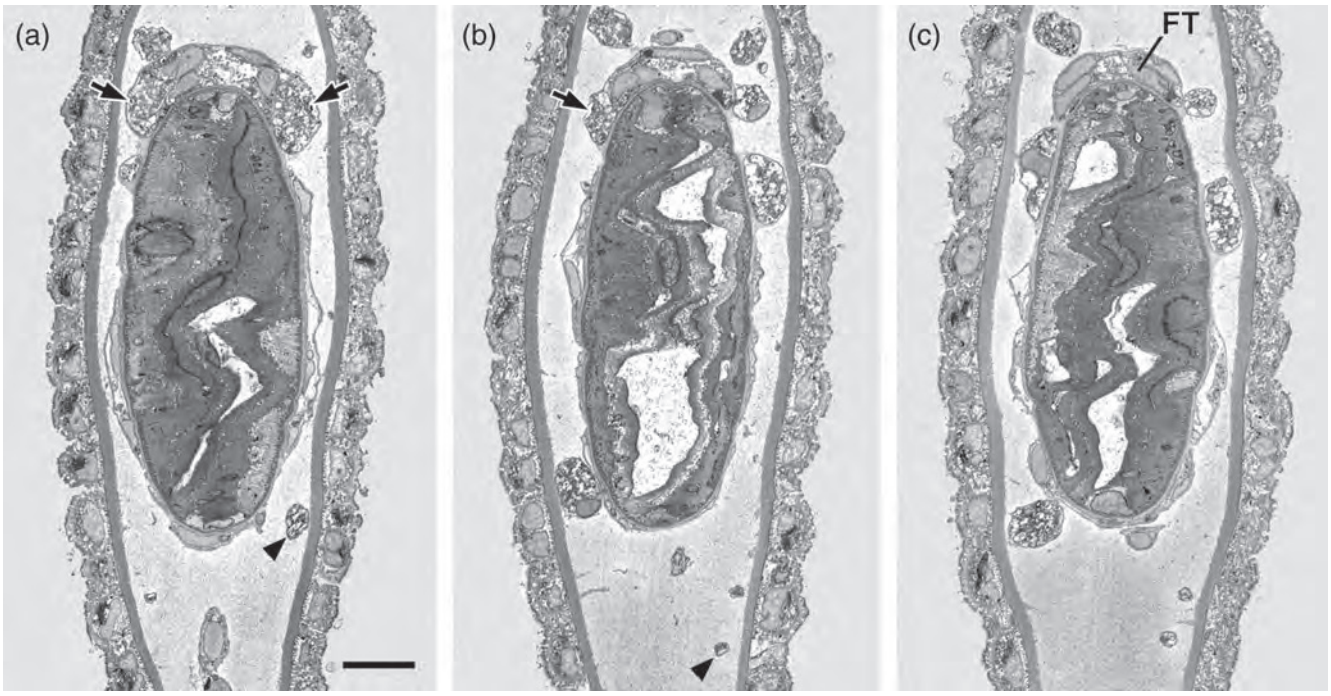

FIGURE 4 (a) Single SBSEM cross-section through Level *x* in 3a, showing neuropil associated with the left and right sides (arrows) of the dorsal nerve cord; the arrowhead indicates a peripheral nerve running right next to the fibril layer; scale line (also applicable to 4b, c) = 10 μm. (b) Cross-section through Level *y* in 3a, showing neuropil (arrow) associated with only left side of dorsal nerve cord; the arrowhead indicates a peripheral nerve running in the dermal matrix a little separated from the fibril layer. (c) Cross-section through Level *z* in 3a showing the nerve cord, now a filum terminale (FT) without any neuropil

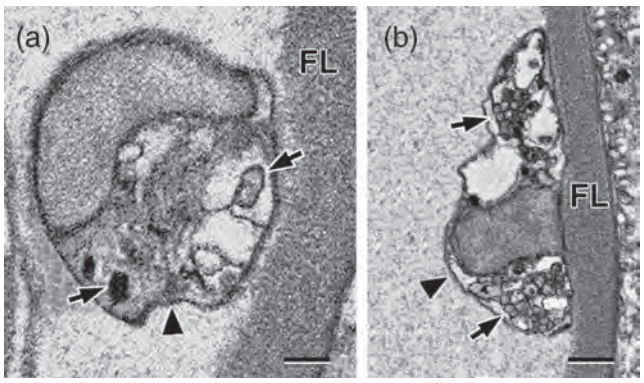

FIGURE 5 Cross-section of a peripheral nerve through the nuclear region of a glial cell adjacent to the collagen fibril layer (FL); the glial cell/neurite complex is surrounded by an external lamina (arrowhead). (a) Single neurites (single arrows) occupy invaginations in the relatively lucent cytoplasm of the glial cell. Scale line = 0.5 μm. (b) Small bundles of neurites (single arrows) occupy invaginations in the glial cell cytoplasm. Scale line = 1 μm

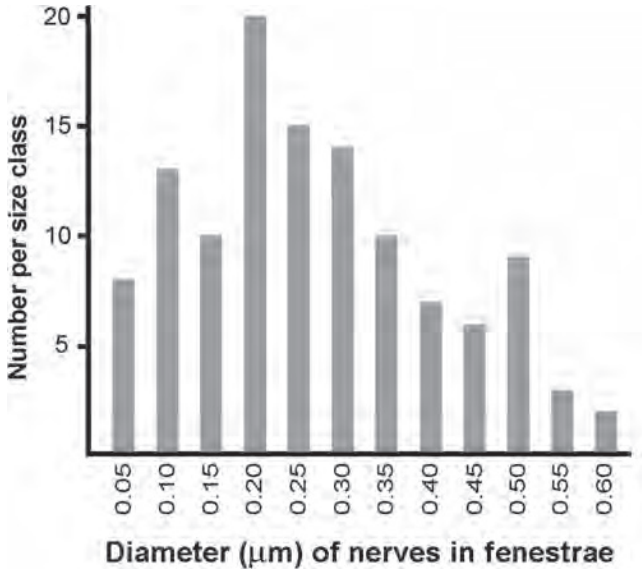

FIGURE 6 Size-frequency distribution of the diameter of nerves of the PNS as they exit through fenestrae in the collagen fibril layer. The data were gathered for all the nerves traversing fenestrae on the left and right sides in tail region illustrated in 3a,b

we could not follow the branches very far. These branches are presumably the neurites of the Retzius bipolar cells that arborize among the epidermal cells (Demski, Beaver, & Morrill, 1996; Kutchin, 1913). It has been suggested by Bone (1959) and by Demski, Beaver, & Morrill (1996) that the Retzius bipolar cells could be homologous to the Rohon-Beard cells of vertebrates (Reyes, Haendel, Grant, Malancon, & Eisen, 2003; Rovainen, 1982).

The epidermal part of the cephalochordate PNS also includes the perikarya of sensory cells. The two chief kinds of sensory cells were designated Type I and Type II in *Branchiostoma* by Schulte & Riehl (1977). The apices of both are narrow and give rise to a single

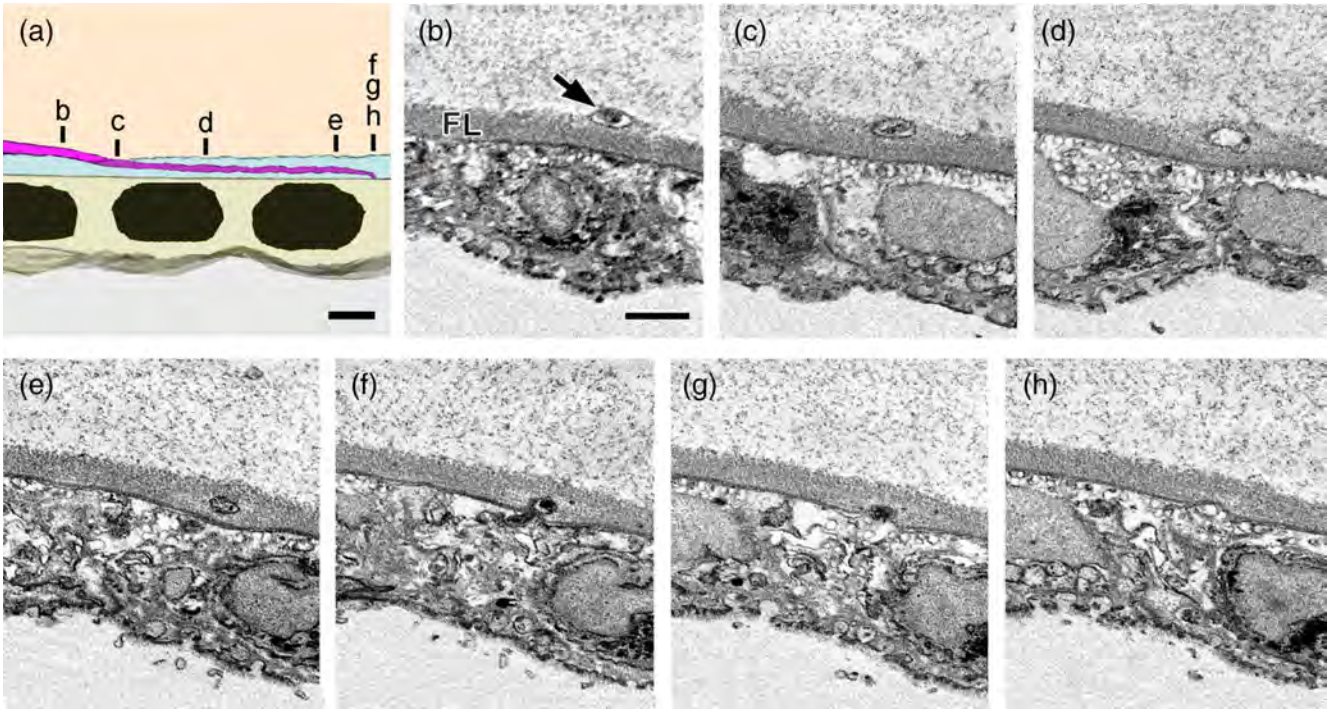

FIGURE 7 (a) SBSEM reconstruction of a region where a peripheral nerve (pink) angles slowly for about 10 μm within the collagen layer (light blue) before entering the epidermis (light yellow). Lower case letters correspond to the cross-sections in 7b–h; scale line = 2 μm. (b) Single SBSEM cross-section of a peripheral nerve (arrow) just before it enters the collagen fibril layer (FL); scale line (also applicable to 7c–h) = 2 μm. (c–h) Series of SBSEM sections showing the foregoing nerve running within the collagen fibril layer at a shallow angle and then exiting to the epidermis [Color figure can be viewed at wileyonlinelibrary.com]

cilium, thus contrasting with the broad, nonciliated, polygonal surfaces of the general epidermal cells. We found the same two cell types in *Asymmetron* (Figure 9a–i).

In Type I sensory cells, the apical cilium is roughly 10 μm long and arises within a ring of microvilli that extend only slightly above the general surface of the epidermis (Figure 9c–e). Previous work on *Branchiostoma* has demonstrates that the perikaryon of each Type I cell belongs to a primary sensory neuron in that its basal axon passes through a fenestra in the collagen fibril layer (Baatrup, 1981; Lacalli & Hou, 1999), traverses the dermis, and enters the dorsal nerve cord (Holland & Yu, 2002). Presumably the Type I cells of *Asymmetron* are similar, but SBSEM at low magnification cannot trace their single, fine neurite.

In Type II sensory cells, the apical cilium is about 4 μm long and has a slightly swollen tip. The basal half of the cilium is surrounded by long, crowded microvilli in a conspicuous cluster (Figure 9f–h). In *Branchiostoma*, Type II cells produce short axons that synapse with neurites—presumably of Retzius bipolar cells, although this important point still needs to be convincingly demonstrated. At least some Type II cells send their axon through a fenestra to synapse in the dermis just beneath (Lacalli & Hou, 1999), although other Type II cells probably form a synapse within the epidermis itself (as considered in section 3.8).

3.8 | Spatial relations of sensory cells and fenestrae; birth of sensory cells in pairs

The spatial patterns of epidermal sensory cells and fenestrae were evaluated by calculating indices of aggregation from nearest neighbor measurements. Indices of aggregation can range from zero (no spacing at all, meaning that all the objects are in a single stack), through unity (random spacing), to a value of 2.15, which describes maximum spacing (which would be a regular hexagonal array). The index of aggregation for the fenestrae was 1.03, which would be expected for a distribution that is neither markedly clumped nor markedly regular.

In contrast, the index of aggregation for the sensory cells was 1.27, indicating a weak tendency toward regular spacing. At first glance, it is surprising that the index is not higher because conventional SEM (Figure 9b) gives one the impression that the epidermal sensory cells are quite regularly distributed. However, when we gathered nearest-neighbor data from high-magnification SEM, we discovered several instances where pairs of nascent sensory cells were arising immediately adjacent to one another (Figure 9i); these pairings resulted in a lowering of the overall index of aggregation. Interestingly, one member of each pair was a Type I cell (with its cilium still in the process of formation) and the other was a Type II cell. This finding

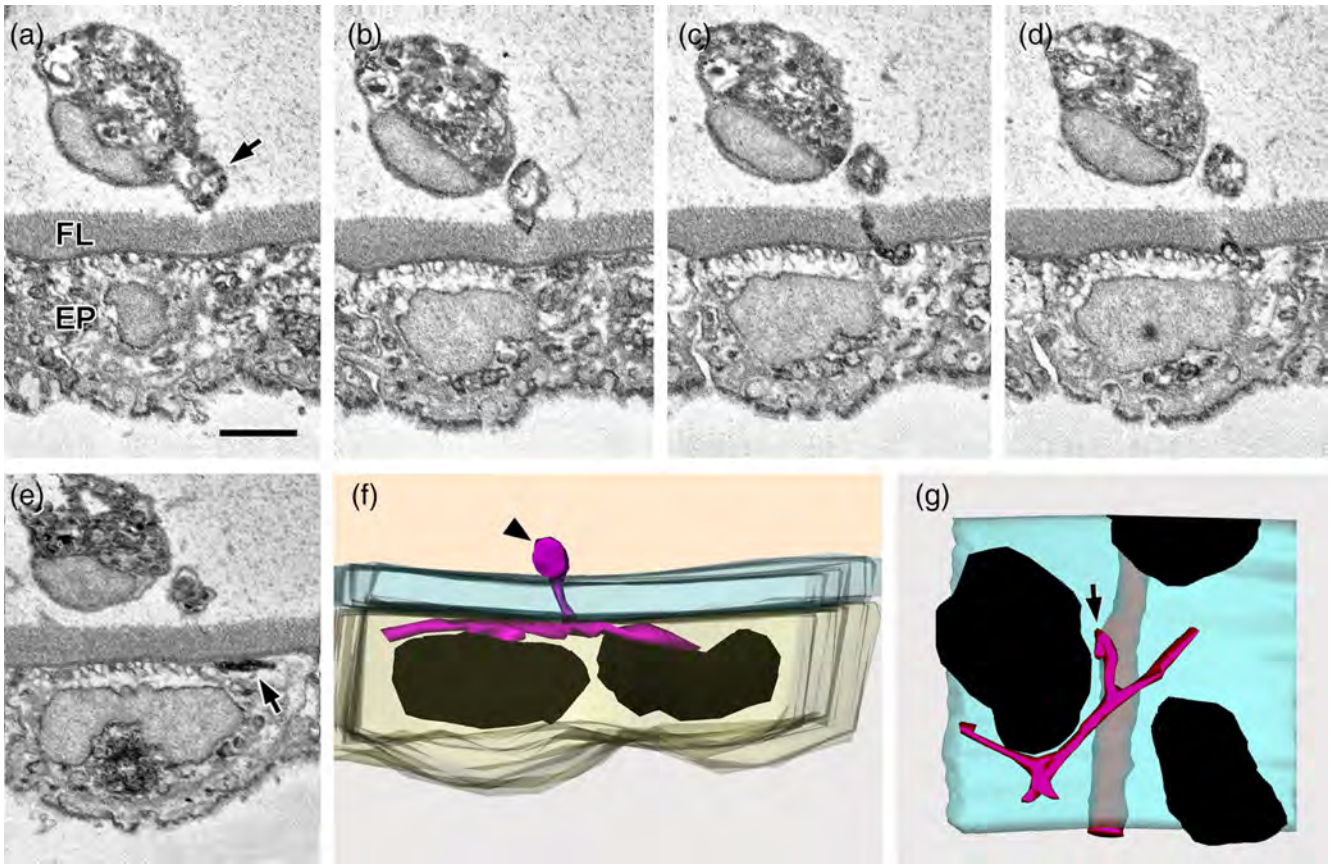

FIGURE 8 (a) Single SBSEM cross-section showing peripheral nerve branch (arrow) shortly before it abruptly projects through the collagen fibril layer (FL) to reach the epidermis (EP). Scale line (also applicable to 8b–g) = 2 μm. (8b–d) Successive SBSEM cross-sections at 0.25-μm intervals show branch of peripheral nerve (arrow) abruptly penetrating fibril layer to enter the epidermis. (e) Cross-section 1 μm posterior to 8d; a short section of a dark peripheral nerve (arrow) is visible in the epidermis. (f) SBSEM reconstruction of a region spanning the previous cross-sections; the peripheral nerve (arrowhead) running in dermal matrix produces a projection that abruptly crosses the collagen fibril layer (light blue) to enter the epidermis (light yellow). (g) Previous illustration viewed from the epidermal side; the arrow indicates where a branch of the peripheral nerve crosses from the dermis, via a fenestra in the collagen fibril layer, and enters the epidermis [Color figure can be viewed at wileyonlinelibrary.com]

in *Asymmetron* is not without precedent: Lacalli and Hou (1999), in their study of a late metamorphic specimen of *Branchiostoma*, previously found Type I + Type II cell pairs in the epidermis. Although some kinds of hair cells in vertebrates are well known to arise as mirror-image pairs (Ghysen & Dambly-Chauère, 2007; Rouse & Pickles, 1991), the apparent production of two strikingly distinctive cell types, presumably from a single precursor, is quite uncommon. Lacalli and Hou (1999) tentatively suggested that the cephalochordate epidermis might include a pool of dividing, neural precursor cells differentiating into definitive sensory cells that ultimately degenerate and require replacement. Certainly, much more needs to be learned about the epidermal sensory cells: their detailed cell kinetics, their possible degeneration/regeneration cycles, and their possible separation from one another by lateral migration in the plane of the epidermis.

When the SBSEM data for the distribution of Type I and Type II sensory cells were mapped onto the SBSEM data for the distribution of fenestrae, it was found that many of the Type I and Type II sensory cells were separated from the nearest fenestra by several to many epidermal cell diameters (Figure 10). Evidently, the axon arising from the base of a Type I sensory cell must often make a horizontal detour in the epidermis before reaching a fenestra, and the short axons of many Type II sensory cells must make synaptic contact with the ramifying nerves in the epidermis at considerable distances from the nearest fenestra. The notion that each epidermal sensory cell sends its axon directly into an underlying fenestra (Baatrup, 1981; Holland & Yu, 2002; Lacalli & Hou, 1999) was evidently an oversimplification.

4 | DISCUSSION

4.1 | A dense peripheral layer of dermis with fenestrae may be ancestral in chordates

In adult cephalochordates, there is a continuous, dense layer of orthogonally arranged collagen fibrils at the periphery of the dermis. To reach the epidermis, nerves of the PNS pass through the dense

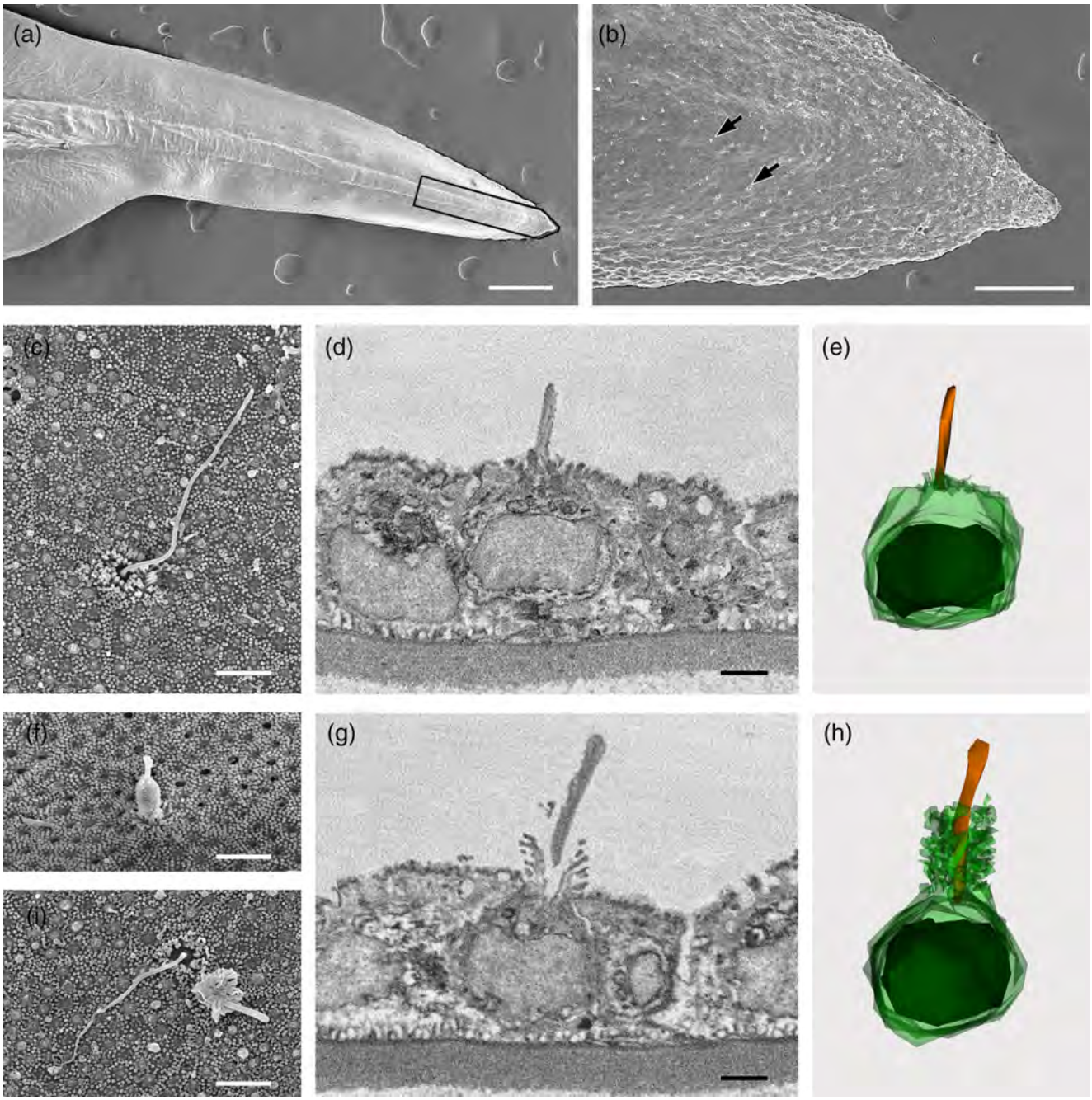

FIGURE 9 (a) Left-side view of the tail by conventional SEM; the region outlined in black in this specimen corresponds to the region studied in the SBSEM part of the present study; scale line = 250 μm. (b) Tip of tail by conventional SEM; arrows indicate two epidermal sensory cells; scale line = 50 μm. (c) Apex of Type I sensory cell surrounded by nonciliated epidermal cells; conventional SEM; scale line = 2 μm. (d) Single SBSEM section showing Type I sensory cell flanked by nonciliated epidermal cells; much of the distal part of the cilium is outside the plane of the section; scale line (also applicable to 9e) = 1 μm. (e) Type I sensory cell reconstructed in 3D from SBSEM sections. (f) Apex of Type II sensory cell surrounded by nonciliated epidermal cells; conventional SEM; scale line = 2 μm. (g) Single SBSEM section showing Type II sensory cell flanked by nonciliated epidermal cells; scale line (also applicable to 9h) = 1 μm. (h) Type II sensory cell reconstructed in 3D from SBSEM sections. (i) Adjacent apices of a pair of sensory cells (on the left Type I and on the right Type II); conventional SEM; scale line = 2 μm [Color figure can be viewed at wileyonlinelibrary.com]

collagen fibril layer in well-defined fenestrae. A similar collagen fibril layer is also the outermost component of the dermis in hagfishes (Clark, Crawford, King, Demas, & Ueno, 2016) and lampreys (Krause, 1923a; Johnels, 1950; Razzauti, 1916). The foregoing references illustrate fine branches of the PNS crossing the fibril layer to the epidermis in fenestrae that are straight or sparingly branched, depending on the body region. The collagen fibril layer of agnathans is considerably thicker than that of cephalochordates, but this is due, at least in part, to the much larger adult body sizes of the former.

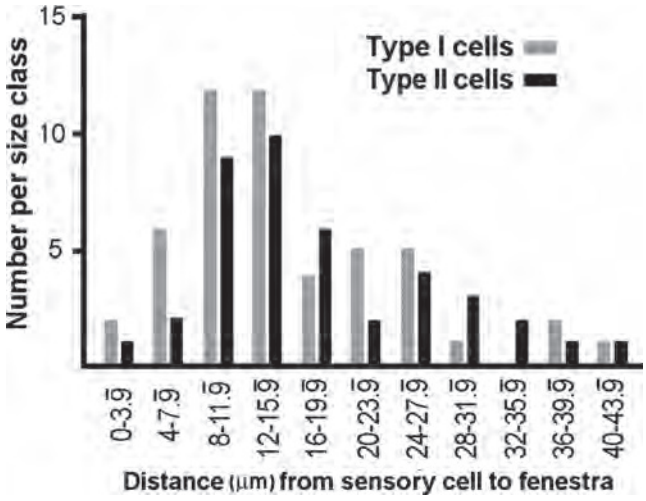

FIGURE 10 Comparing positions of epidermal sensory cells of Type I and Type II relative to the locations of the fenestrae. Data were gathered for both sides of the tail region studied. The graph shows the size-frequency distribution of the lateral distance (in μm) from the base of each epidermal sensory cell to the nearest fenestra in the collagen fibril layer. Each of the 4-μm distance intervals on the horizontal axis is roughly equivalent to one epidermal cell diameter

In teleosts, the dermis in scale-free regions is like that of hagfishes and lampreys in having a dense region of orthogonally arranged collagen fibrils as the most peripheral component of the dermis. In contrast, where scales are present, a loosely organized dermal region of scattered collagen fibrils and well-developed microvasculature overlies the dense collagen layer (Brown & Wellings, 1970; Le Guellec, Morvan-Dubois, & Sire, 2004; Nadol, Gibbins, & Porter, 1969). The elasmobranch dermis resembles the scaled dermal regions of teleosts in having a deep layer of orthogonally arranged collagen fibrils beneath a well-vascularized region with scattered collagen fibrils (Krause, 1923a; Meyer & Seegers, 2012; Motta, 1977). For elasmobranchs, Krause (1923a) illustrates a large nerve (about 25 μm in diameter) crossing the dense collagen layer and then breaking up into a network of smaller nerves ramifying among the overlying loose weave of collagen fibrils to reach the epidermis. The elasmobranch pattern is also seen in the dermis of amphibians and birds in which the dermis consists of a loosely organized layer overlying a dense collagen fibril layer (Krause, 1922, 1923b). In reptiles (Rutland, Cigler, & Kubale, 2019) and mammals (Kanitakis, 2001), the distinction between the superficial (papillary) dermis and the deeper (reticular) dermis is less conspicuous than in other vertebrates, and neither zone includes a dense orthogonally organized collagenous layer. In both the papillary and reticular dermis, the collagen fibrils tend to be bundled together into stouter fibers loosely organized into a mesh, and the peripheral nerves ramify through the rather spacious interstices in this mesh (Krause, 1921; Reinisch & Tschachler, 2012).

The foregoing review suggests that a dense peripheral collagen layer penetrated by fenestrae for passage of the PNS, as seen in cephalochordates and lower vertebrates, is a basal chordate feature that has tended to be lost in more advanced vertebrates. Presumably, this ancestral chordate pattern was also present in the common ancestor of tunicates and vertebrates, but disappeared during tunicate evolution. Tunicates have lost all trace of a collagenous dermis, probably as a consequence of acquiring bacterial cellulose synthase through horizontal gene transfer (Sasakura, 2018) and evolving cellulose skeletons for body support—intraepidermally in appendicularians and supraepidermally in ascidians (Hirose et al., 2011).

4.2 | Comparing likely homologies for the sensory PNS among major chordate groups

The present discussion will be limited to the sensory PNS because our work on *Asymmetron* did not include a motor component, which in cephalochordates is limited to more anterior regions—for example, the efferent innervation of the pterygial muscles (Bone 1961). Moreover, the motor PNS is not prominent in cephalochordates because the trunk musculature synapses directly on the surface of the central nervous system (Ruppert, 1997). When one compares the sensory PNS of cephalochordates and vertebrates, the most likely homology is between neurons with intramedullary perikarya; namely, the Retzius bipolar cells of the former and the Rohon-Beard cells of the latter. On the other hand, a comparison of the *extra*medullary sensory neurons of cephalochordates and vertebrates reveals few similarities. The placode-derived sensory neurons of vertebrates (with the possible exception of the olfactory nerves) have little in common with the epidermal sensory neurons of cephalochordates (Schlosser, 2017). Moreover, the major contribution of neural crest to the vertebrate PNS (Pendergast & Raible, 2014) has no counterpart in cephalochordates.

It is particularly interesting to relate the sensory PNS of tunicates to that of other chordates. The tunicate PNS appears unique in several respects. For example, tunicates, in contrast to other chordates, have no glial cell component in the PNS (Hartenstein & Giangrande, 2018; Olsson, 1998). In addition, tunicates lack sensory neurons with intramedullary perikarya homologous to either the Retzius bipolar cells of cephalochordates or the Rohon-Beard cells of vertebrates (Glover & Fritzsch, 2009). Consequently, the nerve endings that ramify among the epidermal cells of cephalochordates and vertebrates are lacking in tunicates.

In spite of the striking differences mentioned above, the extramedullary part of the sensory PNS of tunicates is comparable to that of vertebrates in some ways and to that of cephalochordates in other ways. This is due to what Hartenstein (2019) aptly refers to as the "chimeric" nature of the extramedullary PNS in larval tunicates. Many of the epidermal sensory neurons of larval ascidians derive from the neural plate boundary and have a molecular fingerprint resembling that of vertebrate neural crest and sensory placodes. In contrast, however, the epidermal sensory neurons along the ventral side of the tunicate tail develop under genetic controls broadly similar to those directing the differentiation of the epidermal sensory neurons of cephalochordates (Waki, Imai, & Satou, 2015). Thus, the extramedullary sensory PNS of tunicates consists of a mixture of cephalochordate-like and vertebrate-like features.

In sum, during the evolution of the sensory PNS of chordates, it is likely that the component with intramedullary perikarya (Retzius

bipolar cells) in cephalochordates carried forward into vertebrates as Rohon-Beard cells. In contrast, the extramedullary component originating from ventral epidermis of cephalochordates was evidently replaced completely by sensory neurons derived from neural crest and placodes by time the earliest vertebrates appeared.

ACKNOWLEDGMENTS

Personnel at the Bimini Biological Field Station (Sharklab) helped collect *Asymmetron*; Greg Rouse photographed the living lancelet; Kimberly Vanderpool (Scripps Research Institute, La Jolla) helped with conventional SEM; and Jennifer Santini and Marcella Erb of the UCSD School of Medicine Microscopy Core assisted with the SBSEM procedures. The SBSEM facility and staff support are funded by the UCSD School of Medicine Microscopy Core Grant P30 NS047101. Cephalochordate research at SIO is supported by NSF Grant Number IOS 1353688. Our text was much improved by the critical comments of Linda Holland and Thurston Lacalli.

CONFLICT OF INTEREST

None declared.

DATA AVAILABILITY STATEMENT

Files supporting the findings of this study are available from the corresponding author upon reasonable request.

ORCID

Nicholas D. Holland https://orcid.org/0000-0002-3448-490X

REFERENCES

Andrews, E. A. (1893). An undescribed acraniate: *Asymmetron lucayanum*. *Studies from the Biological Laboratory, Johns Hopkins University*, *5*, 213–247.

Baatrup, E. (1981). Primary sensory cells in the skin of amphioxus (*Branchiostoma lanceolatum*) (Cephalochordata). *Acta Zoologica Stockholm*, *62*, 147–157.

Balfour, F. M. (1885). *Comparative embryology* (Vol. 2). London: MacMillan.

Bereiter-Hahn, J. (1984). Cephalochordata. In J. Bereiter-Hahn, A. G. Matoltsy, & K. S. Richards (Eds.), *Biology of the integument; volume I, invertebrates* (pp. 817–825). Berlin: Springer.

Bone, Q. (1959). The central nervous system in larval acraniates. *Quarterly Journal of Microscopical Science*, *100*, 509–527.

Bone, Q. (1961). The organization of the atrial nervous system of amphioxus (*Branchiostoma lanceolatum* [Pallas]). *Philosophical Transactions of the Royal Society B*, *243*, 241–269.

Borrett, S., & Hughes, L. (2016). Reporting methods for processing and analysis of data from serial block face scanning electron microscopy. *Journal of Microscopy*, *263*, 3–9.

Braet, F., De Zanger, R., & Wisse, E. (1997). Drying cells for SEM, AFM, and TEM by hexamethyldisilazane: A study on hepatic endothelial cells. *Journal of Microscopy*, *186*, 84–87.

Brown, G. A., & Wellings, S. R. (1970). Electron microscopy of the skin of the teleost, *Hippoglossoides elassodon*. *Zeitschrift für Zellforschung*, *103*, 149–169.

Butler, S. J., & Bronner, M. E. (2015). From classical to current: Analyzing peripheral and spinal cord lineage and fate. *Developmental Biology*, *398*, 135–146.

Clark, A. J., Crawford, C. H., King, B. D., Demas, A. M., & Uyeno, T. A. (2016). Material properties of hagfish skin, with insights into knotting behaviors. *Biological Bulletin*, *230*, 243–256.

Deerinck, T. J., Bushong, E. A., Lev-Ram, V., Tsien, R. Y., & Ellisman, M. H. (2010). Enhancing serial block-face scanning electron microscopy to enable high resolution 3-D nanohistology of cells and tissues. *Microscopy and Microanalysis*, *16*(Suppl S2), 1138–1139.

Demski, L. S., Beaver, J. A., & Morrill, J. B. (1996). The cutaneous innervation of amphioxus: A review incorporating new observations with DiI tracing and scanning electron microscopy. *Israel Journal of Zoology*, *42* (Suppl), 117–129.

Denk, W., & Horstmann, H. (2004). Serial block-face scanning electron microscopy to reconstruct three-dimensional tissue nanostructure. *PLoS Biology*, *2*(11), e329.

Dogiel, A. S. (1903). Das periphere Nervensystem des Amphioxus (*Branchiostoma lanceolaum*). *Anatomische Hefte (Erste Abteilung)*, *21*, 145–213.

Donnelly, K. P. (1978). Simulations to determine the variance and edge effect of total nearest-neighbor distance. In L. Hodder (Ed.), *Simulation studies in archaeology* (pp. 91–95). Cambridge: Cambridge University Press.

Fiala, J. C. (2005). *Reconstruct*: A free editor for serial section microscopy. *Journal of Microscopy*, *218*, 52–61.

Fritzsch, B., & Northcutt, R. G. (1993). Cranial and spinal nerve organization in amphioxus and lampreys: Evidence for an ancestral craniate pattern. *Acta Anatomica*, *148*, 96–109.

Fusari, R. (1889). Contribution à l'étude du système nerveux périphérique de l'*Amphioxus lanceolatus*. *Archives Italiennes de Biologie*, *11*, 237–242.

Ghysen, A., & Dambly-Chauère, C. (2007). The lateral line microcosmos. *Genes & Development*, *21*, 2118–2130.

Glover, J. C., & Fritzsch, B. (2009). Brains of primitive chordates. In L. R. Squire (Ed.), *Encyclopedia of neuroscience* (1st ed., pp. 439–448). Amsterdam: Elsevier.

Hartenstein, V. (2019). Development of nervous systems of invertebrates. In J. H. Byrne (Ed.), *The Oxford handbook of invertebrate neurobiology* (pp. 1–88). Oxford: Oxford University Press.

Hartenstein, V., & Giangrande, A. (2018). Connecting the nervous and immune systems in evolution. *Communications Biology*, *1*(64), 64.

Harty, B. L., & Monk, K. R. (2017). Unwrapping the unappreciated: Recent progress in Remak Schwann cell biology. *Current Opinion in Neurobiology*, *47*, 131–137.

Heymans, J. F., & van der Stricht, O. (1898). Sur le système nerveux de l'amphioxus et en particular sur la constitution et la genèse des racines sensibles. *Mémoires Couronées et Mémoires Des Savants Étrangers Academie Royale Des Sciences, Des Leteres et Des Beaux-Arts de Belgique*, *56*(3), 1–74.

Hirose, E., Nakashima, K., & Nishino, A. (2011). Is there intracellular cellulose in the appendicularian tail epidermis? A tale of the adult tail of an invertebrate chordate. *Communicative & Integrative Biology*, *4*, 768–771.

Holland, L. Z. (2009). Chordate roots of the vertebrate nervous system: Expanding the molecular toolkit. *Nature Reviews Neuroscience*, *10*, 736–746.

Holland, N. D. (2011). Spawning periodicity of the lancelet, *Asymmetron lucayanum* (Cephalochordata), in Bimini, Bahamas. *The Italian Journal of Zoology*, *78*, 478–486.

Holland, N. D. (2018). Formation of the initial kidney and mouth opening in larval amphioxus studied with serial blockface scanning electron microscopy (SBSEM). *EvoDevo*, *9*, 16.

Holland, N. D., Panganiban, G., Henyey, E. L., & Holland, L. Z. (1996). Sequence and developmental expression of *AmphiDll*, an amphioxus *Distal-less* gene transcribed in the ectoderm, epidermis and nervous

system: Insights into evolution of craniate forebrain and neural crest. *Development*, *122*, 2911–2920.

Holland, N. D., & Yu, J. K. (2002). Epidermal receptor development and sensory pathways in vitally stained amphioxus (*Branchiostoma floridae*). *Acta Zoologica Stockholm*, *83*, 309–319.

Johnels, A. G. (1950). On the dermal connective tissue of the head of *Petromyzon*. *Acta Zoologica Stockholm*, *31*, 177–185.

Johnston, J. B. (1905). The cranial and spinal ganglia of the viscero-motor roots in amphioxus. *Biological Bulletin*, *9*, 112–127.

Kaltenbach, S. L., Yu, J. K., & Holland, N. D. (2009). The origin and migration of the earliest-developing sensory neurons in the peripheral nervous system of amphioxus. *Evolution & Development*, *11*, 142–151.

Kanitakis, J. (2001). Anatomy, histology and immunochemistry of human skin. *European Journal of Dermatology*, *12*, 390–399.

Krause, R. (1921). Säugetiere. In *Mikroskopische Anatomie der Wirbeltiere in Einzeldarstellungen* (Vol. I). Berlin: De Gruyter.

Krause, R. (1922). Vögel und Reptilien. In *Mikroskopische Anatomie der Wirbeltiere in Einzeldarstellungen* (Vol. II). Berlin: De Gruyter.

Krause, R. (1923a). Teleostier, Plagiostomen, Zyklostomen und Leptokardier. In *Mikroskopische Anatomie der Wirbeltiere in Einzeldarstellungen* (Vol. IV). Berlin: De Gruyter.

Krause, R. (1923b). Amphibien. In *Mikroskopische Anatomie der Wirbeltiere in Einzeldarstellungen* (Vol. III). Berlin: De Gruyter.

Kutchin, H. L. (1913). Studies on the peripheral nervous system of amphioxus. *Proceedings of the American Academy of Arts & Sciences*, *49*, 571–624.

Lacalli, T. C., & Hou, S. F. (1999). A reexamination of the epithelial sensory cells of amphioxus (*Branchiostoma*). *Acta Zoologica Stockholm*, *80*, 125–134.

Langerhans, P. (1876). Zur Anatomie des *Amphioxus lanceolatus*. *Archiv für Mikroskopische Anatomie*, *12*, 290–348.

Le Guellec, D., Morvan-Dubois, G., & Sire, J. Y. (2004). Skin development in bony fish with particular emphasis on collagen deposition in the dermis of the zebrafish (*Danio rerio*). *International Journal of Developmental Biology*, *48*, 217–231.

Lele, P. P., Palmer, E., & Weddell, G. (1958). Observations on the integument of amphioxus, *Branchiostoma lanceolatum*. *Quarterly Journal of Microscopical Science*, *99*, 421–440.

Lu, T. M., Luo, Y. J., & Yu, J. K. (2012). BMP and Delta/notch signaling control the development of amphioxus epidermal sensory neurons: Insights into the evolution of the peripheral nervous system. *Development*, *139*, 2020–2030.

Meyer, W., & Seegers, U. (2012). Basics of skin structure and function in elasmobranchs: A review. *Journal of Fish Biology*, *80*, 1940–1967.

Motta, F. J. (1977). Anatomy and functional morphology of dermal collagen fibers in sharks. *Copeia*, *1977*, 454–464.

Nadol, J. B., Gibbins, J. R., & Porter, K. R. (1969). A reinterpretation of the structure and development of the basement lamella: An ordered array of collagen in fish skin. *Developmental Biology*, *20*, 304–331.

Olsson, R. (1955). Structure and development of Reissner's fibre in the caudal end of amphioxus and some lower vertebrates. *Acta Zoologica Stockholm*, *38*, 167–198.

Olsson, R. (1998). Reissner's fiber mechanisms: Some common denominators. In A. Oksche, E. M. Rodriguez, & P. Fernández-Llebrez (Eds.), *The subcommissural organ: An ependymal brain gland* (pp. 33–39). Berlin: Springer.

Peddie, C. J., & Collinson, L. M. (2014). Exploring the third dimension: Volume electron microscopy comes of age. *Micron*, *61*, 9–19.

Pendergast, A., & Raible, D. W. (2014). Neural crest cells and peripheral nervous system development. In P. A. Trainor (Ed.), *Neural crest cells: Evolution, development, and disease* (pp. 255–286). Amsterdam: Elsevier.

Peters, A. (1963). The structure of the dorsal root nerves of amphioxus. An electron microscope study. *Journal of Comparative Neurology*, *121*, 287–304.

Razzauti, A. (1916). Struttura del tegmento dei petromizonti: nervi ed organi cutanei del senso. *Archivio Italiano di Anatomia e di Embriologia*, *15*, 1–63.

Reichert, C. B. (1870). Zur Anatomie des *Branchiostoma lubricum*. *Archiv für Anatomie, Physiologie Und Wissenschaftliche Medicin*, *1870*, 755–758.

Reinisch, C. M., & Tschachler, E. (2012). The dimensions and characteristics of the subepidermal nerve plexus in human skin—Terminal Schwann cells constitute a substantial cell population within the superficial dermis. *Journal of Dermatological Science*, *65*, 162–169.

Retzius, G. (1898). Die Methyleneblaufärbung bei dem lebenden Amphioxus. *Biologische Untersuchungen, Neue Folge*, *8*, 118–122.

Reyes, R., Haendel, M., Grant, D., Melancon, E., & Eisen, J. S. (2003). Slow degeneration of zebrafish Rohon-beard neurons during programmed cell death. *Developmental Dynamics*, *229*, 30–41.

Rohon, J. V. (1882). Untersuchungen über *Amphioxus lanceolatus*. Ein Beitrag zur vergleichenden Anatomie der Wirbelthiere. *Denkschriften der Kaiserlichen Akademie der Wissenschaften, Wien, Mathematisch-Naturwissenschaftliche Classe*, *42*(2), 1–64.

Rouse, G. W., & Pickles, J. O. (1991). Paired development of hair cells in neuromasts of the teleost lateral line. *Proceedings of the Royal Society B*, *246*, 123–128.

Rovainen, C. M. (1982). Neurophysiology. In M. W. Hardisty & I. V. Potter (Eds.), *The biology of lampreys* (Vol. 4A, pp. 1–136). London: Academic Press.

Ruppert, E. E. (1997). Cephalochordata (Acrania). In F. W. Harrrison & E. E. Ruppert (Eds.), *Microscopic anatomy of invertebrates; volume 15, Hemichordata, Chaetognatha, and the invertebrate chordates* (pp. 349–504). New York: Wiley-Liss.

Rutland, C. S., Cigler, P., & Kubale, V. (2019). Reptilian skin and its special histological features. In C. Rutland & V. Kubale (Eds.), *Veterinary anatomy and physiology (no pagination)*. Vienna: IntechOpen.

Sasakura, Y. (2018). Cellulose production and the evolution of the sessile lifestyle in ascidians. *Sessile Organisms*, *35*, 21–29.

Schlosser, G. (2017). From so simple a beginning—What amphioxus can teach us about placode evolution. *International Journal of Developmental Biology*, *61*, 633–648.

Schulte, E., & Riehl, R. (1977). Elektronmicroskopische Untersuchungen an den Oralcirren und der Haut von *Branchiostoma lanceolatum*. *Helgoländer Wissenschaftliche Meeresuntersuchungen*, *29*, 337–357.

Seeds, N. W., Siconolfi, L. B., & Haffke, S. P. (1997). Neuronal extracellular proteases facilitate cell migration, axonal growth, and pathfinding. *Cell and Tissue Research*, *290*, 367–370.

Soledad-Ruiz, M., & Anadon, R. (1991). Ultrastructural study of the filum terminale and caudal ampulla of the spinal cord of amphioxus (*Branchiostoma lanceolatum* Pallas). *Acta Zoologica Stockholm*, *72*, 63–71.

Studnicka, F. K. (1909). Vergleichende Untersuchungen über die Epidermis der Vertebraten. *Anatomische Hefte*, *39*(issue 1), 1–267.

Suter, T. A. C. S., & Jaworski, A. (2019). Cell migration and axon guidance at the border between central and peripheral nervous system. *Science*, *365*, eaaw8231.

Titze, B., & Genoud, C. (2016). Volume scanning electron microscopy for imaging biological ultrastructure. *Biology of the Cell*, *108*, 307–323.

Waki, K., Imai, K. S., & Satou, Y. (2015). Genetic pathways for differentiation of the peripheral nervous system of ascidians. *Nature Communications*, *6*, 8719.

Wanner, A. A., Genoud, C., & Friedrich, R. W. (2016). 3-dimensional electron microscopic imaging of the zebrafish olfactory bulb and dense reconstruction of neurons. *Scientific Data*, *3*, 160100.

Welsch, U. (1968). Beobachtungen über die Feinstruktur der Haut und des äusseren Atrialepithels von *Branchiostoma lanceolatum* Pall. *Zeitschrift für Zellforschung*, *88*, 565–575.

Whitear, M. (1983). The question of free nerve endings in the epidermis of lower vertebrates. *Acta Biologica Hungarica*, *34*, 303–319.

Yasui, K., Tabata, S., Ueki, T., Uemura, M., & Zhang, S. C. (1998). Early development of the peripheral nervous system in a lancelet species. *Journal of Comparative Neurology*, *393*, 414–425.

Zieger, E., Garbarino, G., Robert, N. S. M., Yu, J. K., Croce, J., Candiani, S., & Schubert, M. (2018). Retinoic acid signaling and neurogenic niche regulation in the developing peripheral nervous system of the cephalochordate amphioxus. *Cellular and Molecular Life Sciences*, *75*, 2407–2429.

environmental microbiology

Environmental Microbiology (2021) **23**(11), 6569–6586 doi:10.1111/1462-2920.15766

Subcellular architecture and metabolic connection in the planktonic photosymbiosis between Collodaria (radiolarians) and their microalgae

Johan Decelle[1,2*] **Giulia Veronesi**[3,4,5,6] **Charlotte LeKieffre**[1] **Benoit Gallet**[7] **Fabien Chevalier**[1] **Hryhoriy Stryhanyuk**[2] **Sophie Marro**[8] **Stéphane Ravanel**[1] **Rémi Tucoulou**[6] **Nicole Schieber**[9] **Giovanni Finazzi**[1] **Yannick Schwab**[9] **and Niculina Musat**[2]

[1]*Univ. Grenoble Alpes, CNRS, CEA, INRAe, IRIG-LPCV, Grenoble, France.*

[2]*Department of Isotope Biogeochemistry, Helmholtz Centre for Environmental Research – UFZ, Leipzig, Germany.*

[3]*CNRS, Laboratoire de Chimie et Biologie des Métaux (LCBM), UMR 5249 CNRS-CEA-UGA, F-38054, Grenoble, France.*

[4]*CEA, LCBM, F-38054, Grenoble, France.*

[5]*Université Grenoble Alpes, LCBM, F-38054, Grenoble, France.*

[6]*ESRF, The European Synchrotron, 71, Avenue des Martyrs, 38043, Grenoble, France.*

[7]*Institut de Biologie Structurale (IBS), University Grenoble Alpes, CEA, CNRS, 38044, Grenoble, France.*

[8]*Sorbonne Universités, UPMC Université Paris 06, CNRS, Laboratoire d'Océanographie de Villefranche (LOV), UMR 7093, Observatoire Océanologique, 06230, Villefranche-sur-Mer, France.*

[9]*Cell Biology and Biophysics Unit, European Molecular Biology Laboratory (EMBL), 69117, Heidelberg, Germany.*

Summary

Photosymbiosis is widespread and ecologically important in the oceanic plankton but remains poorly studied. Here, we used multimodal subcellular imaging to investigate the photosymbiosis between colonial Collodaria and their microalga dinoflagellate (*Brandtodinium*). We showed that this symbiosis is very dynamic whereby symbionts interact with different host cells via extracellular vesicles within the colony. 3D electron microscopy revealed that the photosynthetic apparatus of the microalgae was more voluminous in symbiosis compared to free-living while the mitochondria volume was similar. Stable isotope probing coupled with NanoSIMS showed that carbon and nitrogen were stored in the symbiotic microalga in starch granules and purine crystals respectively. Nitrogen was also allocated to the algal nucleolus. In the host, low ^{13}C transfer was detected in the Golgi. Metal mapping revealed that intracellular iron concentration was similar in free-living and symbiotic microalgae (c. 40 ppm) and two-fold higher in the host, whereas copper concentration increased in symbionts and was detected in the host cell and extracellular vesicles. Sulfur concentration was around two times higher in symbionts (chromatin and pyrenoid) than their host. This study improves our understanding on the functioning of this oceanic photosymbiosis and paves the way for more studies to further assess its biogeochemical significance.

Received 13 May, 2021; revised 27 August, 2021; accepted 5 September, 2021. *For correspondence. Tel. 00334 38 78 25 09. E-mail johan.decelle@univ-grenoble-alpes.fr.

Introduction

In the surface layer of oceanic waters, planktonic organisms display a wide range of trophic modes to access energy, such as intimate symbiotic partnerships between taxonomically and physiologically different cells (Decelle *et al*., 2015). By increasing connectivity and complexity of food webs, planktonic symbioses contribute to carbon and nitrogen fixation, and biogeochemical cycling of different elements (Karl *et al*., 2012; Thompson *et al*., 2012; Cabello *et al*., 2016). The increasing recognition of the ecological role of planktonic symbioses in the global ocean stresses the need to study their physiology and underlying mechanisms that remain largely unexplored. This knowledge gap is because the large majority of planktonic symbioses are not amenable to laboratory culture and their genomes and life cycle are unknown. One of the most prevalent eukaryotic associations in the open ocean is the photosymbiosis between the unicellular

radiolarian hosts (Rhizaria) and their intracellular symbiotic microalgae (e.g. haptophyte or dinoflagellate) (Decelle *et al*., 2012; de Vargas *et al*., 2015; Caron, 2016). Similar to coral reefs, it is a mutualistic symbiosis whereby microalgae provide photosynthetically derived products to the host, which in turn maintains a sheltered and relatively nutrient-rich microhabitat for their microalgae (Matthews *et al*., 2018). The symbiosis therefore provides a competitive advantage in nutritionally demanding habitats, such as oceanic waters where nutrients (e.g. nitrogen, iron) are extremely limiting. In the context of evolution, we hypothesize that photosymbioses between single-celled hosts and intact microalgae can be a transitional step in eukaryotic plastid acquisition, representing an experimental system to understand how a host cell can control and benefit from the metabolism of a photosynthetic cell.

In the widespread association between the host Acantharia (radiolarians) and the microalga *Phaeocystis* (haptophyte), the microalga is morphologically transformed into a powerful photosynthetic machinery (e.g. multiplication of voluminous plastids and larger C-fixing pyrenoids), and its nutrient homeostasis is significantly altered (i.e. twofold increase in Fe concentration) (Decelle *et al*., 2019; Uwizeye *et al*., 2021b). This partnership can be considered as algal farming where the host has a strong control over the physiology and cell cycle of its microalgae. It is not known whether such morphological and metabolic transformation of algal symbionts is common in other oceanic photosymbioses involving different hosts and microalgal symbionts. Colonial radiolarians (Collodaria) are arguably one of the most abundant photosymbioses in the oceanic plankton (de Vargas *et al*., 2015; Biard *et al*., 2016). Collodaria were also among the first observations of symbiotic associations in nature (i.e. T.H. Huxley during the Rattlesnake expedition in 1847). Collodaria, composed of several cells, are known to host thousands of microalgae (the dinoflagellate *Brandtodinium nutricula*) in their large gelatinous matrix (Anderson, 1976; Probert *et al*., 2014). Large-scale environmental DNA sequencing projects (e.g. Tara-*Oceans*) showed that collodarians are widely distributed in the oceans and tend to numerically dominate the plankton community in surface oligotrophic waters (de Vargas *et al*., 2015; Biard *et al*., 2017; Faure *et al*., 2019). In tropical and subtropical waters their total biomass can be as important as the one of the traditional zooplankton, such as copepods (Biard *et al*., 2016). High densities of colonies (16 000–20 000 colonies m^{-3}) have been reported in different oceanic regions, with marked seasonal episodes of blooming (Swanberg and Caron, 1991; Dennett *et al*., 2002). Their significant participation to carbon fixation (through photosynthesis of their algal symbionts) and carbon export to the deep ocean (Caron *et al*., 1995; Guidi *et al*., 2016) make them key players in oceanic waters. For instance, primary production of Collodaria can be more than four orders of magnitude greater than that in the same volume of the surrounding seawater (Caron *et al*., 1995). In addition to energy provided by their symbionts, *in situ* observations and culture experiments have also described collodarians as active predators feeding on a broad range of prey (e.g. copepods, ciliates, phytoplankton or bacteria) therefore contributing to oceanic food webs (Swanberg and Caron, 1991).

The ecological success of radiolarian photosymbioses in the ocean involving the microalga *Brandtodinium* must rely on the capacity of the partners to intertwine their metabolism and on the efficiency with which they exchange nutrients, such as carbon and the poorly available macronutrients (e.g. nitrogen) and trace metals (e.g. iron). However, the metabolism and physiology of the microalga *Brandtodinium* in symbiosis are not known, as well as the underpinning mechanisms of the host to accommodate this microalga. The study of this uncultured cell-to-cell symbiosis, where partners cannot be separated, calls for dedicated subcellular imaging methods that maintain the physical integrity of the host–symbiont association. Here, using multimodal subcellular imaging (3D electron microscopy and mass spectrometry and X-ray fluorescence imaging), we investigated the cellular architecture and metal homeostasis of the microalga *Brandtodinium* in free-living and symbiotic stages, as well as the carbon and nitrogen flux and transfer between both partners.

Results and discussion

Cellular architecture of the microalga Brandtodinium *in free-living and symbiotic phases*

The metabolism and bioenergetic features of a microalgal cell can be manifested by its cellular architecture organization, such as the arrangement and volume of energy-producing organelles and vacuoles (Uwizeye *et al*., 2021a). Using 2D and 3D electron microscopy [transmission electron microscopy (TEM) and focused ion beam-scanning electron microscopy – FIB-SEM respectively], the cellular organization of the microalga *Brandtodinium* was investigated in the free-living cells (i.e. maintained in artificial culture medium and isolated from Mediterranean collodarians) and symbiotic stage within the host Collodaria collected in surface waters of the Mediterranean Sea. Compared to free-living, the round-shaped microalgae have lost their thick theca in symbiosis (Fig. 1). Of note, plastids, which were located around the cell periphery, occupied a twofold larger surface area of the cell in symbiosis (mean $\pm$ SD $= 26 \pm 6\%$ of the cell surface; $n = 20$) compared to the free-living stage (mean $\pm$ SD $= 12 \pm 2\%$; $n = 41$ cells) (Fig. 1G). In order to

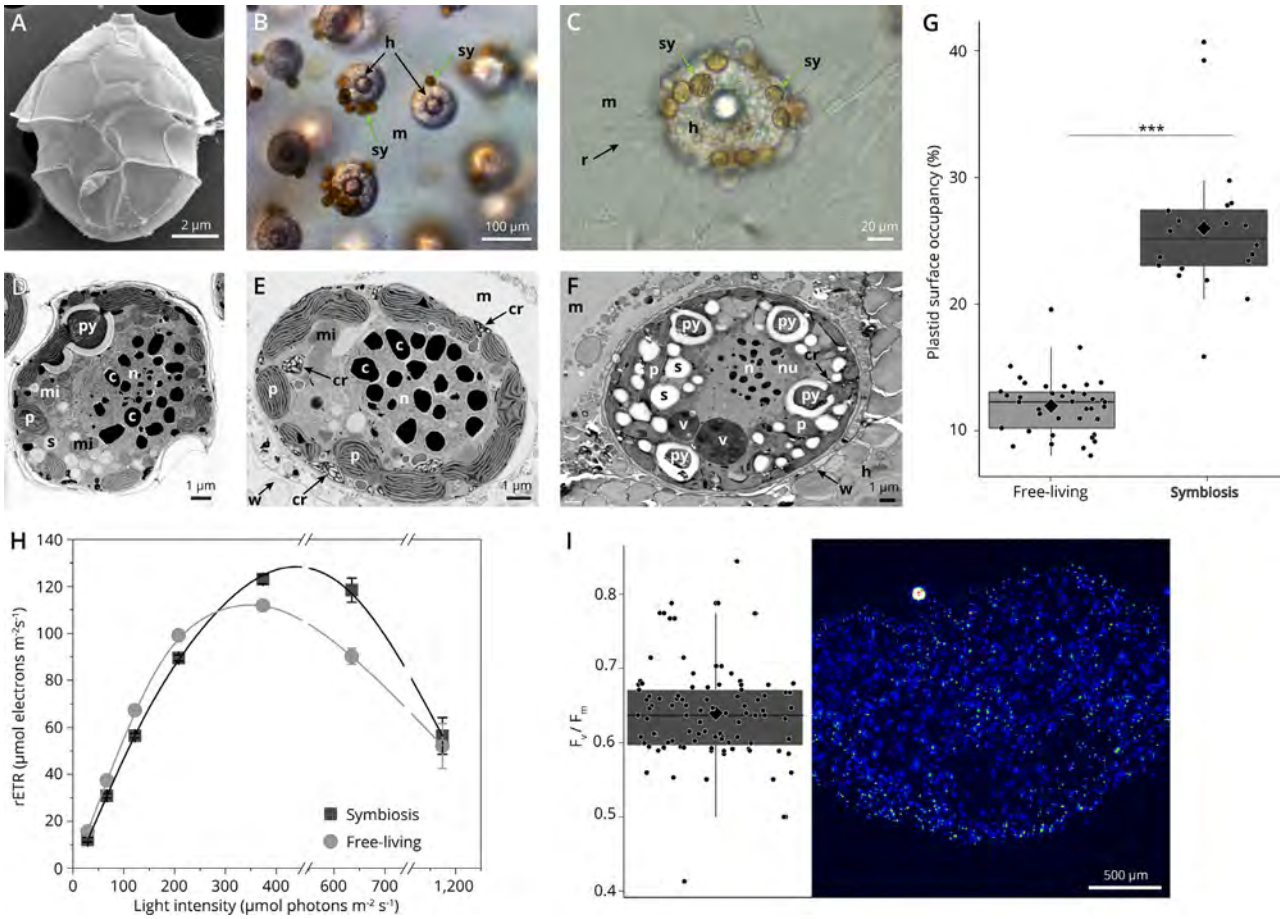

Fig. 1. Ultrastructure and photophysiology of the microalga *Brandtodinium* in free-living and symbiotic stages within collodarians hosts.
A. External morphology of *Brandtodinium* with its thecal plates revealed by scanning electron microscopy.
B. Colony of Collodaria observed with light microscopy, composed of several host cells (black arrow, h) and multiple symbiotic microalgae (Sy; green arrow) embedded in the gelatinous matrix (m).
C. A zoom-in on a host cell surrounded by symbiotic microalgae and cytoplasmic strands (r; rhizopodia).
D. Ultrastructure of free-living *Brandtodinium* revealed by transmission electron microscopy (TEM).
E and F. TEM micrographs showing the ultrastructure of symbiotic *Brandtodinium* within the Collodaria.
G. Plastid surface area occupancy (% of the cell surface) in free-living and symbiotic stages of *Brandtodinium* calculated from TEM micrographs. Plastid surface area is statistically higher in symbiosis ($t = 14.67$, $df = 24.75$, $p < 0.0001$; $N = 59$; based on Cook's distances and high leverage, two outlying data points were excluded from the analysis because of their high influence).
H. Photosynthetic efficiency measured by the relative electron transfer rate (rETR) for free-living (light grey green circles; $n = 4$) and symbiotic (dark grey squares; $n = 4$) microalgae over a range of light intensities up to 1200 µmol photons m^{-2} s^{-1}.
I. F_v/F_m values measured by a PAM microscope from each individual symbiotic microalgal cells within a colony. n: nucleus; c: condensed chromatin (chromosome), py: pyrenoid; p: plastid; s: starch grain; h: Host cell (Collodaria); m: matrix; mi: mitochondria; w: membranous envelope of the host; cr: nitrogen-rich crystals; r: rhizopodia.

confirm and better understand this morphological change of the photosynthetic machinery, we conducted morphometric analyses using 3D electron microscopy (FIB-SEM) on four symbiotic *Brandtodinium* cells and three free-living cells maintained in culture. 3D reconstructions, which were based on >1000 aligned electron micrographs for each cell, showed that the volume of the microalgal cell was similar in both stages (333 ± 82 µm^3, $n = 3$ and 305 ± 44 µm^3, $n = 4$ in free-living and symbiosis respectively). The plastid is a reticulated and thick network (Fig. 2A and D). Morphometric analyses confirmed that the plastids were more voluminous in symbiosis (81 µm^3 ± 12) compared to free-living cells (55 µm^3 ± 10) and can occupy up to 31% of the cell volume (16.8 ± 1.5% on average in free-living) (Fig. 2G–H; Table S1). This expansion of the photosynthetic machinery was also found in the microalga *Phaeocystis* within acantharian hosts, suggesting that it may be a common morphological trait in planktonic photosymbiosis (Decelle *et al*., 2019; Uwizeye *et al*., 2021a). Regarding the carbon fixation capability of *Brandtodinium*, 3D reconstructions unveiled various numbers of pyrenoids in individual cells (i.e. from one to four) in both life stages but in symbiosis, pyrenoid occupancy in the cell was slightly larger (2.4 ± 0.3%) than in free-living cells (1.7 ± 0.2%) (Fig. 2C

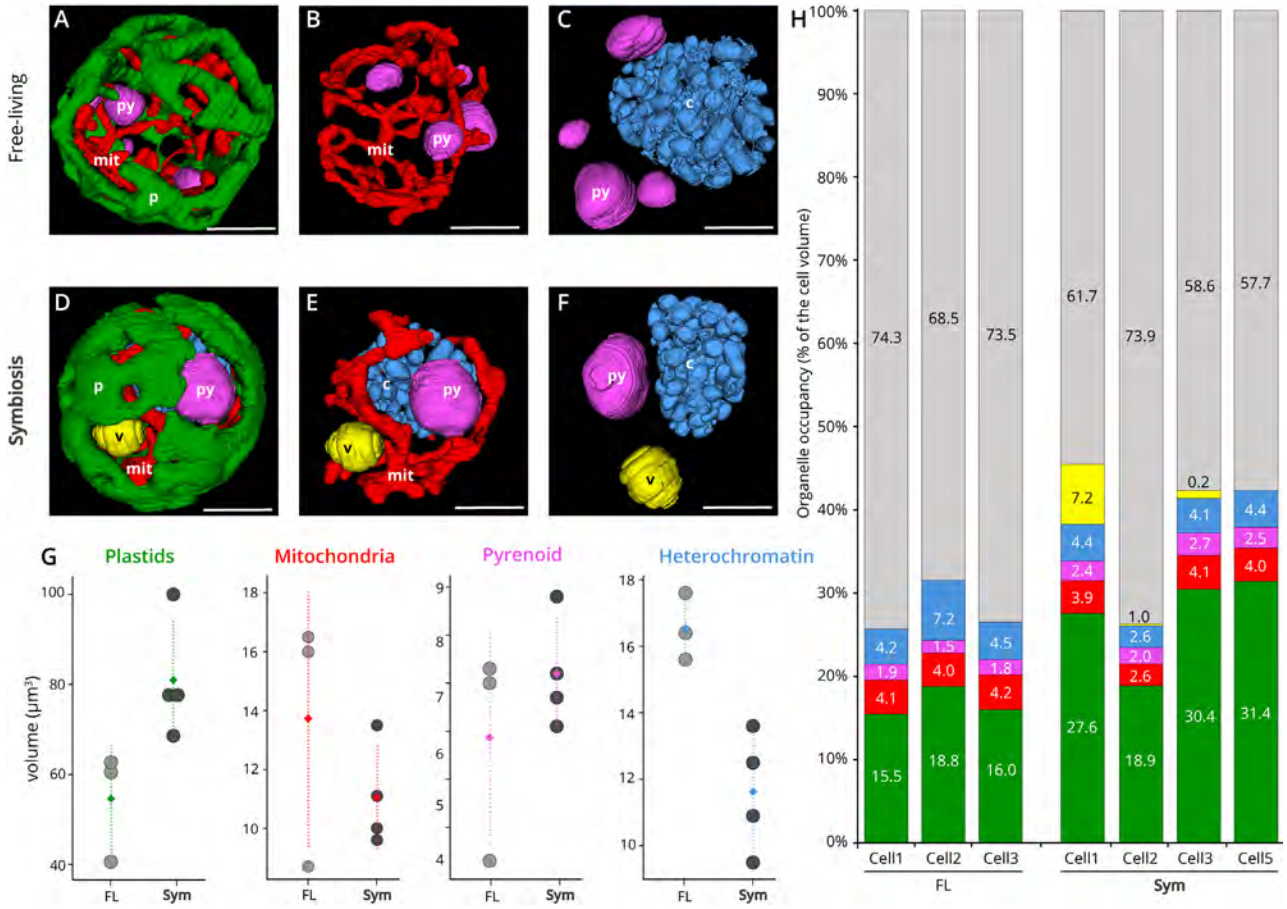

Fig. 2. Cellular architecture in 3D and morphometrics of the microalga *Brandtodinium* in free-living and symbiotic stages revealed by FIB-SEM imaging.
A–C. Topology of the plastid (green), mitochondria (red), pyrenoid (purple) and condensed chromatin (chromosomes, light blue) in a free-living microalgal cell. Scale bar: 3 µm.
D–F. Topology of the plastid (green), mitochondria (red), pyrenoid (purple), vacuole (yellow) and condensed chromatin (chromosomes, light blue), in a symbiotic microalgal cell. Scale bar: 3 µm.
G. Volume (µm^3) of different organelles of the microalga *Brandtodinium* in free-living ($n = 3$) and symbiotic ($n = 4$) stages, such as plastids, mitochondria, pyrenoid and heterochromatin (chromosomes), calculated based on 3D reconstructions.
H. Volume occupancy of organelles (% of the cell volume) in three free-living algal cells and four symbiotic algal cells.

and F). In addition, we observed a correlation between volumes of plastids and pyrenoid ($R = 0.81$, $p = 0.028$; Pearson correlation), suggesting an energetic coupling between the light-dependent and light-independent photosynthetic reactions as found in some microalgae (Uwizeye *et al*., 2021a) (Fig. S1). In the multiple-stalked pyrenoids, we observed that thylakoid membranes (called tubules) penetrated like fingers the C-fixing organelle, which is covered by a thick starch sheath (Fig. 3A). These tubules are thought to be enriched in carbonic anhydrase in order to ensure high local concentration of CO_2 for the Rubisco in the matrix (Engel *et al*., 2015; Meyer *et al*., 2017).

To test possible consequences of this plastid expansion on the photophysiology of *Brandtodinium*, we characterized photosynthetic parameters *in vivo*, based on chlorophyll fluorescence imaging. We found that the photosynthetic efficiency, measured through the electron transfer rate (ETR) parameter on microalgae and collodarian colonies, which is related to carbon assimilation (Genty *et al*., 1989), was similar in free-living and symbiotic stages of the microalga in a light range from 20 to 400 µmol photons m^{-2} s^{-1}, but differed when light was further increased (being 1.3 times higher in symbiosis in the 400–1000 µmol photons m^{-2} s^{-1} range) (Fig. 1H). In addition, photoprotective responses, evaluated though the non-photochemical quenching parameter (NPQ) of photosystem II was lower in the symbiotic stage from 200 to 1200 µmol photons m^{-2} s^{-1} (being three times lower at 400 µmol photons m^{-2} s^{-1}) (Fig. S2). Overall, these data suggest that the photosynthetic capacity is

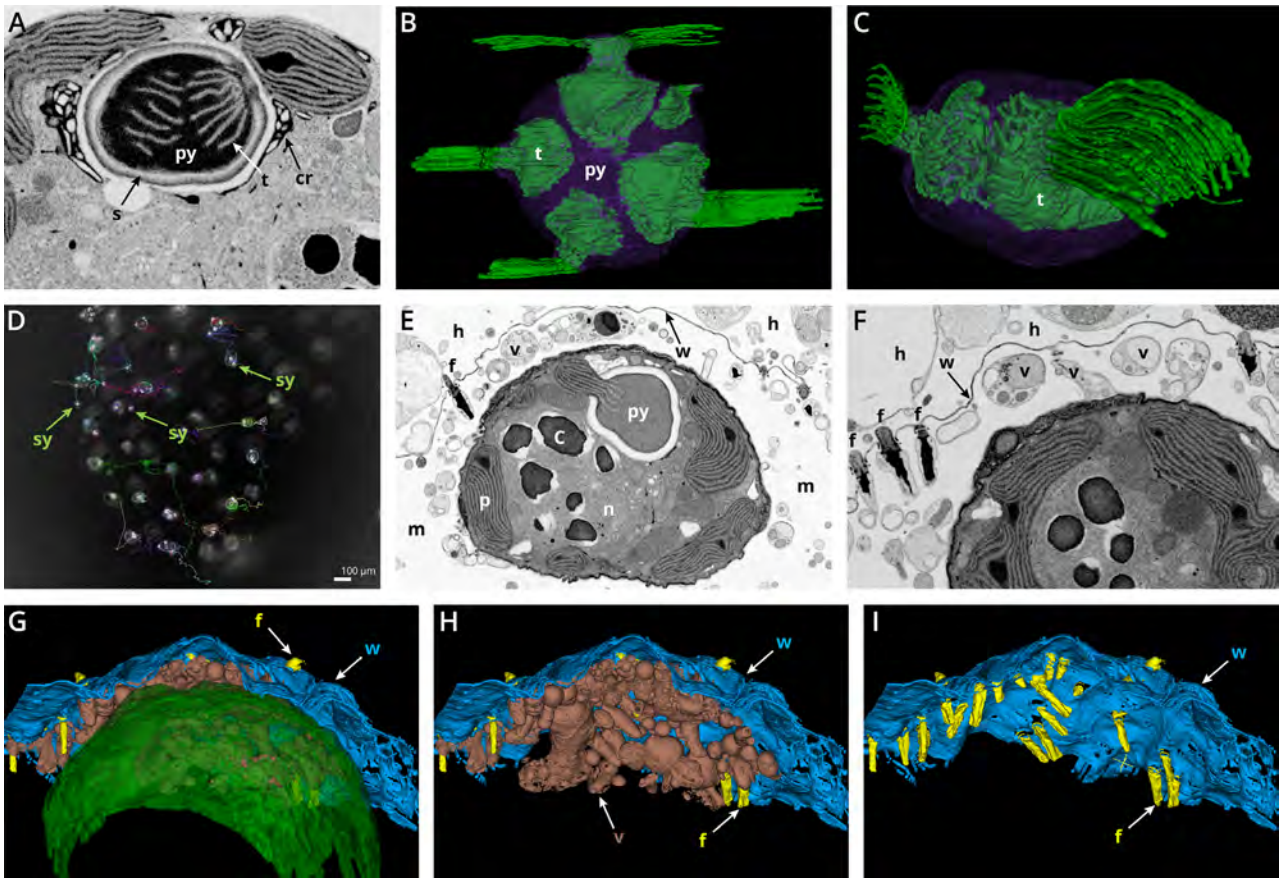

Fig. 3. Pyrenoid architecture and integration of the symbiotic microalga in the host.
A–C. Pyrenoid architecture of the microalga *Brandtodinium* visualized by TEM (A) and FIB-SEM reconstruction (B and C). Pyrenoid (purple) is surrounded by a starch sheath and penetrated by thylakoid membranes (t, in green) from different stalks.
D. Snapshot image of a particle tracking video conducted on a light microscope (See Video S1) where trajectories of symbiotic microalgae (Sy; indicated by a green arrow) during few hours are visible inside the colony (coloured lines). Symbionts were not associated to a specific host cell but interacted with several host cells.
E–F. EM micrographs showing the physical integration of a symbiotic microalga (*Brandtodinium*), which was surrounded by numerous vesicles (v) in the ectoplasm (matrix) and in close contact with the symbiont.
G–I. 3D reconstruction after FIB-SEM of the host–symbiont integration with a focus on the numerous vesicles (v, brown structures) between the membranous envelope of the host (w, blue) and the symbiotic microalga (green). Piston-like structures (called fusules) were also observed at pore sites of the membranous envelope of the host (w). These organelles are known to inject host endoplasm into the matrix (=ectoplasm) as a vacuolated network (Anderson, 1976). [n: nucleus; c: condensed chromatin (chromosome), py: pyrenoid; p: plastid; f: fusules; h: host cell (Collodaria); m: matrix; w: envelope of the host; cr: nitrogen-rich crystals; v: vacuoles in the matrix].

more efficient in symbiotic algae at high light [i.e. light intensity typically experienced in surface waters (Breitbarth *et al*., 2008)], i.e. that absorbed photons are better used for photosynthetic electron flow (ETR) and therefore less dissipated as heat. To test if F_v/F_m (maximum quantum efficiency of PSII photochemistry) is homogeneous among the symbiont population, this parameter was measured on individual algal cells within a colony collected in surface waters (Fig. 1I). The average single-cell F_v/F_m value was 0.64 $\pm$ 0.07 (n = 52 cells), consistent with earlier findings at the symbiont population level (0.58) (Villar *et al*., 2018). The low variability observed among the symbiont population of the colony may reflect relatively homogeneous physiological states of symbiotic microalgae in a colony.

As for the respiratory machinery, the mitochondria formed a reticulated network located between the plastids and nucleus, in close proximity with plastids in some cellular regions (Fig. 2B and E). Total volume of mitochondria tended to be not different between free-living (14 $\mu m^3 \pm 4$) and symbiotic cells (11 $\mu m^3 \pm 2$), occupying a constant 4% of the cell volume with similar topology in both stages (Fig. 2G and H). Based on this finding, it is tempting to propose that the respiratory activity of the microalgal cell is not substantially different between free-living and symbiosis. The nucleus of the microalga (also

called the dinokaryon) was centrally located and contained typical condensed, rod-shaped chromosomes of different sizes and one or two nucleoli (Gautier *et al*., 1986) (Fig. 2C and F). The volume occupancy of the nucleolus in the cell was similar in both life stages (0.26 ± 0.4% and 0.30 ± 0.07% on average in free-living and symbiosis respectively) (Table S1). But total volume of condensed chromatin tended to be slightly lower in symbiosis (12 μm^3 ± 2; 3.9 ± 0.7% of occupancy) compared to that in free-living cells (17 μm^3 ± 1; 5.3 ± 1.4% of occupancy) (Fig. 2G). The number of chromosomes including electron-dense chromatin structures in the nucleoplasm greatly varied from 44 to 88 in symbiotic cells and from 64 to 179 in free-living cells (Fig. S3). This reflects the dynamic level of chromatin compaction, which is known to vary across the life cycle of dinoflagellates (Blank, 1987). For instance, in G1 phase, there are numerous small structures protruding from the chromosomes towards the nucleoplasm (Bhaud *et al*., 2000), which could correspond to our observations in free-living cells (Fig. 2A). Although this needs to be confirmed with more cells, this observation may indicate that the symbiotic microalga is at a different life phase and may be related to the slower growth of symbiotic *Brandtodinium* as suggested by transcriptomics in a different host species and known in corals (Davy *et al*., 2012; Liu *et al*., 2019). For instance, doubling times of the dinoflagellate Symbiodiniaceae within corals can exceed 10 days and up to 70 days while in culture the doubling times are generally 2–5 days (Davy *et al*., 2012). Yet, contrary to photosymbiosis in Acantharia (Uwizeye *et al*., 2021b), symbiotic *Brandtodinium* cells had the same volume as in free-living and were observed to divide within the host colony (Fig. S4), so there is no complete inhibition of symbiont division.

Structural connectivity between the host and its symbiotic microalgae

The physical integration of symbiotic microalgae within the host was then investigated at the nanoscale to identify the possible routes of metabolic exchanges between cells. In Collodaria, microalgae were outside the host endoplasm, being embedded in the translucent gelatinous matrix of the colony (i.e. ectoplasm) (Fig. 3). Cytoplasmic strands (called rhizopodia) embraced microalgae and are known to control their distribution in the matrix [Fig. 1 (Anderson, 1976)]. Particle tracking from light microscopy time-lapse showed that microalgae can move in this matrix (up to hundreds of microns min^{-1}) and stop by different host cells for few minutes (Fig. 3D and Video S1). Of note, TEM and FIB-SEM reconstructions revealed a network of numerous vacuoles in the matrix located between the host cell and the symbiotic microalgae, sometimes physically associated to both cells (Fig. 3E–I). In 3D, some of these round-shaped vacuoles were connected to each other and very likely ensure metabolic connection between the host and the microalgae. In addition, piston-like structures (called fusules) visible on the capsule membranous envelope of the host are known to inject host endoplasm into the matrix as a vacuolated network (Anderson, 1976). Overall, Collodaria photosymbiosis is a dynamic system where host cells interact with several microalgae within the 'greenhouse-like' colony through time via vesicles, raising questions about the nutrient flow between cells and more generally the metabolic connection.

Subcellular visualization of the incorporation and allocation of ^{13}C and ^{15}N

To better understand the metabolic crosstalk between the host and the microalgae and more specifically the exchanges and allocation of carbon and nitrogen, we incubated collodarians in ^{13}C-bicarbonate and ^{15}N-ammonium for a 3-h light period in filtered natural seawater, cryo-fixed with high pressure freezing and prepared them for nanoSIMS (Nanoscale Secondary Ion Mass Spectrometry) (see Experimental procedures). Five different microalgae from two distinct collodarian colonies were analysed. NanoSIMS analyses revealed changes in ^{13}C and ^{15}N fractions (% of ^{13}C or ^{15}N out of total C or N) in different organelles. Since changes in ^{13}C and ^{15}N fractions are not linearly proportional to cellular activity, we also calculated the assimilation activity expressed as the relative assimilation K_A in atom% (Stryhanyuk *et al*., 2018). In the symbiotic microalgae, ^{13}C fraction was mainly detected in multiple starch grains distributed in the cytoplasm (mean ± SD = 21 ± 2 atom%, $n = 38$) and in the extra-plastidial starch sheaths surrounding the pyrenoids (mean ± SD = 19 ± 1 atom%, $n = 12$) (Fig. 4; Table S2). The relative carbon assimilation Ka of 25 ± 4 atom% in starch grains and 23 ± 2 atom% in starch sheaths were calculated [see Experimental procedures for more details and Stryhanyuk *et al*., 2018]. Lower Ka was revealed from starch of the second collodarian colony (10 ± 3 atom% and 9 ± 2 atom% in cytoplasmic grains and sheaths respectively). Starch grains were observed both in free-living and symbiotic stages by TEM observations (Fig. 1) and can represent a volume of *c*. 5% of the cell as calculated from FIB-SEM reconstructions (Fig. 4, Table S1). They were scattered in the cytoplasm and adjacent to plastids and pyrenoids. ^{13}C-labelled starch granules were also observed in another planktonic photosymbiosis in foraminifera involving the dinoflagellate *Pelagodinium beii* (Lekieffre *et al*., 2018). The observed assimilation activity pattern in photosymbiosis

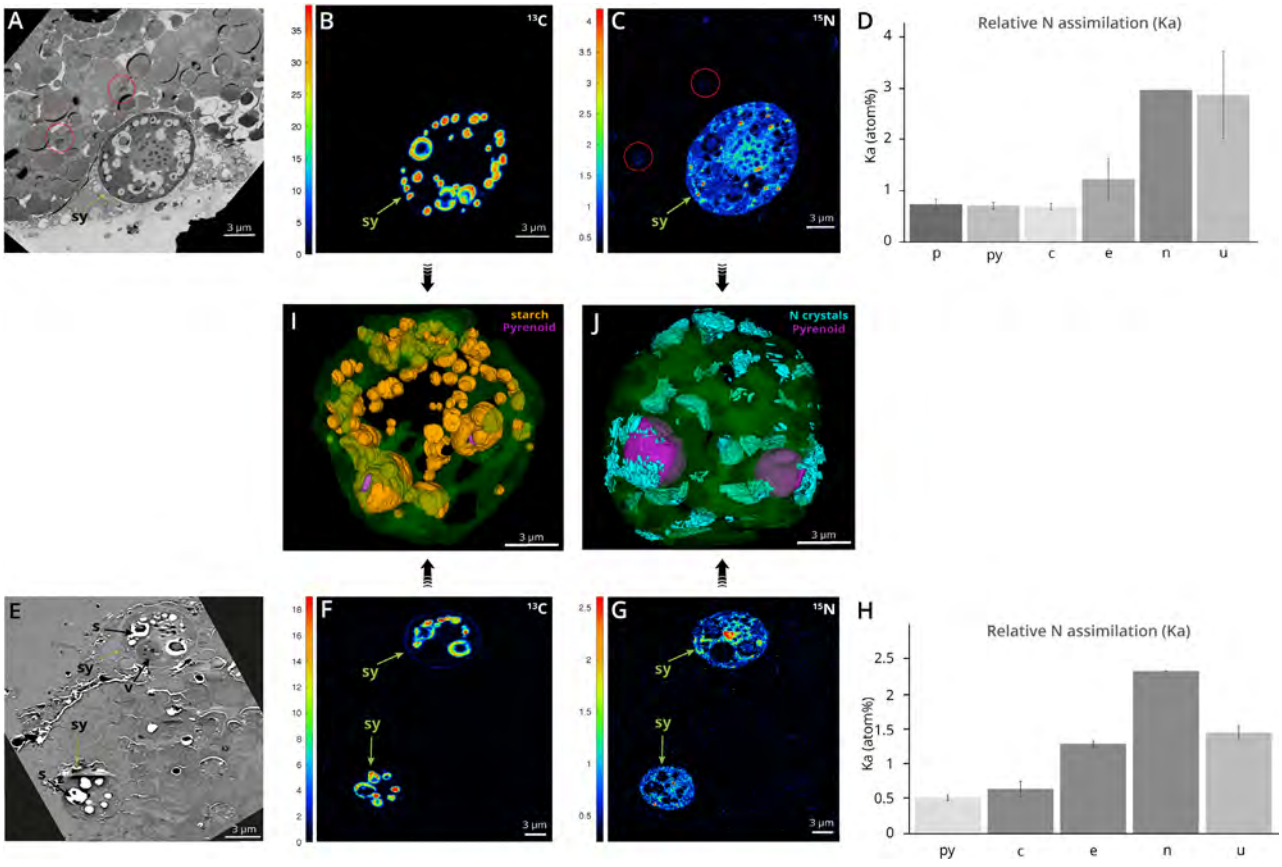

Fig. 4. Carbon and nitrogen flux in the symbiotic cells as revealed by correlated TEM-nanoSIMS and ^{13}C-bicarbonate and ^{15}N-ammonium labelling.
A and E. TEM micrographs of the cellular areas analysed by nanoSIMS, showing three symbiotic microalgae (Sy; indicated by a green arrow) and their host cell from two different colonies. Host Golgi are surrounded by a red circle.
B and F. NanoSIMS mapping showing relative carbon assimilation (Ka) following ^{13}C-bicarbonate 3 h-incubation in starch granules and starch surrounding the pyrenoids.
C and G. NanoSIMS mapping showing the relative nitrogen assimilation (Ka) following ^{15}N-ammonium 3 h-incubation in symbiotic microalgae, more particularly in purine crystals (red hotspots) and in the nucleolus. The latter compartment corresponds to the red hotspot in the middle of the upper cell in panel G. Nitrogen assimilation was also detected in the Golgi apparatus of the host cell, highlighted by the red circles in C (see also Fig. S5).
D and H. Averaged relative N assimilation (Ka) measured by nanoSIMS in different organelles of the symbiotic microalgae from two different colonies (A8 and A7) ($n = 3$ cells in D; $n = 2$ cells in H).
I. 3D reconstruction after FIB-SEM imaging of the starch (orange) that assimilated carbon. In the algal cytoplasm, starch was contained in grains and also surrounding the pyrenoids (purple) and closely associated to the plastid (green, transparent).
J. 3D reconstruction after FIB-SEM imaging of N-rich purine crystals (light blue) that were localized at the periphery of the cell in close association with the pyrenoids (purple). py: pyrenoid; c: condensed chromatin; e: euchromatin+nucleoplasm; n: nucleolus; u: purine crystals.

confirms that the newly fixed carbon is rapidly stored by the microalgae as glucose polymers.

In the host cell, after 3 h of incubation, low ^{13}C fraction was detected and only in the secretory vesicles of multiple Golgi apparatus (1.33 $\pm$ 0.05 atom%, corresponding to a Ka of 1.64 $\pm$ 0.12 atom% (Fig. 4, Fig. S5). This organelle is known to serve as a carbohydrate factory to process oligosaccharide side chains on glycoproteins and glycolipids (Mellman and Simons, 1992). Once translocated from the symbiont to the host, we therefore presume that ^{13}C is incorporated into host biomass such as proteins and lipids through the Golgi apparatus (Boncompain and Perez, 2013). Overall, carbon assimilation into the host seems to be different in Collodaria-*Brandtodinium* symbiosis compared to other dinoflagellate photosymbioses in corals (Symbiodiniaceae) and foraminifera (*Pelagodinium)* (Kopp *et al*., 2015; Lekieffre *et al*., 2018). In these symbioses, ^{13}C enrichment was first observed in the host lipid droplets after 2 h and later elsewhere in the host cell. In our study, no putative lipid droplets were observed in collodarian hosts in different sections imaged with electron microscopy, which may explain the ^{13}C assimilation differences compared to other photosymbioses. We may also consider that most

of the carbon fixed and stored by the symbionts during the day could be transferred overnight to its host, thereby explaining low ^{13}C fraction in the host in the experimental setup of this study. One analytical aspect to take into account is that NanoSIMS provides 2D information so depending on the cellular sections, some important organelles can be missed in the imaging areas, such as lipid droplets or vacuoles. In the matrix of the colony, the extracellular vacuoles observed with 3D electron microscopy (Fig. 3E–I) that are potentially a route for metabolic exchanges were not showing carbon assimilation activity. This may be explained by the fact that soluble photosynthates (sugars), which are transferred to hosts in photosymbioses (Davy *et al*., 2012), are lost during sample preparation, and could not be visualized with nanoSIMS (Loussert-Fonta *et al*., 2020).

The subcellular natural abundance of nitrogen ($^{12}C^{14}N^-/^{12}C_2^-$; without ^{15}N labelling), which is limiting in the ocean (Geider and La Roche, 2002; Moore *et al*., 2013), showed that the microalgae *Brandtodinium* contained a significant amount of nitrogen (N) in plastids, pyrenoids and nucleus (Fig. S6; Table S3). The N-rich photosynthetic machinery is due to the high concentration of photosystems and pigments in the plastid and the CO_2-fixing Rubisco in the pyrenoid. In the nucleus, the chromosomes and the nucleolus were particularly rich in N, likely representing ribosomes and proteins associated to the chromatin [e.g. histone-like (Gornik *et al*., 2019)] (Fig. S6). Overall, subcellular mapping of natural nitrogen pinpointed metabolic needs of the symbiotic microalgae and suggests that the host may provide N to support the functioning of the nucleus and photosynthetic machinery. Collodaria are known to be active predators (Swanberg and Caron, 1991), therefore representing a source of nitrogen for their symbionts. In addition, like benthic and other planktonic hosts (Rädecker *et al*., 2015; LeKieffre *et al*., 2020), we presume that collodarians can uptake inorganic nitrogen such as ammonium and transfer it to its symbionts, but this remains unknown.

In order to reveal the first steps of N flux between the two partners, symbiotic associations were incubated with ^{15}N-labelled ammonium for 3 h. A high ^{15}N fraction was measured in small hotspots in the algal cell from both colonies: up to 3.1 $\pm$ 0.8 atom% which correspond to 2.9 $\pm$ 0.9 atom% of relative N assimilation (Ka). These ^{15}N hotspots correspond to crystalline inclusions as seen by electron microscopy (Figs 1E, 3A, 4J). FIB-SEM reconstruction showed that, in the symbiotic stage, N-rich crystals were located at the cell periphery and can represent *c*. 2% of the algal cell volume (Fig. 4). Based on their morphologies in EM, these crystals likely correspond to the purines guanine or uric acid, which are known to be nitrogenous reserves in microalgae including the symbiotic *Symbiodiniaceae* in corals (Clode *et al*., 2009; Kopp *et al*., 2013; Mojzeš *et al*., 2020). Note that we did not observe these crystals in the free-living microalgae, which may be explained by the fact that they grow in an N-replete culture medium so do not need to store N. These crystals showed close physical contacts with the plastids and pyrenoids (Fig. 3A), indicating that these organelles may either produce or benefit from this N reserve. The presence of purine crystals would ensure N availability in N-depleted waters or when prey feeding by the host is restricted. Future studies are required to better understand the dynamics of this N reserve in symbiotic microalgae over 24 h and in different trophic conditions (e.g. hosts in starved or N-replete conditions).

The ^{15}N fraction was also important in the nucleolus of the algal nucleus (2.9 atom% $\pm$ 0.3 or 2.7 atom% $\pm$ 0.3 Ka). This suggests that N is preferentially utilized and allocated for the synthesis of ribosomes inside the N-rich nuclear apparatus. Euchromatin was also ^{15}N-enriched (1.6 atom% Ka) and similar Ka values were found in the condensed chromatin, plastid and pyrenoid (*c*. 0.6 atom% Ka) (Fig. 4). In addition to N, subcellular mapping of natural phosphorous ($^{31}P/^{12}C_2$) showed that the nucleus of *Brandtodinium* is the organelle that contains the most P in the algal cell, more specifically in the condensed chromatin with up to *c*. 10 times more than in other organelles (Fig. S6; Table S3).

In the host cell, a low ^{15}N fraction was found (0.76 $\pm$ 0.05 atom%; Ka: 0.40 $\pm$ 0.05 atom%) in the Golgi apparatus, including cisternae and secretory vesicles (Fig. 4 and Fig. S5). Whether this ^{15}N originates from a direct ammonium assimilation by the host cell or from N exchanges with the symbiotic dinoflagellates cannot be resolved in this study and would require shorter incubations (e.g. <1 h). Overall, ^{15}N-assimilation in the collodarian host cell seems to be slower compared to other protistan photosymbioses. For example, in foraminiferal symbiosis, ^{15}N-enrichment in the host cell was detected in specific structures already after 1 h of incubation with ^{15}N-ammonium and rapidly spread to the entire host cell (LeKieffre *et al*., 2020).

Subcellular distribution of sulfur in symbiotic cells

Sulfur plays a pivotal role as antioxidant protection with the production of several compounds, such as dimethylsulfoniopropionate (DMSP), which is implied in photosymbiosis and contribute to the global sulfur cycle of the ocean (Simó, 2001; Giordano *et al*., 2005; Raina *et al*., 2010; Decelle *et al*., 2012; Gutierrez-Rodriguez *et al*., 2017). Here, we visualized sulfur distribution in cells to bring new insights into the metabolism and homeostasis of this element in photosymbiosis. Quantification using Synchrotron X-Ray Fluorescence (S-XRF) imaging revealed that symbiotic microalgae contained

around two times more sulfur than their host Collodaria (Fig. 5; Table S4). Similar subcellular distribution and concentrations were found between symbiotic (mean ± SD = 2400 ppm ± 600; $n = 13$) and free-living (mean ± SD = 2100 ppm ± 400; $n = 33$) *Brandtodinium* cells. NanoSIMS showed that sulfur was mostly located in the condensed chromatin, and then about two times less in pyrenoids and plastids in descending order (Fig. 5; Table S4). This is in contrast to what is known in other microalgae where most sulfur is contained in the photosynthetic machinery (Giordano *et al*., 2005; Decelle *et al*., 2019). In addition, in the symbiotic microalgae, nanoSIMS revealed a large vacuole of 2.7 μm in size, which contained much more sulfur than chromatin (Figs 1, 2 and 5). FIB-SEM reconstruction showed that this vacuole can represent up to 7% of the algal cell volume (Fig. 2). This vacuole did not assimilate ^{13}C and ^{15}N and contained no phosphorous (Fig. 6 and Fig. S6). It is known that *Brandtodinium* in symbiosis can produce 100-fold higher DMSP compared to the free-living form (Gutierrez-Rodriguez *et al*., 2017). Therefore, this S-rich vacuole could contain DMSP and DMS as also observed in Symbiodiniaceae in culture (Raina *et al*., 2017) or other S-rich molecules involved in the algal metabolism. Of note, in the matrix of the host Collodaria, sulfur was also highly concentrated (5400 ppm ± 800) in the numerous extracellular vacuoles reconstructed in 3D above (Figs 3 and 5, Table S4). These vacuoles contained four and two times more sulfur than in the host endoplasm and symbiont respectively. This would indicate that sulfur-

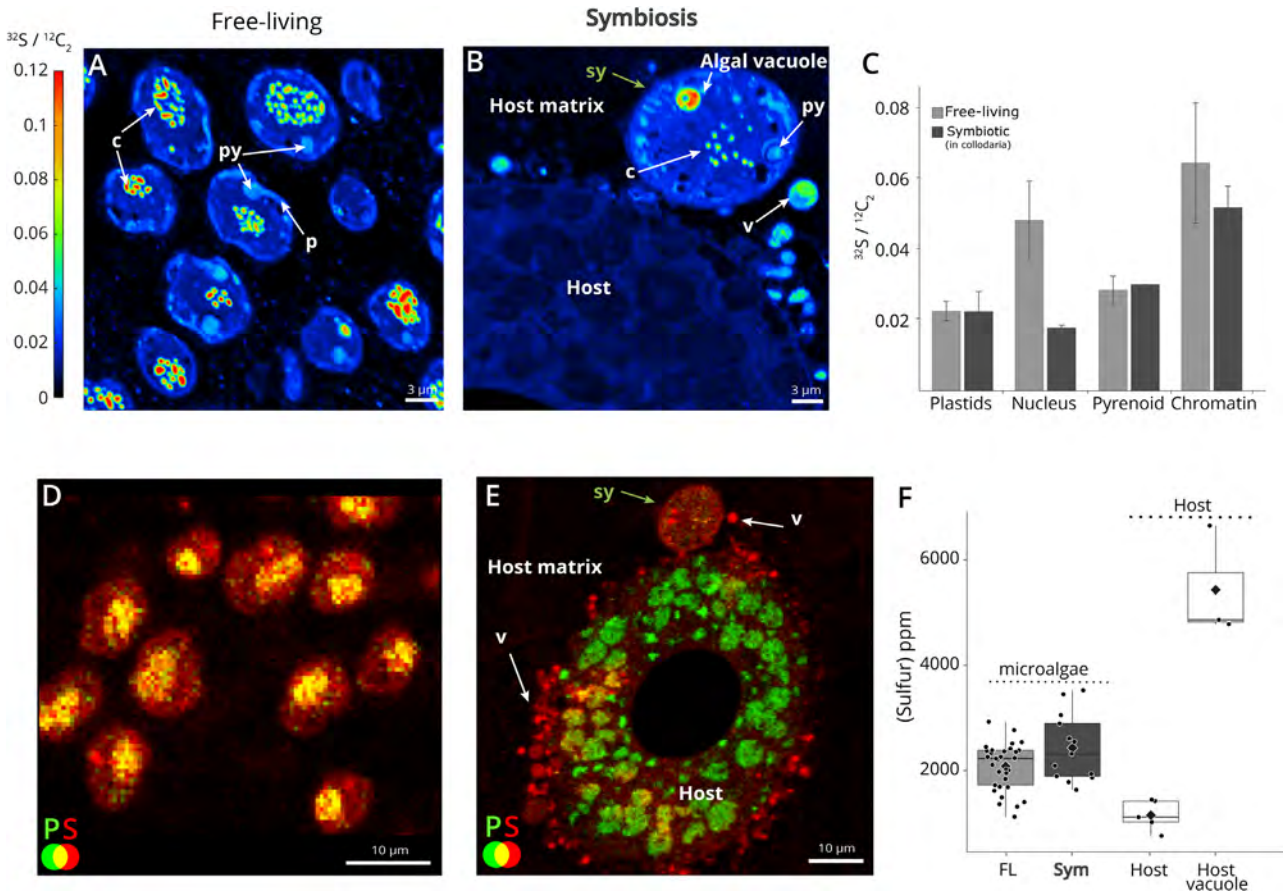

Fig. 5. Subcellular distribution of sulfur in the collodaria photosymbiosis unveiled by nanoSIMS and synchrotron X-ray fluorescence (S-XRF).
A and B. Sulfur ($^{32}S/^{12}C_2$) mapping in free-living (A) and symbiotic (B) microalgae unveiled by nanoSIMS. Sulfur was mainly localized in chromatin of microalgae, but also in a large vacuole in the symbiotic cell (green arrow in B). Sulfur was also concentrated in vacuoles of the matrix between the host cell and the symbiotic microalga. Scale size: 3 μm.
C. Normalized sulfur content ($^{32}S/^{12}C_2$) measured by nanoSIMS in different organelles (plastids, nucleus, pyrenoid and chromatin) of free-living (light grey) and symbiotic (dark grey) microalgae (Table S3).
D and E. Sulfur (red) and phosphorous (green) distribution unveiled by S-XRF imaging showing high concentration of sulfur in microalgae (plastids, chromatin) and the vacuoles of the matrix. The co-localization of S and P is indicated by the yellow colour (nucleus of the microalgae in D).
F. Sulfur concentration (ppm) measured by S-XRF in the free-living ($n = 33$) and symbiotic *Brandtodinium* ($n = 13$) cells (dark and light grey respectively), as well as in the host cell ($n = 5$) and the vacuoles of the matrix. (n: nucleus; c: condensed chromatin; py: pyrenoid; p: plastid; h: host cell (Collodaria); m: matrix; v: vacuoles in the matrix).

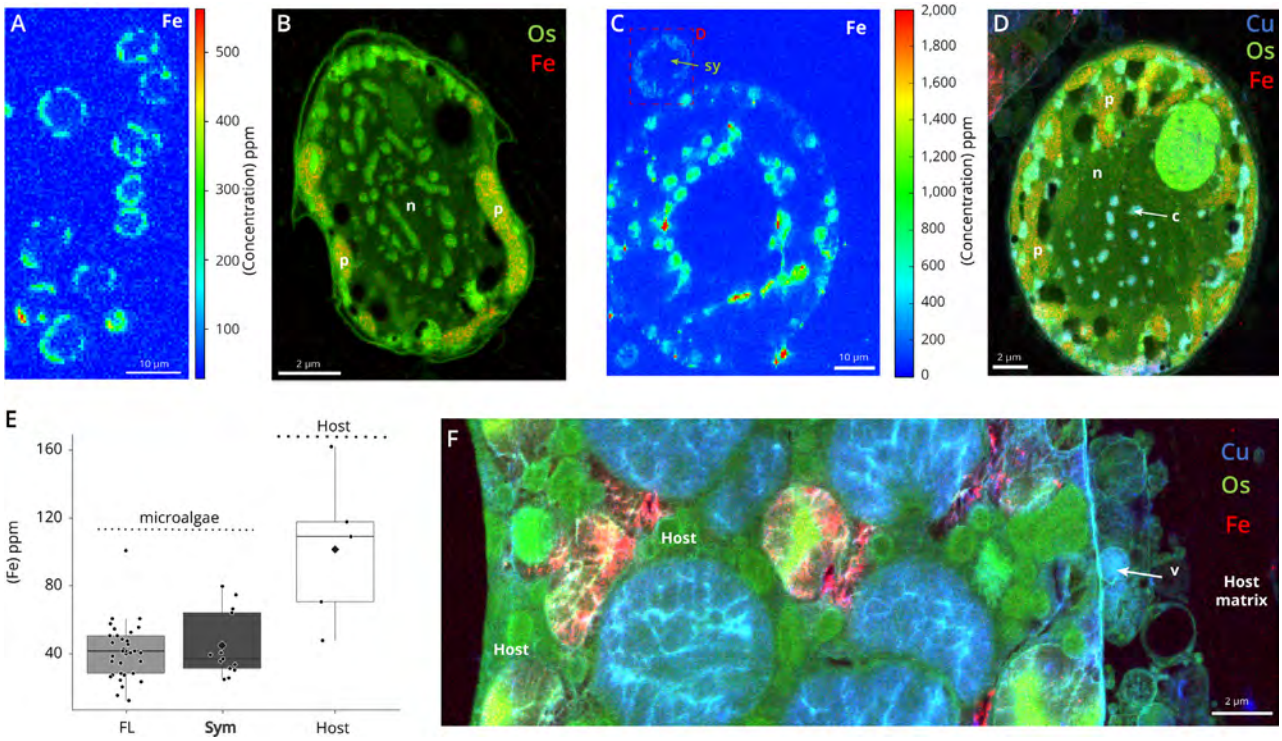

Fig. 6. Concentration and subcellular distribution of the trace metals iron (Fe) and copper (Cu) in microalgal and host cells unveiled by synchrotron X-ray fluorescence.
A, C. Subcellular quantitative mapping of iron (Fe) showing its concentration (ppm) in free-living microalgae (A), and in a host and its symbiotic microalga (C) (500 nm lateral resolution and at 7.3 keV). Scale bar: 10 µm.
B, D and F. High-resolution mapping (50 nm lateral resolution and at 17.5 keV) of osmium (Os, green, providing ultrastructure information), iron (Fe, red) and copper (Cu, blue) in free-living (B) and symbiotic (D) microalgae, and in the host cell (F) extracted from XRF hyperspectral images. Scale bars: 2 µm. Fe was mainly concentrated in plastids and host vacuoles. Note that Cu was only detected in symbiotic microalgae in the condensed chromatin (c) and cytoplasmic vacuoles, and was below the detection limit in free-living cells (see also Fig. S8).
E. Intracellular iron concentration (ppm) measured by S-XRF in the free-living (FL; $n = 33$) and symbiotic *Brandtodinium* (Symb, $n = 13$) cells (dark and light grey respectively), as well as in the host cell ($n = 5$). (n: nucleus; c: condensed chromatin; py: pyrenoid; p: plastid; h: host cell (Collodaria); m: matrix; v: vacuoles in the matrix).

containing molecules and/or proteins could be exchanged between both partners, thus stressing the role of the sulfur metabolism in photosymbiosis. Future analyses using complementary mass spectrometry imaging (e.g. ToF-SIMS) should be conducted to identify the S compounds in symbiotic cells at relatively high resolution (<1 µm) (Passarelli *et al*., 2017; Raina *et al*., 2017).

Subcellular mapping of metals in symbiotic cells

Trace metals are essential for diverse biochemical functions, such as photosynthesis, antioxidant and photoprotection (Morel and Price, 2003; Twining and Baines, 2013). The ecological success of photosymbiosis in oceanic waters must therefore rely on efficient mechanisms to uptake and regulate the exchange of these elements. More particularly, iron (Fe) has been shown to be pivotal for the physiology and health of coral photosymbioses (Reich, 2020). Yet, trace metal contents in planktonic photosymbioses remain largely unexplored, and their visualization and quantification in cells can provide information not only on the functioning of photosymbiosis but also of the impact in trace element cycling, especially because collodarians are important agents in vertical flux of organic matter (Guidi *et al*., 2016).

In collodarian colonies (including the symbiotic microalgae), metallome analyses showed that Mn, Fe, Zn and Ni were the main trace metals (intracellular metal quotas normalized against phosphorus as the biomass indicator: ranging from 10 to 30 mmol mol^{-1} P), while Co and Cu were measured in relatively lower concentration (from 0.1 to 20 mmol mol^{-1} P) (Fig. S7; Table S5). We can note that Fe quota is about three times more than that of zooplankton (4.6 and 4.9 mmol Fe/mol P) and phytoplankton (5.2 and 4.7 mmol Fe/mol P) communities sampled in different oceanic regions (Twining and Baines, 2013). In other words, one collodarian colony of several millimetres long can contain 100–300 ng of Fe.

Two S-XRF beam lines were used to visualize and quantify Fe in cells at 500 and 50 nm spatial resolution

with a beam energy of 7.3 and 17.5 keV respectively. In the host, Fe concentration tended to be twofold higher (mean ± SD = 100 ± 40 ppm; $n = 5$) than Fe in their symbiotic microalgae (mean ± SD = 45 ± 18 ppm; $n = 13$) (Fig. 6). More specifically, the host cytoplasm exhibited round structures with high concentration of Fe (*c*. 400 ppm). In microalgae, Fe was mainly concentrated in plastids and its concentration tended to be similar between free-living (42 ± 16 ppm; $n = 33$) and symbiotic cells (45 ± 18 ppm; $n = 13$) (Fig. 6B). Yet, the comparison is difficult between free-living and symbiotic microalgae, which grow in Fe-replete culture medium (5.85 μM) and in the host cell respectively. Nevertheless, the fact that microalgae seem to have similar Fe concentrations may indicate that the host could provide a Fe-replete microhabitat for its symbionts. It is known that the dinoflagellates Symbiodiniaceae increase their intracellular Fe concentration as the external Fe concentration increases (Rodriguez *et al*., 2016; Reich, 2020).

Using high-resolution and high-energy S-XRF beam line, copper (Cu) was also detected and its distribution mapped in cells. Of note, Cu was only detected in the symbiotic stage of the microalga but not in free-living (below the detection level) (Fig. 6 and Fig. S8). More specifically, within the cell, Cu was highly concentrated (6900 ppm) in the condensed DNA chromatin and vacuoles physically associated to plastids. In the host, Cu was present in large round structures and in some small vacuoles of the matrix (1900 ppm) (Fig. 6), which, like sulfur, may reflect the exchange of this metal between the host and the symbionts. The increase of Cu concentration in symbiotic microalgae represents a symbiotic fingerprint and stresses the influence of the host on their metal homeostasis. It is known that Cu is needed in the electron transport chain of the plastid (plastocyanin) and mitochondria (cytochrome c oxidase) and is a key cofactor in many proteins (Morel *et al*., 2003), but this study cannot resolve the function of this metal in the symbiosis. Nevertheless, Cu is known to be toxic at very low concentration (Morel and Price, 2003), to induce ROS production and DNA damage and is implicated in various neurological disorders, implying that its exchange between symbiotic partners should be highly regulated. Overall, the subcellular mapping of trace metals calls for more studies on the role of these metals in the symbiotic interaction. Because collodaria are significant contributors to the vertical flux in the ocean (Biard *et al*., 2016), these results also stress the role of photosymbiosis in the biogeochemical cycles of trace metals.

Conclusions

The aim of this study was to improve our understanding on the functioning and metabolism of the uncultivated yet ubiquitous oceanic photosymbiosis between Collodaria and its symbiotic microalgae *Brandtodinium* using multimodal subcellular imaging. We showed that the volume occupancy of the plastid and C-fixing pyrenoid of the microalga was higher in symbiosis and was accompanied by a higher photosynthetic performance at high light. By contrast, the topology and volume of the mitochondria were similar, suggesting similar respiration rate in free-living and symbiotic microalgae. The enlargement of the photosynthetic apparatus seems to be a morphological trait in planktonic photosymbiosis as it was also found in other radiolarians (Acantharia) living with the microalga *Phaeocystis* (Decelle *et al*., 2019; Uwizeye *et al*., 2021b). Yet, the expansion of the photosynthetic machinery observed here in *Brandtodinium* is less substantial than in *Phaeocystis*, which can increase by 100-fold the volume of total plastids (Uwizeye *et al*., 2021b). This may be explained by the level of integration and growth of the microalgal cell within its host. In Collodaria, symbiotic microalgae are outside the host endoplasm in the gelatinous matrix, can divide [possibly at lower rate than free-living cells in culture like in coral photosymbioses (Davy *et al*., 2012)] and they are not associated to a single host cell but can freely move within the greenhouse-like colony interacting with several host cells over time. By contrast, the level of integration and host control is higher in Acantharia since the microalga *Phaeocystis* is constrained within the endoplasm of its host and its cell division is blocked but plastids continue to divide producing a highly voluminous algal cell. This indicates that radiolarian hosts have different strategies to control and accommodate their symbiotic microalgae. Note that the comparison between free-living and symbiotic microalgae in this study cannot provide a complete understanding of the metabolism and physiology of symbiotic microalgae in their host. The different nutrient and light conditions and potentially cell growth in both life stages could be confounding variables. Therefore, future studies should use new techniques and methods to strengthen the comparison between *ex hospite* and *in hospite* lifestyles (Maruyama and Weis, 2021). Manipulation of the free-living stage (e.g. different nutritional conditions) or harvesting cultured microalgae at different growth phases (e.g. stationary phase) could be considered to better understand the metabolic and morphological flexibility of the microalgal cell.

Based on 3D electron microscopy and chemical imaging, we suggest that the metabolic connection between partners in Collodaria between partners occurs through numerous extracellular vacuoles in the matrix, which contained nutrients, such as nitrogen, sulfur and copper. These nutrients are therefore important for the functioning of the symbiosis and future analyses are required to identify the underlying metabolites. We demonstrated that

carbon and nitrogen were stored by the symbiotic microalgae during the day and transferred in low amount in the Golgi apparatus of the host. This transfer seems to be less efficient than other planktonic and benthic photosymbioses (Kopp *et al*., 2013; LeKieffre *et al*., 2020), presumably due to the loose interaction between the symbionts and the host cells. Dynamic nutrient exchange at different time points during day and night periods should be carried out in future stable isotope labelling studies to fully understand the metabolic connection and flux of nutrients in this ecologically successful photosymbiosis. Overall, the visualization of the morphology and metabolism of this symbiosis at the nanoscale calls for more studies to better assess the importance of Collodaria in the biogeochemical cycles of carbon, sulfur and metals in the ocean.

Experimental procedures

Sampling and isolation of collodaria and microalgae

Colonies of collodarians (radiolarians) were gently collected at the subsurface in the Mediterranean Sea (Villefranche-sur-Mer, France) using a plankton net of 150 μm in mesh size. Live collodarians (*Collozoum* spp. from the family Sphaerozoidae) were then isolated through the binocular, maintained in filtered seawater and controlled light and temperature conditions, and cryofixed with high pressure freezing to preserve the native ultrastructure and chemistry of cells (Moore *et al*., 2012; Kashiv *et al*., 2016; Decelle *et al*., 2020). In parallel, the microalgae [the dinoflagellate *B. nutricula* RCC 3387; isolated from Collodaria in Villefranche-sur-Mer (Probert *et al*., 2014)] grown in culture medium K2 (http://roscoff-culture-collection.org/culture-media) at 20°C were also cryofixed in the exponential phase in the same conditions. Time-lapse video using an inverted microscope was conducted on live colonies upon collection during several hours with image capture every 20 s. Trajectory of symbiotic microalgae over time was reconstructed with the plugin Particle Tracker for Fiji (Sbalzarini and Koumoutsakos, 2005).

Photophysiology

Photosynthetic activity was imaged with a fluorescence imaging setup described in Decelle *et al*. (2019). The photosynthetic ETR was calculated as the product of the light intensity times the photochemical yield in the light: PFD $\times$ ($F_m' - F$)/F_m'), where F and F_m' are the steady-state and maximum fluorescence intensities in light-acclimated cells respectively, and photosynthetic flux density (PFD) is the light irradiance in μmol quanta $\times$ m^{-2} s^{-1}. The light intensity was increased stepwise from 29 to 1200 μmol quanta $\times$ m^{-2} s^{-1}. The photoprotective responses were evaluated by measuring the NPQ of fluorescence (Maxwell and Johnson, 2000) using the fluorescence setup described above. The NPQ was calculated as $1 - (F_m'/F_m)$. The F_v/F_m parameter (maximum potential quantum efficiency of Photosystem II) was assessed as $F_m - F_o/F_m$ where F_m and F_0 are the maximum and minimum fluorescence intensities. This parameter was also measured on single symbiont cells using a homemade fluorescence imaging setup. The system uses a high sensitivity camera (Orca Flash 4.0 LT, Hamamatsu, Japan) equipped with a near-infrared long-pass filter (RG 695 Schott, Germany), mounted on an optical microscope (CKX 53 Olympus, Japan). Fluorescence was measured upon excitation with short pulses (duration 260 μs) of blue light ($\lambda = 470$ nm $\pm$ 12 nm), and green LEDs were used to generate short saturating pulses (intensity 3000 μmol photons m^{-2} s^{-1}, duration 250 ms) to induce the maximum fluorescence F_m. The blue and green LEDs were mounted on an array located on the upper part of the microscope, i.e. opposite to the objectives used for detection. We used a 20$\times$ (numerical aperture = 0.45) objective to scan the slits in the transmission mode.

Sample preparation for electron microscopy and chemical imaging

Rapid freezing methods are universally accepted as superior to chemical fixation in preserving cell ultrastructure and chemistry (Decelle *et al*., 2020). Symbiotic collodarians (host and algal symbionts) and free-living microalgae (previously centrifugated at 3000*g* for 2 min) were therefore cryo-fixed in seawater as in Decelle *et al*. (2019), using high-pressure freezing (HPM100, Leica) where cells were subjected to a pressure of 210 MPa at −196°C for 30 ms, followed by freeze substitution (FS) (EM ASF2, Leica). For the FS, a mixture 2% (wt./vol.) osmium tetroxide and 0.5% (wt./vol.) uranyl acetate in dried acetone was used. The FS machine was programmed as follows: 60–80 h at −90°C, heating rate of 2°C h^{-1} to −60°C (15 h), 10–12 h at −60°C, heating rate of 2°C h^{-1} to −30°C (15 h), 10–12 h at −30°C. Samples were then washed in acetone four times for 20 min at −30°C and embedded in anhydrous araldite. Without accelerator, a graded resin/acetone (vol./vol.) series was used (30%, 50% and 70% resin) with each step lasting 2 h at increased temperature: 30% resin/acetone bath from −30°C to −10°C, 50% resin/acetone bath from −10°C to 10°C, 70% resin/acetone bath from 10°C to 20°C. Samples were then placed in 100% resin without accelerator for 8–10 h and in 100% resin with accelerator (BDMA) for 8 h at room temperature. Prior to ultra-sectioning, symbiotic cells were observed in the resin block

to define the trimming region and the *z*-position of cells in the block. Trimming around the targeted cells was performed with razor blades and the EM Trimming Leica machine. Thin sections (200–400 nm thick) were then obtained using an ultramicrotome (Leica EM) with ultra-diamond knife (Diatom) and placed on 10-mm arsenic-doped silicon wafers for NanoSIMS, and on Si_3N_4 membrane windows for synchrotron X-rays fluorescence. Adjacent sections of 60–80 nm thick were also obtained for TEM analysis.

FIB-SEM acquisition and analysis

For FIB-SEM, upon high-pressure freezing, the cocktail of the freeze substitution contained 2% (wt./vol.) osmium tetroxide and 0.5% (wt./vol.) uranyl acetate in dried acetone as in Uwizeye *et al*. (2021a, 2021b). The cells were washed four times in anhydrous acetone for 15 min each at −30°C and gradually embedded in anhydrous araldite resin. The sample was trimmed with a 90° diamond knife (Diatome) to expose the cells at two surfaces (the imaging surface and the surface perpendicular to the FIB) and optimize the acquisition (Maco *et al*., 2014). When targeting the symbiotic microalgae within its host, the trimming was targeted towards the periphery of the organisms where they were in higher numbers. After the sample was trimmed, it was mounted onto the edge of an SEM stub (Agar Scientific) using silver conductive epoxy (CircuitWorks) with the trimmed surfaces facing up and towards the edge of the stub. The sample was gold sputter coated (Quorum Q150RS; 180 s at 30 mA) and placed into the FIB-SEM for acquisition (Crossbeam 540, Carl Zeiss Microscopy GmbH). Once the region of interest (ROI) was located in the sample, Atlas3D software (Fibics and Carl Zeiss Microscopy GmbH) was used to perform sample preparation and 3D acquisitions. First, a 1 μm platinum protective coat (20–30 μm^2 depending on ROI) was deposited with a 1.5 nA FIB current. The rough trench was then milled to expose the imaging cross-section with a 15 nA FIB current, followed by a polish at 7 nA. The 3D acquisition milling was done with a 1.5 nA FIB current. For SEM imaging, the beam was operated at 1.5 kV/700 pA in analytic mode using an EsB detector (1.1 kV collector voltage) at a dwell time of 8 μs with no line averaging. For each slice, a thickness of 8 nm was removed, and the SEM images were recorded with a pixel size of 8 nm, providing an isotropic voxel size of $8 \times 8 \times 8$ nm^3. Whole volumes were imaged with 1000–1200 frames, depending on the *Brandtodinium* cells. Raw electron microscopy data are deposited in EMPIAR, accession code EMPIAR-47483651. Source data are provided with this article.

The first step of image processing was to crop the free-living and symbiotic *Brandtodinium* cells using the open software Fiji (https://imagej.net/Fiji), followed by image registration (stack alignment), noise reduction, semi-automatic segmentation, 3D reconstruction of microalgae cells and morphometric analysis as in (Uwizeye *et al*., 2021a). Image registration was done by the FIJI plugin 'Linear Stack Alignment with SIFT' (Lowe, 2004), then fine-tuned by AMST (Hennies *et al*., 2020). Aligned image stacks were filtered to remove noise and highlight contours using a Mean filter in Fiji (0.5 pixel radius). Segmentation of organelles and other cellular compartments of *Brandtodinium* and Collodaria was carried out with 3D Slicer software (Kikinis *et al*., 2014) (www.slicer.org), using a manually curated, semi-automatic pixel clustering mode (5–10 slices are segmented simultaneously in *z*) as in Uwizeye *et al*. (2021a). We assigned colours to segmented regions using paint tools and adjusted the threshold range for image intensity values. Morphometric analyses were performed with the 3D slicer module 'segmentStatistics' on the different segments (segmented organelles) and converted to μm^3 or μm^2 taking into account the voxel size of 8 nm (Table S1).

Synchrotron X-ray fluorescence imaging

S-XRF hyperspectral images were acquired on the ID21 and ID16B-NA beamlines of the European Synchrotron Radiation Facility (Cotte *et al*., 2017, Martinez-Criado *et al*. 2016). 300 nm-thick cell sections were laid on Si_3N_4 membranes. On ID21 the incoming X-rays were tuned to the energy of 7.3 keV with a fixed-exit double crystal Si (111) monochromator, and focused to 0.3×0.8 μm^2 with a Kirkpatrick–Baez (KB) mirror system, yielding a flux of 5×10^{10} ph s^{-1}. The experiment was performed under vacuum (10^{-5}–10^{-4} mbar). The emitted fluorescence signal was detected with energy dispersive, large area (80 mm^2) SDD detectors equipped with a Be window (SGX from RaySpec). Images were acquired by raster-scanning the sample in the X-ray focal plane, with a 0.5×0.5 μm^2 step and 500 ms dwell time. The detector response was calibrated over a thin film reference sample consisting of layers of elements in ng mm^{-2} concentration sputtered on a 200 nm thick Si_3N_4 membrane (RF7-200-S2371 from AXO), measured using the same acquisition parameters.

On ID16B-NA, a beam of 17.5 keV focused to 50×50 nm^2 through KB mirrors was used to excite the samples. The photon flux at sample was $\sim 2 \times 10^{11}$ ph s^{-1}. High-resolution XRF images (50×50 nm^2 step size) were acquired in air, with a dwell time of 100 ms/pixel. Two 3-element SDD detector arrays were used to collect fluorescence from the sample. The detector response was calibrated over a thin film reference sample (RF8-200-S2453 from AXO). High-resolution images were acquired for free and symbiotic microalgae, and in selected areas of the hosts.

Hyperspectral images acquired in both beamlines were normalized by the incoming photon flux and subjected to the same data analysis protocol. Elemental mass fractions were calculated from fundamental parameters with the PyMca software package (Solé *et al*., 2007), assuming a biological matrix of light elements (H, C, N, O) and a density of 1 g cm^{-3}, as reported in the NIST Star database for the standard composition of soft tissue (https://www.physics.nist.gov/cgi-bin/Star/compos.pl?matno=261). The calculation of the elemental concentrations in specific areas was performed by manually selecting the pixels in the ROI and summing up their fluorescence signal; the sum spectrum normalized by the number of pixels was then subjected to spectral deconvolution, and the peak areas were converted in mass fractions (see also Table S4).

NanoSIMS mapping of C, N, P and S in samples of natural isotopic composition

The wafers containing thin sections were first coated with 20 nm gold–palladium and analysed with a NanoSIMS 50 L (Cameca, Gennevilliers, France), using 2 pA beam of 16 keV Cs^+ primary ions focused to 70 nm spot. The analysed sample area of 25 × 25 μm^2 was scanned in 512 × 512 pixel raster with a dwelling time of 2 ms/pixel. Prior to the analysis, the area of 100 × 100 μm^2 involving the analysis FoV was pre-implanted for 15 min with 200 pA Cs^+ beam to equilibrate the secondary ion yield. The data were acquired in 20–30 plains upon consecutive scanning with the primary ion beam. Secondary ions extracted from each pixel of the sample surface ($^{16}O^-$, $^{12}C_2{}^-$, $^{12}C^{13}C^-$, $^{12}C^{14}N^-$, $^{13}C^{14}N^-$, $^{31}P^-$ and $^{32}S^-$) were separated according to their mass to charge ratio (*m*/*z*) with mass resolving power above 8000 (MRP = M/dR) achieved with 20 × 140 μm nominal size (width × height) of the entrance slit, 200 × 200 μm aperture, 40 × 1800 μm exit slits and the energy slit blocking 20% of ions at their high-energy distribution site. Complete 200 nm of section depth was consumed upon the analysis. The acquired data were evaluated using Look@nanoSIMS (LANS) software (Polerecky *et al*., 2012).

^{13}C- and ^{15}N-labeling for TEM-NanoSIMS analysis

Collodarians were collected at the subsurface in the Mediterranean Sea (Villefranche-sur-Mer, France) in September 2019. Live collodarians were then isolated under a binocular, transferred in 50 ml plastic flasks filled with filtered (0.22 μm) natural seawater (collected at the sea surface the same day). The day after the sampling, the incubation was initiated at 2 pm under controlled light and temperature conditions (20°C) by spiking with $H^{13}CO_3^-$ and $^{15}NH_4^+$ (99%, Sigma-Aldrich) to reach final concentrations of 2 mM and 10 μM respectively. After 3 h of incubation, the experiment was stopped by removing the collodarian colonies from the spiked seawater and transferring them in filtrated seawater. The samples were then immediately cryofixed with high-pressure freezing and processed as explained above. For correlated EM – NanoSIMS, ultrathin sections of 70 or 200 nm thick were obtained. The 70 nm sections were mounted onto copper grids or slots coated with a formvar – carbon film. Sections were then stained in 1% uranyl acetate (10 min) and lead citrate (5 min). Micrographs were obtained using a Tecnai G2 Spirit BioTwin microscope (FEI) operating at 120 kV with an Orius SC1000 CCD camera (Gatan). The 200 nm sections were mounted on silicon wafers and imaged with a GeminiSEM (Zeiss) operating in ESB mode at 3 kV. For NanoSIMS observations, sections were coated with 10 nm of gold and analysed with a NanoSIMS 50 l (Cameca, Lausanne, Switzerland), using a caesium (Cs^+) primary ion beam with a current of about 2 pA and an energy of 16 keV. The primary ion beam was focused to a nominal spot size of ∼120–150 nm and stepped over the sample in a 256 × 256 pixel raster to generate secondary ions with a dwelling time of 5 ms/pixel. The raster areas (scanning surface area) were defined based on previous SEM/TEM observations and were between 10 × 10 μm^2 to 40 × 40 μm^2. Secondary ions ($^{19}F^-$, $^{12}C_2{}^-$, $^{13}C^{12}C^-$, $^{12}C^{14}N^-$, $^{12}C^{15}N^-$, $^{31}P^-$ and $^{32}S^-$) were simultaneously collected in electron multipliers at a mass resolution ($M/\Delta M$) of about 8000 (Cameca definition). Each NanoSIMS image consists of 6–10 sequential images, drift corrected and accumulated using the software LANS (Polerecky *et al*., 2012) to quantify mean ^{13}C and ^{15}N enrichments of different sub-cellular structures. For control (i.e. not enriched) samples, four images were acquired including five symbiotic dinoflagellates and two different areas of the host cell (Table S2). These control images were used to determine the standard ratio against which the experimental ^{13}C-and ^{15}N-enrichments were quantified. For ^{13}C and ^{15}N-enriched samples, two distinct collodarian colonies were analysed.

Quantitation of assimilation activity

The cellular activity in assimilation of carbon and nitrogen was derived from the detected changes in nitrogen and carbon isotopic composition. Changes in ^{13}C and ^{15}N fractions are not directly proportional to cellular activity and the assimilation activity was therefore expressed as the relative assimilation K^i_A (Stryhanyuk *et al*., 2018):

$$K^i_A = \frac{R_f - R_i}{(1 + R_i) \times \{D_{gs} \times (1 + R_f) - R_f\}}$$

The K^i_A represents the *fraction* (in at.%) of carbon (^{12}C and ^{13}C) or nitrogen (^{14}N and ^{15}N) assimilated from a

growth substrate into a biomass unit *relatively to its initial* content (carbon or nitrogen; before incubation with a labelled substrate) in a biomass unit, e.g. cell or cell fragment.

$$K_A = \frac{D_f - D_i}{D_{gs} - D_f}$$

where R_i/D_i is the initial isotope ratio/fraction in biomass unit (before incubation with isotope-labelled growth substrate); R_f/D_f is the final isotope ratio/fraction in biomass unit (after incubation with isotope-labelled growth substrate) and D_{gs} is the fraction of heavy isotope in growth substrate.

Bulk quantification of metals in collodaria (metallome)

Free-living microalgae (*Brandtodinium*) in culture and collodarian colonies (single colonies and a mix of different colonies) collected in surface waters of the Mediterranean Sea were centrifugated to remove the medium and seawater respectively. Cells were then cryofixed and preserved at −80°C. For metal extraction, samples were dehydrated and mineralized in 200 µl 65% (wt./vol.) ultrapure HNO_3 at 90°C for 4 h. Digested samples were diluted in distilled water and analysed using an iCAP RQ quadrupole mass instrument (Thermo Fisher Scientific GmbH, Germany). The instrument was used with a MicroMist U-Series glass concentric nebulizer, a quartz spray chamber cooled at 3°C, a Qnova quartz torch, a nickel sample cone and a nickel skimmer cone equipped with a high-sensitivity insert. Elements were analysed using either the standard mode (for ^{27}Al, ^{31}P, ^{111}Cd) and/or the kinetic energy discrimination mode with helium as the collision cell gas (for ^{31}P, ^{55}Mn, ^{56}Fe, ^{57}Fe, ^{58}Ni, ^{59}Co, ^{60}Ni, ^{63}Cu, ^{64}Zn, ^{65}Cu, ^{66}Zn). Concentrations were determined using standard curves and corrected using an internal standard solution of 103Rh added online. Data integration was done using the Qtegra software (version 2.8.2944.115). Element content was normalized to phosphorus (P) content as in Twining and Baines (2013)) (see Table S5).

Acknowledgements

This research was supported by the Dept. of Isotope Biogeochemistry, Centre for Chemical Microscopy (ProVIS), Helmholtz Centre for Environmental Research (UFZ). We thank Estelle Bigeard and Fabien Lombard for sample collection and the institutes the Laboratoire d'Océanographie de Villefranche-sur-Mer (LOV) and the marine service crew. This research is also supported by EMBRC-France, whose French state funds are managed by the ANR within the Investments of the Future program under reference ANR-10-INBS-02. This work used the platforms of the Grenoble Instruct centre (ISBG; UMS 3518 CNRS-CEA-UJF-EMBL) with support from FRISBI (ANR-10-INSB-05-02) and GRAL (ANR-10-LABX-49-01) within the Grenoble Partnership for Structural Biology (PSB). We thank Guy Schoehn and Christine Moriscot, and the electron microscope facility, which is supported by the Rhône-Alpes Region, the Fondation Recherche Medicale (FRM), the fonds FEDER, the Centre National de la Recherche Scientifique (CNRS), the CEA, the University of Grenoble, EMBL and the GIS-Infrastructures en Biologie Sante et Agronomie (IBISA). The FIB-SEM work was done in collaboration with the electron microscopy core facility at EMBL Heidelberg. The authors acknowledge the support and the use of resources of Instruct, a Landmark ESFRI project. The authors acknowledge the ESRF for providing beamtime for this project (LS-2625 and LS-2857 on ID16B-NA, in-house beamtime on ID21), and Marine Cotte and Hiram Castillo-Michel for their help in the experiments. We thank Louise Soegaard Jensen for access and help with SEM imaging, and Abby Ren, Stephane Escrig and Anders Meibom for NanoSIMS access and assistance. The authors are grateful to Dr. Lubos Polerecky (Utrecht University) for the continuous development of the LANS software, technical assistance and prompt implementation of software features.

Author Contributions

J.D. conceived and designed research, and drafted the manuscript; J.D., G.V., C.L., H.S., S.R., G.F. participated in data analysis, and helped draft and critically revised the manuscript. N.M., B.G., F.C., S.M., R.T., N.S., Y.S. contributed to data acquisition, culture collection, sample preparation and helped draft the manuscript. All authors gave final approval for publication and agree to be held accountable for the work performed therein.

References

Anderson, O.R. (1976) Ultrastructure of a colonial radiolarian *Collozoum inerme* and a cytochemical determination of the role of its zooxanthellae. *Tissue Cell* **8**: 195–208.

Bhaud, Y., Guillebault, D., Lennon, J.F., Defacque, H., Soyer-Gobillard, M.O., and Moreau, H. (2000) Morphology and behaviour of dinoflagellate chromosomes during the cell cycle and mitosis. *J Cell Sci* **113**: 1231–1239.

Biard, T., Bigeard, E., Audic, S., Poulain, J., Gutierrez-Rodriguez, A., Pesant, S., *et al*. (2017) Biogeography and diversity of Collodaria (Radiolaria) in the global ocean. *ISME J* **11**: 1331–1344.

Biard, T., Stemmann, L., Picheral, M., Mayot, N., Vandromme, P., Hauss, H., *et al*. (2016) In situ imaging reveals the biomass of giant protists in the global ocean. *Nature* **532**: 504–507.

Blank, R.J. (1987) Cell architecture of the dinoflagellate *Symbiodinium* sp. inhabiting the Hawaiian stony coral *Montipora verrucosa*. *Mar Biol* **94**: 143–155.

Boncompain, G., and Perez, F. (2013) The many routes of Golgi-dependent trafficking. *Histochem Cell Biol* **140**: 251–260.

Breitbarth, E., Wohlers, J., Kläs, J., LaRoche, J., and Peeken, I. (2008) Nitrogen fixation and growth rates of *Trichodesmium* IMS-101 as a function of light intensity. *Mar Ecol Prog Ser* **359**: 25–36.

Cabello, A.M., Cornejo-Castillo, F.M., Raho, N., Blasco, D., Vidal, M., Audic, S., *et al*. (2016) Global distribution and vertical patterns of a prymnesiophyte-cyanobacteria obligate symbiosis. *ISME J* **10**: 693–706.

Caron, D.A. (2016) Ocean science: the rise of Rhizaria. *Nature* **532**: 444–445.

Caron, D.A., Michaels, A.F., Swanberg, N.R., and Howse, F. A. (1995) Primary productivity by symbiont-bearing planktonic sarcodines (Acantharia, Radiolaria, Foraminifera) in surface waters near Bermuda. *J Plankton Res* **17**: 103–129. https://doi.org/10.1093/plankt/17.1.103

Clode, P.L., Saunders, M., Maker, G., Ludwig, M., and Atkins, C.A. (2009) Uric acid deposits in symbiotic marine algae. *Plant Cell Environ* **32**: 170–177.

Cotte, M., Pouyet, E., Salomé, M., Rivard, C., De Nolf, W., Castillo-Michel, H., *et al*. (2017) The ID21 X-ray and infrared microscopy beamline at the ESRF: status and recent applications to artistic materials. *J Anal At Spectrom* **32**: 477–493.

Davy, S.K., Allemand, D., and Weis, V.M. (2012) Cell biology of cnidarian-dinoflagellate symbiosis. *Microbiol Mol Biol Rev* **76**: 229–261.

de Vargas, C., Audic, S., Henry, N., Decelle, J., Mahe, F., Logares, R., *et al*. (2015) Eukaryotic plankton diversity in the sunlit ocean. *Science* **348**: 1261605.

Decelle, J., Colin, S., and Foster, R.A. (2015) Photosymbiosis in marine planktonic protists. In *Marine Protists: Diversity and Dynamics*, Ohtsuka, S., Suzaki, T., Horiguchi, T., Suzuki, N., and Not, F. (eds). Japan, Tokyo: Springer, pp. 1–637. 10.1007/978-4-431-55130-0_19

Decelle, J., Probert, I., Bittner, L., Desdevises, Y., Colin, S., de Vargas, C., *et al*. (2012) An original mode of symbiosis in open ocean plankton. *Proc Natl Acad Sci U S A* **109**: 18000–18005.

Decelle, J., Stryhanyuk, H., Gallet, B., Veronesi, G., Schmidt, M., Balzano, S., *et al*. (2019) Algal remodeling in a ubiquitous planktonic photosymbiosis. *Curr Biol* **29**: 968–978.e4.

Decelle, J., Veronesi, G., Gallet, B., Stryhanyuk, H., Benettoni, P., Schmidt, M., *et al*. (2020) Subcellular chemical imaging: new avenues in cell biology. *Trends Cell Biol* **30**: 173–188. https://doi.org/10.1016/j.tcb.2019.12.007

Dennett, M.R., Caron, D.A., Michaels, A.F., Gallager, S.M., and Davis, C.S. (2002) Video plankton recorder reveals high abundances of colonial radiolaria in surface waters of the central north pacific. *J Plankton Res* **24**: 797–805. https://doi.org/10.1093/plankt/24.8.797

Engel, B.D., Schaffer, M., Cuellar, L.K., Villa, E., Plitzko, J. M., and Baumeister, W. (2015) Native architecture of the *Chlamydomonas* chloroplast revealed by in situ cryo-electron tomography. *Elife* **4**: e04889.

Faure, E., Not, F., Benoiston, A.S., Labadie, K., Bittner, L., and Ayata, S.D. (2019) Mixotrophic protists display contrasted biogeographies in the global ocean. *ISME J* **13**: 1072–1083.

Gautier, A., Michel-Salamin, L., Tosi-Couture, E., McDowall, A. W., and Dubochet, J. (1986) Electron microscopy of the chromosomes of dinoflagellates in situ: confirmation of Bouligand's liquid crystal hypothesis. *J Ultrastruct Res Mol Struct Res* **97**: 10–30.

Geider, R., and La Roche, J. (2002) Redfield revisited: variability of C:N:P in marine microalgae and its biochemical basis Redfield revisited: variability of C:N:P in marine microalgae and its biochemical basis. *Eur J Phycol* **37**: 1–17.

Genty, B., Briantais, J.M., and Baker, N.R. (1989) The relationship between the quantum yield of photosynthetic electron transport and quenching of chlorophyll fluorescence. *Biochim Biophys Acta - Gen Subj* **990**: 87–92. https://doi.org/10.1016/S0304-4165(89)80016-9

Giordano, M., Norici, A., and Hell, R. (2005) Sulfur and phytoplankton: acquisition, metabolism and impact on the environment. *New Phytol* **166**: 371–382. doi: 10.1111/j.1469-8137.2005.01335.x.

Gornik, S.G., Hu, I., Lassadi, I., and Waller, R.F. (2019) The biochemistry and evolution of the dinoflagellate nucleus. *Microorganisms* **7**: 245.

Guidi, L., Chaffron, S., Bittner, L., Eveillard, D., Larhlimi, A., Roux, S., *et al*. (2016) Plankton networks driving carbon export in the oligotrophic ocean. *Nature* **532**: 465–470.

Gutierrez-Rodriguez, A., Pillet, L., Biard, T., Said-Ahmad, W., Amrani, A., Simó, R., and Not, F. (2017) Dimethylated sulfur compounds in symbiotic protists: a potentially significant source for marine DMS(P). *Limnol Oceanogr* **62**: 1139–1154.

Hennies, J., Lleti, J.M.S., Schieber, N.L., Templin, R.M., Steyer, A.M., and Schwab, Y. (2020) AMST: alignment to median smoothed template for focused ion beam scanning electron microscopy image stacks. *Sci Rep* **10**: 1–10.

Karl, D.M., Church, M.J., Dore, J.E., Letelier, R.M., and Mahaffey, C. (2012) Predictable and efficient carbon sequestration in the North Pacific Ocean supported by symbiotic nitrogen fixation. *Proc Natl Acad Sci U S A* **109**: 1842–1849.

Kashiv, Y., Austin, J.R., Lai, B., Rose, V., Vogt, S., and El-Muayed, M. (2016) Imaging trace element distributions in single organelles and subcellular features. *Sci Rep* **6**: 21437.

Kikinis, R., Pieper, S.D., and Vosburgh, K.G. (2014) 3D slicer: a platform for subject-specific image analysis, visualization, and clinical support. In *Intraoperative imaging and image-guided therapy*. New York, NY: Springer New York, pp. 277–289.

Kopp, C., Domart-Coulon, I., Escrig, S., Humbel, B.M., Hignette, M., and Meibom, A. (2015) Subcellular investigation of photosynthesis-driven carbon assimilation in the symbiotic reef coral *Pocillopora damicornis*. *MBio* **6**: 1–9.

Kopp, C., Pernice, M., Domart-Coulon, I., Djediat, C., Spangenberg, J.E., Alexander, D.T.L., *et al*. (2013) Highly dynamic cellular-level response of symbiotic coral to a sudden increase in environmental nitrogen. *MBio* **4**: 1–9.

Lekieffre, C., Jauffrais, T., Geslin, E., Jesus, B., Bernhard, J. M., Giovani, M.E., and Meibom, A. (2018) Inorganic carbon and nitrogen assimilation in cellular compartments of a benthic kleptoplastic foraminifer. *Sci Rep* **8**: 1–12.

LeKieffre, C., Spero, H.J., Fehrenbacher, J.S., Russell, A.D., Ren, H., Geslin, E., and Meibom, A. (2020) Ammonium is the preferred source of nitrogen for planktonic foraminifer

and their dinoflagellate symbionts. *Proc Biol Sci* **287**: 20200620.

Liu, Z., Mesrop, L.Y., Hu, S.K., and Caron, D.A. (2019) Transcriptome of *Thalassicolla nucleata* holobiont reveals details of a radiolarian symbiotic relationship. *Front Mar Sci* **6**: 1–11.

Loussert-Fonta, C., Toullec, G., Paraecattil, A.A., Jeangros, Q., Krueger, T., Escrig, S., and Meibom, A. (2020) Correlation of fluorescence microscopy, electron microscopy, and NanoSIMS stable isotope imaging on a single tissue section. *Commun Biol* **3**: 362.

Lowe, D.G. (2004) Distinctive image features from scale-invariant keypoints. *Int J Comput Vis* **60**: 91–110.

Maco, B., Cantoni, M., Holtmaat, A., Kreshuk, A., Hamprecht, F.A., and Knott, G.W. (2014) Semiautomated correlative 3D electron microscopy of in vivo-imaged axons and dendrites. *Nat Protoc* **9**: 1354–1366.

Maruyama, S., and Weis, V.M. (2021) Limitations of using cultured algae to study cnidarian-algal symbioses and suggestions for future studies. *J Phycol* **57**: 30–38.

Matthews, J.L., Oakley, C.A., Lutz, A., Hillyer, K.E., Grossman, A.R., Weis, V.M., and Davy, S.K. (2018) Partner switching and metabolic flux in a model cnidarian – symbiodinium symbiosis. *Proc R Soc B* **285**(1892). https://doi.org/10.1098/rspb.2018.2336

Martínez-Criado G., Villanova J., Tucoulou R., Salomon D., Suuronen J.-P., Labouré S., *et al*. (2016) ID16B: a hard X-ray nanoprobe beamline at the ESRF for nano-analysis. *J Synchrotron Radiat*, **23**(1): 344–352. https://doi.org/10.1107/s1600577515019839

Maxwell, K., and Johnson, G.N. (2000) Chlorophyll fluorescence – a practical guide. *J Exp Bot* **51**: 659–668.

Mellman, I., and Simons, K. (1992) The Golgi complex: In vitro veritas?. *Cell*, **68**(5): 829–840. https://doi.org/10.1016/0092-8674(92)90027-a

Meyer, M.T., Whittaker, C., and Griffiths, H. (2017) The algal pyrenoid: key unanswered questions. *J Exp Bot* **68**: 3739–3749.

Mojzeš, P., Gao, L., Ismagulova, T., Pilátová, J., Moudříková, Š., Gorelova, O., *et al*. (2020) Guanine, a high-capacity and rapid-turnover nitrogen reserve in microalgal cells. *Proc Natl Acad Sci U S A* **117**: 32722–32730.

Moore, C.M., Mills, M.M., Arrigo, K.R., Berman-Frank, I., Bopp, L., Boyd, P.W., *et al*. (2013) Processes and patterns of oceanic nutrient limitation. *Nat Geosci* **6**: 701–710.

Moore, K.L., Lombi, E., Zhao, F.J., and Grovenor, C.R.M. (2012) Elemental imaging at the nanoscale: NanoSIMS and complementary techniques for element localisation in plants. *Anal Bioanal Chem* **402**: 3263–3273.

Morel, F.M.M., Milligan, A.J., and Saito, M.A. (2003) Marine bioinorganic chemistry: the role of trace metals in the oceanic cycles of major nutrients. In Henry Elderfield (ed.), *Treatise on Geochemistry*, Vol. 6. Elsevier, pp. 113–143. https://doi.org/10.1016/B0-08-043751-6/06108-9

Morel, F.M.M., and Price, N.M. (2003) The biogeochemical cycles of trace metals in the oceans. *Science* **300**: 944–947.

Passarelli, M.K., Pirkl, A., Moellers, R., Grinfeld, D., Kollmer, F., Havelund, R., *et al*. (2017) The 3D OrbiSIMS – label-free metabolic imaging with subcellular lateral resolution and high mass-resolving power. *Nat Methods* **14**: 1175–1183.

Polerecky, L., Adam, B., Milucka, J., Musat, N., Vagner, T., and Kuypers, M.M.M. (2012) Look@NanoSIMS - a tool for the analysis of nanoSIMS data in environmental microbiology. *Environ Microbiol* **14**: 1009–1023.

Probert, I., Siano, R., Poirier, C., Decelle, J., Biard, T., Tuji, A., *et al*. (2014) *Brandtodinium* gen. nov. and *B. nutricula* comb. Nov. (Dinophyceae), a dinoflagellate commonly found in symbiosis with polycystine radiolarians. *J Phycol* **50**: 388–399.

Rädecker, N., Pogoreutz, C., Voolstra, C.R., Wiedenmann, J., and Wild, C. (2015) Nitrogen cycling in corals: the key to understanding holobiont functioning? *Trends Microbiol* **23**: 1–8.

Raina, J.B., Clode, P.L., Cheong, S., Bougoure, J., Kilburn, M.R., Reeder, A., *et al*. (2017) Subcellular tracking reveals the location of dimethylsulfoniopropionate in microalgae and visualises its uptake by marine bacteria. *Elife* **6**: 1–17.

Raina, J.B., Dinsdale, E.A., Willis, B.L., and Bourne, D.G. (2010) Do the organic sulfur compounds DMSP and DMS drive coral microbial associations? *Trends Microbiol* **18**: 101–108.

Reich, H.G. (2020) Endosymbiotic dinoflagellates pump iron: differences in iron and other trace metal needs among the Symbiodiniaceae Endosymbiotic dinoflagellates pump iron: differences in iron and other trace metal needs among the Symbiodiniaceae. *Coral Reefs* **39**: 915–927.

Rodriguez, I.B., Lin, S., Ho, J., and Ho, T.Y. (2016) Effects of trace metal concentrations on the growth of the coral endosymbiont Symbiodinium kawagutii. *Front Microbiol* **7**: 1–10.

Sbalzarini, I.F., and Koumoutsakos, P. (2005) Feature point tracking and trajectory analysis for video imaging in cell biology. *J Struct Biol* **151**: 182–195.

Simó, R. (2001) Production of atmospheric sulfur by oceanic plankton: biogeochemical, ecological and evolutionary links. *Trends Ecol Evol* **16**: 287–294.

Solé, V.A., Papillon, E., Cotte, M., Walter, P., and Susini, J. (2007) A multiplatform code for the analysis of energy-dispersive X-ray fluorescence spectra. *Spectrochim Acta - Part B At Spectrosc* **62**: 63–68.

Stryhanyuk, H., Calabrese, F., Kümmel, S., Musat, F., Richnow, H.H., and Musat, N. (2018) Calculation of single cell assimilation rates from sip-nanosims-derived isotope ratios: a comprehensive approach. *Front Microbiol* **9**: 1–15.

Swanberg, N.R., and Caron, D.A. (1991) Patterns of sarcodine feeding in epipelagic oceanic plankton. *J Plankton Res* **13**: 287–312.

Thompson, A.W., Foster, R.A., Krupke, A., Carter, B.J., Musat, N., Vaulot, D., *et al*. (2012) Unicellular cyanobacterium symbiotic with a single-celled eukaryotic alga. *Science* **337**: 1546–1550.

Twining, B.S., and Baines, S.B. (2013) The trace metal composition of marine phytoplankton. *Ann Rev Mar Sci* **5**: 191–215.

Uwizeye, C., Decelle, J., Jouneau, P., Flori, S., Gallet, B., Keck, J., *et al*. (2021a) Morphological bases of phytoplankton energy management and physiological

responses unveiled by 3D subcellular imaging. *Nat Commun* **12**: 1049.

Uwizeye, C., Mars Brisbin, M., Gallet, B., Chevalier, F., Charlotte, L., Schieber, N., *et al*. (2021b) Cytoklepty in the plankton: a host strategy to optimize the bioenergetic machinery of endosymbiotic algae. *Proc Natl Acad Sci U S A* **118**: e2025252118. 10.1073/pnas.2025252118

Villar, E., Dani, V., Bigeard, E., Linhart, T., Mendez-Sandin, M., Bachy, C., *et al*. (2018) Symbiont chloroplasts remain active during bleaching-like response induced by thermal stress in Collozoum pelagicum (Collodaria, Retaria). *Front Mar Sci* **5**: 1–11.

Supporting Information

Additional Supporting Information may be found in the online version of this article at the publisher's web-site:

Fig. S1. Correlation between volume of pyrenoid and volume of plastids (μm3) of free-living and symbiotic microalgae (Brandtodinium) after FIB-SEM imaging and 3D reconstruction. ($R = 0.81$, $p = 0.028$; Pearson correlation).

Fig. S2. The non-photochemical quenching (NPQ) parameter indicated that the light energy absorption of symbiotic microalgae *Brandtodinium* (blue line; $n = 4$) was less sensitive in high-light conditions than it was in free-living phase grown in culture (red line; $n = 4$).

Fig. S3. Distribution of heterochromatin volume of free-living and symbiotic microalgae *Brandtodinium* (colour coded: red bars correspond to high numbers of heterochromatin). Heterochromatin, which includes rod-shaped chromosomes and condensed chromatin present in the nucleus, has been reconstructed in 3D after FIB-SEM imaging and its volume quantified. In free-living, we observed a high number of protruding small condensed chromatin structures in the nucleus compared to symbiosis.

Fig. S4. Observation with light microscopy (A), nanoSIMS ($^{14}N^{12}C/^{12}C_2$ ratio) (B) and Transmission Electron microscopy (C) of dividing microalgal cells (*Brandtodinium*) embedded in the gelatinous matrix of the Collodaria (host).

Fig. S5. Correlated Transmission Electron microscopy (A and B) with nanoSIMS images showing relative assimilation (log(ka)) of carbon (C and G) and nitrogen (D and H) in symbiotic microalgae *Brandtodinium* and in the Golgi apparatus (highlighted by a red circle) of the host cell (Collodaria).

Fig. S6. Subcellular quantitative mapping with nanoSIMS of natural nitrogen and phosphorous in the free-living and symbiotic stage of *Brandtodinium*. A and B: Nitrogen ($^{12}C^{14}N/^{12}C_2$) mapping in the free-living (A) and symbiotic (B) stages. Note that part the host cell is visible in B and the symbiotic microalga is indicated by a green arrow. D and E: Phosphorous ($^{31}P/^{12}C_2$) mapping in the free-living (D) and symbiotic (E, green arrow) stages. Nitrogen ($^{12}C^{14}N/^{12}C_2$) and phosphorous ($^{31}P/^{12}C_2$) content in different organelles (plastids, nucleus, pyrenoid and chromatin) of free-living (light green) and symbiotic (dark green) microalgae. (n: nucleus; nu: nucleolus; py: pyrenoid; p: plastid; h: host cell (Collodaria); m: matrix; v: vacuoles in the matrix) (See also Table S3).

Fig. S7. Metallome analyses of Collodaria (containing symbiotic microalgae, *Brandtodinium*) showing the intracellular metal quotas normalized against phosphorus as the biomass indicator (mmol of metal mol^{-1} of P). Al: Aluminium, Mn: Manganese, Fe: iron, Ni: nickel, Zn: Z = zinc, Co: cobalt, Cu: copper, Cd: cadmium. Bloom sample correspond to a pool of different collodarian colonies, Collo 1, 6 and 7 are individual colonies and sample 3387 represents the free-living microalgae *Brandtodinium* from culture medium. (See also Table S1).

Fig. S8. Subcellular quantitative mapping using S-XRF (Synchrotron X-ray Fluorescence) of copper (Cu) showing its concentration (ppm) in free-living (A), and symbiotic microalga *Brandtodinium* (B) with a xy resolution of 50 nm and at 7.3 keV. Note that Cu was below the detection level in free-living while in symbiosis it was concentrated in condensed chromatin and vacuoles closed to plastids. C: Average S-XRF spectrum per pixel in subcellular compartments (chloroplasts, pyrenoid and condensed chromatin or DNA) of *Brandtodinium* in free-living (black lines) and symbiotic (red lines) stages, showing high Cu concentration in condensed chromatin and vacuoles of symbiotic microalgae. Osmium peak is not interfering with Cu as such concentration.

Table S1. Morphometric data of Brandtodinium cells in free-living and symbiotic stages.

Table S2. Nanosims data of stable isotope labeling (^{13}C and ^{15}N).

Table S3. Nanosims data of natural abundance of nitrogen and phosphorous in cells.

Table S4. Sulfur and Iron concentration and distribution in cells measured by Synchrotron X-ray Fluoresence imaging.

Table S5. Bulk analyses of metal concentration (metallome) in collodaria and *Brandtodinium* cells.

Video S1. Live imaging in time-lapse of a Collodaria showing the movement of symbiotic microalgae within the colony.

ORIGINAL ARTICLE

Journal of Cachexia, Sarcopenia and Muscle 2021; **12**: 933–954
Published online 13 June 2021 in Wiley Online Library (wileyonlinelibrary.com) **DOI:** 10.1002/jcsm.12742

Superiority of focused ion beam-scanning electron microscope tomography of cardiomyocytes over standard 2D analyses highlighted by unmasking mitochondrial heterogeneity

Jacqueline Heinen-Weiler[1,2†], Mike Hasenberg[2†], Martin Heisler[1], Stephan Settelmeier[1], Anna-Lena Beerlage[1], Hannah Doepper[1], Bernd Walkenfort[2], Andrea Odersky[1], Peter Luedike[1], Elke Winterhager[1,2], Tienush Rassaf[1] & Ulrike B. Hendgen-Cotta[1*]

[1]*Department of Cardiology and Vascular Medicine, West German Heart and Vascular Center, Medical Faculty, University of Duisburg-Essen, Essen, Germany*
[2]*Imaging Center Essen (IMCES), Electron Microscopy Unit (EMU), Medical Faculty, University of Duisburg-Essen, Essen, Germany*

Abstract

Background Cardioprotection by preventing or repairing mitochondrial damage is an unmet therapeutic need. To understand the role of cardiomyocyte mitochondria in physiopathology, the reliable characterization of the mitochondrial morphology and compartment is pivotal. Previous studies mostly relied on two-dimensional (2D) routine transmission electron microscopy (TEM), thereby neglecting the real three-dimensional (3D) mitochondrial organization. This study aimed to determine whether classical 2D TEM analysis of the cardiomyocyte ultrastructure is sufficient to comprehensively describe the mitochondrial compartment and to reflect mitochondrial number, size, dispersion, distribution, and morphology.

Methods Spatial distribution of the complex mitochondrial network and morphology, number, and size heterogeneity of cardiac mitochondria in isolated adult mouse cardiomyocytes and adult wild-type left ventricular tissues (C57BL/6) were assessed using a comparative 3D imaging system based on focused ion beam-scanning electron microscopy (FIB-SEM) nanotomography. For comparison of 2D vs. 3D data sets, analytical strategies and mathematical comparative approaches were performed. To confirm the value of 3D data for mitochondrial changes, we compared the obtained values for number, coverage area, size heterogeneity, and complexity of wild-type cardiomyocyte mitochondria with data sets from mice lacking the cytosolic and mitochondrial protein BNIP3 (BCL-2/adenovirus E1B 19-kDa interacting protein 3; *Bnip3*$^{-/-}$) using FIB-SEM. Mitochondrial respiration was assessed on isolated mitochondria using the Seahorse XF analyser. A cardiac biopsy was obtained from a male patient (48 years) suffering from myocarditis.

Results The FIB-SEM nanotomographic analysis revealed that no linear relationship exists for mitochondrial number ($r = 0.02$; $P = 0.9511$), dispersion ($r = -0.03$; $P = 0.9188$), and shape (roundness: $r = 0.15$, $P = 0.6397$; elongation: $r = -0.09$, $P = 0.7804$) between 3D and 2D results. Cumulative frequency distribution analysis showed a diverse abundance of mitochondria with different sizes in 3D and 2D. Qualitatively, 2D data could not reflect mitochondrial distribution and dynamics existing in 3D tissue. 3D analyses enabled the discovery that BNIP3 deletion resulted in more smaller, less complex cardiomyocyte mitochondria (number: $P < 0.01$; heterogeneity: C.V. wild-type 89% vs. *Bnip3*$^{-/-}$ 68%; complexity: $P < 0.001$) forming large myofibril-distorting clusters, as seen in human myocarditis with disturbed mitochondrial dynamics. *Bnip3*$^{-/-}$ mice also show a higher respiration rate ($P < 0.01$).

Conclusions Here, we demonstrate the need of 3D analyses for the characterization of mitochondrial features in cardiac tissue samples. Hence, we observed that BNIP3 deletion physiologically acts as a molecular brake on

mitochondrial number, suggesting a role in mitochondrial fusion/fission processes and thereby regulating the homeostasis of cardiac bioenergetics.

Keywords Cardiac mitochondria; Focused ion beam-scanning electron microscopy; BNIP3; 3D morphometry; Mitochondrial energetics; Mitochondrial dynamics

Received: 18 September 2020; Revised: 16 April 2021; Accepted: 21 May 2021
**Correspondence to: Ulrike B. Hendgen-Cotta, Department of Cardiology and Vascular Medicine, West German Heart and Vascular Center, Medical Faculty, University of Duisburg-Essen, Hufelandstraße 55, 45147 Essen, Germany. Phone: +49-201-723-6053, Fax: +49-201-723-6973, Email: ulrike.hendgen-cotta@uk-essen.de*
†Jacqueline Heinen-Weiler and Mike Hasenberg contributed equally to this study.

Introduction

Proper cardiac function is dependent on the complex orchestration of a variety of cellular and organelle components. Mitochondria comprise up to one-third of the cellular volume of a left ventricular (LV) cardiomyocyte.[1–3] The primary function of mitochondria is energy production, an important task, especially for cells with a high energy demand, such as cardiomyocytes, which show a high mitochondrial content. In line with their role in bioenergetic and biosynthetic pathways and serving as an important node for cellular Ca^{2+} signalling, they are also involved in cell growth, ion homeostasis, redox signalling, and cell survival.[1,3,4] Structural and functional integrity are maintained by the mitochondrial dynamism/turnover/mitophagy interactome under natural conditions.[5] Preclinical studies of mitochondrial dynamism have shown that the combined abrogation of fusion and fission provoked massive progressive mitochondrial accumulation in cardiomyocytes, severely distorting the sarcomere architecture.[6] Numerous studies have linked dysfunctional mitochondria and alterations in mitochondrial morphology to cardiac pathologies, including myocardial infarction and heart failure, with a focus on parameters of LV mitochondrial morphology, including shape, volume, size, number, and cristae density, even finding gender-specific differences.[7–12] Remarkably, studies have shown a connection between mitochondrial dysfunctions in skeletal and heart muscle. For example, myopathies like Duchenne muscular dystrophy are associated with mitochondrial dysregulations,[13] in which not only skeletal muscles are impaired[14] but also cardiac muscle cells are being damaged.[15] These cardiomyopathies also seem to arise from mitochondrial dysregulations.[16] To clearly characterize these morphological abnormalities among mitochondria, precise and reproducible image acquisition and analysis at the nanoscale is indispensable. Several publications have demonstrated a relationship between mitochondrial morphology and proper mitochondrial function,[10,17,18] but most of these studies relied on just two-dimensional (2D) routine transmission electron microscopy (TEM). Compared with conventional scanning electron microscopy (SEM), the Riva group has developed a high-resolution SEM with a high value for uncovering the membranous structure of heart mitochondria.[19–21] However, the detection of mitochondria in the real three-dimensional (3D) tissue in respect to localization, number, and shape variations is limited. To overcome the 2D limitations, different 3D EM analysis techniques, such as TEM tomography, serial block-face SEM (SBF-SEM), and focused ion beam-SEM (FIB-SEM) have been developed. FIB-SEM nanotomography is based on the integration of a high-energy ion beam into the column of an SEM system. FIB-SEM technique generates an image stack often consisting of several hundreds of single-image planes, which can subsequently be reconstructed *in silico* into a 3D model offering a wide variety of parameter analyses.[22]

In this study, we initially used FIB-SEM to accurately assess the spatial distribution of the complex mitochondrial network and the morphology of mouse cardiomyocyte mitochondria in isolated adult cardiomyocytes as well as in cardiac biopsies. We developed analytical strategies and defined comparative approaches to relate 2D data to results from 3D analyses. Thus, we elucidated deviations between analyses performed on either 2D or 3D data sets, which are important to properly describe and understand pathological conditions of cardiomyocyte mitochondria. To test the value of our 3D wild-type (WT) mouse analysis approach, we compared those data sets with 3D mitochondrial data sets generated from cardiac biopsies of *Bnip3*-deficient ($Bnip3^{-/-}$) mice. BNIP3 belongs to the BCL-2 family and regulates cell death *via* apoptosis as well as necrosis and mitophagy under pathological conditions.[23–25] It is associated with pathological LV remodeling[26] and the development of cardiac hypertrophy by mediating mitophagy, the inflammatory response and other related signalling pathways in cardiomyocytes.[27–29] The physiological role of cardiac BNIP3 remains unresolved. Hence, we used the FIB-SEM analysis approach to precisely characterize the cardiomyocyte mitochondrial compartment of $Bnip3^{-/-}$ mice compared with that of WT mice in a 3D manner.

Methods

Mice

All animal procedures were performed in accordance with institutional guidelines and approval from the local ethics committee in compliance with the European Convention for the Protection of Vertebrate Animals Used for Experimental and

other Scientific Purposes (Directive 2010/63/EU, 84-02.04.2014A144; 81-02.04.2019A369). Male WT mice (C57Bl/6J), aged 12 ± 5 weeks, were purchased from the Jackson Laboratory (Bar Harbour, ME, USA) and first acclimated at the local animal facility for one week. C57BL/6J-TgH (*Bnip3*$^{-/-}$ mice), aged 12 ± 5 weeks, were bred and nursed in the animal facility of the University Hospital Essen. All mice were kept under a 12 h light and dark cycle with unlimited access to water and food. For subsequent analyses, mice were killed by cervical dislocation.

Human patient

This study was approved by the University Hospital Essen Ethics Committee (17-7392-BO). The experiment was carried out in accordance with the approved guidelines. A cardiac biopsy was obtained from a male patient (48 years) suffering from myocarditis.

Isolation of adult mouse cardiomyocytes

Cardiomyocytes were isolated from the cardiac tissue of adult WT and *Bnip3*$^{-/-}$ mice. Immediately after cervical dislocation, the explanted heart was rapidly perfused through the aorta with a digestion solution containing 25 mM HEPES, 110 mM NaCl, 1.2 mM KH_2PO_4, 2.5 mM KCl, 2.5 mM $MgSO_4$, 100 μM $CaCl_2$, 10 mM glucose-monohydrate and 4 μM collagenase type II (pH 7.4). After 25 min of perfusion at 37°C, the cardiac tissue was fully disintegrated using a microtome (McIlwain Tissue Chopper, Mickle Laboratory Engineering Co., Ltd., Guildford, UK), and the resulting tissue was filtered through a 200 μm nylon mesh immediately before centrifugation at 100 × *g* for 1 min. The cell pellet was resuspended in 100 μM HEPES buffer, followed by four more centrifugation steps at 100 × *g*. Between each step, the supernatant was removed, and the pellet was resuspended in 100 μM HEPES buffer containing an incrementally increasing concentration of 100 mM $CaCl_2$ (0.125%, 0.25%, 0.5%, 1%). Ultimately, 24 × 10^3 cells were cultured in poly-L-lysine-coated cell culture dishes with a gridded glass bottom (MatTek Corporation, Ashland, USA) in modified Media 199 (100 IU/mL penicillin + 100 μg/mL streptomycin, 2 mM carnitine, 5 mM creatine, 5 mM taurine and 10 μM cytosine-D-arabinofuranoside) for 2.5 h at 37°C and 5% CO_2.

Staining and fluorescence imaging of isolated cardiomyocytes

Isolated cardiomyocytes from WT and *Bnip3*$^{-/-}$ were cultured in a laminin (Roche Diagnostics GmbH, Rotkreuz, Switzerland) coated 16 well chamber slide (Thermo Fisher Scientific, Waltham, Massachusetts, USA). Ultimately, 5 × 10^3 cells were seeded in each well. After 2 h, cells were stained with MitoTracker™ Orange (Thermo Fisher Scientific) for 15 min at 37°C, followed by fixation with 4% formaldehyde for 20 min at 37°C. Then the cells were permeabilized with phosphate buffered saline containing 0.5% Triton X-100 (Sigma Aldrich, St. Louis, Missouri, USA) for 5 min at room temperature (RT). Subsequently, non-specific binding sites were blocked with normal goat serum (Thermo Fisher Scientific) for 15 min at RT. After that, cells were stained with Alexa Fluor™ 488 Phalloidin (1 h at RT, Thermo Fisher Scientific) and 4′, 6-diamidino-2-phenylindole (DAPI) (15 min, RT, Thermo Fisher Scientific). Finally, gaskets were removed, and cells were embedded using ProLong™ Gold anti-fade reagent (Thermo Fisher Scientific). Z-stacks were acquired by inverted epifluorescence microscope (Zeiss AxioObserver.Z1/7, Carl Zeiss, Oberkochen, Germany) with Zeiss ApoTome additional feature. The Plan-Apochromat 40×/0.95 Korr M27 objective was used and digital images of 16 bit were acquired with a 0.163 μm × 0.163 μm × 1.000 μm voxel size, using 4.2 Megapixel monochrome sCMOS camera (Orca-flash 4.0 V2, Hamamatsu Photonics, Hamamatsu, Japan). Each z-stack, containing 10–20 images, was acquired in three excitations wavelengths (633, 493, and 353 nm) and exposure with 1.9 s, 16 ms, and 300 ms. Post-processing of the resulting z-stack files was performed with Fiji version 1.52p.[29]

Measurement of the volume of isolated cardiomyocytes

The following image processing workflow was carried out to the image processing software Fiji (version 1.52p).

From the resulting hyperstack, the channel representing the Alexa Flour 488 Phalloidin signal was extracted as 3D greyscale image stack. Binarization was done by choosing a grey value threshold excluding most of unwanted background signal. Adjacent areas were closed by performing a morphological closing operation 1 to 5 times with a 1 count square structuring element. Small speckles (max. radius 2–20 pixels), which were falsely assigned as foreground were removed with the 'remove outliers'-function. The resulting areas were analysed with the 'analyse particles' tool, assuming a circularity of 0.0–0.7 for each area. The resulting areas on each slide were multiplied by the slice thickness and summarized to get the volume of each cell.

Transmission electron microscopy/focused ion beam-scanning electron microscopy tissue preparation

For TEM and FIB-SEM analysis of mouse LV tissue, heart specimens were prepared in a similar way. Explanted mouse

hearts were rapidly dissected into small slices and transferred into a petri dish filled with primary fixative (<20 s, 2% formaldehyde, 2.5% glutaraldehyde and 2 mM $CaCl_2$ in 0.15 M cacodylate buffer). Biopsies of 1 mm^3 were collected in a 1.5 mL tube (Eppendorf, Hamburg, Germany) filled with the same primary fixative. After fixation (3 h, RT), the biopsies were rinsed three times with 0.15 M cacodylate buffer, followed by post-fixation and contrasting according to a modified protocol of the OTO method.[30] Subsequently, specimens were dehydrated in an ascending ethanol gradient (30%, 50% 60%, 70%, 80%, 96% and three times 100%; each step 15 min) and embedded in Durcupan™ with an incrementally increasing resin concentration (2× pure propylene oxide (PO) for 2 min, followed by Durcupan™: PO 1:1 (1 h) and 3:1 (1.5 h) at RT, and finally pure Durcupan™ first overnight (O/N) and then freshly refilled with pure Durcupan™) followed by polymerization for 72 h at 60°C.

Isolated cardiomyocytes from adult mice were cultured for 2.5 h after seeding and fixed in 2.5% glutaraldehyde for 3 h. Post-fixation and contrasting process were performed as described earlier for heart specimens. The following steps of the process were modified: phosphate-buffered 1% osmium tetroxide for 30 min on ice and 0.5% aqueous solution of uranyl acetate without Walton's lead aspartate staining. Instead of Durcupan embedding, EPON with an incrementally increasing resin concentration (EPON:EtOH 1:1 [1 h] and 3:1 [2 h] at RT), and then pure EPON O/N was used. The resin was then polymerized at 60°C for 48 h before the glass bottom of the dish was removed by incubation in 40% hydrofluoric acid for 30 min at RT.

Human heart biopsy was immediately transferred to a 1.5 mL tube, containing primary fixative as described earlier and processed as described for mouse LV tissue.

Transmission electron microscopy images

Ultrathin sections of heart specimens (55 nm) were generated (EM UC7, Leica)[31] and transferred to 200 mesh copper grids. Imaging was conducted using a LaB6 cathode-equipped JEM 1400Plus (JEOL, Ltd., Tokyo Akishima, Japan) instrument at 120 kV with magnifications as indicated. Digital images were acquired with a CMOS camera with 4096 × 4096 pixels (TemCam-F416, TVIPS, Gauting, Germany). Post-processing of the resulting 8-bit TIFF image files was performed with Fiji version 1.52p.[32]

Focused ion beam-scanning electron microscopy and data acquisition

The resin disc containing isolated myocytes were trimmed with a scalpel to a macroscopically chosen region approximately 1 cm in diameter and glued onto an SEM aluminium stub using conductive silver paste (Plano GmbH, Wetzlar, Germany). The embedded tissue was cut off the resin block with a razor blade and was also glued onto an SEM aluminium stub. The surface was then coated with a 15 nm-thick platinum/palladium layer (208HR, Cressington Scientific Instruments, Watford, UK) before the stub was transferred into the FIB-SEM (Crossbeam 540, Carl Zeiss AG) column for O/N vacuum stabilization. The embedded sample was screened for representative cells using the SmartSEM software package (Carl Zeiss AG, version 6.04) at an accelerating voltage of 1.5 and 10 kV and a beam current of 1 nA (working distance, 5.1 mm; analytic column mode; 164 × magnification, Everhart-Thornley detector). A coarse trench was milled directly in front of the region of interest (ROI) using the FIB at 30 kV/65 nA and the SmartFIB software package (Carl Zeiss AG, version 1.8.0). For 3D image acquisition of isolated myocytes, the Atlas System (Carl Zeiss AG; software version 5.2.2.85) was used while the system operated at the following parameters: gallium ion beam: 30 kV/30 nA, electron beam: 1.5 kV/1 nA, field of view: 97.8 μm, cutting thickness: 100 nm, pixel size: 8.1 nm and pixel dwell time: 3.5 μs. Eight-bit TIF images were acquired using both a column energy selective backscatter detector with a 700 V energy selective backscatter grid and an S1-selective in-lens detector at a resolution of 12 032 × 12 032 pixels.

For heart tissue, a 40 × 20 μm protection pad was additionally generated with SmartFIB using a gas injection system (gallium ion beam: 30 kV/3 nA). Image acquisition was performed with the following parameters: gallium ion beam: 30 kV/3 nA, electron beam: 1.5 kV/1 nA, field of view: 30 μm, cutting thickness: 150 nm, pixel size: 2 nm, and pixel dwell time: 10 μs.

Three-dimensional reconstructions

Subsequent image processing was carried out by a combination of various computer programs. Image brightness and contrast adjustment, image stack alignment, image inversion, and image/stack cropping were performed using either Atlas or Amira (Thermo Fisher Scientific, Inc., Waltham, MA, USA; version 2019.4). Segmentation of the cellular ultrastructure was performed using either the magic wand or the brush tool of Amira on all consecutive images of one stack. Amira was also used for 3D reconstruction and the generation of parameters, such as volume, shape, and number, for quantitative analyses. Fiji was used to generate rendered 3D movies from the TIF series, initially composed in Amira.

Isolation of mitochondria

The isolated mouse heart was disrupted in 2 mL of ice-cold isolation buffer (250 mM sucrose, 10 mM HEPES, and 1 mM

EGTA, pH 7.4) using a TissueRuptor.[33] The homogenate was centrifuged (700 × *g* for 10 min at 4°C) to remove debris. Then, the supernatant was centrifuged at an increased speed (15 000 × *g* for 10 min at 4°C) to precipitate mitochondria. The mitochondria were washed twice with isolation buffer through resuspension and centrifugation at 12 500 × *g* for 5 min at 4°C. Finally, the mitochondria were resuspended in 300 μL of isolation buffer. The total protein concentration was measured by DC Protein Assay (Bio-Rad Laboratories, Inc., Hercules, CA, USA) according to the manufacturer's instructions. The measured protein concentration was used to determine the total number of mitochondria per heart.

Mitochondrial respiration

Based on the protein quantification, the mitochondrial suspensions, isolated mitochondria from WT (*n* = 5) and *Bnip3*$^{-/-}$ mice (*n* = 5) were diluted to the working concentration of 4 μg/mL total protein with cold 1× mitochondrial assay solution (MAS) (2 mM HEPES, 10 mM KH_2PO_4, 220 mM mannitol, 1 mM EGTA, 70 mM sucrose, 5 mM $MgCl_2$, 0.2% fatty acid-free bovine albumin serum (BSA), pH 7.2) supplemented with 10 mM succinate and 2 μM rotenone. The wells of an XF24 V7 PS 24-well cell culture microplate[34] (Agilent Technologies, Santa Clara, CA, USA) were loaded with five replicates of 50 μL of diluted mitochondria suspension (2 μg protein/well). For background correction, the corners were filled with only 1 × MAS. The microplate was centrifuged for 20 min at 2000 × *g* at RT to attach the mitochondria to the bottom of the plate. Finally, 450 μL of pre-warmed (37°C) 1 × MAS was added to each well. During centrifugation, the ports of an XFe24 cartridge were filled as follows: port a: 55 μL of 40 mM adenosine diphosphate, port b: 62 μL of 25 μg/mL oligomycin, port c: 69 μL of 40 μM carbonyl cyanide 4-(trifluoromethoxy) phenylhydrazone (FCCP), port d: 75 μL of 40 μM antimycin A. The oxygen consumption rate was then detected with a Seahorse XF24e Analyser (Bioscience, North Billerica, USA). The software suite WAVE (Agilent Technologies; version 2.6.0) was used for data analysis.

Western blot analysis

After the isolation of mitochondria and homogenization of whole hearts, the protein concentration was determined by DC Protein Assay (Bio-Rad Laboratories Inc., Hercules, CA, USA). Samples were diluted in lithium dodecyl sulfate sample buffer and Reducing Agent (Invitrogen, Carlsbad, CA, USA) and boiled for 5 min at 95°C. The denatured samples were loaded onto NuPAGE™ 4–12% Bis-Tris protein gels (Invitrogen). Then, the proteins were transferred to nitrocellulose membranes and stained with SYPRO Ruby (Thermo Fisher Scientific, USA) following the manufacturer's instructions. Subsequently, non-specific binding sites were blocked, and the blots were subjected to primary antibody incubation overnight at 4°C. After exposure to the horseradish peroxidase (HRP)-conjugated secondary antibody for 1 h at RT, the blots were imaged using SuperSignal West Pico PLUS Substrate (Thermo Fisher Scientific, USA).

Antibody list

Antibody	Host	Manufacturer (catalogue number)
Actin	Mouse	MP Biomedicals (691001)
Anti-rabbit-HRP	Goat	Cell Signaling (7074)
Anti-OMA-1	Rabbit	Cell Signaling (95473)
Anti-OPA-1	Rabbit	Cell Signaling (80471)

Echocardiography

A high-frequency ultrasound system (Vevo 3100, FUJIFILM VisualSonics, Toronto, Canada) was used to acquire ultrasound images. An MX400 38 MHz (21–44 MHz) transducer with up to 449 fps and an image axial resolution of 50 μm was used (FUJIFILM VisualSonics). Mice were anaesthetized using 3% isoflurane initially. Anaesthesia was maintained with 1.5–2% isoflurane with a 100% dioxygen flow of 1–2 L/min.[35,36] The animals were placed in the supine position and taped to a heated electrocardiogram table to record electrocardiogram signals. Body temperature was monitored *via* a rectal thermometer and maintained using infrared light. Hair was removed using a chemical depilatory agent. 2D B- and M-mode cine loop images were acquired in the parasternal long (PSLAX) and parasternal short-axis (SAX) view as well as the apical four-chamber (4CH) view.[37,38] M-mode images in the SAX view were recorded at the mid-papillary LV level. Conventional analysis of the images as well as strain analysis was performed in a blinded manner using Vevo LAB software version 3.2.2 (FUJIFILM VisualSonics) and Vevo Strain software (FUJIFILM VisualSonics), respectively. Fractional shortening was calculated based on strain analysis.

Quantification and statistical analysis

Samples from three mice per genotype (WT and *Bnip3*$^{-/-}$) were included. From each mouse, one biopsy was taken, and four randomly chosen FIB-SEM stacks were recorded. One image stack from a *Bnip3*$^{-/-}$ mouse was excluded because it contained only 11 mitochondria and hence was not representative. In summary, 729 mitochondria from WT mice and 1285 mitochondria from *Bnip3*$^{-/-}$ mice were analysed. The spatial parameters of the cellular compartments and, in particular, of the mitochondria (area, volume, and perimeter) were calculated using Amira software (version 2019.4).

Mitochondrial complexity was described through the mitochondrial complexity index (MCI), which was developed by Koopmann *et al*. and adapted by Vincent *et al*.[39,40] The following formula was used:

$$\mathrm{MCI} = \left(\frac{\left(SA^{3/2}\right)}{4\pi V}\right)^2 = \frac{SA^3}{16\pi^2 V^2}$$

with *SA* as the surface area, and *V* as the volume.

The following mitochondrial shape parameters were calculated using Amira software. As described in the user's manual, anisotropy (a), elongation (e), and flatness (f) were derived from the eigenvalues and eigenvectors given by the inertia tensor of the segmented mitochondria. The formula for anisotropy was one minus the ratio of the smallest to the largest eigenvalue. Elongation was calculated as the ratio of the medium to the largest eigenvalue. Flatness was derived from the ratio of the smallest to the medium eigenvalue. The final conclusion regarding mitochondrial shape was made through the collective consideration of these parameters. To illustrate how each single parameter describes the mitochondrial shape, we used representative mitochondria and formed the corresponding ellipsoids from the resulting *x*, *y*, and *z* eigenvalues.

Corresponding to the observed shapes from 3D recalculations, all segmented mitochondria were considered globular (r: 0–0.4; e: 0.6–1; f: 0.6–1), rod-shaped (r: 0.6–1; e: 0–0.4; f: 0.5–1), long-striped (r: 0.8–1; e: 0–0.4; f: 0–0.4), flattened (r: 0.6–1; e: 0.5–1; f: 0–0.4), or soft square-shaped (r: 0.5–1; e: 0.5–1; f: 0.5–1). Therefore, we used a custom python script (Supplementary Listing S1).

For statistical testing and the generation of graphs, Prism 8 software was used (GraphPad, San Diego, CA, USA). Data are presented as the mean ± SD. For each group, the Shapiro–Wilk test was performed (normal distribution). If normally was assumed, comparisons were performed using Student's *t* test. Otherwise, data were analysed by the Mann–Whitney test. The correlation coefficients and determination coefficients were calculated using the Pearson method. To compare multidimensional parameters, root extraction was performed. Skewness and kurtosis were extracted by heuristic prism analysis (GraphPad Software, San Diego, CA, USA, version 8.4.3). These parameters show how much a given distribution deviates from the normal distribution (Gaussian distribution). While skewness describes deviations in terms of symmetry, kurtosis describes deviations in terms of steepness. An increasing absolute skewness reflects a more asymmetrical distribution. A positive value represents a peak shift to the left, whereas a negative value reflects a peak shift to the right. In contrast, high kurtosis indicates an increased value number at the edges (tails). Thus, kurtosis describes how flat or steep the distribution curve appears. A negative kurtosis indicates a flat distribution with short tails. Such distributions are also called platykurtic.[41]

Results

Overall workflow

For the reliable and efficient analysis of mouse cardiac tissue biopsies, we established the following workflow (*Figure* 1), based on a published 3D SBF-SEM protocol.[42] Cubic cardiac biopsies with an edge length of 1 mm were collected from the left ventricle of adult mouse hearts (*Figure* 1A) and immediately immersion-fixed with aldehyde. To enhance the sample contrast, we used five different heavy metals during sample processing before embedding the biopsies (*Figure* 1B). From the resin blocks, semi-thin sections were cut to identify representative ROIs (*Figure* 1C) around which the blocks were then coarsely trimmed. Finally, FIB-SEM was performed to analyse the mitochondria inside the cardiac tissue. For these analyses, single volumes of 10 × 10 × 3.15 μm (*x*–*y*–*z*) were recorded at a voxel size of 2 × 2 × 150 nm, which resulted in 21 individual image planes per volume (*Figure* 1D,E). This setting allows to fully record the variations of the mitochondrial size while preserving the mitochondrial ultrastructure. A representative example of such an image stack is depicted in *Figure* 1E. In the upper row of *Figure* 1F, two images from this stack (the first = top and the last = bottom) are shown, whereas the row below represents the corresponding segmentation maps of the mitochondria. For the accurate quantification of mitochondrial features, all mitochondria were segmented manually on each section of the z-stack. Because manual segmentation, in particular related to the surface area, depends on individual hand movements of the person tracing, intra-individual and inter-individual variability with a coefficient of variation less than 10% is recommended. Finally, 3D rendering and parameter analyses were carried out using a combination of different software tools. *Figure* 1G shows a visualization of the resulting 3D model of the example data set. The entire workflow is summarized in *Figure* 1H. The cardiomyocytes were processed for FIB-SEM as were the cardiac tissues with only minor changes, which are listed in the Methods section. This workflow is instantly adaptable to laboratories that have access to any of the FIB-SEM, SBF-SEM, or array tomography (serial sectioning) instruments.

Three-dimensional mapping of mitochondria in isolated cardiomyocytes and cardiac tissue

In the resulting 3D model of a representative isolated cardiomyocyte, the mitochondrial reticular network appeared to be mostly arranged in a linear manner between the myofibrils (*Figure* 2A). Moreover, as shown in the cross-sections, mitochondria aggregated in proximity to the nucleus (*Figure* 2B,C). 3D mapping of this cardiomyocyte revealed that

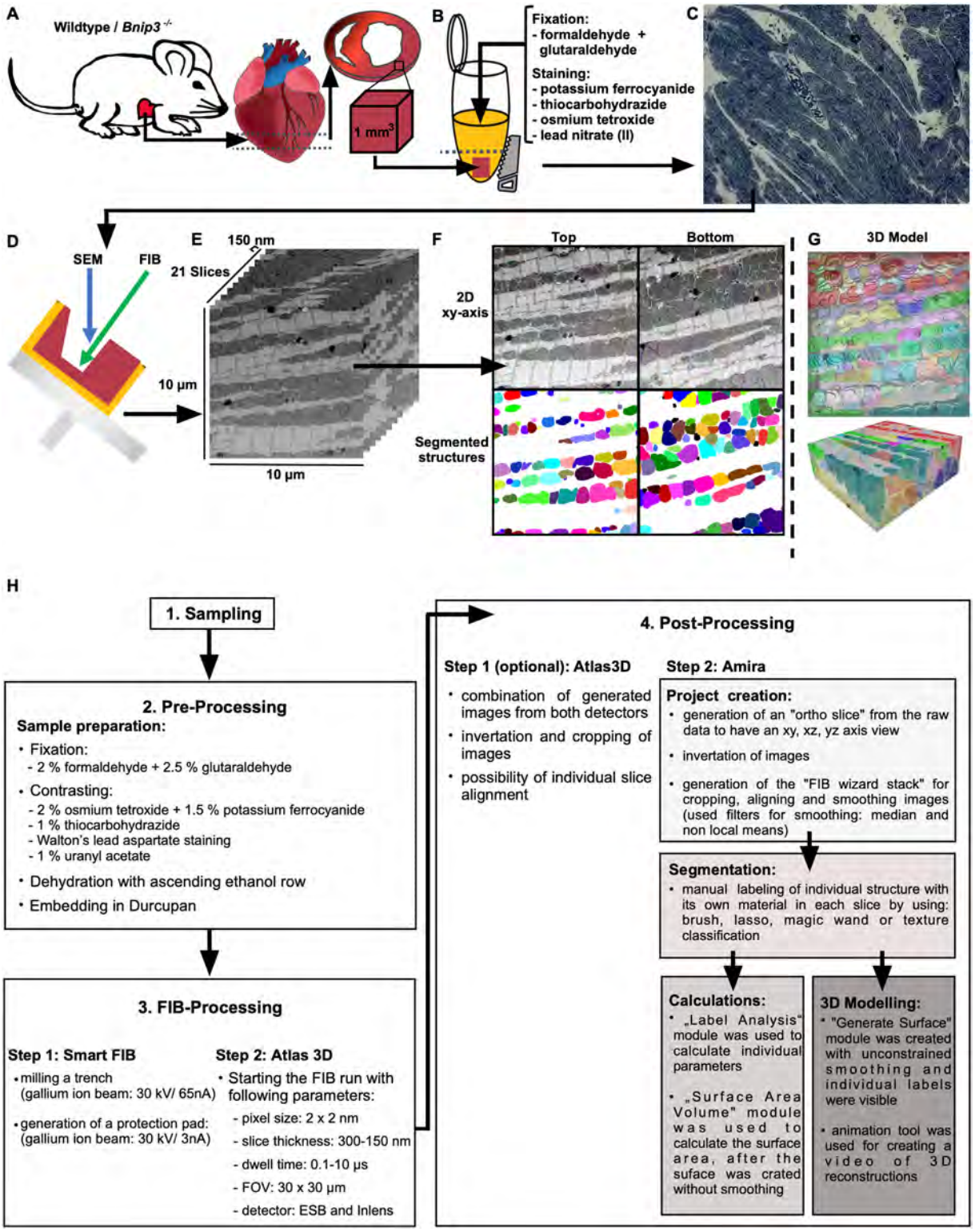

Figure 1 Workflow. (*A*,*B*) schematic diagram of sample acquisition and preparation for focused ion beam-scanning electron microscopy (FIB-SEM) (n = 3 mice per group). (*C*) Representative light micrograph of a semi-thin section used to identify the regions of interest (ROIs). (*D*) Schematic of the FIB-SEM process illustrating cutting and imaging. (*E*) Z-stack of two-dimensional (2D) images from FIB-SEM with an imaging depth of 3.15 µm. (*F*) Top and bottom images of the z-stack and the corresponding segmentation maps of mitochondria. Each fully mapped mitochondrion is represented by a colour. (*G*) Three-dimensional (3D) reconstruction representing segmented mitochondria. (*H*) Flow chart indicating the significant steps of sample processing.

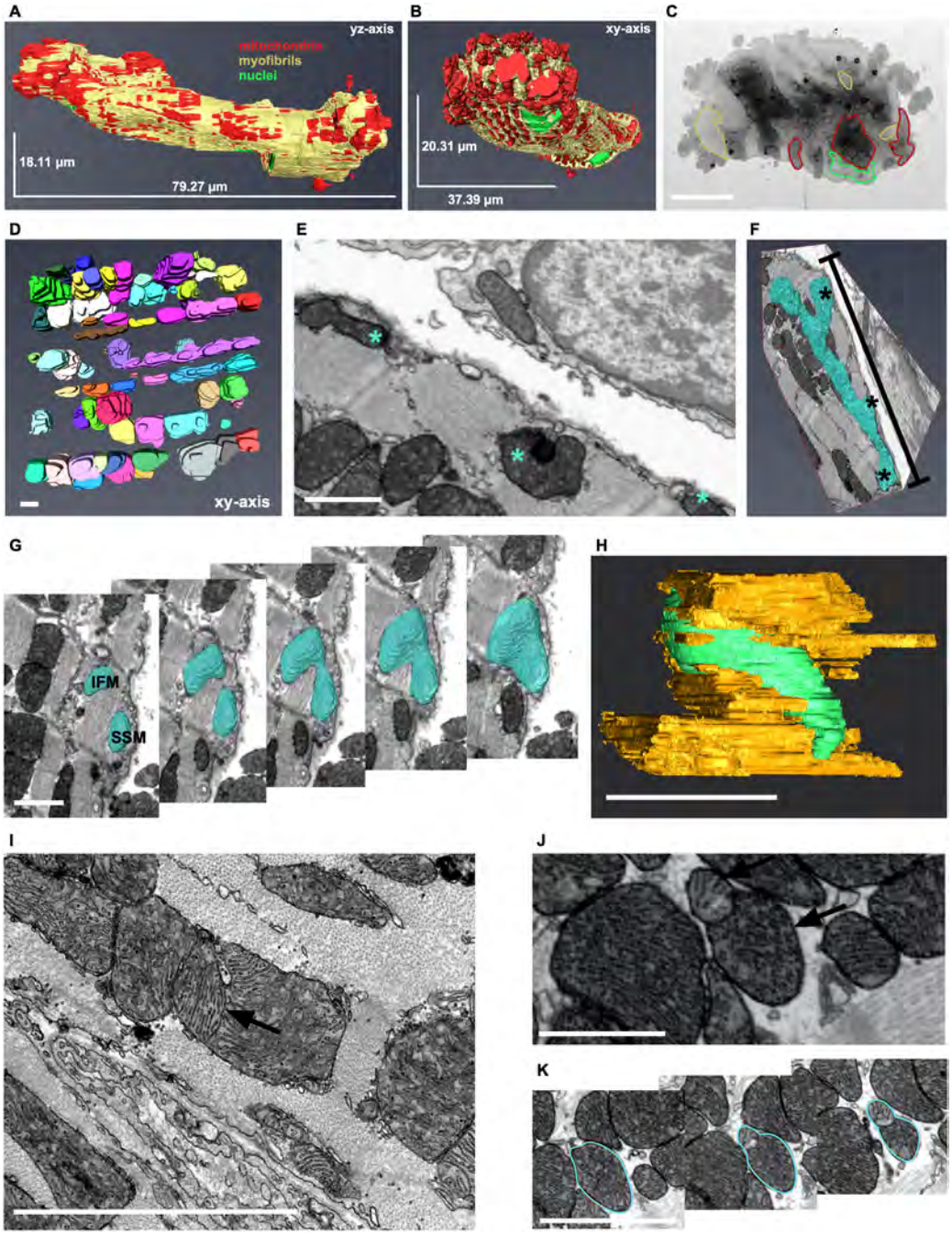

Figure 2 Three-dimensional (3D) mapping of mitochondria in isolated cardiomyocytes (n = 3 from 1 mice) and cardiac tissue. (*A*,*B*) 3D reconstructions of a longitudinally (*A*) and transversally (*B*) oriented isolated mouse cardiomyocyte with mitochondria highlighted in red, myofibrils in yellow and nuclei in green. Refer to Supporting information, *Movie* S1 for animation. (*C*) Electron micrograph of an isolated cardiomyocyte in a transverse orientation. Scale bar, 5 µm. (*D*) 3D reconstruction of the cardiomyocyte mitochondrial network in cardiac tissue (n = 3 wild-type mice, each with four z-stacks). Each mitochondrion is represented by a different colour. Scale bar, 1 µm. Refer to *Movie* S2 for animation. (*E*,*F*) two-dimensional (2D) image depicting three separate mitochondria (*E*, asterisks). Note that the 3D reconstruction reveals merely one complex mitochondrion up to 6 µm with two branches (*F*, cyan). Scale bar, 1 µm (1 wild-type mouse, n = 1 z-stack). Refer to *Movie* S3 for animation. (*G*) Z-stack images obtained by focused ion beam-scanning electron microscopy (FIB-SEM) (cyan) depicting disparate parts of the same mitochondrion, appearing as one subsarcolemmal (SSM) and one interfibrillar (IFM) mitochondrion in one single 2D section. Scale bar, 1 µm (1 wild-type mouse, n = 1 z-stack). Refer to *Movie* S4 for animation. (*H*) 3D reconstruction of a single mitochondrion (green) extending across a myofibril bundle (yellow). Scale bar, 1 µm (1 wild-type mouse, n = 1 z-stack). Refer to *Movie* S5 for animation. (*I*) 2D transmission electron microscopy (TEM) image depicting fragmented mitochondria (black arrows). Scale bar, 3 µm (1 wild-type mouse, n = 1 z-stack). (*J*) 2D image depicting two individual mitochondria (black arrows). (*K*) Z-stack images obtained by FIB-SEM illustrating fission. Scale bar, 3 µm (1 wild-type mouse, n = 1 z-stack). Refer to *Movie* S6 for animation.

mitochondria accumulated at distal cell boundaries on the *z*-axis, whereas fewer mitochondria were detected in the centre of the cell (Supporting information, *Movie* S1). In addition, they showed a more dispersed arrangement on the x-y plane than those in intact cardiac tissue.[43] This different organelle arrangement could be due to the isolation process followed by cultivation in an artificial cell culture dish. Therefore, mitochondria might adapt their spatial distribution according to the physiological demand within the isolated cardiomyocyte.

As the isolation and cultivation process leads to an artificially altered distribution of mitochondria within the cardiomyocyte, we evaluated intact LV tissue. Depicting only the mitochondrial network of the cardiomyocyte, the complex shape and size of mitochondria became obvious (*Figure* 2D, *Movie* S2). The mitochondrial appearance varied from spherically round to elongated and from uniform to polymorph shapes. The linear arrangement of the mitochondria was clearly connected to the spatial course of the myofibrils. Along the course of myofibrils, a preference for elongation was detected (*Figure* 2D, *Movie* S2).

The heterogeneous appearance of the cardiomyocyte mitochondria indicates that an analysis of single 2D images from a z-stack was prone to misinterpretation regarding the mitochondrial number, localization, and dynamics. As depicted in *Figure* 2E,F mitochondria that appeared as distinct organelles with different shapes located in either subsarcolemmal (SSM) or interfibrillar (IFM) regions in the 2D plane turned out to be one and the same mitochondrion when 3D analyses were applied. Moreover, the 3D volume revealed that this elongated mitochondrion branched and was present in the interfibrillar and subsarcolemmal regions (*Figure* 2E,F, *Movie* S3). In a previous study, we had already challenged the concept that IFM and SSM generally belong to different mitochondrial subpopulations[43] and can provide here the ultimate proof of our hypothesis. Another example with a high likelihood of such a misinterpretation is shown in *Figure* 2G (*Movie* S4). Two mitochondria separated by a myofibril bundle could easily be described as IFM and SSM on 2D examination, but in reality, they turned out to be one mitochondrion present in both compartments. This phenomenon can be explained by the fact that mitochondria are able to cross myofibril bundles, as shown in *Figure* 2H, where the elongated mitochondrion (green) bypasses the cardiac myofibril bundle (yellow) (*Figure* 2H, *Movie* S5). Another drawback of 2D analysis applies to the examination of fragmented mitochondria during the fission process. Whereas in *Figure* 2I the demarcation line of fission is apparent, *Figure* 2J even suggests the existence of two individual mitochondria. Assembling the z-stack into a 3D model, however, unmasked the fission process of one mitochondrion (*Figure* 2K, *Movie* S6).

Quantitative two-dimensional analyses of cardiomyocyte mitochondria cannot reflect the real situation in three-dimensions

Because the 3D analysis of cardiac tissue (*Figure* 2) impressively unmasked the heterogeneity of cardiomyocyte mitochondria in size, shape and distribution, we focused on the question of whether classical 2D analyses can reflect the outcome of 3D quantifications. To allow proper comparison of the parameters describing the relative values of number, size and shape of individual mitochondria and coverage area of mitochondria, we compared 12 3D reconstructions of LV specimens totalling 315 μm^3 with 12 2D intersections (10 × 10 μm). Here we used the 12 z-stack top and bottom intersections. To reveal whether a linear association existed for mitochondrial number and coverage space between the 2D values and 3D results, we calculated the Pearson correlation coefficient (r) and the determination coefficient (r^2) for 12 corresponding samples. Because r was close to zero, no correlation for mitochondrial number could be confirmed (*Figure* 3A; top section: $r = 0.02$, $r^2 = 0.004$, $P = 0.9511$ and bottom section: $r = -0.06$, $r^2 = 0.004$, $P = 0.8466$). Furthermore, r^2 showed that only 4% of the difference in the 2D values was accounted for by the difference in the 3D values. This was not surprising because the 2D data deviated from the 3D results by up to 66% (*Figure* S1A; top section 66% and bottom section 57%). A low r was also calculated for the mitochondrial dispersion space, which indicated no linear relationship between data obtained by 2D and 3D analysis (*Figure* 3B; top section: $r = -0.03$, $r^2 = 0.001$, $P = 0.9188$ and bottom section: $r = -0.51$, $r^2 = 0.255$, $P = 0.0936$). Here, the deviation in the 2D data reached 395% (*Figure* S1B; top section 338% and bottom section 395%). Related to r^2, only 26% of the variation in the 3D results was represented in the 2D data. Overall, 2D analyses generally do not predict the corresponding proportions that exist under 3D conditions in terms of mitochondrial number or coverage space.

Alterations in mitochondrial size and shape have been reported as hallmarks of many pathologies, including heart failure, and have been attributed to impaired mitochondrial dynamics.[44–46] To verify these reports, we next evaluated the size of individual mitochondria in 2D and 3D and analysed the resulting populations using cumulative frequency distribution calculations. In 3D, size corresponds to volume, whereas in 2D, size equals an area. To avoid a bias in direct comparison, the value dimensions (μm^2 and μm^3, respectively) were removed through the extraction of their roots. The cumulative frequency distributions illustrated a diverse abundance of mitochondria with different sizes in 3D and 2D (*Figure* 3C). Hence, we consider that size determination depends on the observation dimension. To confirm this presumption, we focused on the symmetry and tailedness of

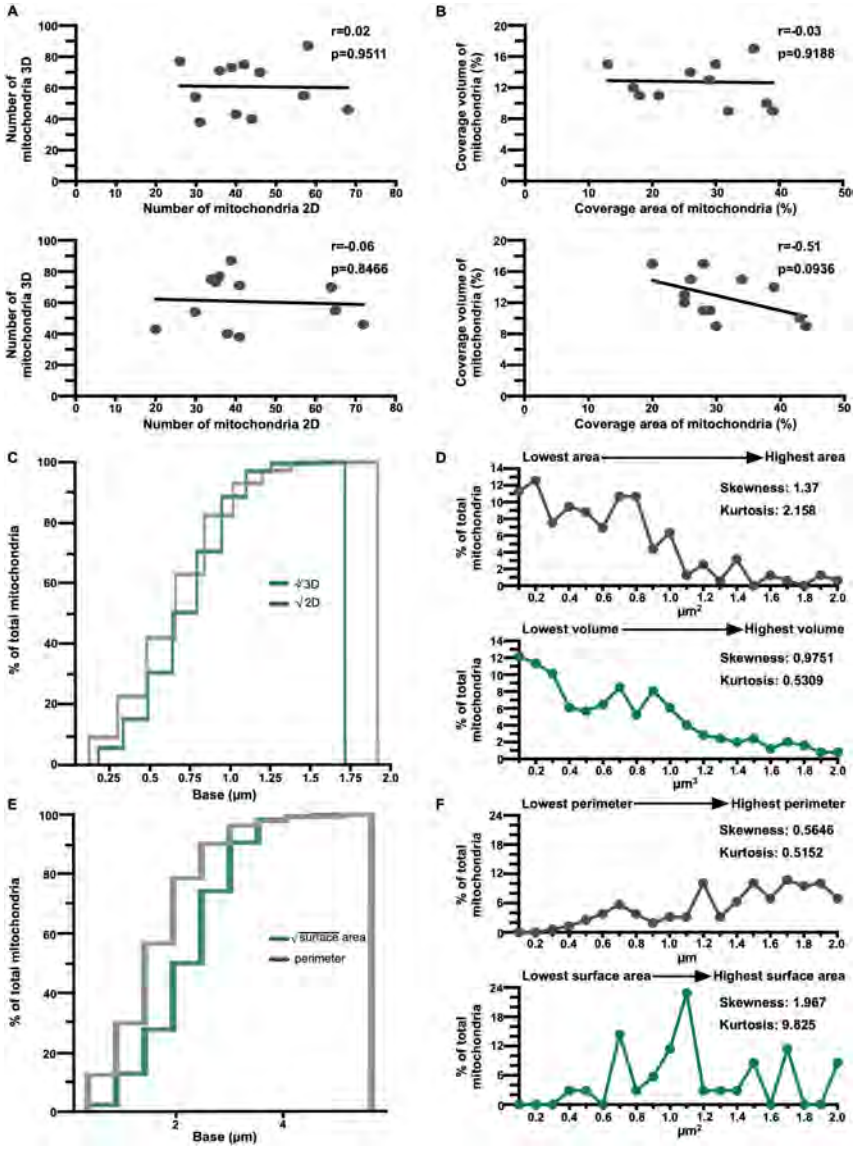

Figure 3 Quantitative two-dimensional (2D) analyses of cardiomyocyte mitochondria cannot reflect the real situation in three-dimensional (3D). (*A*) Mitochondrial number in 3D reconstructions and corresponding 2D top (upper panel) and bottom sections (lower panel) from 12 focused ion beam-scanning electron microscopy (FIB-SEM) stacks (n = 3 wild-type mice). Pearson analysis does not prove a linear correlation. Refer also to Supporting information, *Figure* S1A. (*B*) Mitochondrial coverage volume and area from 12 FIB-SEM stacks and corresponding 2D top (upper panel) and bottom sections (lower panel) (n = 3 wild-type mice). Pearson analysis does not prove a linear correlation. Refer also to *Figure* S1B. (*C*) Cumulative frequency distribution of individual mitochondrial size in 3D and 2D (top section) (n = 3 wild-type mice, 12 z-stacks). In 3D, size is indicated by the mitochondrial volume (green), and in 2D, size is indicated by the mitochondrial area (grey). The roots of absolute values were extracted. Refer also to *Figure* S1C. (*D*) Representative histograms of individual mitochondrial size. The mitochondrial surface area frequency in the top section of four FIB-SEM stacks is shown in the upper panel (grey), and the corresponding volume frequency in the 3D reconstruction is shown in the lower panel (green) (n = 1 wild-type mouse). (*E*) Cumulative frequency distribution of individual mitochondrial shape parameters in 3D and 2D (top sections) (n = 3 wild-type mice, 12 z-stacks). In 3D, the shape is indicated by the mitochondrial surface area (green), and in 2D, it is indicated by the mitochondrial perimeter (grey). The roots of absolute values were extracted. Refer also to *Figure* S1D. (*F*) Representative histograms of individual mitochondrial shapes (n = 1 wild-type mouse). The mitochondrial perimeter frequency in the top section of four FIB-SEM stacks is shown in the upper panel (grey), and the corresponding surface area frequency in the 3D reconstruction is shown in the lower panel (green).

the size distribution. In this respect, we calculated skewness and kurtosis. These population distribution values differed in histograms of four 3D volumes and their corresponding 2D top intersections (*Figure* 3D; skewness 1.37 vs. 0.9751; kurtosis 2.158 vs. 0.5309) and 2D bottom intersections (*Figure* S1C,D; skewness 1.446 vs. 0.9751; kurtosis 3.593 vs. 0.5309). From these data, a 2D analysis was suggestive of a more asymmetric and leptokurtic size distribution with a shift to smaller size values overall compared with a 3D analysis. Mitochondrial shape could be determined by connecting

perimeter (2D) and surface area (3D) data with size properties. Therefore, we next compared these parameters in 2D and 3D analyses. Here, we adjusted surface areas by extracting roots to create comparability with perimeters. Cumulative frequency distribution comparison suggested a diverse but overall increased abundance of mitochondria with a larger perimeter than the corresponding 3D descriptor surface area (*Figure* 3E). Additionally, the distribution symmetry and tailedness of the surface area and perimeter appeared asymmetric, with heavier tails on 3D than 2D analysis (*Figure* 3E), which was apparent in histograms of four 3D volumes and their corresponding 2D top intersections (*Figure* 3F; skewness 0.5646 vs. 1.967; kurtosis 0.5152 vs. 9.825) and 2D bottom intersections (*Figure* S1E,F; skewness 0.8319 vs. 1.967, kurtosis 1.824 vs. 9.825).

Next, we tested whether the assessment of mitochondrial shape differs between an experimental 2D and 3D approach using anisotropy and elongation scores. Anisotropy values close to zero represented a rounder object, whereas elongation values close to zero represented a more elongated object (*Figure* 4A). Correlation analyses of 12 3D reconstitutions with their corresponding top and bottom 2D intersections did not show a relationship between the number of mitochondria with a round shape (anisotropy: 0–0.4) (*Figure* 4B; top: $r = 0.15$; $r^2 = 0.023$; $P = 0.6397$; bottom: $r = 0.09$; $r^2 = 0.008$; $P = 0.7839$). This also applied to the number of elongated mitochondria (elongation: 0–0.4) (*Figure* 4C; top: $r = -0.09$; $r^2 = 0.008$; $P = 0.7804$; bottom: $r = -0.09$; $r^2 = 0.008$; $P = 0.7758$). Quantifying mitochondria at the aggregated level within the 12 3D volumes and 12 2D slices revealed a markedly different rating of shape abundance and variety (*Figure* 4D). Compared with the number of round mitochondria identified by 3D mapping, the number of mitochondria counted as round by 2D analysis was 4.5-fold higher (top section: 31% *vs*. 7%, bottom section: 32% *vs*. 7%). Elongated mitochondria were 50% more abundant on 3D than 2D analysis (top section: 93% vs. 69%; bottom section: 93% vs. 68%).

These data clearly indicate that a 2D observation is inadequate to reflect cardiomyocyte mitochondrial characteristics with respect to number, coverage area, and shape. To properly evaluate the mitochondrial parameters and to understand the relationships between mitochondrial morphology and physiology in cells displaying a substantial 'thickness' in the axial (*z*) direction, as do cardiomyocytes, 3D image analysis is indispensable.

BNIP3 deletion leads to alterations in mitochondrial number and dispersion

As shown earlier, for proper comparison of the mitochondrial compartment between physiological and pathological conditions, ultrastructural 3D characterizations are of crucial importance. FIB-SEM was subsequently performed to identify the role of BNIP3 under natural conditions *in situ* using genetically modified mice deficient in this protein.[26]

From 2D image material obtained by FIB-SEM as well as conventional TEM analyses, we gained the impression that mitochondria were more abundant in the LV tissue of *Bnip3*$^{-/-}$ mice (*Figure* 5C,D) than WT mice (*Figure* 5A,B). In the cardiomyocytes of the *Bnip3*$^{-/-}$ mice, mitochondria formed large clusters between the myofibril bundles, and they filled a large portion of the cardiomyocyte area (*Figure* 5C,D). The cardiomyocytes of the *Bnip3*$^{-/-}$ mice seemed to have a decreased dispersion of actin bundles, and most of the mitochondria displayed a round shape (*Figure* 5C,D). In these 2D analyses, no obviously damaged mitochondria were found in the *Bnip3*$^{-/-}$ mice (*Figure* 5C,D,F), and their mitochondrial ultrastructure was comparable with that in their WT counterparts (*Figure* 5A,B,E). Furthermore, alterations in neither the spatial distribution nor the morphology of the sarcoplasmic reticulum or the T-system were detectable (*Figure* 5E,F), and morphological features of impaired mitophagy could not be found in cardiomyocytes lacking BNIP3 expression.

As we have shown that such a classical 2D TEM analysis of cardiac cells is generally prone to data misinterpretation and therefore might deliver debatable results, we next aimed to verify our subjective 2D description by a comparative, quantitative 3D FIB-SEM approach. The first, again, just qualitative impression, we gained from the resulting 3D mappings was the formation of dense mitochondrial clusters in different areas/volumes of the investigated cell (*Movie* S7). Then, we addressed the number of mitochondria and, in parallel, the mitochondrial and fibrillar coverage in 315 μm^3 volumes of LV tissue. For the WT mice, we found an arithmetic average of 212 mitochondria inside the analysed volume (=0.67 mitochondria/μm^3; *Figure* 5G), which covered on average 128 μm^3 (*Figure* 5H) and therefore accounted for approximately 41% of the total observed volume. Among these organelles counted in the 'total number', many mitochondria were located at the outer borders of the volume and were not acquired as completely closed organelle bodies. As shown earlier, there is a certain likelihood that such incompletely acquired mitochondrial structures ultimately fuse in non-visible 3D planes to become one and the same organelle. To take this source of error risk into account, we also analysed the tissue volume for just fully acquired, closed mitochondrial bodies. In the WT mice, we thereby assessed an average number of 61 mitochondria (=0.19 mitochondria/μm^3; *Figure* 5I) occupying 40 μm^3 of the analysed volume (*Figure* 5J), which accounted for approximately 13% of the 315 μm^3. Inside the investigated *Bnip3*$^{-/-}$ sample volumes, a total of 359 mitochondria were counted on average (=1.14 mitochondria/μm^3; *Figure* 5G), accounting for 167 μm^3 = 53% of the total tissue volume (*Figure* 5H). Counting only fully acquired organelle bodies, an average number of 117 mitochondria (=0.37

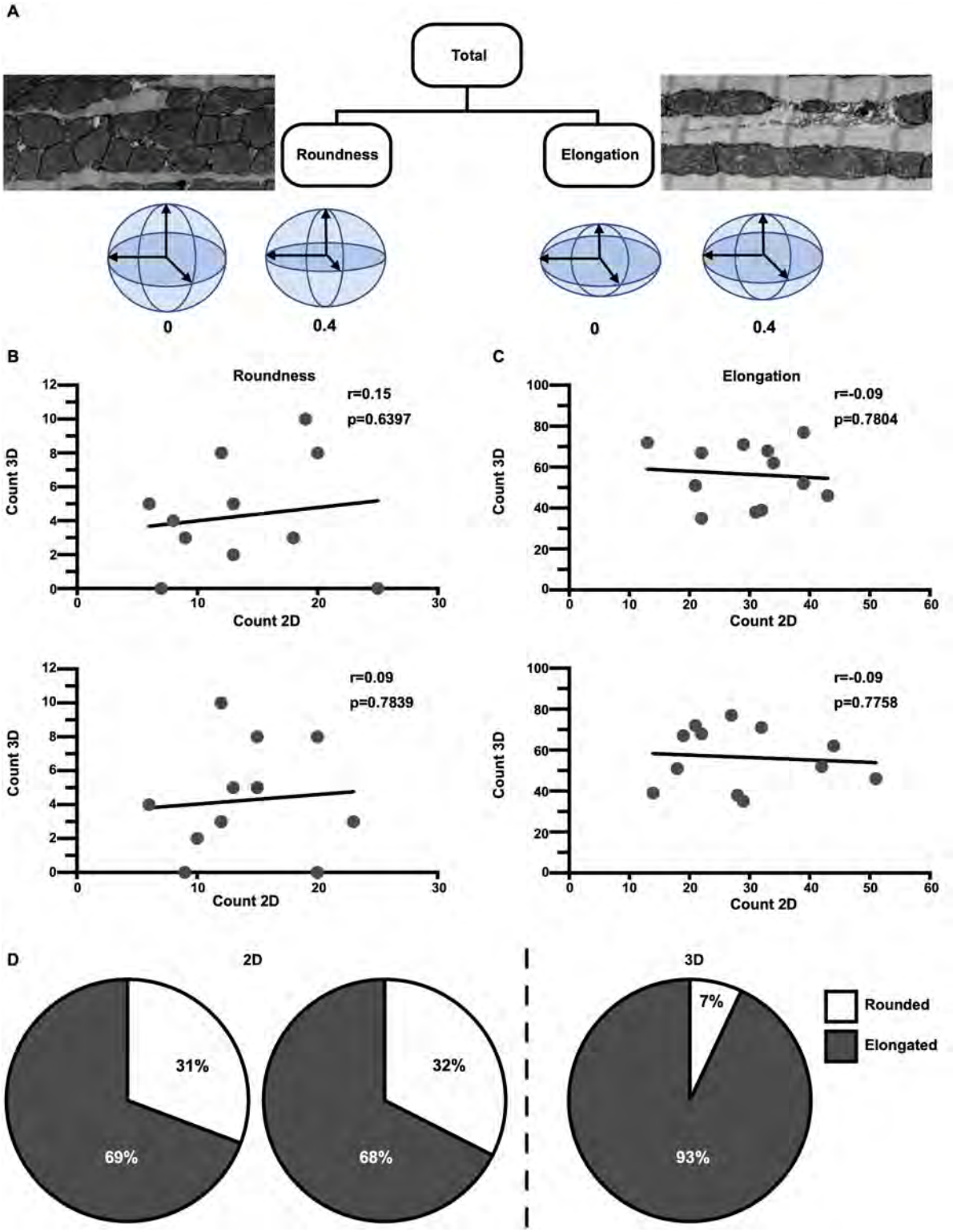

Figure 4 Quantitative two-dimensional (2D) analyses do not reflect three-dimensional (3D) facts in terms of shape. (*A*) Assessment scheme for mitochondrial shape. The anisotropy score was used to assign mitochondria to the 'rounded' group (≤0.4; left side), and the elongation score was used to assign mitochondria to the 'elongated' group (≤0.4; right side). (*B*,*C*) Mitochondrial shape divided according to 'roundness' (*B*) and 'elongation' (*C*) in the 3D reconstructions and corresponding 2D top (upper panel) and bottom sections (lower panel) from 12 focused ion beam-scanning electron microscopy (FIB-SEM) stacks (n = 3 wild-type mice). Pearson analysis does not prove a linear correlation. (*D*) Proportions of the mitochondrial shapes in the top and bottom sections (2D, left panel) and 3D reconstructions (right panel) of 12 FIB-SEM stacks (n = 3 wild-type mice).

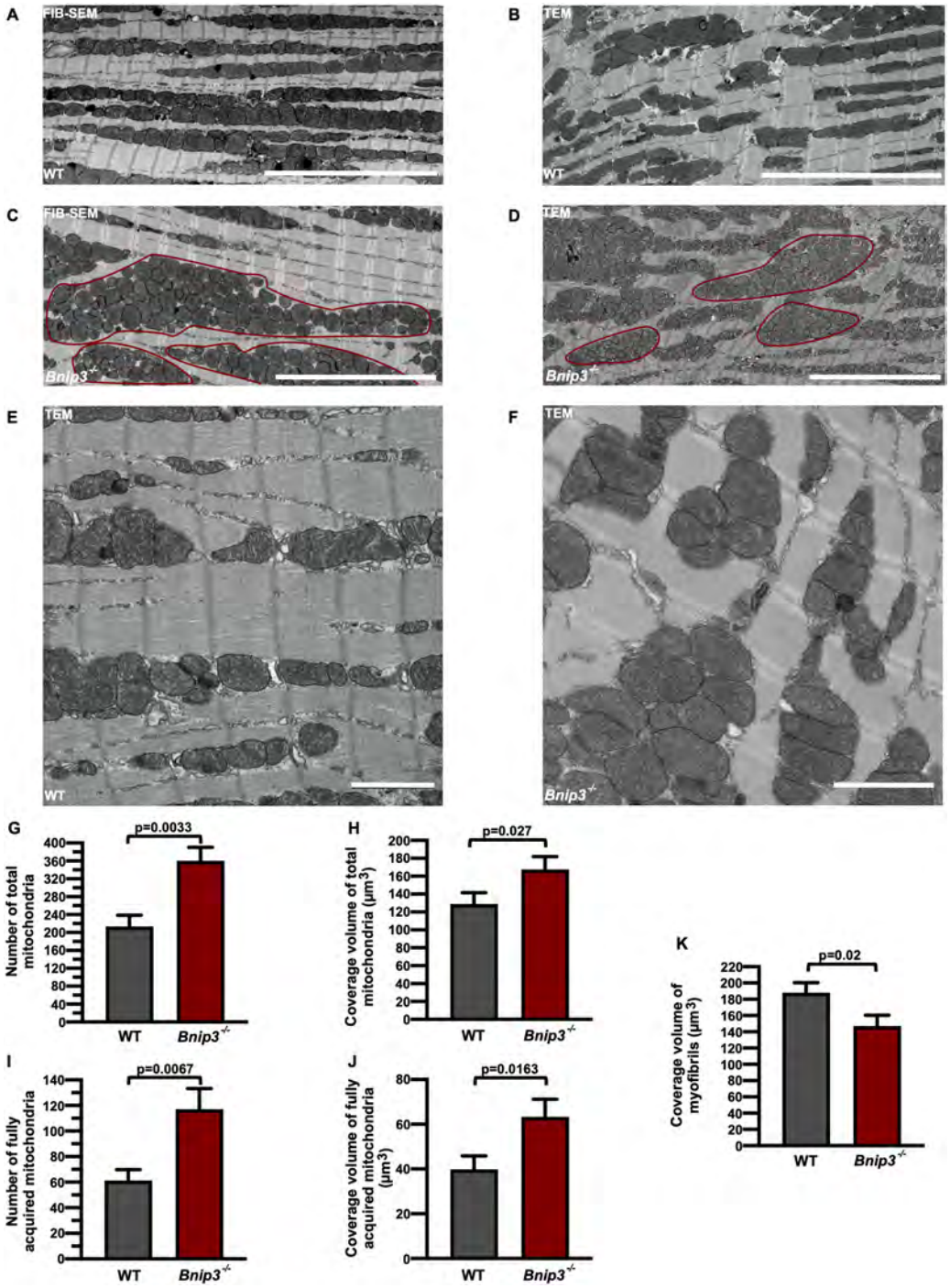

Figure 5 *Bnip3* deletion leads to alterations in mitochondrial number and dispersion. (*A*,*B*) representative section of a focused ion beam-scanning electron microscopy (FIB-SEM) stack (*A*) and a two-dimensional (2D) transmission electron microscopy (TEM) image (*B*) showing the arrangement and distribution of wild-type (WT) left ventricular (LV) mitochondria. Scale bar, 10 μm. (*C*,*D*) Representative section of a FIB-SEM stack (*C*) and a 2D TEM image (*D*) showing the arrangement, distribution and especially the cluster formation of mitochondria (red outline) in *Bnip3*$^{-/-}$ LV tissue. Scale bar, 10 μm. Refer to *Movie* S7 for animation. (*E*,*F*) Representative 2D electron micrographs of WT and *Bnip3*$^{-/-}$ LV tissue generated by TEM. Scale bar, 2 μm. (*G*) Average number of WT and *Bnip3*$^{-/-}$ total mitochondria. Data are the mean ± SD; *n* = 3 WT (4 FIB-SEM stacks) and three *Bnip3*$^{-/-}$ mice (3–4 FIB-SEM stacks). (*H*) Average coverage volume for WT and *Bnip3*$^{-/-}$ total mitochondria. Data are the mean ± SD; *n* = 3 WT (4 FIB-SEM stacks) and three *Bnip3*$^{-/-}$ mice (3–4 FIB-SEM stacks). (*I*) Average number of WT and *Bnip3*$^{-/-}$ mitochondria. Data are the mean ± SD; *n* = 3 WT (4 FIB-SEM stacks) and three *Bnip3*$^{-/-}$ mice (3–4 FIB-SEM stacks). (*J*) Average coverage volume of WT and *Bnip3*$^{-/-}$ mitochondria. Data are the mean ± SD; *n* = 3 WT (4 FIB-SEM stacks) and three mice (3–4 FIB-SEM stacks) *Bnip3*$^{-/-}$. (*K*) Average coverage volume of WT and *Bnip3*$^{-/-}$ myofibrils. Data are the mean ± SD; *n* = 3 WT (4 FIB-SEM stacks) and three *Bnip3*$^{-/-}$ mice (3–4 FIB-SEM stacks). Refer also to *Figure* S2.

mitochondria/μm^3; *Figure* 5I) was found, with a mean volume coverage of 63 μm^3 = 20% (*Figure* 5J). Regarding the number of completely acquired organelle bodies, these results suggested that the *Bnip3*$^{-/-}$ cardiomyocytes contained on average 1.9× more mitochondria than the WT cardiomyocytes (117 for *Bnip3*$^{-/-}$ vs. 61 for WT) with similar volume of the *Bnip3*$^{-/-}$ and WT cardiomyocytes (*Bnip3*$^{-/-}$: 2.0×10^4 $\mu m^3 \pm 0.5 \times 10^4$ μm^3, WT: 2.1×10^4 $\mu m^3 \pm 0.4 \times 10^4$ μm^3, *Figure* S2A,C). This difference in organelle number corresponds to the outcome of mitochondrial isolation from whole mouse hearts. Here, it was found that on average, 1.52× more mitochondria could be isolated from the *Bnip3*$^{-/-}$ hearts than the WT counterparts (*Figure* S2D; $P < 0.0001$). Because we measured a significantly greater volume coverage by mitochondria in *Bnip3*$^{-/-}$ cardiomyocytes than in WT cardiomyocytes, we examined whether this increase was accompanied by a corresponding decrease in volume coverage by myofibrils (*Figure* 5K). Although the average myofibril volume coverage was significantly lower in the *Bnip3*$^{-/-}$ LV tissue samples (147 μm^3) than in the WT LV tissue samples (188 μm^3), a decrease in the myofibril protein actin could not be demonstrated statistically (*Figure* S2E). Hence, the decrease in the myofibril coverage area is due to a greater degree of myofibril compression in *Bnip3*$^{-/-}$ cardiomyocytes rather than attenuated myofibril biosynthesis.

Bnip3$^{-/-}$ *mitochondria are smaller and less complex than WT mitochondria*

Because approximately 25% more mitochondria occupied the same space in the analysed volume of *Bnip3*$^{-/-}$ LV tissue compared with the WT samples, the mitochondria were expected to be smaller in size, accordingly. To prove this assumption, we compared the volumes of 729 WT and 1285 *Bnip3*$^{-/-}$ fully acquired mitochondria in cardiac tissue samples. The mean individual mitochondrial volume did not appear to differ significantly (*Figure* 6A inset). However, cumulative frequency analyses showed considerable variations (*Figure* 6A). Therefore, we focused the volume distribution more precisely. *Bnip3*$^{-/-}$ cardiomyocytes showed a volume range from 0.2735 to 0.742 μm^3 for 50% of mitochondria and a mitochondrial volume maximum of 3.674 μm^3, whereas 50% of WT mitochondria ranged from a similar numerical baseline (0.214 μm^3) to 0.948 μm^3 (*Figure* 6B). Remarkably, the WT mitochondria showed a 38% greater maximum volume (5.062 μm^3) than the *Bnip3*$^{-/-}$ mitochondria (*Figure* 6B). Comparison of the distribution parameter in the population of either single samples or of the mice showed a significantly higher coefficient of variation in both cases for the WT group, which confirmed the more heterogeneous volume distribution under WT conditions (*Figure* 6C; samples $P < 0.0001$; mice $P = 0.0221$).

Because an altered fission/fusion cycle can lead to smaller mitochondria and increased number, we performed semi-quantitative western blot analysis of the fusion-related proteins OPA1 and OMA1 in *Bnip3*$^{-/-}$ and WT mouse heart homogenates. Whereas *Bnip3*$^{-/-}$ and WT mouse mice showed similar OPA1 levels (*Figure* S2F; $n = 3$ mice per group; $P = 0.7913$), the level of OMA1, which plays a key role in the stress-induced cleavage of OPA1 into a shorter, fusion-inactive form,[47] was higher in *Bnip3*$^{-/-}$ mouse hearts in comparison to WT mouse hearts (*Figure* S2G; $n = 3$ mice per group; $P = 0.0875$). This might indicate an increased inhibition of fusion in *Bnip3*$^{-/-}$ mice, thereby causing a shift of mitochondrial fission/fusion regulation in favour of fission. Future experiments are needed here.

Because the 3D mapping of mitochondria disclosed a high complexity of mitochondrial shape with round, elongated, flattened, and polymorphic entities (*Figure* 2D, *Movie* S2), we evaluated whether mitochondrial complexity significantly differed between the two genetically different mouse strains. Therefore, we used the 729 WT and 1285 *Bnip3*$^{-/-}$ mitochondria and calculated the MCI,[39] which describes the relationship between the mitochondrial surface area and volume without taking size values into consideration. Compared with the WT organelles, the *Bnip3*$^{-/-}$ mitochondria were on average 12% less complex (*Figure* 6D, inset; $P < 0.0001$). The MCI population dispersions were significantly different as determined by cumulative frequency distribution analysis (*Figure* 6D,E). Fifty per cent of the *Bnip3*$^{-/-}$ mitochondria displayed MCI values ranging from 4.156 to 5.931, whereas the MCI values of the WT mitochondria ranged from 4.236 to 6.791. The MCI population distributions differed considerably in the abundance of complex mitochondria (above the 90th percentile), with maxima of 25.42 (WT) and 21.27 (*Bnip3*$^{-/-}$). Comparison of the distribution between the WT and *Bnip3*$^{-/-}$ mitochondrial MCI yielded a similar coefficient of variation for samples and mice (*Figure* 6F; samples $P < 0.2875$; mice $P = 0.1595$).

To capture the shape complexity, we examined the form variability of the 729 WT and 1285 *Bnip3*$^{-/-}$ mitochondria. Therefore, we calculated the roundness (r), elongation (e), and flatness (f) values of each mitochondrion. The degree of each parameter is described by a range from 0–1. Mitochondria were classified as globular (r: 0–0.4; e: 0.5–1; f: 0–1), rod-shaped (r: 0.5–1; e: 0–0.4; f: 0.5–1), long-striped (r: 0.5–1; e: 0–0.4; f: 0–0.4), flattened (r: 0.5–1; e: 0.5–1; f: 0–0.4), and soft square-shaped (r: 0.5–1; e: 0.5–1; f: 0.5–1) (*Figure* 6G; *Figure* S3). In the *Bnip3*$^{-/-}$ group, more than 80% of the mitochondria were distributed along the three axes, being globular (17%), rod-shaped (20%) or soft square-shaped (47%). Sixteen per cent of mitochondria were limited along two of three axes, possessing a long-striped (6%) or flattened shape (10%) (*Figure* 6H). In contrast, there were 3.3 times more WT than *Bnip3*$^{-/-}$ mitochondria that were long-striped (16%) or flattened (36%). Seven per cent

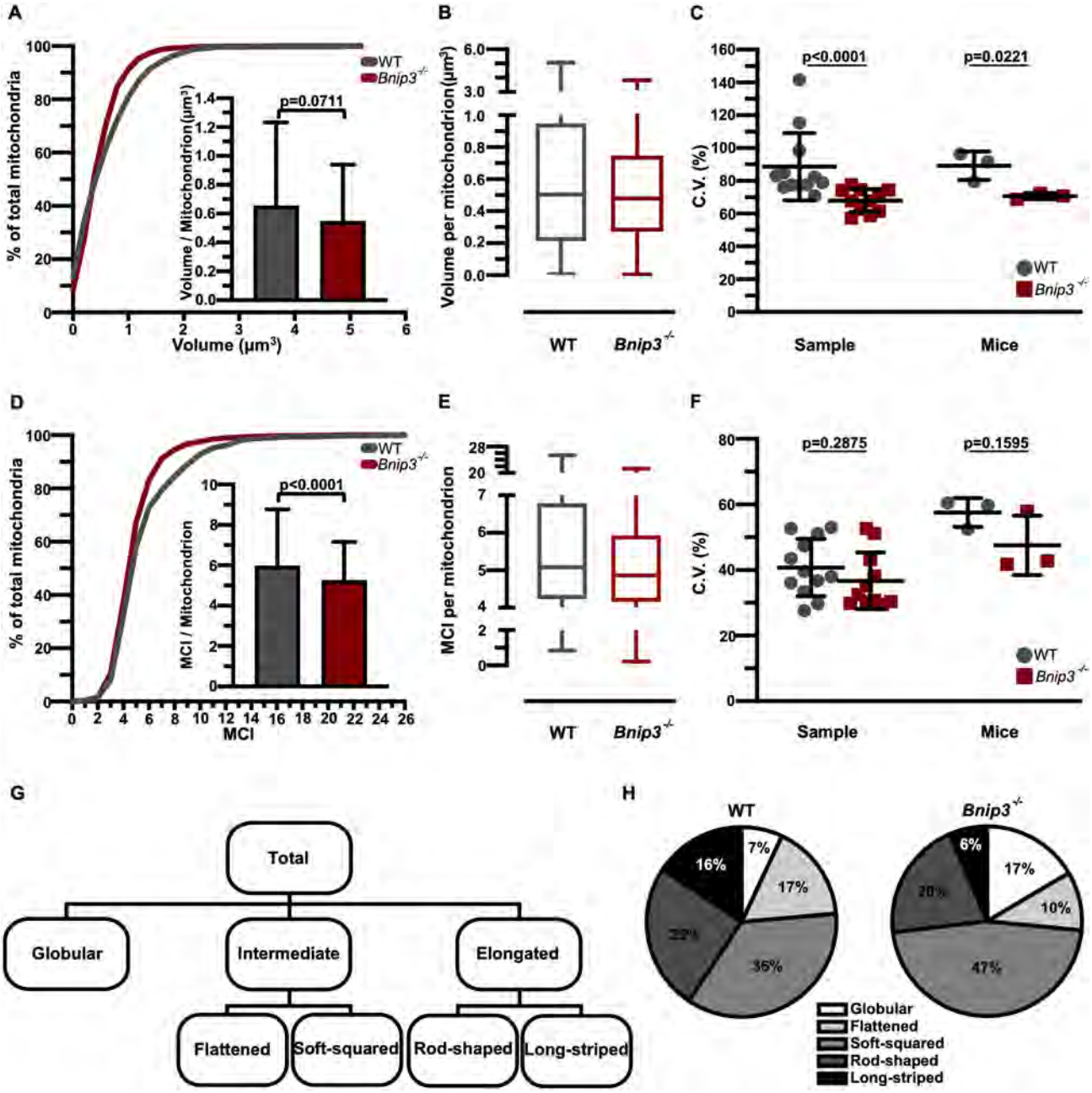

Figure 6 *Bnip3*$^{-/-}$ cardiac mitochondria are smaller and less complex than wild-type (WT) cardiac mitochondria. (*A*,*B*) Population distribution of individual mitochondrial volume in focused ion beam-scanning electron microscopy (FIB-SEM) stacks from WT (grey) and *Bnip3*$^{-/-}$ (red) mice. (*A*) Shown as cumulative frequency distribution, inset: mean ± SD (n = 729 in WT; n = 1285 in *Bnip3*$^{-/-}$, Mann–Whitney test). (*B*) Shown as box and whisker plots (min to max percentiles and median). (*C*) Coefficient of variation (CV) for mitochondrial volume in wild-type (WT) and *Bnip3*$^{-/-}$ mice. CV values are shown for mitochondria in FIB-SEM samples (n = 11–12) and in mice (n = 3). Data are shown as the mean ± SD. (*D*) Mitochondrial complexity index (MCI) in WT and *Bnip3*$^{-/-}$ mice shown as cumulative frequency distribution and average (inset). Mean ± SD (n = 729 in WT; n = 1285 in *Bnip3*$^{-/-}$, Mann–Whitney test). (*E*) MCI in WT and *Bnip3*$^{-/-}$ mice shown as box and whisker plots (min to max percentiles and median). (*F*) CV for MCI in WT and *Bnip3*$^{-/-}$ mice (n = 11–12 samples; n = 3 mice). Data are shown as the mean ± SD. (*G*) Assessment scheme of mitochondrial shape. Three-dimensional (3D) approaches enable the determination of a further spatial dimension and hence allow better alignment in shape groups. Roundness (r), elongation (e) and flatness (f) scores were used to classify mitochondria as globular (r: 0–0.4; e: 0.6–1; f: 0.6–1), rod-shaped (r: 0.6–1; e: 0–0.4; f: 0.5–1), long-striped (r: 0.8–1; e: 0–0.4; f: 0–0.4), flattened (r: 0.6–1; e: 0.5–1; f: 0–0.4) and soft square-shaped (r: 0.5–1; e: 0.5–1; f: 0.5–1). Refer also to *Figure* S3. (*H*) Proportions of the mitochondrial shape populations in WT (left panel) and *Bnip3*$^{-/-}$ (right panel) mice.

of WT mitochondria depicted a globular shape, 25% a rod shape and 36% a soft square shape (*Figure* 6H).

Collectively, *Bnip3*$^{-/-}$ cardiomyocytes had more mitochondria arranged in clusters than WT cardiomyocytes, at the expense of a decreased myofibril area. *Bnip3*$^{-/-}$ mitochondria, when compared with WT mitochondria, appeared more often with a lower volume and were less complex, while being almost globular, rod-shaped or soft square-shaped and less flattened in shape. These data indicate a physiological role of BNIP3 in the control of mitochondrial quantity and morphology.

Changes in Bnip3$^{-/-}$ *mitochondrial morphology and organization alter energy metabolism*

To understand the correlation between the size, shape and density distribution of mitochondria and energy metabolism, we mapped functional differences between WT and *Bnip3*$^{-/-}$ mitochondria by quantifying the oxygen consumption rate (OCR) using Seahorse® XF extracellular flux analyser technology (*Figure* 7A). *Bnip3*$^{-/-}$ mitochondria showed higher respiratory indices than WT mitochondria, as evidenced by significantly elevated oxygen consumption at baseline (*Figure* 7B). Compared with WT mitochondria, they also exhibited greater respiration activity after adenosine diphosphate injection (*Figure* 7C). Blockage of adenosine triphosphate (ATP) synthase with oligomycin resulted in a greater drop in the OCR in *Bnip3*$^{-/-}$ mitochondria than in WT mitochondria, reflecting greater ATP production in mitochondria in the genetically modified animals (*Figure* 7D). Remarkably, *Bnip3*$^{-/-}$ mitochondria also displayed greater proton leak. As proton leak represents protons that migrate into the mitochondrial matrix without producing ATP, BNIP3 ablation is attributed to a more incomplete coupling of substrate oxygen to ATP generation (*Figure* 7E). We conclude that the increased quantity and function associated with a distorted myofibril region in *Bnip3*$^{-/-}$ cardiomyocytes might play a compensatory role for contractility by increasing ATP levels. This was also supported by the echocardiographic observation that the LV function of *Bnip3*$^{-/-}$ animals was not impaired compared with that of WT animals, as judged by the similarity in the ejection fraction (55.5% vs. 51.68%), cardiac output (14.6 mL/min vs. 15.72 mL/min) and stroke volume (30.3 μL vs. 32.99 μL). *Bnip3*$^{-/-}$ mouse hearts even showed slightly increased fractional shortening (33.6% vs. 25.61%; *Figure* 7F).

Discussion

Although several studies on different cell systems have described a correlation between the morphology and function of mitochondria,[39,48,49] it remains challenging to identify clear links between cardiomyocyte mitochondrial ultrastructure and dysfunction in cardiac diseases. Notably, mitochondria of cardiomyocytes distinguish from non-cardiac mitochondria, for example, in that they are rather static than dynamic and immobile compared with mitochondria of fibroblasts, which are highly dynamic and motile, and mitochondria of neurons, which are dynamic and highly motile. Therefore, the findings from non-cardiac systems are not directly transferable to cardiac systems.[50] Our work aimed to shed light on the crucial question of whether a 2D EM analysis of the cardiomyocyte ultrastructure is sufficient to comprehensively describe the mitochondrial compartment and whether such planar imaging data are suited to correlate mitochondrial morphological data. To be able to judge acquired 2D EM data, we established a comparative 3D imaging system based on FIB-SEM nanotomography.

In the past, many widely recognized studies have used a variety of cell culture models to improve our understanding of the molecular and cellular basis of cardiac function and differentiation and to develop valuable therapeutic concepts. Hence, we first used FIB-SEM to investigate the ultrastructure of isolated cardiomyocytes. Only a few studies describe morphological differences between isolated cardiomyocytes either grown in 2D or 3D culture or remaining inside the 3D environment of cardiac tissue.[51] Most of these works dealt with differences in physiological parameters or in gene expression patterns.[51,52] Our first 3D analysis on the mitochondrial distribution pattern inside isolated cardiomyocytes demonstrated that the isolation process already altered the mitochondrial network distribution inside the cell. In contrast to cardiomyocytes *in situ*, most of the mitochondria inside the isolated cells were located at the cellular borders. This finding immediately underlined the importance of always taking structural post-isolation modifications into account and highlights that isolated cardiomyocytes are not the best-suited model for the characterization of the spatial distribution pattern of cardiomyocyte mitochondria. The differences in 3D over a 2D analysis for qualitative image interpretation holds true for parameters, including the mitochondrial number, dispersion space, size, and shape variety. The absence of any correlation or equivalent pattern of changes between the 2D and 3D data substantiated that apart from qualitative descriptions, 3D analysis was also indispensable for the accurate quantification of mitochondrial alterations. Moreover, the value of a 3D reconstruction was found in the numerous observations that one and the same mitochondrion is able to intersperse within the fibrillar network. In contrast to other studies,[53,54] these findings corroborate our former results showing that a general morphological discrimination of cardiac mitochondria between subtypes,[55] such as IFM or SSM is not meaningful.[43] Because most of these interfibrillar mitochondria located near the cell border crossed myofibril bundles in higher or lower cell areas and finally branched into

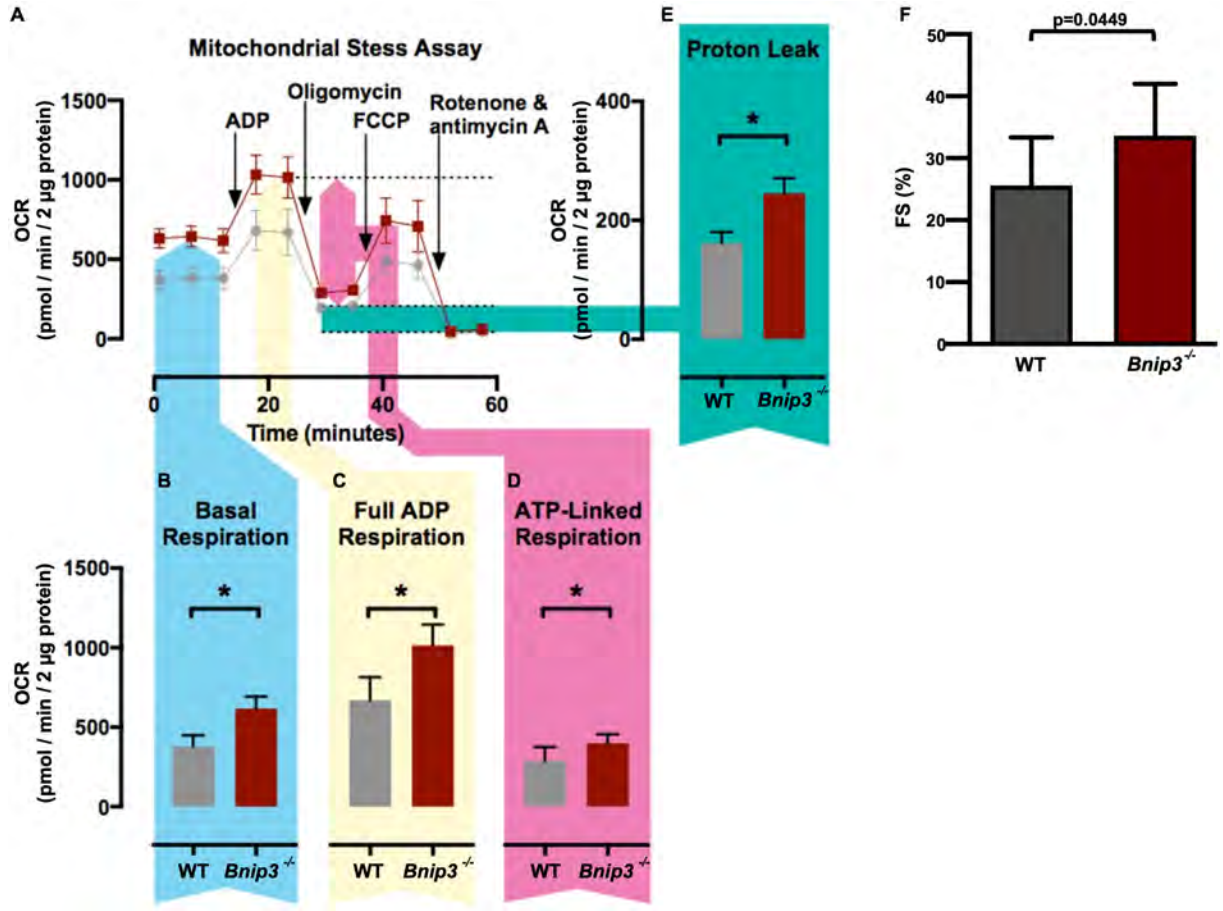

Figure 7 Changes in *Bnip3*$^{-/-}$ mitochondrial morphology and organization alter energy metabolism. (*A*–*E*) Respiration in isolated mitochondria from wild-type (WT, red) and *Bnip3*$^{-/-}$ mice (grey). Data are the mean ± SD (*n* = 5 mice). (*A*) Development of the oxygen consumption rate (OCR) after the addition of adenosine diphosphate (ADP) [adenosine triphosphate (ATP) synthesis initiation], oligomycin (respiratory chain complex V blocking), 4-(trifluoromethoxy) phenylhydrazone (FCCP; uncoupling of ATP synthesis from electron transport), rotenone and antimycin A (entire electron chain blocking through inhibition of Complexes I and III). (*B*) Basal respiration. (*C*) Full ADP respiration. (*D*) ATP-linked respiration. (*E*) Proton leakage. (*F*) Echocardiography of wild-type (WT) and *Bnip3*$^{-/-}$ mice showing fractional shortening (FS). Data are the mean ± SD (*n* = 5 mice per group).

the subsarcolemmal space, therefore, these mitochondria could be assigned to both subpopulations. Nevertheless, it can be assumed that mitochondria according to their *in situ* localization in different environments such as myofibrils or close to the sarcolemma, respectively, may depict different biochemical activities.

Crucial for an appropriate number and morphology of mitochondria is a dynamic balance between antagonistic forces of mitochondrial fusion and fission.[56] In contrast to confocal microscopy, EM represents the best suited microscopy technique for analysing ultrastructural changes in the course of membrane fusion and fission processes due to a sufficiently high resolution. Our results depict that 3D has the advantage to discriminate two individual only closely attached mitochondria from a mitochondrion being in the fusion or fission process but we are aware that we have to improve FIB-SEM technique for better resolution with a gain in uncovering membrane ultrastructures with focus on the cristae. In addition, our results confirmed that the lack of z-axis information does not allow precise definition of the actual morphological architecture of cardiomyocyte mitochondria with a high degree of complexity and spatial spread, underlining the need for 3D rendering.[57] In summary, a comparison of the 3D results with the corresponding 2D data revealed that a plain 2D analysis yielded biased data regarding mitochondrial quantity and morphology and therefore was unable to accurately reflect cardiac mitochondrial peculiarities *in situ*.

The value of the 3D analysis was verified by evaluation of the morphological, quantitative and distributional differences in cardiomyocyte mitochondria lacking BNIP3. BNIP3 is supposed to constitute a key factor in the induction of mitophagy described in various cell types associated with cell-protective effects as well as with cell death.[58–64] BNIP3's promitophagic activity in cardiomyocytes *in vivo* is linked to pathologies and has been shown to be maladaptive.[26,65,66] Despite the increased appearance of mitochondria in cardiomyocytes

lacking *Bnip3*, no evident damaged or dysfunctional mitochondria could be observed, indicating that mitophagy was not substantially impaired. But the observation of a greater number of mitochondria, which were smaller and less complex in *Bnip3*$^{-/-}$ cardiomyocytes suggests a role of BNIP3 in the fusion/fission cycle. At first glance, this cycle does not appear to be a relevant process for myocardial biology, as cardiomyocyte mitochondria are regarded to be rather static due to the dense myofilament arrangement.[67] Studies with the combined abrogation of fission and fusion proteins or a disturbed balance indicated the relevance of the fusion/fission cycle to cardiac health, as its perturbation was detrimental to the heart. This is also observed in, for example, dilated cardiomyopathy, heart failure, and LV hypertrophy.[67–70] In these cases, mitochondria are accumulated, shortened, and damaged. In addition, as in our observations, displacement of sarcomeres by superabundant centrally located mitochondria was noted. These alterations were also apparent in the cardiac biopsy of a human patient suffering from myocarditis (*Figure* S4, *Movie* S8). In preclinical studies, myocarditis has also been linked to an imbalance in the fusion/fission cycle.[71,72] All of these features, except damaged mitochondria, were equally observed in cardiomyocytes lacking BNIP3 under natural conditions. The phenomenon of an increased number of smaller mitochondria without obvious ultrastructural damage in cardiomyocytes lacking BNIP3 was likewise observed in mouse hearts overexpressing the fission protein DRP1.[6] Taking into consideration that both DRP1 overexpression and BNIP3 deletion led to advanced fission, a regulatory involvement of BNIP3 in fusion processes is tempting to speculate. Regarding that, BNIP3 interacts with the fusion-related protein OPA1 in HeLa cells.[73] BNIP3 may regulate OPA1 in an activating manner in cardiomyocytes. This is supported by the finding that the level of OMA1, which plays a key role in cleavage of OPA 1 into a fusion-inactive form, is elevated in *Bnip3*$^{-/-}$ mouse hearts, which might result in an increased inhibition of fusion, thereby causing a shift in favour of fission.

In terms of bioenergetics, our data show that the loss of BNIP3 also affects the cardiomyocyte energy metabolism, with an increase in dioxygen consumption and ATP generation. This effect was associated with a slight increase in fractional shortening. The increase in respiration reflects the fitness of cardiomyocyte mitochondria in *Bnip3*$^{-/-}$ mice and could point to a compensatory mechanism to rescue cardiomyocyte contraction. As a mode of action, we hypothesize that the apparent clustering of more rounded mitochondria may result in greater interconnectivity.[74] A similar phenomenon was also observed in diabetes, where clusters of mitochondria showed increased respiration.[75] These morphological and biochemical data suggest a physiological function of BNIP3 as a primary driver of the fusion/fission cycle regulating the homeostasis of cardiac bioenergetics.

In conclusion, this work demonstrates and underlines the need for 3D imaging approaches when the cardiomyocyte mitochondrial network is the target of a qualitative or quantitative microscopic analysis. Our data clearly prove that 2D image materials are prone to misinterpretation and that the superior 3D approach allows the accurate interpretation of mitochondrial alterations, providing a suggestion of the role of mitochondrial regulatory proteins such as BNIP3.

Funding

J. H.-W. was funded by Juergen Manchot Stiftung; S. S. was supported by the German Research Foundation (UMEA Junior Clinician Scientist); P. L. (LU 2139/2-1) and U. B. H.-C (HE 6317/2-1) were funded by the German Research Foundation; and T. R. was funded by Else-Kroener-Fresenius-Stiftung (2014_A216) and the German Research Foundation (RA 969/12-1).

Author contributions

Conceptualization was carried out by Ulrike B. Hendgen-Cotta; methodology was created by Elke Winterhager, Mike Hasenberg, and Ulrike B. Hendgen-Cotta; supervision was provided by Tienush Rassaf, Mike Hasenberg, and Ulrike B. Hendgen-Cotta; investigation was performed by Jacqueline Heinen-Weiler, Anna-Lena Beerlage, Stephan Settelmeier, and Hannah Doepper; human tissue acquisition and clinical information was carried out by Peter Luedike; data analysis and interpretation was performed by Jacqueline Heinen-Weiler, Anna-Lena Beerlage, Stephan Settelmeier, Martin Heisler, Elke Winterhager, and Ulrike B. Hendgen-Cotta; statistical analysis was performed by Jacqueline Heinen-Weiler, Martin Heisler, Bernd Walkenfort, Ulrike B. Hendgen-Cotta; writing of the original draft of the manuscript was carried out by Elke Winterhager, Mike Hasenberg, Ulrike B. Hendgen-Cotta; all authors performed critical revision of the manuscript.

Acknowledgements

The authors certify that they comply with the ethical guidelines for authorship and publishing in the *Journal of Cachexia, Sarcopenia and Muscle*.[76]

We gratefully acknowledge the technical assistance of Pia Stock (Department of Cardiology and Vascular Medicine). In addition, we would like to thank the Imaging Center Essen (IMCES) for unlimited technical support, Sylvia Voortmann for technical assistance and Dr Holger Jastrow for his scientific input. Further, we thank Dr Gerald Dorn II, MD, for the gift of the *Bnip3*$^{-/-}$ mice.

Online supplementary material

Additional supporting information may be found online in the Supporting Information section at the end of the article.

Movie S1. 3D reconstruction of the mitochondrial network inside an isolated cardiomyocyte. Related to Figure 1A-C. The movie first shows the virtual flight through an isolated mousecardiomyocyte. The mitochondrial areas are visible in dark grey whereas myofibrils can be identified from their light grey appearance. All individual images represent x-y single plane pictures of a FIB-SEM analysis of which the resulting z stack was composed of 705 images at a z-distance of 100 nm. The total dimensions of the analysed volume equaled 77.35 x 49.96 x 70.5 μm (isolated cardiomyocyte size 37.39 x 20.31 μm (xy-axis) and 79.27 x 18.11 μm (yzaxis)). In the second part of the movie, the result of an ultrastructural segmentation of that cardiomyocyte is developed as 3D model. For that, the outer cell membrane is displayed in blue, myofibrils are highlighted in yellow, nuclei in green and mitochondria in red. Please note that the myofibril compartment was rendered transparent at the end of the movie to clearly depict the course of the mitochondrial network in a 360° rotation. Scale bar 15 μm.

Movie S2. 3D reconstruction of the mitochondrial network inside mouse cardiac tissue. Related to Figure 1D. The movie first shows the virtual flight through a mouse cardiac biopsy sample. The mitochondrial areas are visible in dark grey whereas myofibrils can be identified from their light grey appearance. All individual images represent x-y single plane pictures of a FIB/SEM analysis of which the resulting z stack was composed of 21 images at a z-distance of 150 nm. The total dimensions of the analysed volume equaled 10 x10 x 3.15 μm. In the second part of the movie, the result of an ultrastructural tissue segmentation is shown as 3D model. In the beginning of the rotation just the surface view of the volume is visualized where the contours of the mitochondria are depicted in dark blue and the interspersed myofibrils in light blue. Subsequently, the myofibril compartment is rendered transparent so that the inner part of the volume is revelled. Now, all mitochondria are shown as 3D objects in individual colours and lipid droplets in black. After a 360 ° rotation, all partially acquired mitochondrial bodies are removed so that the shape variety of the individual mitochondria of round, elongated and polymorph can be easily assessed. Scale bar 1.6 μm.

Movie S3. 3D Reconstruction of a complex mitochondrion inside mouse cardiac tissue is a prerequisite for proper quantification. Related to Figure 1E, F. The movie first shows the virtual flight through a mouse cardiac biopsy sample. The mitochondrial areas are visible in dark grey whereas myofibrils can be identified from their light grey appearance. All individual images represent x-y single plane pictures of a FIB-SEM analysis of which the resulting z stack was composed of 100 images at a z-distance of 20 nm. The total dimensions of the analysed volume equaled 6.45 x 3.78 x 2 μm (x/y/z-axis). In the second part of the movie, the result of an individual mitochondrial segmentation is shown as very large 3D model in turquoise (mitochondrion size up to 6 μm). Please note the appearance of this single but branched mitochondrion as several organelles at different planes of the z-stack. Scale bar 1.2 μm.

Movie S4. 3D Reconstruction of a complex mitochondrion inside mouse cardiac tissue is a prerequisite for proper classification. Related to Figure 1G. The movie shows the virtual flight through a mouse cardiac biopsy sample during which the result of an individual mitochondrial segmentation is shown as 3D model in turquoise. The mitochondrial areas are visible in dark grey whereas myofibrils can be identified from their light grey appearance. All individual images represent x-y single plane pictures of a FIB-SEM analysis of which the resulting z stack was composed of 48 images at a z-distance of 30 nm. The total dimensions of the analysed volume equaled 3.24 x 4.9 x 1.44 μm (x/y/z-axis). Please note the appearance of this single but branched mitochondrion as several organelles of the subsarcolemmal (SSM) or interfibrillar (IFM) type at different planes of the z-stack.

Movie S5. 3D Reconstruction of a single mitochondrion interspersing myofibrils. Related to Figure 1H. The movie shows the result of an ultrastructural segmentation of a mouse cardiac biopsy sample as 3D model. The single mitochondrion is visualized in green whereas the myofibrillar compartment which gets interspersed by the mitochondrion is highlighted in yellow. The underlying 3D model is a part of a FIB-SEM analysis which was performed on a sample volume of 4.51 x 6.69 x 3.57 μm generating Y individual single plane images at a voxel size of 3 x 3 x 30 nm. Scale bar 1 μm.

Movie S6. 3D analysis of cardiac mitochondrial fission process. Related to Figure 1 J, K. The movie shows the virtual flight through a mouse cardiac biopsy sample at the border zone during which ongoing fission process is visible. Also, a 3D model of both involved mitochondria is visible in turquoise coloured. The mitochondrial areas are visible in dark grey whereas myofibrils can be identified from their light grey appearance. All individual images represent x-y single plane pictures of a FIB-SEM analysis of which the resulting z stack was composed of 21 images at a z-distance of 20 nm. The total dimensions of the analysed volume equaled 3.06 x 2.08 x 0.42 μm (x/y/z-axis) (x/y/z-axis). Scale bar 1 μm.

Movie S7. 3D analysis of the mitochondrial network inside cardiac tissue of *Bnip3*$^{-/-}$ mice. Related to Figure 5C,D. The movie shows the virtual flight through a left ventricular biopsy sample of *Bnip3*$^{-/-}$ mice during which the contours of the segmented mitochondria are highlighted in red. The mitochondrial areas are visible in dark grey whereas myofibrils can be identified from their light grey appearance.

All individual images represent x-y single plane pictures of a FIB-SEM analysis of which the resulting z stack was composed of 21 images at a z-distance of 150 nm. The total dimensions of the analysed volume equaled 26.09 × 18.56 x 3.15 μm (x/y/z-axis). Please note the obviously altered arrangement, distribution and especially the cluster formation of the mitochondria compared to the wildtype situation. Scale bar 8.4 μm.

Movie S8. 3D Reconstruction of damaged mitochondria inside a human tissue biopsy of a myocarditis patient. Related to Supplemental Figure 4A, B. The movie first shows the virtual flight through a human cardiac biopsy sample of a patient suffering from myocarditis. The mitochondrial areas are visible in dark grey whereas myofibrils can be identified from their light grey appearance. All individual images represent x-y single plane pictures of a FIB-SEM analysis of which the resulting z stack was composed of 100 images at a z-distance of 20 nm. The total dimensions of the analysed volume equaled 4.64 x 6.21 x 2 μm. In the second part of the movie, the result of a mitochondrial segmentation is shown for which just mitochondria with an obvious damage of their ultrastructure were included. The 3D models of these mitochondria with affected ultrastructure are shown in individual colours. Please also note other indications of myocarditis, such as cluster formation of mitochondria with relatively small size and myofibril distortion. Scale bar 1.22 μm.

Figure S1. Quantitative 2D analyses does not reflect 3D facts. Related to Figure 3. (A) Individual deviation (%) of mitochondrial number in 2D (top section: upper panel; bottom section: lower panel) from mitochondrial number obtained from 3D reconstructions. (B) Individual deviation (%) of mitochondrial coverage areas (top section: upper panel; bottom section: lower panel) from mitochondrial volumes. (C) Cumulative frequency distribution of individual mitochondrial size in 3D and 2D. In 3D the size is considered as mitochondrial volume in 3D reconstructions (green). For 2D the size is considered as mitochondrial area in bottom section (grey). To enable comparisons despite unequal dimension number, roots of absolute values were extracted. (D) Representative histograms of individual mitochondrial size. Mitochondrial area frequency in the bottom section of four FIB-SEM stack was plotted in the upper panel (grey) and corresponding volume frequency in the 3D reconstruction in the lower panel (green). The curve shape describing parameters skewness and kurtosis are indicated. (E) Cumulative frequency distribution of individual mitochondrial shape parameter in 3D and 2D. In 3D, the shape is considered as mitochondrial surface area (green). For 2D, the shape is considered as mitochondrial perimeter in top sections (grey). To enable comparisons despite unequal dimension number, roots of absolute values were extracted. (F) Representative histograms of individual mitochondrial shape. Mitochondrial perimeter frequency in the bottom section of four FIB-SEM stack was plotted in the upper panel (grey) and corresponding surface area frequency in the 3D reconstruction in the lower panel (green). The curve shape describing parameters skewness and kurtosis are indicated. (12 FIB-SEM stacks, n = 3 wild-type mice).

Supplementary Figure S2. *Bnip3* deletion leads to mitochondrial protein changes. (A, B) Representative fluorescence images of isolated mouse cardiomyocytes from wild-type (WT) (A) and *Bnip3*$^{-/-}$ mice (B) (n = 3 mice each group; n = 6 cardiomyocytes each mouse). Cardiomyocytes were acquired in z-stacks, mitochondria (red), actin (green) and nuclei (blue). Scale bar, 50 μm. (C) Average volumes of isolated cardiomyocytes from WT (grey) and *Bnip3*$^{-/-}$ mice (red) (n = 3 mice each group; n = 6 cardiomyocytes each mouse). (D) Relative mitochondrial amount from WT and *Bnip3*$^{-/-}$ mouse hearts. (n = 8 mice each group). (E) Average of actin expression from WT and *Bnip3*$^{-/-}$ mouse hearts. (n = 3 each group). (F) Relative OMA1 expression from WT and *Bnip3*$^{-/-}$ mouse hearts (n = 3 each group). (G) Relative OPA1 expression from WT and *Bnip3*$^{-/-}$ mouse hearts (n = 3 each group). Data are mean ± SD.

Supplementary Figure S3. Mitochondrial shape classification. Related to Figure 6. Overview of shape groups with representative corresponding ellipsoids and 3D models from either xy-, xz- and yx-view. Polymorphic mitochondria are not represented in globular group.

Supplementary Figure S4. Imaging of human myocarditis. (A-D) 2D electron micrographs of heart tissue in human myocarditis (n = 1). TEM overview (A) and closeup image (B) of a longitudinal orientated cardiomyocyte depicting cluster formation (red) and damaged mitochondria (cyan) as well as distorted myofibrils (yellow). See also Supporting Information Movie S8

Supplementary Listing S1. Mitochondrial classification algorithm. Custom script to align mitochondria into shape groups based on Python coding language. Data are extracted from a coma separated value (.csv) file that listed the shape parameters of each unique mitochondrion in a separate row. Parameter ranges enter the algorithm via the dictionary object that refers to 'limits'.

Conflict of interest

Jacqueline Heinen-Weiler, Mike Hasenberg, Martin Heisler, Stephan Settelmeier, Anna-Lena Beerlage, Hannah Doepper, Bernd Walkenfort, Andrea Odersky, Peter Luedike, Elke Winterhager, Tienush Rassaf, Ulrike B. Hendgen-Cotta declare that they have no conflict of interest.

Data availability statement

Image stacks and model files are available from the authors upon request.

References

1. Bonora M, Wieckowski MR, Sinclair DA, Kroemer G, Pinton P, Galluzzi L. Targeting mitochondria for cardiovascular disorders: therapeutic potential and obstacles. *Nat Rev Cardiol* 2019;**16**:33–55.
2. Murphy E, Ardehali H, Balaban RS, DiLisa F, Dorn GW 2nd, Kitsis RN, et al. Mitochondrial function, biology, and role in disease: a scientific statement from the American Heart Association. *Circ Res* 2016;**118**: 1960–1991.
3. Tian R, Colucci WS, Arany Z, Bachschmid MM, Ballinger SW, Boudina S, et al. Unlocking the secrets of mitochondria in the cardiovascular system: path to a cure in heart failure—a report from the 2018 National Heart, Lung, and Blood Institute Workshop. *Circulation* 2019;**140**: 1205–1216.
4. Hendgen-Cotta UB, Giorgio V, Hool L. Mitochondria at the crossroads of survival and demise. *Oxid Med Cell Longev* 2019;**2019**:2608187.
5. Song M, Dorn GW 2nd. Mitoconfusion: noncanonical functioning of dynamism factors in static mitochondria of the heart. *Cell Metab* 2015;**21**:195–205.
6. Song M, Franco A, Fleischer J, Zhang L, Dorn GW 2nd. Abrogating mitochondrial dynamics in mouse hearts accelerates mitochondrial senescence. *Cell Metab* 2017;**26**:872–883, e5.
7. Brown DA, Perry JB, Allen ME, Sabbah HN, Stauffer BL, Shaikh SR, et al. Expert consensus document: mitochondrial function as a therapeutic target in heart failure. *Nat Rev Cardiol* 2017;**14**:238–250.
8. Treskatsch S, Shakibaei M, Feldheiser A, Shaqura M, Dehe L, Roepke TK, et al. Ultrastructural changes associated with myocardial apoptosis, in failing rat hearts induced by volume overload. *Int J Cardiol* 2015;**197**:327–332.
9. Takemura G, Onoue K, Kashimura T, Kanamori H, Okada H, Tsujimoto A, et al. Electron microscopic findings are an important aid for diagnosing mitochondrial cardiomyopathy with mitochondrial DNA mutation 3243A>G. *Circ Heart Fail* 2016;**9**:e003283.
10. Daghistani HM, Rajab BS, Kitmitto A. Three-dimensional electron microscopy techniques for unravelling mitochondrial dysfunction in heart failure and identification of new pharmacological targets. *Br J Pharmacol* 2019;**176**:4340–4359.
11. Sabbah HN. Targeting the mitochondria in heart failure: a translational perspective. *JACC Basic Transl Sci* 2020;**5**:88–106.
12. Garnham JO, Roberts LD, Caspi T, Al-Owais MM, Bullock M, Swoboda PB, et al. Divergent skeletal muscle mitochondrial phenotype between male and female patients with chronic heart failure. *J Cachexia Sarcopenia Muscle* 2020;**11**:79–88.
13. Hughes MC, Ramos SV, Turnbull PC, Rebalka IA, Cao A, Monaco CMF, et al. Early myopathy in Duchenne muscular dystrophy is associated with elevated mitochondrial H_2O_2 emission during impaired oxidative phosphorylation. *J Cachexia Sarcopenia Muscle* 2019;**10**: 643–661.
14. Walter MC, Reilich P. Recent developments in Duchenne muscular dystrophy: facts and numbers. *J Cachexia Sarcopenia Muscle* 2017;**8**:681–685.
15. McNally EM, Kaltman JR, Benson DW, Canter CE, Cripe LH, Duan D, et al. Contemporary cardiac issues in Duchenne muscular dystrophy. Working Group of the National Heart, Lung, and Blood Institute in collaboration with Parent Project Muscular Dystrophy. *Circulation* 2015;**131**:1590–1598.
16. Hughes MC, Ramos SV, Turnbull PC, Edgett BA, Huber JS, Polidovitch N, et al. Impairments in left ventricular mitochondrial bioenergetics precede overt cardiac dysfunction and remodelling in Duchenne muscular dystrophy. *J Physiol* 2020;**598**: 1377–1392.
17. Knowlton AA, Liu TT. Mitochondrial dynamics and heart failure. *Compr Physiol* 2015;**6**:507–526.
18. Liesa M, Shirihai OS. Mitochondrial dynamics in the regulation of nutrient utilization and energy expenditure. *Cell Metab* 2013;**17**:491–506.
19. Hoppel CL, Tandler B, Fujioka H, Riva A. Dynamic organization of mitochondria in human heart and in myocardial disease. *Int J Biochem Cell B* 2009;**41**:1949–1956.
20. Riva A, Faa G, Loffredo F, Piludu M, Riva FT. An improved OsO_4 maceration method for the visualization of internal structures and surfaces in human bioptic specimens by high-resolution scanning electron microscopy. *Scanning Microsc* 1999;**13**:111–122.
21. Riva A, Tandler B, Lesnefsky EJ, Conti G, Loffredo F, Vazquez E, et al. Structure of cristae in cardiac mitochondria of aged rat. *Mech of Age Develop* 2006;**127**: 917–921.
22. Xu CS, Hayworth KJ, Lu Z, Grob P, Hassan AM, Garcia-Cerdan JG, et al. Enhanced FIB-SEM systems for large-volume 3D imaging. *Elife* 2017;**6**:e25916.
23. Kubli DA, Quinsay MM, Huang C, Lee Y, Gustafsson AB. Bnip3 functions as a mitochondrial sensor of oxidative stress during myocardial ischemia/reperfusion. *Am J Physiol Heart Circ Physiol* 2008;**295**: H2025–H2031.
24. Hamacher-Brady A, Brady NR, Logue SE, Sayen MR, Jinno M, Kirshenbaum LA, et al. Response to myocardial ischemia/reperfusion injury involves Bnip3 and autophagy. *Cell Death Differ* 2007;**14**:146–157.
25. Mehrabani S, Bagherniya M, Askari G, Read MI, Sahebkar A. The effect of fasting or calorie restriction on mitophagy induction: a literature review. *J Cachexia Sarcopenia Muscle* 2020;**11**:1447–1458.
26. Diwan A, Krenz M, Syed FM, Wansapura J, Ren X, Koesters AG, et al. Inhibition of ischemic cardiomyocyte apoptosis through targeted ablation of Bnip3 restrains postinfarction remodeling in mice. *J Clin Invest* 2007;**117**:2825–2833.
27. Bravo-San Pedro JM, Kroemer G, Galluzzi L. Autophagy and mitophagy in cardiovascular disease. *Circ Res* 2017;**120**:1812–1824.
28. Du Q, Zhu B, Zhai Q, Yu B. Sirt3 attenuates doxorubicin-induced cardiac hypertrophy and mitochondrial dysfunction via suppression of Bnip3. *Am J Transl Res* 2017;**9**:3360–3373.
29. Li E, Li X, Huang J, Xu C, Liang Q, Ren K, et al. BMAL1 regulates mitochondrial fission and mitophagy through mitochondrial protein BNIP3 and is critical in the development of dilated cardiomyopathy. *Protein Cell* 2020;**11**:661–679.
30. Seligman A, Wasserkrug H, Hanker JA. A new staining method (OTO) for enhancing contrast of lipid-containing membranes and droplets in osmium tetroxide-fixed tissue with osmiophilic thiocarbohydrazide (TCH). *J Cell Biol* 1966;**30**:424–432.
31. Zhang Q, Duplany A, Moncollin V, Mouradian S, Goillot E, Mazelin L, et al. Lack of muscle mTOR kinase activity causes early onset myopathy and compromises whole-body homeostasis. *J Cachexia Sarcopenia Muscle* 2019;**10**:35–53.
32. Schindelin J, Arganda-Carreras I, Frise E, Kaynig V, Longair M, Pietzsch T, et al. Fiji: an open-source platform for biological-image analysis. *Nat Methods* 2012;**9**: 676–682.
33. Hendgen-Cotta UB, Esfeld S, Rudi K, Miinalainen I, Klare JP, Rassaf T. Cytosolic BNIP3 dimer interacts with mitochondrial BAX forming heterodimers in the mitochondrial outer membrane under basal conditions. *Int J Mol Sci* 2017;**18**:687.
34. Abreu P, Kowaltowski AJ. Satellite cell self-renewal in endurance exercise is mediated by inhibition of mitochondrial oxygen consumption. *J Cachexia Sarcopenia Muscle* 2020;**11**:1661–1676.
35. Rammos C, Hendgen-Cotta UB, Totzeck M, Pohl J, Ludike P, Flogel U, et al. Impact of dietary nitrate on age-related diastolic dysfunction. *Eur J Heart Fail* 2016;**18**:599–610.
36. Tsuda M, Fukushima A, Matsumoto J, Takada S, Kakutani N, Nambu H, et al. Protein acetylation in skeletal muscle mitochondria is involved in impaired fatty acid oxidation and exercise intolerance in heart failure. *J Cachexia Sarcopenia Muscle* 2018;**9**:844–859.
37. Lindsey ML, Kassiri Z, Virag JAI, de Castro Brás LE, Scherrer-Crosbie M. Guidelines for measuring cardiac physiology in mice. *Am J Physiol Heart Circ Physiol* 2018;**314**: H733–H752.
38. Bauer M, Cheng S, Jain M, Ngoy S, Theodoropoulos C, Trujillo A, et al. Echocardiographic speckle-tracking based strain imaging for rapid cardiovascular phenotyping in mice. *Circ Res* 2011;**108**: 908–916.
39. Vincent AE, White K, Davey T, Philips J, Ogden RT, Lawless C, et al. Quantitative 3D mapping of the human skeletal muscle

mitochondrial network. *Cell Rep* 2019;**27**:321.
40. Koopman WJH, Visch H-J, Verkaart S, van den Heuvel LWPJ, Smeitink JAM, Willems PHGM. Mitochondrial network complexity and pathological decrease in complex I activity are tightly correlated in isolated human complex I deficiency. *Am J Physiol Cell Physiol* 2005;**289**:C881–C890.
41. Cain MK, Zhang Z, Yuan KH. Univariate and multivariate skewness and kurtosis for measuring nonnormality: prevalence, influence and estimation. *Behav Res Methods* 2017;**49** :1716–1735.
42. Deerinck TJ, Bushong E, Thor A, Ellisman MH. NCMIR methods for 3D EM: A new protocol for preparation of biological specimens for serial block-face SEM. *Microscopy* 2010;**6**.
43. Hendgen-Cotta UB, Esfeld S, Jastrow H, Totzeck M, Altschmied J, Goy C, et al. Mouse cardiac mitochondria do not separate in subsarcolemmal and interfibrillar subpopulations. *Mitochondrion* 2018;**38**:1–5.
44. Rosca MG, Tandler B, Hoppel CL. Mitochondria in cardiac hypertrophy and heart failure. *J Mol Cell Cardiol* 2013;**55**:31–41.
45. Rosca MG, Hoppel CL. Mitochondrial dysfunction in heart failure. *Heart Fail Rev* 2013;**18**:607–622.
46. Dorn GW 2nd. Mitochondrial dynamism and heart disease: changing shape and shaping change. *EMBO Mol Med* 2015;**7**:865–877.
47. Ehses S, Raschke I, Mancuso G, Bernacchia A, Geimer S, Tondera D, et al. Regulation of OPA1 processing and mitochondrial fusion by m-AAA protease isoenzymes and OMA1. *J Cell Biol* 2009;**28**:1023–1036.
48. Gomes LC, Di Benedetto G, Scorrano L. During autophagy mitochondria elongate, are spared from degradation and sustain cell viability. *Nat Cell Biol* 2011;**13**:589–598.
49. Trushina E, Nemutlu E, Zhang S, Christensen T, Camp J, Mesa J, et al. Defects in mitochondrial dynamics and metabolomic signatures of evolving energetic stress in mouse models of familial Alzheimer's disease. *PLoS One* 2012;**7**: e32737.
50. Dorn GW 2nd. Cardiac-specific research platforms engender novel insights into mitochondrial dynamism. *Curr Opin Physiol* 2018;**3**:110–115.
51. Soares CP, Midlej V, de Oliveira MEW, Benchimol M, Costa ML, Mermelstein C. 2D and 3D-organized cardiac cells shows differences in cellular morphology, adhesion junctions, presence of myofibrils and protein expression. *PLoS One* 2012;**7**: e38147.
52. Akins RE Jr, Rockwood D, Robinson KG, Sandusky D, Rabolt J, Pizarro C. Three-dimensional culture alters primary cardiac cell phenotype. *Tissue Eng Part A* 2010; **16**:629–641.
53. Boengler K, Stahlhofen S, van de Sand A, Gres P, Ruiz-Meana M, Garcia-Dorado D, et al. Presence of connexin 43 in subsarcolemmal, but not in interfibrillar cardiomyocyte mitochondria. *Basic Res Cardiol* 2009;**104**:141–147.
54. Koncsos G, Varga ZV, Baranyai T, Ferdinandy P, Schulz R, Giricz Z, et al. Nagarse treatment of cardiac subsarcolemmal and interfibrillar mitochondria leads to artefacts in mitochondrial protein quantification. *J Pharmacol Toxicol Methods* 2018;**91**:50–58.
55. Boengler K, Kosiol M, Mayr M, Schulz R, Rohrbach S. Mitochondria and ageing: role in heart, skeletal muscle and adipose tissue. *J Cachexia Sarcopenia Muscle* 2017;**8**: 349–369.
56. Chen Y, Dorn GW 2nd. PINK1-phosphorylated mitofusin 2 is a Parkin receptor for culling damaged mitochondria. *Science* 2013;**340**:471–475.
57. Kalkhoran SB, Hall AR, White IJ, Cooper J, Fan Q, Ong S-B, et al. Assessing the effects of mitofusin 2 deficiency in the adult heart using 3D electron tomography. *Physiol Rep* 2017;**5**:e13437.
58. Daido S, Kanzawa T, Yamamoto A, Takeuchi H, Kondo Y, Kondo S. Pivotal role of the cell death factor BNIP3 in ceramide-induced autophagic cell death in malignant glioma cells. *Cancer Res* 2004;**64**:4286–4293.
59. Kanzawa T, Zhang L, Xiao L, Germano IM, Kondo Y, Kondo S. Arsenic trioxide induces autophagic cell death in malignant glioma cells by upregulation of mitochondrial cell death protein BNIP3. *Oncogene* 2005;**24**:980–991.
60. Gao A, Jiang J, Xie F, Chen L. Bnip3 in mitophagy: novel insights and potential therapeutic target for diseases of secondary mitochondrial dysfunction. *Clin Chim Acta* 2020;**506**:72–83.
61. Mammucari C, Milan G, Romanello V, Masiero E, Rudolf R, Del Piccolo P, et al. FoxO3 controls autophagy in skeletal muscle in vivo. *Cell Metab* 2007;**6**:458–471.
62. Tracy K, Dibling BC, Spike BT, Knabb JR, Schumacker P, Macleod KF. BNIP3 is an RB/E2F target gene required for hypoxia-induced autophagy. *Mol Cell Biol* 2007;**27**:6229–6242.
63. Hirano M, Emmanuele V, Quinzii CM. Emerging therapies for mitochondrial diseases. *Essays Biochem* 2018;**62**:467–481.
64. Oost LJ, Kustermann M, Armani A, Blaauw B, Romanello V. Fibroblast growth factor 21 controls mitophagy and muscle mass. *J Cachexia Sarcopenia Muscle* 2019;**10**: 630–642.
65. Hamacher-Brady A, Brady NR, Gottlieb RA, Gustafsson AB. Autophagy as a protective response to Bnip3-mediated apoptotic signaling in the heart. *Autophagy* 2006;**2**: 307–309.
66. Chaanine AH, Gordon RE, Kohlbrenner E, Benard L, Jeong D, Hajjar RJ. Potential role of BNIP3 in cardiac remodeling, myocardial stiffness, and endoplasmic reticulum mitochondrial calcium homeostasis in diastolic and systolic heart failure. *Circ Heart Fail* 2013;**6**:572–583.
67. Chen Y, Liu Y, Dorn GW 2nd. Mitochondrial fusion is essential for organelle function and cardiac homeostasis. *Circ Res* 2011;**109**:1327–1331.
68. Papanicolaou KN, Kikuchi R, Ngoh GA, Coughlan KA, Dominguez I, Stanley WC, et al. Mitofusins 1 and 2 are essential for postnatal metabolic remodeling in heart. *Circ Res* 2012;**111**:1012–1026.
69. Ikeda Y, Shirakabe A, Maejima Y, Zhai P, Sciarretta S, Toli J, et al. Endogenous Drp1 mediates mitochondrial autophagy and protects the heart against energy stress. *Circ Res* 2015;**116**:264–278.
70. Wai T, Garcia-Prieto J, Baker MJ, Merkwirth C, Benit P, Rustin P, et al. Imbalanced OPA1 processing and mitochondrial fragmentation cause heart failure in mice. *Science* 2015;**350**:aad0116.
71. Lin L, Zhang M, Yan R, Shan H, Diao J, Wei J. Inhibition of Drp1 attenuates mitochondrial damage and myocardial injury in Coxsackievirus B3 induced myocarditis. *Biochem Biophys Res Commun* 2017;**484**: 550–556.
72. Wu B, Li J, Ni H, Zhuang X, Qi Z, Chen Q, et al. TLR4 activation promotes the progression of experimental autoimmune myocarditis to dilated cardiomyopathy by inducing mitochondrial dynamic imbalance. *Oxid Med Cell Longev* 2018;**2018**: 3181278.
73. Landes T, Emorine LJ, Courilleau D, Rojo M, Belenguer P, Arnauné-Pelloquin L. The BH3-only Bnip3 binds to the dynamin Opa1 to promote mitochondrial fragmentation and apoptosis by distinct mechanisms. *EMBO Rep* 2010;**11**:459–465.
74. Picard M, McManus MJ, Csordas G, Varnai P, Dorn GW 2nd, Williams D, et al. Trans-mitochondrial coordination of cristae at regulated membrane junctions. *Nat Commun* 2015;**6**:6259.
75. Jarosz J, Ghosh S, Delbridge LMD, Petzer A, Hickey AJR, Crampin EJ, et al. Changes in mitochondrial morphology and organization can enhance energy supply from mitochondrial oxidative phosphorylation in diabetic cardiomyopathy. *Am J Physiol Cell Physiol* 2017;**312**:C190–C197.
76. von Haehling S, Morley JE, Coats AJS, Anker SD. Ethical guidelines for publishing in the Journal of Cachexia, Sarcopenia and Muscle: update 2019. *J Cachexia Sarcopenia Muscle* 2019;**10**:1143–1145.

Received: 25 June 2021 | Revised: 31 August 2021 | Accepted: 31 August 2021

DOI: 10.1111/jmi.13056

Journal of Microscopy RMS

INVITED REVIEW

Correlative light and volume electron microscopy (vCLEM): How community participation can advance developing technologies

Christopher J. Guerin | **Saskia Lippens**

VIB Bio Imaging Core, VIB – Ghent University, Ghent, Belgium

Correspondence
Saskia Lippens, VIB Bio Imaging Core, VIB – Ghent University, Ghent, Belgium.
Email: saskia.lippens@irc.vib-ugent.be

Abstract

Correlative light and electron microscopy is a valuable tool to image samples across resolution scales and link data on structure and function. While studies using this technique have been available since the 1960s, recent developments have enabled applying these workflows to large volumes of cells and tissues. Much of the development in this area has been facilitated through the collaborative efforts of microscopists and commercial companies to bring the methods, hardware and image processing technologies needed into laboratories and core imaging facilities. This is a prime example of how what was once a niche area can be brought into the mainstream of microscopy by the efforts of imaging pioneers who push the boundaries of possibility.

KEYWORDS

correlative light and electron microscopy, correlative volume electron microscopy, electron microscopy, volume electron microscopy

In the 1980s when confocal microscopes became commercially available some electron microscopy (EM) labs invested in the technology. Since electron microscopists generally used light microscopy (LM) mostly to examine semi-thin sections before taking ultra-thin ones to examine in the transmission electron microscope (TEM), this must have seemed to many an extravagant purchase. However, the confocal was able to reveal the wonder of cell structure in three dimensions (3D), and because of its ability to image at resolutions approaching the Abbe LM limits it also resolved details previously obscured by light scattering from out of focus image planes. This reduced the resolution gap between the two microscopy technologies and thereby made it easier to target EM studies to specific areas. Through newly improved immunohistochemical techniques, as well as better fluorescent probes, electron microscopists were also able to focus their TEM studies to areas where proteins of interest were located. This was in many ways the beginning of modern 3D correlative light and electron microscopy (CLEM). Unfortunately true CLEM where microscopists could use the same probe in the LM and EM was still years away. While confocal microscopy was a big leap forward in 3D light microscopic resolution and visualisation there was little hope to extend this to the world of ultrastructure. The only method available at the time to achieve real volume in an electron microscopy data set was serial ultra-thin sectioning. One study from 1986 reconstructed 4 retinal amacrine cells from serial TEM sections[1] and it took 4 years to complete, so for all practical purposes 3D

correlative microscopy was still a pleasant but unachievable dream.

CLEM as a technique can be dated back to the1960s when pioneering microscopists such as Larry W. McDonald and Hans Dieter Geissinger attempted to use the resolving power of the electron microscope to add ultrastructural information to that produced by their light microscopic studies.[2] These early CLEM studies were almost exclusively performed in two dimensions (2D) typically combining LM imaging of sliced tissues with either SEM or TEM. Beginning in the early 1980s the 3D information from these studies was increased through the use of confocal microscopes but adding 3D EM to CLEM studies was still very challenging.[3] The obvious advantages of 2D CLEM were that the equipment was widely available, but the disadvantages were the lack of dimensional information resulting from the limited sample size in Z produced by SEM and TEM. TEM tomography could also produce results in 3D[4]; however, the volumes that could be studied were limited by the accelerating voltages of the TEMs used, and samples could normally not exceed a Z thickness of 300 nm. Thus, CLEM studies from the 1980s and early 90s lacked the depth of information that only comes with large correlative 3D volume electron microscopy (vEM) studies. Like all complicated techniques CLEM developed over time with many complex variations, some of which combined multiple advanced techniques such as colloidal gold labelling, live cell video microscopy, scanning electron microscopy (SEM) and high-voltage transmission electron microscopy (hv-TEM). While these studies remained rare, the numbers saw a small increase just after the year 2000 that became exponential in the next two decades. This increase parallels the growing increase in the establishment of institutional imaging cores where the expertise and equipment necessary for complicated workflows were available.

The increase in CLEM studies was also accelerated by a major breakthrough in 3D volume EM when in 1994 Richard J Young and colleagues published a study of the 3D ultrastructure of a mite, *Halarachnidae mesostigmata*,[5] using a scanning electron microscope (SEM) equipped with a focused gallium ion beam that allowed fine milling of the specimen in the SEM chamber interspersed with serial imaging. The technology was termed focused ion beam scanning electron microscopy (FIB-SEM) and had originated in the materials sciences as a method of nanofabrication. In 2006, Jurgen Heymann and colleagues expanded the scope of this technique to cells and tissues using the vEM data for 3D reconstructions of cellular membranes and organelles.[6] Another technology was available for vEM of cells and tissues. In 1983, Steve Leighton and Alan Kuzirian working at the National Institutes of Health and the Woods Hole Marine Biology Laboratory developed a device for serial sectioning resin embedded blocks with a diamond knife placed within the SEM chamber.[7] As personal computer technology and digital imaging were in the very early stages of development this complex instrument was never developed beyond the prototype stage. When computing technology had progressed the in chamber ultramicrotome was further developed by Winfried Denk and Heinz Horstmann for use in vEM of neuronal tissue.[8] The process involved trimming and slicing to smoothen the face of a block of resin embedded tissue, imaging the blockface within the SEM, then slicing the blockface away to reveal a new tissue level and repeating the imaging process. This 'slice and view' technique was commercialised by Gatan and sold under the name of 3View and became known as serial block face scanning electron microscopy (SBF-SEM). The advent of vEM technologies spurred on an increase in 3D correlative light and volume electron microscopy (vCLEM). Studies such as the ones by Bohumil Maco et al, Hannah Armer et al, and Lidia Llorca et al using FIB-SEM,[9–11] and those of Olivier Urwyler et al., and Robert Lees et al. using SBF-SEM,[12,13]. They employed high resolution 3D LM fluorescence for locating tagged proteins combined with 3D vEM to precisely match localisation information with ultrastructure. Other studies have combined vEM techniques to adapt the workflow to utilise the different advantages of the two technologies (Figure 1). Other techniques such as array tomography have also been used to increase the 3D information of EM studies and these techniques continue to be refined and developed.[14]

While vCLEM studies are becoming more frequent the technologies and the techniques leading to successfully implementing these complex methods has taken some time to develop. In a large part this has been a community effort. In 2011, a meeting was held in Munich hosted by Carl Zeiss microscopy that brought together around 50 microscopists from Europe and the United States for 1 1/2 days of lectures and discussion concerning the future of CLEM as a 3D technique. Although at this time the techniques and workflows were in a very early stage of development, the enthusiasm for moving them forward was high. This small group formed the nucleus for a community centered around vEM and from that came the plan for a second larger and longer meeting that was held at the Vlaanderen Institute of Biotechnology (VIB) in Ghent in 2014. The organisers chose the title of 'From 3D Light to 3D Electron Microscopy' and a scientific committee was formed to construct the program and choose the speakers. Carl Zeiss provided financial and logistical support but left the specifics of the program to the scientific committee. The response from the scientific community to this new congress was enthusiastic, and the 160 available participant slots filled up quickly. In addition to the United States and Europe, participants came from Africa,

Journal of Microscopy RMS

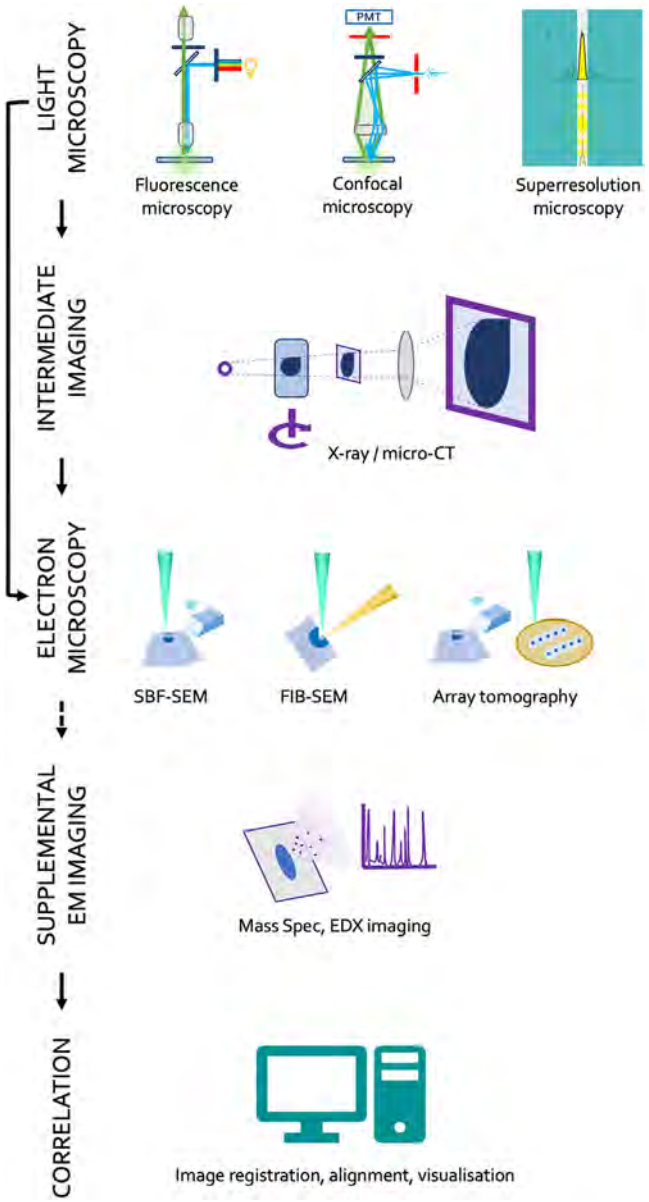

FIGURE 1 Possible workflows for vCLEM. A number of light microscopic imaging techniques can be incorporated into a vCLEM experiment with the aim of identifying particular structures of interest usually by fluorescently staining a protein or structure of interest. Intermediate imaging steps using X-Ray microscopy or micro CT can further assist in identifying a region of interest (ROI) to be targeted in the electron microscope. Typical vEM methods used would be in chamber sectioning either with a diamond knife (SBF-SEM) or a focused ion beam (FIB-SEM) or external sectioning of a resin block followed by serial imaging (AT) of the resulting sections. Supplemental imaging techniques such as EDX or mass spectrometry can be used to provide elemental or protein signatures. Finally, the LM and vEM images and any associated data are compiled in the registered sections and visualisation is carried out via computer modelling of the data stack

the Middle East, South America and India indicating that the growing interest in vEM was international. The idea was to create a very interactive meeting that would combine lectures and discussion groups and there was a strong focus placed on practical workshops to demonstrate the instrumentation and techniques used in the vCLEM workflow. Workshops covered sample preparation, SBF-SEM, FIB-SEM and image processing. The meeting was highly successful and at the end, plans were put in place for another congress. Feedback from attendees indicated that a biennial schedule was preferred so it was decided to hold next congress in 2016 at the European Molecular Biology Laboratory (EMBL) in Heidelberg. Scientific sessions in this 3rd edition covered examples of CLEM methods, sample diversity, image processing and analysis and extending vCLEM by including other techniques such as energy dispersive spectroscopy (EDS),[15] Micro CT[16] and X-Ray microscopy.[17] Once again the registration slots were taken up rapidly and the program for this meeting very closely followed the 2014 Ghent format, interspersing lectures, workshops and discussion groups. Up until this point, the congress had focused on FIB-SEM and SBF-SEM but at this edition it was decided to add array tomography as it was a technique that could also provide 3D volume information and was becoming mature enough to attract a considerable number of laboratories and imaging core facilities to adopt it.[18]

The 4th edition was held in 2018, again in Ghent, and by this time it was obvious that many laboratories and imaging cores were adopting vCLEM techniques with the numbers of international participants and institutions represented increasing. Plans were made for a 5th edition of the congress to be held at the Francis Crick Institute in London in March of 2020. However, the SARS-CoV-2 pandemic forced its postponement. It was decided to hold the event online as a virtual congress and that took place in February of 2021. While the committee had some regrets that the warm and very personal nature of the preceding congresses would be lost it was more than made up for by being able to open the registration without limits thus making this edition more inclusive than before. In the end over 1450 participants registered representing more than 40 countries on 6 continents. It was challenging to adapt the format of the previous meetings to a virtual space, but again with support from Carl Zeiss the meeting was able to provide webinar based scientific sessions, interactive practical workshops and Zoom meeting format round table discussions. The meeting was held in 3 half-day sessions to try and accommodate the many time zones of the participants and each day concluded with virtual open lounges in which participants could interact with speakers, workshop leaders and round table moderators.

One of the hallmarks of this event has been the very interactive nature of the congresses and the remarkable openness and level of networking and sharing that occurred. This has helped drive the vCLEM technologies forward and brought about many collaborations that have resulted in peer reviewed published works. When looking back on the different congress editions, one can notice an evolution in the discussions, which represents how vCLEM had evolved in merely a handful of years. The earlier editions covered practical details on getting started in vCLEM, explored which data reconstruction tools were available, and looked at possibilities to expand protocols and workflows to various sample types. The latest editions have focused on future challenges such as setting standards for data repositories and automating workflows. The congresses were an important barometer for 'sensing' and capturing the areas in which work needed to be done, and out of those interactions, a great many new tools and even some instrumentation advances have been developed. For example, discussions on the problems of sample charging led directly to the development of a focal charge compensation system in Mark Ellisman's laboratory at the National Center for Microscopy and Imaging Research that was later adopted and commercialised by Carl Zeiss.[19] Other developments have been seen in the area of image reconstruction and analysis. The Microscopy Image Browser was significantly influenced based upon community discussions.[20]

As before, the 2021 congress was able to bring more new techniques and innovations into focus. In her Keynote lecture on array tomographic approaches Professor Kristina Micheva of Stanford University showed how the technique of Thomas Templier (MagC) uses a resin block containing magnetic particles as well as fluorescent beads to greatly simplify both serial section manipulation as well as alignment for reconstruction.[21] The number of innovative correlative workflows also demonstrated how multi-modal aspects of vCLEM are progressing, and examples combining novel approaches were presented including: XRay microscopy, Micro-CT, elemental analysis using EDX and micro image mass spectrometry (CLEIMiT). In his keynote, Professor Wah Chiu of Stanford University showed that whole cell high-voltage TEM cryotomography could be used for vCLEM incorporating structural biology approaches to localise and examine individual protein molecules in situ.[22] Image analysis and reconstruction, which has been a real bottleneck to widespread implementation of vCLEM, has also seen new developments based upon discussions in previous congresses. Perrine Paul-Gilloteaux from Centre National de la Recherche Scientifique presented EC-CLEM software for combining multi-scale multi-modal images,[23] John Bogovic from Howard Huges Medical Institute demonstrated a deep learning based pipeline for image recognition and segmentation,[24] Joris Roels of the Vlaanderen Institute of Biotechnology demonstrated an automated segmentation method using advanced transfer learning techniques[25] and Ilya Belevich from the University of Helsinki talked about improvements to the microscopy image browser software using deep learning to automate the analysis of multiple datasets (DeepMIB).[26] Although applying vCLEM on diverse biological specimens has been a topic of interest since the first edition, the 2021 conference covered a broad range of biological studies showing that the neuroscience focus of early vCLEM research had been widely extended. Another feature was the showcasing of many biological conclusions that could only be achieved through correlative volume microscopy. vCLEM has matured to a method that can push science forward by deepening our understanding of structure-function relationships. The potential of correlating vEM with single cell data was highlighted in the closing Keynote by Yannick Schwab, who showed how this approach was used to create an atlas of gene expression profiles and cell morphology for the whole polychaete worm *Platinereis dumerilii*.[27]

In the virtual workshop sessions, practical tools and techniques were demonstrated and workflows for Confocal-X-Ray-SBF-SEM, array tomography, and targeted FIB-SEM were presented.[28] Carl Zeiss demonstrated new hardware to facilitate cryo-vCLEM enabling a complete cryo-workflow from widefield to confocal to FIB-SEM. The workshops were hosted in multiple locations demonstrating that it is possible to use vCLEM techniques even if all the equipment necessary for a given workflow is not present in the same facility. They also presented possibilities for individuals without local access to high-end vCLEM equipment to gain access through collaborations and initiatives such as Euro-BioImaging.

As in previous years, the discussion of vCLEM issues by the community was indicative of both current challenges and long-term goals. Besides troubleshooting and improving different steps in workflows, the community is also focusing on how to disseminate workflows and provide general access to technology and data. One of the round table discussions evolved around the need to 'simplify' workflows and how to set these up with 'low tech' solutions. Also the concept of executing a workflow across labs and facilities in different locations, an especially important strategy in times where people cannot travel to centres with specialised equipment, was discussed as a solution to provide access to technology. Proof-of-concept for this was highlighted in one of the workshops where EMBL and VIB performed a vCLEM experiment with samples and data (but not people) travelling between the two institutes. On the data front, there is a general consensus that sharing raw data is of utmost value, and although everyone agrees on

the general philosophy a framework with ground rules and standards would be required to bring this idea into practice. On that subject comparison to other fields (like astronomy and protein databases) are looked to as models for best practice standards and practical implementation of tools for vCLEM repositories.

It is reasonable to ask why this technique and this niche area of EM has been so rapidly advanced by these congresses. Clearly, any meeting where like-minded scientists gather will engender changes that advance science. However, to we who have attended, these meetings seem to have accomplished more in a shorter time. It could be that this small group of techniques, that appeared to be so challenging just 10 years ago, have evolved rapidly because of the relatively small group of scientists who use them needed each other's help to be successful. It is also true that these techniques require equipment that until recently was primarily found in imaging cores, and that two of these cores which have hosted congresses (VIB and EMBL) have as part of their mission educating the scientific community regarding the application of novel techniques. When the congresses began, there were no organised courses where vCLEM could be learned or textbooks that could provide guidance so that the congresses also acted as mini-training courses. It is also true that these meetings have attracted a very stable group of participants, many from core imaging facilities whose willingness to share was not as hampered by individual competition, since serving their users needs was their principal goal. In any event it is clear that the rapidly increasing number of vCLEM publications has paralleled the initiation of the congress series and that many of these papers have come from people who have also attended the congresses.

vCLEM remains a developing technique, but it has proven it's potential to reveal novel structural information that was previously unappreciated or misinterpreted in 2D studies.[29] What began as a rather far-fetched idea grew into an achievable technique and is now moving into the mainstream of CLEM based research. A great deal of the credit should accrue to the microscopists who demonstrated the practicality and possibilities of this technology by working together and publishing their research. Significant credit is also due to companies such as Carl Zeiss and Gatan who developed the instrumentation and promoted the technique despite the fact that the global market was, at least at the beginning, quite limited. Out of the congresses, a vEM community has arisen and is actively involved in standardising, developing and promoting many aspects of vEM. The vEM community initiative is being coordinated by numerous scientists (https://www.volumeem.org/) and working groups are addressing sample preparation, training, data handling and analysis, outreach and instrumentation. Developing complex imaging techniques requires more resources than a single institution, company or individual can provide. Specialist scientific congresses, such as 'From 3D Light to 3D Electron Microscopy', are essential if disruptive technologies are to thrive and grow. The next edition, which is hoped to be a hybrid in person and virtual event, will be held at EMBL in Heidelberg March 13–16, 2022. While imaging across wide resolution scales in three dimensions once seemed a wonderful but impractical idea, the rise of vCLEM shows what can be accomplished by a few intrepid microscopists who believe in pushing boundaries to enable new ways of seeing the micro world.

ACKNOWLEDGEMENTS

The authors thank Drs Lucy Collinson and Yannick Schwab for reading the draft manuscript and providing valuable suggestions. We also appreciate the helpful suggestions provided by the journal's reviewers.

REFERENCES

1. Linberg, K. A., & Fisher, S. K. (1986). An ultrastructural study of interplexiform cell synapses in the human retina. *Journal of Comparative Neurology*, *243*(4), 561–576.
2. Guerin, C. J., Nalan, L., & Klumperman, J. (2020). It's a small, small world: A brief history of biological correlative microscopy. In P. Verkade & L.M. Collinson (Eds.), *Correlative imaging: Focusing on the future*. Wiley: UK.
3. <number>3.</number (1987). *Correlative microscopy in biology: Instrumentation and methods*. M.A. Hyatt (Ed.). Orlando, Florida: Academic Press Inc.
4. Hoppe, W., et al. (1974). Three-dimensional reconstruction of individual negatively stained yeast fatty-acid synthetase molecules from tilt series in the electron microscope. *Hoppe-Seyler's Zeitschrift für Physiologische Chemie*, *355*(11), 1483–1487.
5. Young, R. J., et al. (1993). An application of scanned focused ion beam milling to studies on the internal morphology of small arthropods. *Journal of Microscopy*, *172*(1), 81–88.
6. Heymann, J. A., et al. (2006). Site-specific 3D imaging of cells and tissues with a dual beam microscope. *Journal of Structural Biology*, *155*(1), 63–73.
7. Leighton, S. B. (1981) SEM images of block faces, cut by a miniature microtome within the SEM — A technical note. *Scanning Electron Microscopy*, (Pt 2), 73–76.
8. Denk, W., & Horstmann, H. (2004). Serial block-face scanning electron microscopy to reconstruct three-dimensional tissue nanostructure. *PloS Biology*, *2*(11), e329.
9. Armer, H. E., et al. (2009). Imaging transient blood vessel fusion events in zebrafish by correlative volume electron microscopy. *PloS One*, *4*(11), e7716.
10. Blazquez-Llorca, L., et al. (2015). Correlation of two-photon in vivo imaging and FIB/SEM microscopy. *Journal of Microscopy*, *259*(2), 129–136.
11. Maco, B., et al. (2014). Correlative in vivo 2-photon imaging and focused ion beam scanning electron microscopy: 3D analysis of neuronal ultrastructure. *Methods in Cell Biology*, *124*, 339–361.
12. Lees, R. M., et al. (2017). Correlative two-photon and serial block face scanning electron microscopy in neuronal tissue using 3D

near-infrared branding maps. *Methods in Cell Biology*, *140*, 245–276.
13. Urwyler, O., et al. (2015). Investigating CNS synaptogenesis at single-synapse resolution by combining reverse genetics with correlative light and electron microscopy. *Development (Cambridge, England)*, *142*(2), 394–405.
14. Titze, B., & Genoud, C. (2016). Volume scanning electron microscopy for imaging biological ultrastructure. *Biologie Cellulaire*, *108*(11), 307–323.
15. Madsen, S. J., et al. (2020). Correlative microscopy to localize and characterize iron deposition in Alzheimer's disease. *Journal of Alzheimer's Disease Reports*, *4*(1), 525–536.
16. Morales, A. G., et al. (2016). Micro-CT scouting for transmission electron microscopy of human tissue specimens. *Journal of Microscopy*, *263*(1), 113–117.
17. Bushong, E. A., et al. (2015). X-ray microscopy as an approach to increasing accuracy and efficiency of serial block-face imaging for correlated light and electron microscopy of biological specimens. *Microscopy and Microanalysis*, *21*(1), 231–238.
18. Micheva, K. D., et al. (2010). Array tomography: Imaging stained arrays. *Cold Spring Harbor Protocols*, *2010*(11), pdb prot5526.
19. Deerinck, T. J., et al. (2018). High-performance serial block-face SEM of nonconductive biological samples enabled by focal gas injection-based charge compensation. *Journal of Microscopy*, *270*(2), 142–149.
20. Belevich, I., et al. (2016). Microscopy image browser: A platform for segmentation and analysis of multidimensional datasets. *PloS Biology*, *14*(1), p. e1002340.
21. Templier, T. (2019). MagC, magnetic collection of ultrathin sections for volumetric correlative light and electron microscopy. *Elife*, *8*.
22. Wu, G. H., et al. (2020). Multi-scale 3D cryo-correlative microscopy for vitrified cells. *Structure (London, England)*, *28*(11), 1231–1237 e3.
23. Paul-Gilloteaux, P., et al. (2017). eC-CLEM: Flexible multidimensional registration software for correlative microscopies. *Nature Methods*, *14*(2), 102–103.
24. Scheffer, L. K., et al. (2020). A connectome and analysis of the adult Drosophila central brain. *Elife*, *9*.
25. Roels, J., et al. Domain adaptive segmentation in volume electron microscopy imaging. ISBI 2019. 2019, IEEE: Venice.
26. Belevich, I., & Jokitalo, E. (2021). DeepMIB: User-friendly and open-source software for training of deep learning network for biological image segmentation. *PloS Computational Biology*, *17*(3), e1008374.
27. Vergara, H. M., et al. (2021). Whole-body integration of gene expression and single-cell morphology. *Cell*, *184*(18), 4819–4837. e22.
28. Ronchi, P., et al. (2021). High-precision targeting workflow for volume electron microscopy. *Journal of Cell Biology*, *220*(9).
29. Ornelas, S., et al. (2021). Three-dimensional ultrastructure of the brain pericyte-endothelial interface. *Journal of Cerebral Blood Flow and Metabolism*, *41*(9), 2185–2200.

TEM-like imaging with your SEM

ZEISS

Seeing beyond

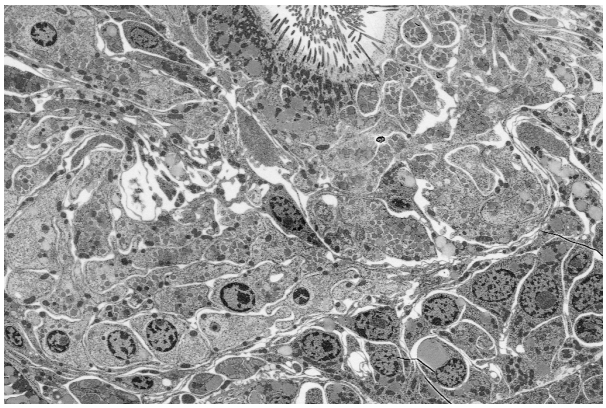

ZEISS Sense BSD

Imaging biological samples with an SEM can be challenging. Rapid acquisition with the desired resolution requires high electron doses and acceleration voltages, which can cause charging effects and sample damage.
ZEISS Sense BSD combines high-resolution ultrastructural imaging with a new degree of efficiency and image quality, making TEM-like imaging possible with your SEM.

zeiss.com/microscopy